

One-step CO₂ hydrogenation to dimethyl ether via packed bed membrane reactors

Citation for published version (APA):

Poto, S. (2023). *One-step CO₂ hydrogenation to dimethyl ether via packed bed membrane reactors*. [Phd Thesis 1 (Research TU/e / Graduation TU/e), Chemical Engineering and Chemistry]. Eindhoven University of Technology.

Document status and date:

Published: 02/06/2023

Document Version:

Publisher's PDF, also known as Version of Record (includes final page, issue and volume numbers)

Please check the document version of this publication:

- A submitted manuscript is the version of the article upon submission and before peer-review. There can be important differences between the submitted version and the official published version of record. People interested in the research are advised to contact the author for the final version of the publication, or visit the DOI to the publisher's website.
- The final author version and the galley proof are versions of the publication after peer review.
- The final published version features the final layout of the paper including the volume, issue and page numbers.

[Link to publication](#)

General rights

Copyright and moral rights for the publications made accessible in the public portal are retained by the authors and/or other copyright owners and it is a condition of accessing publications that users recognise and abide by the legal requirements associated with these rights.

- Users may download and print one copy of any publication from the public portal for the purpose of private study or research.
- You may not further distribute the material or use it for any profit-making activity or commercial gain
- You may freely distribute the URL identifying the publication in the public portal.

If the publication is distributed under the terms of Article 25fa of the Dutch Copyright Act, indicated by the "Taverne" license above, please follow below link for the End User Agreement:

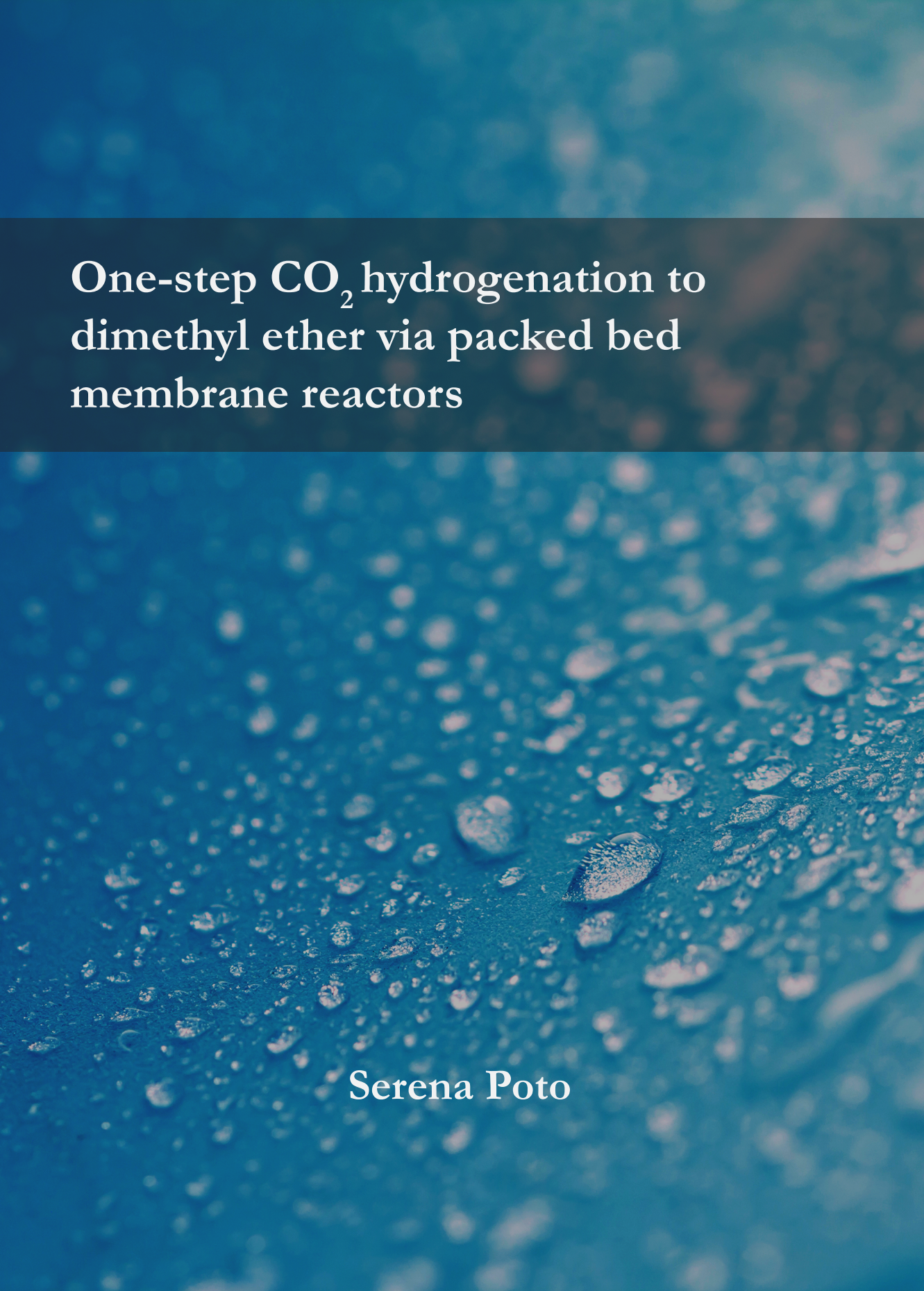
www.tue.nl/taverne

Take down policy

If you believe that this document breaches copyright please contact us at:

openaccess@tue.nl

providing details and we will investigate your claim.

The background of the entire page is a close-up photograph of numerous water droplets of various sizes on a dark blue, textured surface. The droplets are in sharp focus in the foreground, while those in the background are blurred, creating a sense of depth. The lighting highlights the spherical shape and reflective surfaces of the droplets.

One-step CO₂ hydrogenation to dimethyl ether via packed bed membrane reactors

Serena Poto

One-step CO₂ hydrogenation to dimethyl ether via packed bed membrane reactors

PROEFSCHRIFT

ter verkrijging van de graad van doctor aan de Technische Universiteit Eindhoven, op gezag van de rector magnificus prof.dr. S.K. Lenaerts, voor een commissie aangewezen door het College voor Promoties, in het openbaar te verdedigen op vrijdag 2 Juni 2023 om 13:30 uur

door

Serena Poto
Geboren te Battipaglia, Italië

Dit proefschrift is goedgekeurd door de promotoren en de samenstelling van de promotiecommissie is als volgt:

Voorzitter:	prof.dr.ir. J.A.M. Kuipers
1 ^e promotor:	prof.dr. F. Gallucci
Copromotor:	dr. M.F. Neira d'Angelo
Leden:	prof.dr.ir J. van der Schaaf prof.dr. Ž. Tomović prof.dr. A. Urakawa (Technische Universiteit Delft) prof.dr. M. De Falco (Università Campus Bio-Medico, Roma)
Adviseur:	dr. M.A. Llosa Tanco (Tecnalia Research and Innovation)

Het onderzoek of ontwerp dat in dit proefschrift wordt beschreven is uitgevoerd in overeenstemming met de TU/e Gedragscode Wetenschapsbeoefening.

To my family
To Fabio

The research described in this thesis has been carried out in the framework of the European project *C2Fuel*. This project has received funding from the European Union's Horizon 2020 research and innovation program under grant agreement No 838014.



Copyright © 2023 by Serena Poto, Eindhoven, The Netherlands.

All rights reserved. No part of the material protected by this copyright notice may be reproduced or utilized in any form or by any means, electronic or mechanical, including photocopying, recording or by any information storage and retrieval system, without the prior permission of the author.

A catalogue record is available from the Eindhoven University of Technology Library.

ISBN: 978-90-386-5736-3

Cover design by Serena Poto

Printed by Proefschriftspecialist

CONTENTS

List of Abbreviations.....	
Summary.....	xiii
CHAPTER 1: General Introduction	xvi
1.1 CO ₂ emissions and mitigation strategies.....	17
1.2 Dimethyl ether synthesis as CCU pathway	20
1.3 Enhancement of CO ₂ conversion to DME in membrane reactors	24
1.4 Membrane materials for water separation in membrane reactors	26
1.5 Thesis outline	29
References	31
CHAPTER 2: Direct conversion of CO ₂ to dimethyl ether in a packed bed membrane reactor: influence of membrane properties and process conditions	43
2.1 Introduction	44
2.2 Reactor configuration and modeling.....	45
2.3 Simulation results and discussion.....	53
2.4 Conclusions	64
References	70
CHAPTER 3: Vapor/gas separation through carbon molecular sieve membranes (CMSM). Part I: boehmite-phenolic resin with improved hydrophilicity.....	77
3.1 Introduction	78
3.2 Experimental.....	80
3.3 Theory of water transport through CMSM.....	84
3.4 Results and discussion	87
3.5 Conclusions	100
References	110
CHAPTER 4: Vapor/gas separation through carbon molecular sieve membranes (CMSM). Part II: effect of the carbonization temperature	113
4.1 Introduction	114
4.2 Experimental.....	115
4.3 Results and discussion	118
4.4 Conclusions	137
References	144

CHAPTER 5: Experimental investigation of a packed bed membrane reactor for the direct conversion of CO ₂ to dimethyl ether	147
5.1 Introduction	148
5.2 Experimental	150
5.3 Modeling	157
5.4 Results and discussion	157
5.5 Conclusions	168
References	176
CHAPTER 6: Evaluation of the relevant mass and heat transfer phenomena in a packed bed membrane reactor for the direct conversion of CO ₂ to dimethyl ether	179
6.1 Introduction	180
6.2 Methodology and numerical implementation	182
6.3 Heat and mass transfer phenomena at particle scale	184
6.4 Heat and mass transfer phenomena at the particle-fluid interphase	190
6.5 1D packed bed reactor model: heterogeneous vs pseudo-homogeneous model and deviation from plug flow behavior	193
6.6 1D pseudo-homogeneous packed bed membrane reactor model: effect of diffusion limitations on a large scale PBR and PBMR	198
6.7 2D pseudo-homogeneous packed bed membrane reactor model: effect of concentration polarization phenomena	204
6.8 Conclusions	212
References	224
CHAPTER 7: Tecno-economic assessment of the one-step CO ₂ conversion to dimethyl ether in a membrane-assisted process	227
7.1 Introduction	228
7.2 Methodology and assumptions	229
7.3 Results of process modeling	237
7.4 Technical analysis	247
7.5 Economic analysis	251
7.6 Forecasting and sensitivity analysis	253
7.7 Conclusions	263
References	283
CHAPTER 8: Conclusions and Outlook	287

8.1	Conclusions	287
8.2	Outlook and recommendation for future research.....	291
	References	292
	List of publications	293
	Journal Articles	293
	Journal Articles out of the scope of this thesis.....	293
	Oral presentations	294
	Poster presentations.....	295
	Acknowledgements.....	297
	Curriculum Vitae.....	301

LIST OF ABBREVIATIONS

Abbreviation	Definition
1D, 2D, 3D	1 dimensional, 2 dimensional, 3 dimensional
ACAPEX	Annualized capital expenditure
AD	Adsorption-diffusion
AE	Alkaline electrolysis
Al-CMSM	Alumina supported carbon molecular sieve membranes
BET	Brunauer, Emmett and Teller (analysis)
BJH	Barrett, Joyner and Halenda (analysis)
CAGR	Compound annual growth rate
CAPEX	Capital expenditure
CCS	Carbon capture and storage
CCU	Carbon capture and utilization
CE	Chemical equipment (index)
CEM	Controlled evaporation mixer
CGE	Cold gas efficiency
CMR	Carbon membrane reactor
CMSM (or CM)	Carbon molecular sieve membrane (or carbon membrane)
CP	Concentration polarization
CuZA	Copper-zinc-alumina (catalyst)
CW	Cooling water
DCFA (or DCF)	Discounted cash flow analysis (or discounted cash flow)
DME	Dimethyl ether
DMFC	Direct methanol fuel cell
EUR	Euro
EXP.	Experimental
FCI	Fixed capital investment
FID	Flame ionization detector
FTIR	Fourier transform infrared (spectroscopy)
GC	Gas chromatography
GHSV	Gas hourly space velocity
HEN	Heat exchanger network
HP	High pressure
IC	Indirect cost
ISBL	Inside battery limits
KPI	Key process indicator

kTA	Kilotons per annum (year)
LHV	Low heating value
LPG	Liquified petroleum gas
MCU	Multistage compression unit
MDSP	Minimum dimethyl ether selling price
MeOH	Methanol
MMT	Million metric tons
MR	Membrane reactor
MS	Molecular sieving
MSW	Municipal solid waste
MT _{ext}	External mass transfer
MT _{int}	Internal mass transfer
MTG	Methanol to gasoline
NG	Natural gas
NMP	N-methyl-2-pyrrolidone
OPEX	Operational expenditure
OSBL	Outside battery limits
PBMR	Packed bed membrane reactor
PBR	Packed bed reactor
PEC	Purchase equipment cost (or photoelectrochemical)
PEM	Polymer electrolyte membrane (electrolysis)
PFR	Plug flow reactor
PV	Pore volume
rWGS	Reverse water gas shift
REN	Renewable
SA	Surface area
SEM	Scanning electron microscopy
SEWGS	Sorption enhanced water gas shift
SMR	Steam methane reforming
SOEC (or SOE)	Solid oxide electrolyzer cell (or solid oxide electrolyzer)
SW	Sweep gas ratio
TAC	Total annual cost
TCD	Thermal conductivity detector
TGA (or GA)	Thermogravimetric analysis (or gravimetric analysis)
TPD	Temperature programmed desorption
TPR	Temperature programmed reduction
ULEV	Ultra-low emission vehicles
USD	US dollars
WACC	Weighted average cost of capital

WC	Working capital
WGS	Water gas shift
WR	Water removal
XPS	X-ray photoelectron spectroscopy
XRD	X-ray diffraction (analysis)

SUMMARY

The growing concerns about CO₂ emissions and their effects on climate change have driven the research agenda of the last decades in strive for more sustainable processes.

The carbon capture and storage technology (CCS) has been recognized as one of the most powerful short-term solutions to mitigate anthropogenic CO₂ emissions, mostly coming from flue gases of fossil-based power and chemical plant. However, the carbon capture and utilization approach (CCU) becomes even more attractive when a long-term solution is desired. Furthermore, reconverting the collected CO₂ to produce more valuable carbon-based products would significantly contribute to reduce the use of conventional fossil-based feedstocks.

Among the different products that can be produced from CO₂, dimethyl ether (DME) is very attractive. DME is a particularly clean fuel, which can replace LPG or diesel without any (or limited) changes in the current engines. Currently, DME is produced from fossil fuels via an energy intensive process: natural gas is first converted into syngas (i.e., a mixture of H₂ and CO) via steam reforming, followed by the methanol synthesis and dehydration to DME. Thus, producing DME from captured CO₂ and renewable H₂ is not only a valid route for CO₂ valorisation and/or H₂ storage, but also a way to render the process more sustainable.

Nevertheless, replacing the carbon source from CO to CO₂ is not trivial and comes with some challenges that needs to be tackled. One of the biggest challenges is the strong thermodynamic limitation of the reaction system. Combining the methanol synthesis and dehydration in a single reactor, in the so-called one-step – or direct – route, is a first effective solution to improve reaction performance, based on the in-situ consumption of methanol to form DME.

However, the main issues of these reactions derive from the high volume of water produced, which contributes to pose even stronger thermodynamic limitations, as well as to accelerate catalyst deactivation phenomena. As a result, this process could enormously benefit from the in-situ removal of water from the reaction environment, using the membrane reactor (MR) technology.

In this thesis, the use of the membrane reactor technology for the one-step CO₂ hydrogenation to DME reaction is thoroughly studied under different perspectives, ranging from the selection and development of the membrane materials, to the experimental demonstration of the technology.

A general introduction to the topic is given in **Chapter 1**, which, after stressing on the urgency of limiting CO₂ emissions as an essential step to tackle the climate crisis, it provides an overview of the possible solutions which could be implemented in the

chemical and energy sectors. Thereafter, the synthesis of DME is presented as a promising CO₂ utilization pathway. The benchmark DME production process is first described to later highlight the main challenges which come with replacing the carbon source with pure CO₂. Finally, the membrane reactor technology is described, together with an overview on the suitable membrane materials, with particular focus on carbon molecular sieve membranes.

In **Chapter 2**, a one dimensional phenomenological membrane reactor model is developed and used to determine the optimal membrane performance in terms of water permeability and perm-selectivity, to shed light into suitable material as well as to set a target for the membrane development. The cocurrent circulation of a sweep gas stream containing the reactants (i.e., CO₂ and H₂), is proposed as an effective strategy to promote the selective water removal from the reaction environment, lowering the membrane requirements in terms of perm-selectivity. Based on this study, ceramic supported carbon molecular sieve membranes (CMSMs) are selected as promising materials given their potential hydrophilicity and the possibility to tune their properties, acting on different parameters of the synthesis procedure. Based on the optimal membrane properties, the reactor model is used to study the effect of different process conditions, such as the sweep gas flow and the gradient in total pressure.

Chapter 3 and **4** focus on the study of phenolic resin CMSMs to promote the high temperature (i.e., 150-250 °C) separation of H₂O vapor from (hydrogen-rich) gaseous streams. First the incorporation of hydrophilic boehmite nanosheets (γ -AlO(OH)) in the polymeric resin as a way to improve the membrane hydrophilicity is assessed in **Chapter 3**. The boehmite nanosheets were found to induce an optimum in the hydrophilicity of the membranes as well as into the water permeability and separation factors. The decrease observed both in the membrane hydrophilicity and in the separation performance at larger content of boehmite is linked to the gradual transformation of the boehmite nanosheets into a less hydrophilic γ -Al₂O₃ and to the increase in the tortuosity of the porous structure. In this chapter, the H₂O permeation mechanism is further investigated by modeling the mono- and multi- layer adsorption and capillary condensation of water in microporous media, which result as the main transport mechanisms in the explored conditions.

Further, in **Chapter 4**, the effect of the carbonization temperature on the vapor/gas separation performance is studied, with particular focus on the water interaction with the membrane surface. FTIR analysis is first used to determine the changes in the surface functionality of the CMSM occurring during the carbonization step. Then, the membrane interaction with water is assessed via in-situ FTIR analysis from which it is clear that the membrane loses its hydrophilicity upon increasing the carbonization temperature. The analysis of the permeation properties of these membranes reveal that the trend induced by the carbonization temperature solely depends on the differences in the pore size distribution. On the other hand, the trend induced by the operating temperature depends on the dominant transport

mechanism. Highest permeabilities were found for the membranes carbonized in the range 600-700 °C, given the bi-modal nature of their pore size distribution, combined with a large fraction of pores in the molecular sieve region.

In **Chapter 5**, an experimental proof-of-concept of the membrane reactor technology is presented, which also allows for the validation of the previously developed phenomenological reactor models. This result is of high relevance, since the reactor models could be used for further optimization studies and to simulate conditions which were not explored experimentally. Despite the permeance of the CMSM used in this work not perfectly matching with the previously set target, the packed bed membrane reactor (PBMR) outperforms the conventional packed bed reactor (PBR) in most of the experimental conditions. Larger improvements were found at low space velocities, due to the system approaching thermodynamic equilibrium (i.e., larger water content). However, given the large extent of product removal, at temperatures higher than 200 °C, the membrane reactor enhances the formation of CO (i.e., through r-WGS) more than DME. Finally, as predicted in Chapter 1, the circulation of the sweep gas proved to be an effective way to promote the removal of water from the reaction environment.

In **Chapter 6**, the membrane reactor is modeled under a multi-scale perspective with a particular focus on the heat and mass transfer phenomena occurring at different scales (i.e., from the particles, to the membrane and the reactor scale). Intra-particle diffusion limitation and concentration polarization were found to have a significant influence on the reactor performance when simulated at conditions/sizes which are relevant to large scale operation. Given the complexity of the model obtained with the incorporation of both these phenomena, short-cut methods are developed to account for such effects, to be implemented in a simplified 1D pseudo-homogeneous reactor model. The simplified model predicts with high accuracy the simulation results of the more rigorous models, with maximum deviation below 5%, in the range of conditions which are relevant to this process. Finally, a further optimization of the reactors in terms of mass and composition of the catalyst bed is proposed, based on the new findings.

Chapter 7 presents a techno-economic evaluation of the conventional and MR-assisted CO₂-to-DME process, in order to identify the economic bottlenecks of this technology, as well as to make a realistic prediction about when this CO₂ utilization route would become convenient at industrial scale. The MR-assisted plant was found to require less energy input to produce the same amount of DME and to convert the feedstock (CO₂+H₂) more effectively. Both processes are OPEX intensive, with the largest impact given by the cost of H₂. Despite the MR-assisted process allows for a considerable reduction in the production cost (i.e., 1.12 times lower), the process is still not economically viable in the current DME market conditions. Yet, the forecast analysis predicts that the MR-assisted system could become competitive with the benchmark between 2025 to 2050.

Finally, the main conclusions of this thesis and the research outlook are summarized in **Chapter 8**.

CHAPTER 1

General introduction

1.1 CO₂ EMISSIONS AND MITIGATION STRATEGIES

Nowadays, climate change is widely recognized as one of the biggest challenges of our times, which needs to be tackled with undisputed urgency. Industrialization and urbanization have led to an enormous increase in the anthropogenic CO₂ emissions and thus the CO₂ concentration in the atmosphere, such that already in 1950, the world emitted ca. 6 billion tons of CO₂ [1]. Emissions have continued to grow rapidly (**Figure 1.1**), achieving a value of 37 billion tons in 2021. Only in 2020, due to the COVID-19 pandemic, the CO₂ emission levels decreased from 37 (in 2019) to 35 billion tons, which underlines how crucial is the impact of human activities to the carbon footprint, especially concerning the transportation sector, which was the most affected by the lockdown measures adopted worldwide [2].

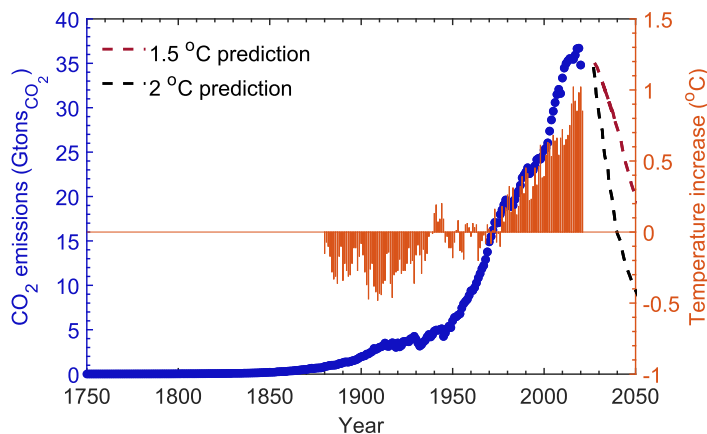


Figure 1.1. Annual CO₂ emissions from fossil fuel and industry, worldwide (left side). The dashed lines represent the predicted reduction in the CO₂ emissions required to keep the average temperature rise below 1.5 °C or 2 °C. The increase in the average surface temperature is reported on the right. Data retrieved from references [2], [3].

A drastic consequence of the anthropogenic CO₂ emissions is that the surface temperature of our planet has risen of ca. 0.08 °C per decade since 1880 [3], such that 2021 was the World's 6th warmest year on record. This has led to significant climate anomalies and events (i.e., increased number of storms, hurricanes, cyclones, etc.) [4]. Climate change is a complex issue with the potential of harming human health, the ecosystem, as well as the infrastructures and the production of food. Thus, limiting the temperature rise below 1.5-2 °C compared to pre-industrial levels (i.e., target of the Paris Agreement set in 2015) is crucial to mitigate the threats of

global warming [5]. From **Figure 1.1** it is clear that to achieve this target, CO₂ emissions should decrease by more than 50% before 2050.

The combustion of fossil fuels is widely recognized as the main responsible of carbon emissions. As a matter of fact, the energy sector (i.e., electricity, heat and transport) covers ca. 73.2 % of the total emissions [1], [2]. In particular, fossil-fuels power plant contribute to 33-40 % of the global CO₂ emissions, with still a large fraction of coal-fired plants [6]–[8]. In addition to the power and heat generation, a considerable portion of carbon emissions derive from the natural gas sweetening, H₂ and syngas production (i.e., reforming processes), iron and steel production and from the manufacturing of limestone and cement. Thus, strategies are required to mitigate carbon emissions, especially in these sectors.

Amongst the different strategies proposed so far, the carbon capture and storage (CCS) has emerged as a short-term solution to minimize the environmental impact derived from the currently inevitable use of fossil fuels, especially in industrial heat and power generation processes [9]. Several technologies have been already developed for the CO₂ capture, such as adsorption, absorption, membrane separation and cryogenic distillation [10]. The choice for a specific capture technology lies not only on its cost, but, most importantly, on the characteristic of the CO₂ containing stream, such as the partial pressure of CO₂, the size of the stream itself and the type of impurities [11]. After its capture and purification, CO₂ is then compressed to either liquid or supercritical conditions, depending on the selected storage solution. For example, to safely and permanently store CO₂ in geological sites, supercritical conditions and 20 bar overpressure for the injection are required [12]. Thereafter, CO₂ is transported via trucks, ships, or through pipelines, to be finally stored in different locations such as under the ocean, in geological formation or in depleted natural gas/oil reservoirs.

Nevertheless, recently there has been quite some concerns regarding the CCS pathway, mainly related to its safety and feasibility. Indeed, especially when CO₂ is stored in geological reservoirs, there might be the risk of leakage in the atmosphere, as well as blowouts. In addition, ground movements could compromise the storage and increase the risk of earthquakes [13]. Thus, the carbon capture and utilization (CCU) approach has been identified as a long-term solution, even more attractive than the CCS option. The simplest CCU pathway consists of the direct (i.e., physical) use of CO₂, as for example in the production of carbonated soft drinks, dry ice or its direct use as a fire extinguisher, as a solvent for supercritical separation processes or for the enhanced oil recovery [14]–[16]. However, with these methods, the overall reduction of CO₂ emissions is very limited. On the contrary, processing (i.e., via chemical transformation) the captured CO₂ to obtain more valuable products would allow, at the same time, to synthesize carbon-based products (e.g., methane, methanol, olefins), reducing our dependency on fossil fuels [17]–[20].

There are already several CO₂ conversion technologies under investigation, with urea and methanol synthesis being the technologies with the highest readiness level [21]. Urea is mainly used to produce fertilizers or for polymer synthesis (i.e., urea-

formaldehyde resins). In 2021, ca. 178 MMT of urea were produced worldwide and its demand is expected to increase by 0.8% between 2023 and 2028 [22]. Nowadays, Stamicarbon and Saipem represents the largest market shares of the urea technology, based on the reaction of CO₂ and ammonia [23], [24]. The methanol synthesis using CO₂ and renewable H₂ has been recently implemented at commercial scale. Carbon Recycling International (CRI) has first demonstrated the CO₂-to-methanol technology at pilot scale in Iceland and last year, the first commercial-scale plant, as well as the world's largest one, has started production in Anyang, Henan Province, China, with a capacity of 110'000 tons of methanol per year [25]. Methanol is a very important building block for the chemical industry. On average, ca. 110 million metric tons of methanol are produced worldwide each year and about 35%, 19% and 10% of it is used to produce formaldehyde, MTBE and acetic acid, respectively [26]. Furthermore, methanol has large potential to replace transportation fuel, which makes its synthesis from CO₂ and H₂ (i.e., no fossil fuel based) much more attractive. Indeed, methanol can be converted to gasoline (MTG) or to dimethyl ether (DME), which can be directly used as transportation fuels. Alternatively, methanol can be directly converted in fuel cells (DMFC) [27]–[29]. Besides its direct uses as chemical intermediate or as a fuel, methanol has been recently identified as an attractive H₂ carrier, with a hydrogen mass density of 12.5%, which makes it the second option soon after ammonia (i.e., hydrogen mass density of 17.6%) [30].

Besides the abovementioned technologies, there are several possibilities for CO₂ chemical conversion. Three main categories can be identified: 1) CO₂ utilization as soft oxidant (i.e., for oxidative dehydrogenation processes); 2) CO₂ transformation into carbonates and 3) CO₂ reduction with H₂ (i.e., synthesis of CH₄, methanol, dimethyl ether, formic acid, etc.) [31]. The last category is the most attractive since, a variety of hydrocarbons can be synthesized via the combination of CO₂ and H₂, allowing to replace conventional fossil fuel feedstocks. As a matter of fact, although with some challenges, CO₂ and H₂ can replace or even be converted into syngas (i.e., reverse water gas shift reaction). Of course, to dismantle the fossil fuel economy, the required H₂ must be produced from renewable resources (i.e., green hydrogen), rather than via conventional methods (i.e., steam reforming of hydrocarbons). Green hydrogen could be produced from biomass, via thermochemical or biological processes [32]. Nevertheless, the most promising approach is the water splitting using electrolysis, thermolysis or photo-electrolysis [33]–[35]. In this way, the power surplus generated by discontinuous renewable energy sources (i.e., wind, solar, hydroelectric etc.), can be converted in a stable form of chemical energy, such as H₂ [36]. However, its low volumetric energy density makes H₂ storage and transport challenging as well as expensive, such that the scientific community has been focusing on studying efficient routes to convert H₂ in dense energy carriers [37].

Thus, combining green H₂ with the captured CO₂ is a crucial strategy for the decarbonization of the energy and chemical industry for at least two purposes: 1) to produce hydrocarbons with high gravimetric H₂ density, to safely transport the H₂ and to produce it on demand for its use in fuel cells; 2) to produce alternative and

green fuels (i.e., methanol, dimethyl ether, gasoline, etc.), which can be directly used as energy sources, mainly in the transportation sector.

Therefore, CCU to chemicals and fuels is seen as a fundamental piece of the energy and material transition to a fossil-free economy. However, as long as the captured CO₂ has fossil origin, the final CO₂ emissions (i.e., after a fuel is burnt) may be considered as delayed (thus not entirely mitigated) emissions. Nevertheless, upon gradual implementation of these and other renewable technologies, all captured CO₂ will no longer trace back to a fossil origin.

1.2 DIMETHYL ETHER SYNTHESIS AS CCU PATHWAY

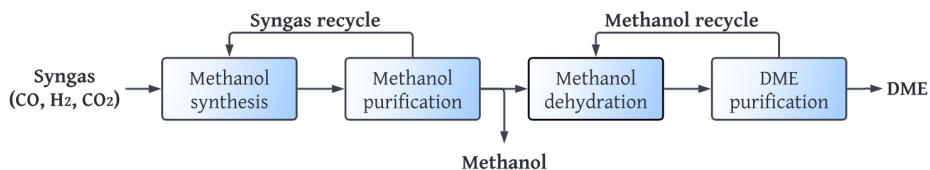
Among the large variety of products which can be obtained via CO₂ hydrogenation processes, dimethyl ether (DME) is particularly attractive. DME global market was valued around 4363.9 million USD in 2021 and is expected to achieve 8755.17 million USD in 2028 (i.e., CAGR of 10.5%) [38]. DME is conventionally used as propellant for aerosol spray (ca. 8% of global production), as refrigerant and as chemical feedstock (i.e., production of dimethyl sulfate, acetic acid, etc.). However, given its similarities to the liquefied petroleum gas (LPG), especially in terms of handling characteristics, the biggest market share consists in its use as LPG blending. Particularly, DME can be used to reduce the LPG demand especially for domestic scopes, for which it was proved that mixtures containing 15-50 vol. % of DME perform better than pure DME [39], [40]. In addition, DME has been identified as a high-efficiency compression ignition fuel, due to its autoignition properties, high cetane number (i.e., 60), low boiling point (i.e., -24.8 °C), and the lack of C-C bonds [41]–[44]. It is one of the simplest aliphatic ether, with low environmental impact, producing only CO₂ and H₂O upon its decomposition. All these features make DME an attractive alternative to diesel, as transportation fuel, requiring any (or limited) changes in the existing engines [41], [45]. With a properly designed injection system, NO_x emissions can achieve ultra-low emission vehicle (ULEV) limits [46]. Furthermore, DME has proved to have excellent properties as gas turbine fuel, with emissions comparable to the natural gas, although with ca. 8% lower CO₂ [47].

1.2.1 Benchmark production routes

Currently, the synthesis of DME can proceed via two routes (**Figure 1.2**). First, the indirect route is based on the initial conversion of syngas to methanol as intermediate product, and its subsequent dehydration to DME. The second route is the direct synthesis of DME from syngas in a single reactor, using bifunctional catalysts. Both routes are currently operated in industry: Haldor Topsoe, Air Products, Korea Gas Corporation, JFE Holdings and NKK own the direct (or one-step) synthesis technology, while Lurgi, Toyo, MGC and Udhe produce DME via the indirect pathway [48]. The main advantage of the indirect synthesis method is the possibility to separately optimize reaction conditions for either methanol synthesis and dehydration. Furthermore, the indirect route allows to set a different scale for the methanol synthesis and dehydration reactor steps, to meet the different market

demands of methanol and DME. Nevertheless, it is well known that the methanol synthesis is a thermodynamically limited process [49]. Therefore, the immediate consumption of methanol to form DME in the direct route has the beneficial effect of shifting the equilibrium towards higher conversions. Thus, the direct route has the advantage of a more efficient conversion, coupled with a more compact design (i.e., one reaction step rather than two) and lower energy demands in terms of recirculation of the unconverted feedstock [50], [51].

1. INDIRECT DME SYNTHESIS



2. DIRECT DME SYNTHESIS

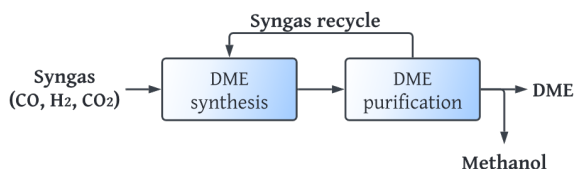


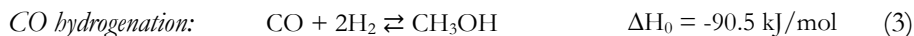
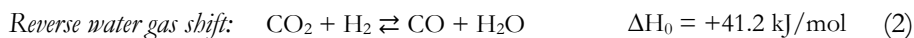
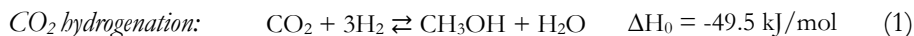
Figure 1.2. Schematic representation of the DME synthesis via the indirect and direct method

The feedstock for the methanol – and, as a consequence, DME – benchmark production is syngas, which is in turn a product of either steam reforming of natural gas, or gasification of crude oil, coal, or more rarely biomass and municipal solid waste (MSW) [52], [53]. As a result, the benchmark DME process is mostly fossil-based, with a CO_2 footprint in the range of $89\text{--}98 \text{ gCO}_2/\text{M}_{\text{DME}}$ [54]–[56].

1.2.2 Direct (one-step) conversion of CO_2 to Dimethyl Ether

Given the considerably large CO_2 footprint of the DME synthesis via the benchmark process, producing DME from captured CO_2 and renewable H_2 is not only a valid CO_2 valorization route, but also a way to render the process more sustainable [57]. Furthermore, in view of its potential to replace diesel in compression-ignition engines, the DME produced via CO_2 hydrogenation would definitely play a significant role in the circular carbon economy as well as to reduce our dependency on fossil fuels for transportation purposes.

Due to the higher efficiency of the direct route, this work focuses on the CO_2 direct (or one-step) hydrogenation to DME, which can be summarized by the following reaction scheme:



The synthesis of methanol (1-3) is typically carried out over a Cu-ZnO-Al₂O₃ catalyst [58]–[60], which also activates the water gas shift reaction (2) [61], [62]. Indeed, among reaction 1 to 3, the CO₂ hydrogenation to methanol is the most desired. Inevitably, the reverse water gas shift (r-WGS) takes place in parallel, accelerating the H₂ depletion and, at the same time, contributing to the production of water. As a matter of fact, water is the main reaction by-product, which limits the system thermodynamically and causes catalyst deactivation [63]. Depending on the catalyst, the CO hydrogenation to methanol (3) could take place simultaneously, partially balancing the negative effect of the r-WGS. Thus, although two reactions are sufficient to thermodynamically describe the methanol synthesis, CO₂ and CO hydrogenation should both be accounted for, since they were both proved to affect the methanol production rate [64]–[66].

Since the benchmark technology involves only traces of CO₂ in the feedstock [67], the corresponding catalyst (Cu-ZnO-Al₂O₃), although sufficiently active, is not necessarily optimal when using pure CO₂, i.e., a thermodynamically very stable molecule, as the sole carbon source [68], [69]. Over the years, researchers have proposed a variety of different catalysts for the CO₂ hydrogenation to methanol, with particular focus on Cu-based systems, in combination with different metal oxides as carrier and/or promoters [70]–[73]. First, important research efforts aimed at replacing the hydrophilic Al₂O₃ support, which could deactivate in presence of the large amounts of water produced in all the reactions [74]. In most of the catalyst formulations, the ZnO oxide still acts as main promoter, since it guarantees both a higher Cu dispersion and the formation of Cu^{δ+} sites at the Cu-ZnO interface [75]–[77]. Nevertheless, various carriers/promoters have been proposed in literature such as ZrO₂ [68], [77]–[81], CeO₂ [74], [82]–[86], Fe₂O₃ [86]–[88], SiO₂ [89]–[91], and TiO₂ [82] [92]–[95]. On the other hand, the methanol dehydration (4) is catalyzed by acid catalysts, such as γ -Al₂O₃ or HZSM-5 [96]–[98]. However, several works have proved that the γ -Al₂O₃ suffers from strong and fast deactivation with high concentration of water in the reaction medium. Indeed, the selectivity to DME drastically decreases when the CO₂ content in the syngas feed is increased [99]. More recently, several acid catalysts, especially zeolites with different dimensional framework (e.g., FER, MOR, MFI) and Si:Al ratios have been proposed for the methanol dehydration to DME, where the balance between Bronsted and Lewis acid sites is carefully tuned to selectively dehydrate methanol to DME. The main drawback of these catalysts is their strong hydrophilicity, and consequent deactivation due to strong water adsorption on the acid sites [100]–[102]. When DME is synthesized via the direct route, the two catalysts are physically mixed to

form a bifunctional catalyst [98], [103], although hybrid catalyst formulations have recently received considerable attention [102], [104], [105].

Besides the kinetic considerations, the process has important thermodynamic constraints and recycling of the unconverted CO_2 and H_2 stream is essential at process scale, given that the one-pass CO_2 conversion is often below 50% (**Figure 1.3a**). Although the overall process is exothermic, this complex reaction network combines exothermic and endothermic reactions, so the CO_2 equilibrium conversion (**Figure 1.3a**) is a non-monotonic function with temperature. Indeed, at lower temperatures, the exothermic reaction is enhanced, and the equilibrium conversion decreases with temperature. As temperature increases, the endothermic r-WGS reaction is enhanced and the conversion increases, in favor of the CO formation. As a matter of fact, low temperatures thermodynamically favor DME formation (**Figure 1.3b**), which means that DME selectivity drops as temperature increases. Furthermore, given the stoichiometry of the reactions, high pressures enhance methanol, and thus DME formation.

Thus, process-wise, the selection of the total pressure lies on a trade-off between one-pass conversion, which directly affect recycling and separation costs, and cost of feedstock conditioning. The temperature is instead optimized based on a trade-off between catalyst mass and DME selectivity, considering that a temperature of at least 200 °C is required for catalytic activity. Nevertheless, given the exothermicity of the system, a proper heat management strategy is crucial to prevent hotspots and the consequent conversion losses.

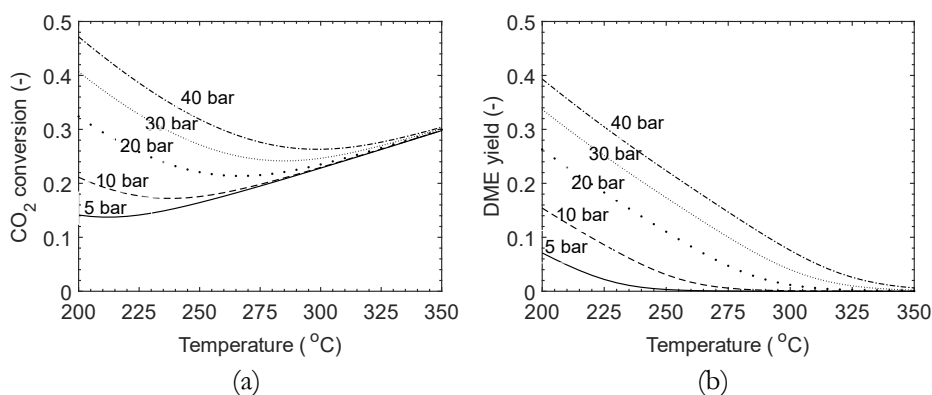


Figure 1.3. Equilibrium CO_2 conversion (a) and DME yield (b) as a function of temperature and pressure for a H_2 : CO_2 molar feed ratio of 3. Data obtained via Aspen Plus V11 simulations using RGibbs block and Peng-Robinson equation of state.

The most common reactor configuration, as well as the technology currently used at industrial scale, is the fixed (or packed) bed reactor [48], [106], [107]. This type of reactor is usually much simpler and less expensive than other technologies. However, a proper heat management solution is required to prevent the formation of hot spots and to avoid catalyst sintering. The temperature profile in the reactor

can be optimized by feeding a cold fluid in either a cooling jacket or in the mantle of a multi-tubular packed bed reactor. Another possibility is feeding the cold syngas (or CO₂-H₂) in different locations along the reactor or implementing the configuration of multistage (intercooled) adiabatic packed bed reactors. Slurry bubble columns have also been used for the direct synthesis of DME [108], [109]. Nevertheless, the mass transfer of the syngas from the bubble (gas) phase to the solvent where the catalyst is dispersed usually limits the overall DME formation rate, making the reaction less efficient [110]. Finally, fluidized bed reactors with enhanced heat and mass transfer, have been investigated, mainly from a theoretical perspective, but their feasibility at large scale has not yet been assessed [111], [112].

1.3 ENHANCEMENT OF CO₂ CONVERSION TO DME IN MEMBRANE REACTORS

Besides the optimization of reaction conditions, another strategy to improve the CO₂-to-DME process and to overcome thermodynamic limitations is the in-situ removal of the large amount of water produced in all individual reactions [113]–[118]. Indeed, removing one or more by-product – in this case water – from a reaction environment with thermodynamic limitations, allow to boost the production of the targeted product (*Le Chatelier* principle).

The in-situ removal of water to improve DME production is even more important in the direct hydrogenation of CO₂ than in the benchmark process starting from syngas. As a matter of fact, when CO is the main carbon source for the methanol/DME synthesis, the r-WGS (2) occurs in the opposite direction (i.e., WGS), partially consuming the water produced by the CO₂ hydrogenation (1) and methanol dehydration reactions (4). This indicates that, as soon as CO is replaced with CO₂, larger amount of water is produced, leading to more severe thermodynamic limitations and to catalyst stability issues. Indeed, water accelerates both Cu and ZnO crystallization, and it affects the acidity of the zeolite within long-term operation, favoring the dealumination (i.e., changes in the Si:Al ratio) [119], [120]. As a result, the CO₂-to-DME becomes much more challenging and requires a dedicated attention.

A promising technology for the in-situ removal of water is a membrane reactor (MR), where reaction and product separation are coupled in a single unit. The incorporation of membranes in a conventional reactor allows not only to overcome thermodynamic limitations, but often to reduce separation costs, given that the separation of product or by-products takes place already at the reactor stage. Furthermore, given the higher efficiency in the conversion, usually membrane reactors lead to a more compact reactor design, often reducing also its cost [121], [122].

In most of the applications, the membrane material implemented in the reactor is inert with respect to the reaction system. Thus, the membrane has the sole scope of separating reaction products, without taking part in the reaction itself. However,

more recently, catalytic membrane reactor applications, also for the synthesis of DME, are receiving some attention [123], [124], although they may be limited in the amount of catalyst loading.

Given that the preferred reactor configuration for the methanol/DME synthesis is a packed bed reactor [48], two membrane reactor configurations can be identified (**Figure 1.4**), depending on whether the membrane is implemented inside (configuration A) or outside (configuration B) the catalytic bed. Although configuration B is less invasive and does not introduce nuisance in the gas flow pattern in the catalytic bed, configuration A is preferred for at least two reasons: 1) the membrane selective layer is placed in the center of the catalytic bed, where usually product concentration – thus water – is higher; 2) the membrane aspect ratio can be more easily tuned, being decoupled from the characteristic sizes of the catalytic bed. As a result, the gas contact time with the membrane and catalyst can be independently optimized. As a matter of fact, when configuration A is selected, the membrane area can be optimized based on multiple parameters, such as number of membranes, length and diameter of each membrane. Thus, for industrial applications, a multi-tubular packed bed membrane reactor can be implemented, as sketched in **Figure 1.5**.

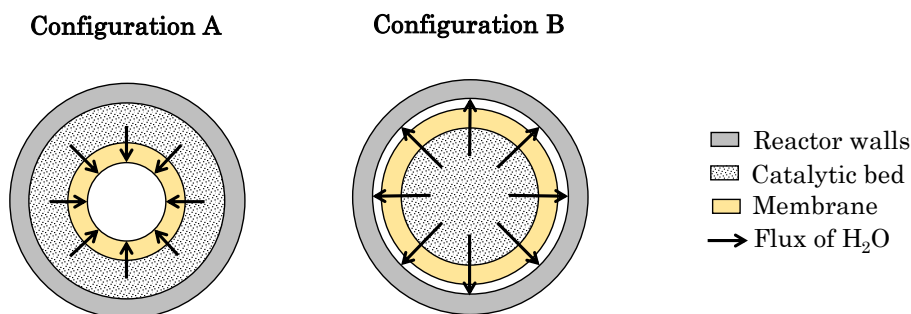


Figure 1.4. Packed bed membrane reactor configurations: in configuration A, the membrane is inside the catalytic bed; in configuration B, the membrane is outside the catalytic bed.

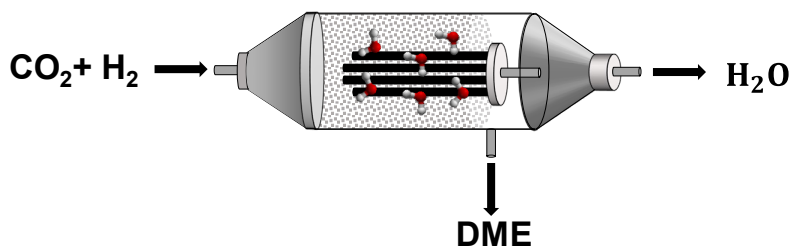


Figure 1.5. Sketch of a multi-tubular packed membrane reactor to enhance the CO₂ direct conversion to DME via the in-situ removal of water.

To promote the separation of water from the reaction ambient, the membrane material must be properly selected. Nevertheless, a driving force for the water transmembrane flux is necessary to guarantee the separation. In most of the cases, this driving force is a gradient in concentration/partial pressure, which is generated by either applying vacuum or lower pressure in the permeate side of the membrane or by feeding a sweep gas to dilute the permeated species. The former solution leads to more mechanical stress on the membrane, as well as higher operating costs, if vacuum conditions are required. Thus, the circulation of a sweep gas is usually preferred.

1.4 MEMBRANE MATERIALS FOR WATER SEPARATION IN MEMBRANE REACTORS

The membrane material must be properly selected to guarantee the selective removal of water and, at the same time, to retain reactants (including methanol) in the reaction environment. It is known that higher permeability corresponds also to lower selectivity to the separation (i.e., perm-selectivity) [125]. Thus, the membrane should be chosen based on a trade-off between water vapor permeability and vapor/gas perm-selectivity.

The selection of the membrane material is crucial, especially in terms of stability in hot humid environment [126]. For this reason, polymeric membranes are not suitable, since they cannot work at very high temperatures, and undergo plasticization and swelling phenomena. Porous inorganic membranes, on the other hand, have been extensively studied for pervaporation [127]–[132]. Ceramic membranes, in particular zeolites, have been mostly proposed for the in-situ removal of H₂O in different reactive systems [113], [114], [116], [118], [126], [133]–[136]. Despite their excellent properties in terms of vapor permeability, mainly deriving from their strong hydrophilicity, zeolite membranes suffer from: 1) poor reproducibility, due to the complexity of the synthesis procedure [137], [138] and 2) poor long-term stability due to dealumination when in contact with large volume of hot water [120], [138]. Alternatively, carbon molecular sieve membranes (CMSM) offer superior thermo-chemical stability in humid and corrosive environments, as well as an excellent balance between gas permeance and perm-selectivity, especially with respect to polymeric membranes [139]–[141]. Thus, CMSM are a potentially attractive candidate to selectively separate H₂O from other gases in the temperature conditions of the CO₂ hydrogenation processes (i.e., 200–400 °C) [142], [143].

Carbon-based membranes have emerged as promising material for gas separation processes, with a wide application spectrum, owing to the possibility to tailor the properties of the carbon active layer and thus the governing permeation mechanism to the desired separation. Most of these applications include the separation of mixtures of (dry) gases such as CO₂, N₂, CH₄, H₂ or mixtures of alkane/alkene at relatively low temperature (i.e., 20–80 °C) [141], [144]–[145]. Only very recently, they have been demonstrated for water vapor permeation, at temperatures above 150 °C [146], including the work reported in this thesis.

Carbon molecular sieve membranes derive from the pyrolysis, often referred to as carbonization, of a thermoset polymeric membrane precursor, carried out at high temperature and under inert atmosphere or vacuum. Self-standing membranes are brittle and difficult to handle. Thus, often supported CMSM with improved mechanical stability are prepared via the deposition of the selective carbon layer on the surface of a porous ceramic support (e.g., α -Al₂O₃). The pyrolysis or carbonization step is a process that transforms the dense polymeric membrane precursor into a porous carbon membrane which can display, at the same time, ultra-micropores (i.e., $d_p \leq 0.6$ nm) and micropores (i.e., $0.6 \leq d_p \leq 2$ nm). Pores in the mesopores and macropores region are considered mostly as defects in the selective layer. These pores do not contribute to the membrane selectivity, but usually enhance the permeability of all species, favoring both Knudsen diffusion and viscous flow. The ultra-micropores are responsible for the molecular sieving (MS) character of these membranes, according to which the separation of molecules is based on size-exclusion. The second important transport/separation mechanism is adsorption-diffusion (AD), mainly occurring in the micropores, which is based on the physicochemical interaction of the molecules with the pore surface [147], [148]. An overview of the gas transport mechanisms potentially occurring in a CMSM is given in **Figure 1.6**.

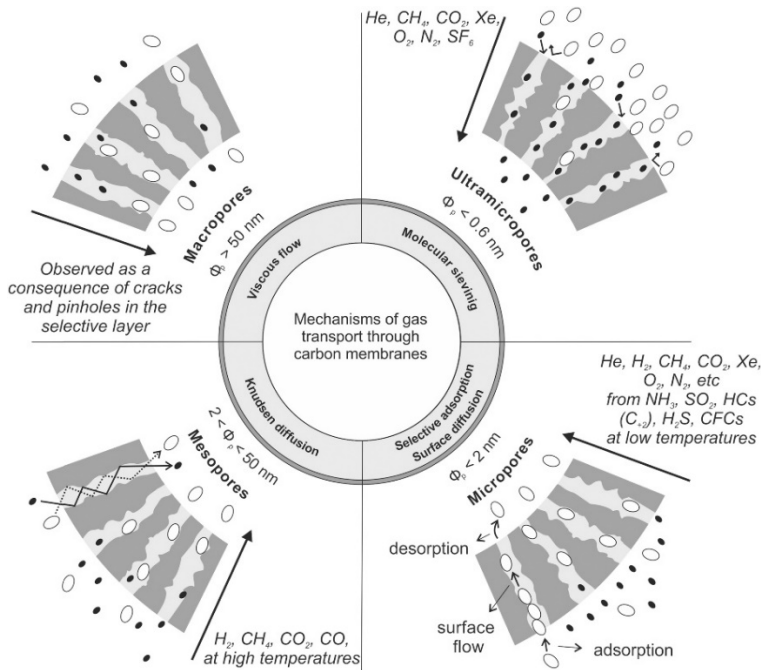


Figure 1.6. Schematic drawing of the main mechanisms used to explain gas transport through carbon membranes. Figures adapted from reference [148]

Depending on the conditions of the carbonization step (e.g., atmosphere, temperature, time and heating rate) and on the physicochemical properties of the polymeric precursor, the porous structure and degree of hydrophilicity/hydrophobicity of the CMSM can be tuned according to the desired application and its perm-selectivity requirements [146], [149]–[151]. As a matter of fact, with the pyrolysis of the polymeric precursor, the chemistry of the membrane changes, towards the direction of graphitization. Thus, the membrane gradually loses its hydrogen and oxygen content. At the same time, the dense polymeric layer transforms into a complex system of pores which eventually, at higher temperature (i.e., above 850-900 °C) collapses in a graphitic structure. This means that the carbonization step also influences the pore size and distribution of the CMSM.

Besides the pore structure and surface properties of the membrane, the operating temperature is a well-known parameter that determines the governing permeation mechanism. At higher temperatures, corresponding to higher molecular energy level, the collisions of the molecules with the pore walls are more frequent, slowing down the permeation process. This phenomenon is known as Knudsen diffusion [152]. Therefore, higher temperatures hinder the adsorption phenomena, and the transport mechanism inevitably turns into the molecular sieving or Knudsen diffusion [147], [153]. For each diffusing gas, a specific temperature exists at which the adsorption-diffusion is not relevant anymore [154]. At lower temperatures, on the other hand, when the adsorption-diffusion mechanism is dominant, the diffusing species could reduce the effective pore size of the membranes, hindering the permeation of the non-diffusing species. Therefore, at low temperatures, higher perm-selectivity values can be achieved.

While most of the literature on CMSM deals with (low temperature) gas separation processes, which are usually described as a combination of molecular sieving and/or adsorption-diffusion, very limited attention has been paid to the separation of mixtures containing condensable species like H₂O. In these cases, an additional transport mechanism via viscous flow of capillary condensate [155]–[157] should be contemplated. Indeed, for wetting systems (e.g., H₂O on a hydrophilic solid surface) the vapor pressure in a capillary is lower than that on a planar surface, as described by the Kelvin's equation [158]. Thus, water can condense in the micropores of the carbon membranes with sufficient hydrophilicity. Whereas the existence of capillary condensation may be considered as a nuisance (i.e. lower gas permeability), or even complexing factor that obscures the interpretation of experimental data, it can surely be used for the rational design of a selective membrane if properly understood. When looking at the case of water separation, a hydrophilic carbon membrane is an obvious choice given their well-established affinity to H₂O [42],[50]. Water is known to adsorb on the pores already at ambient conditions, reducing the active pore size of the membranes [159] and thereby increasing the separation factors between water and other gases. Even more, when capillary condensation occurs, water could partially or totally block the pores of the membranes, further suppressing the permeation of the other gases. In processes involving CO₂ hydrogenation, where the

focus is the selective separation of H₂O from reactants and products such as H₂, CO₂ and CO, this is an enormous advantage.

1.5 THESIS OUTLINE

In this thesis, the use of the membrane reactor technology for the one-step CO₂ hydrogenation to DME reaction is thoroughly studied from different perspectives, ranging from the development of the membrane materials, to the demonstration of the technology at reactor and process scales, combining both experimental and numerical tools.

In **Chapter 2**, a 1D-phenomenological membrane reactor model is described and used to determine the optimal membrane performance in terms of water permeability and perm-selectivity, to shed light into suitable material as well as to set a target for the membrane development. The cocurrent circulation of a sweep gas stream containing the reactants (i.e., CO₂ and H₂), is proposed as an effective strategy to promote the selective water removal from the reaction environment, lowering the membrane requirements in terms of perm-selectivity. Based on this study, ceramic supported carbon molecular sieve membranes (CMSMs) are selected as promising materials given their potential hydrophilicity and the possibility to tune their properties by acting on different parameters of the synthesis procedure.

Chapter 3 and **4** focus on the study of phenolic resin CMSMs to promote the high temperature (i.e., 200-250 °C) separation of H₂O vapor from (hydrogen-rich) gaseous streams. First the incorporation of hydrophilic boehmite nanosheets (γ -AlO(OH)) in the polymeric resin as a way to improve the membrane hydrophilicity is assessed in Chapter 3. Then, the effect of the carbonization temperature on the vapor/gas separation performance is thoroughly studied in Chapter 4, with particular focus on the water interaction with the membrane surface.

In **Chapter 5**, an experimental proof of concept of the membrane reactor technology is presented, which also allows for the validation of the previously developed phenomenological reactor model. The effect of the main reaction parameters (i.e., temperature, pressure gradient, sweep gas flow ratio) is studied and the membrane reactor configuration proposed in Chapter 2 (i.e., circulation of the sweep gas containing the reactant) is proved as effective way to mitigate poor vapor/gas membrane selectivity issues.

In **Chapter 6**, the membrane reactor is modeled under a multi-scale perspective with a particular focus on the heat and mass transfer phenomena occurring at different scales (i.e., from the particles, to the membrane and the reactor scale). 2D heterogeneous models are implemented and solved to first investigate the relevant phenomena with a rigorous approach. Thereafter, short-cut methods (i.e., Thiele modulus-efficiency approach, mass transfer coefficient correlations) are proposed to simplify the reactor model, accounting for all the phenomena which significantly affect the reactor performance.

Chapter 7 proposes a comparison on a techno-economic level of two routes for the one-step DME synthesis via CO₂ hydrogenation: 1) the conventional route, based on a packed bed reactor (PBR) technology; and 2) the MR-assisted route, based on the packed bed membrane reactor (PBMR) technology. The scope of this study is to identify the advantages of using a membrane reactor on a process scale, analyzing both technical and economic performance. Furthermore, this chapter aims at identifying the economic bottlenecks of this technology, as well as to make a realistic prediction about when this CO₂ utilization route would become competitive at industrial scale.

Finally, the main conclusions of this thesis and the research outlook are summarized in **Chapter 8**.

REFERENCES

- [1] K. O. Yoro and M. O. Daramola, *CO₂ emission sources, greenhouse gases, and the global warming effect*. Elsevier Inc., 2020.
- [2] H. Ritchie and M. Roser, “CO₂ and Greenhouse Gas Emissions,” *Our World Data*, 2020.
- [3] R. Lindsey and L. Dahlman, “Climate Change: Global Temperature,” 2022.
- [4] N. N. C. for E. Information, “Monthly Global Climate Report for Annual 2021,” 2022.
- [5] E. Bell, J. Cullen, and S. Taylor, “Adoption of the Paris Agreement, 21st Conference of the Parties, Paris: United Nations,” *United Nations/Framework Conv. Clim. Chang.*, 2016.
- [6] A. Williams, *Combustion and Gasification of Coal*. New York, 2000.
- [7] A. Meisen and X. Shuai, “Research and development issues in CO₂ capture,” *Energy Convers. Manag.*, vol. 38, no. 96, pp. 37–42, 1997.
- [8] Z. H. Tian and Z. L. Yang, “Scenarios of carbon emissions from the power sector in Guangdong Province,” *Sustain.*, vol. 8, no. 9, 2016,
- [9] F. M. Baena-Moreno, M. Rodríguez-Galán, F. Vega, B. Alonso-Fariñas, L. F. Vilches Arenas, and B. Navarrete, “Carbon capture and utilization technologies: a literature review and recent advances,” *Energy Sources, Part A Recover. Util. Environ. Eff.*, vol. 41, no. 12, pp. 1403–1433, 2019,
- [10] J. C. M. Pires, F. G. Martins, M. C. M. Alvim-Ferraz, and M. Simões, “Recent developments on carbon capture and storage: An overview,” *Chem. Eng. Res. Des.*, vol. 89, no. 9, pp. 1446–1460, 2011,
- [11] R. Steeneveldt, B. Berger, and T. A. Torp, “Co₂ capture and storage: Closing the knowing-doing gap,” *Chem. Eng. Res. Des.*, vol. 84, no. 9 A, pp. 739–763, 2006,
- [12] K. Volkart, C. Bauer, and C. Boulet, “Life cycle assessment of carbon capture and storage in power generation and industry in Europe,” *Int. J. Greenh. Gas Control*, vol. 16, pp. 91–106, 2013,
- [13] A. Parekh, G. Chaturvedi, and A. Dutta, “Sustainability analyses of CO₂ sequestration and CO₂ utilization as competing options for mitigating CO₂ emissions,” *Sustain. Energy Technol. Assessments*, vol. 55, no. December 2022, p. 102942, 2023,
- [14] R. M. Cuéllar-Franca and A. Azapagic, “Carbon capture, storage and utilisation technologies: A critical analysis and comparison of their life cycle environmental impacts,” *J. CO₂ Util.*, vol. 9, pp. 82–102, 2015,
- [15] B. A. S. Machado, C. G. Pereira, S. B. Nunes, F. F. Padilha, and M. A. Umsza-Guez, “Supercritical Fluid Extraction Using CO₂: Main Applications and Future Perspectives,” *Sep. Sci. Technol.*, vol. 48, no. 18, pp. 2741–2760, 2013,
- [16] B. Metz, O. Davidson, H. De Coninck, M. Loos, and L. Mever, *IPCC Special report*

- on Carbon Dioxide Capture and Storage*. New York: Cambridge University Press, 2005.
- [17] J. Ma *et al.*, “A short review of catalysis for CO₂ conversion,” *Catal. Today*, vol. 148, no. 3–4, pp. 221–231, 2009,
- [18] D. Chery, V. Lair, and M. Cassir, “Overview on CO₂ valorization: Challenge of molten carbonates,” *Front. Energy Res.*, vol. 3, no. OCT, pp. 1–10, 2015,
- [19] J. Liu, K. Li, Y. Song, C. Song, and X. Guo, “Selective Hydrogenation of CO₂ to Hydrocarbons: Effects of Fe₃O₄ Particle Size on Reduction, Carburization, and Catalytic Performance,” *Energy and Fuels*, vol. 35, no. 13, pp. 10703–10709, 2021,
- [20] K. P. Kuhl, T. Hatsukade, E. R. Cave, D. N. Abram, J. Kibsgaard, and T. F. Jaramillo, “Electrocatalytic conversion of carbon dioxide to methane and methanol on transition metal surfaces,” *J. Am. Chem. Soc.*, vol. 136, no. 40, pp. 14107–14113, 2014,
- [21] M. Pérez-Fortes, A. Bocin-Dumitriu, and E. Tzimas, “CO₂ utilization pathways: Techno-economic assessment and market opportunities,” *Energy Procedia*, vol. 63, no. i, pp. 7968–7975, 2014,
- [22] “Global Urea Market Outlook,” 2022. <https://www.expertmarketresearch.com/reports/urea-market>
- [23] M. Hamidipour, N. Mostoufi, and R. Sotudeh-Gharebagh, “Modeling the synthesis section of an industrial urea plant,” *Chem. Eng. J.*, vol. 106, no. 3, pp. 249–260, 2005,
- [24] M. Brouwer, “The Comparison of Stamicarbon and Saipem Urea Technology,” *Urea Know How*, vol. 1, no. December, pp. 1–9, 2016, [Online]. https://www.researchgate.net/profile/Prem_Baboo/publication/309385422_The_Comparison_of_Stamicarbon_and_Saipem_Urea_Technology/links/580ce51b08ae2cb3a5e3c195.pdf
- [25] Carbon Recycling International (CRI) News, “World largest CO₂-to-methanol plant starts production,” 2022. [Online]. <https://www.carbonrecycling.is/news-media/worlds-largest-co2-to-methanol-plant-starts-production>
- [26] F. Dalena, A. Senatore, A. Marino, A. Gordano, M. Basile, and A. Basile, *Methanol Production and Applications: An Overview*. Elsevier B.V., 2018.
- [27] M. Peters, B. Köhler, W. Kuckshinrichs, W. Leitner, P. Markewitz, and T. E. Müller, “Chemical technologies for exploiting and recycling carbon dioxide into the value chain,” *ChemSusChem*, vol. 4, no. 9, pp. 1216–1240, 2011,
- [28] A. Bocin-dumitriu, M. del M. Perez Fortes, E. Tzimas, and T. Sveen, *Carbon Capture and Utilisation Workshop Background and proceedings*. 2013.
- [29] S. Wasmus and A. Küver, “Methanol oxidation and direct methanol fuel cells: A selective review,” *J. Electroanal. Chem.*, vol. 461, no. 1–2, pp. 14–31, 1999,
- [30] R. Zhu, Z. Wang, Y. He, Y. Zhu, and K. Cen, “LCA comparison analysis for two types of H₂ carriers: Methanol and ammonia,” *Int. J. Energy Res.*, vol. 46, no. 9, pp. 11818–11833, 2022,

- [31] C. B. Peres, P. M. R. Resende, and L. J. R. Nunes, “clean technologies Advances in Carbon Capture and Use (CCU) Technologies : A Comprehensive Review and CO₂ Mitigation Potential Analysis,” *Clean Technol.*, pp. 1193–1207, 2022.
- [32] H. Nazir *et al.*, “Is the H₂ economy realizable in the foreseeable future? Part I: H₂ production methods,” *Int. J. Hydrogen Energy*, vol. 45, no. 27, pp. 13777–13788, 2020,
- [33] J. Jia *et al.*, “Solar water splitting by photovoltaic-electrolysis with a solar-to-hydrogen efficiency over 30%,” *Nat. Commun.*, vol. 7, no. May, pp. 1–6, 2016,
- [34] S. Shiva Kumar and V. Himabindu, “Hydrogen production by PEM water electrolysis – A review,” *Mater. Sci. Energy Technol.*, vol. 2, no. 3, pp. 442–454, 2019,
- [35] G. Liu, Y. Sheng, J. W. Ager, M. Kraft, and R. Xu, “Research advances towards large-scale solar hydrogen production from water,” *EnergyChem*, vol. 1, no. 2, p. 100014, 2019,
- [36] G. Varvoutis, A. Lampropoulos, E. Mandela, M. Konsolakis, and G. E. Marnellos, “Recent Advances on CO₂ Mitigation Technologies: On the Role of Hydrogenation Route via Green H₂,” *Energies*, vol. 15, no. 13, 2022,
- [37] M. Jang *et al.*, “A High-Capacity, Reversible Liquid Organic Hydrogen Carrier: H₂-Release Properties and an Application to a Fuel Cell,” *ACS Sustain. Chem. Eng.*, vol. 7, no. 1, pp. 1185–1194, 2019,
- [38] Fortune Business Insight, “Dimethyl Ether Market Size, Share & COVID-19 Impact Analysis, by application (LPG blending, aerosol propellant, transportation fuel and others), and regional forecast, 2021-2028,” 2021.
- [39] M. Marchionna, R. Patrini, D. Sanfilippo, and G. Migliavacca, “Fundamental investigations on di-methyl ether (DME) as LPG substitute or make-up for domestic uses,” *Fuel Process. Technol.*, vol. 89, no. 12, pp. 1255–1261, 2008,
- [40] R. Anggarani, C. S. Wibowo, and D. Rulianto, “Application of dimethyl ether as LPG substitution for household stove,” *Energy Procedia*, vol. 47, pp. 227–234, 2014,
- [41] T. H. Fleisch, A. Basu, M. J. Gradassi, and J. G. Masin, “Dimethyl ether: A fuel for the 21st century,” *Stud. Surf. Sci. Catal.*, vol. 107, pp. 117–125, 1997.
- [42] C. Arcoumanis, C. Bae, R. Crookes, and E. Kinoshita, “The potential of di-methyl ether (DME) as an alternative fuel for compression-ignition engines: A review,” *Fuel*, vol. 87, no. 7, pp. 1014–1030, 2008,
- [43] T. E. Society, F. A. Mobility, and L. S. Air, “r rl s Reconstruction,” *Automot. News*, 1988.
- [44] U. Mondal and G. D. Yadav, “Perspective of dimethyl ether as fuel: Part II- analysis of reactor systems and industrial processes,” *J. CO₂ Util.*, vol. 32, no. February 2019, pp. 299–320, 2019,
- [45] M. De Falco, M. Capocelli, and G. Centi, “Dimethyl ether production from CO₂ rich feedstocks in a one-step process: Thermodynamic evaluation and reactor simulation,” *Chem. Eng. J.*, vol. 294, pp. 400–409, 2016,

- [46] C. Arcoumanis, C. Bae, R. Crookes, and E. Kinoshita, "The potential of di-methyl ether (DME) as an alternative fuel for compression-ignition engines: A review," vol. 87, pp. 1014–1030, 2008,
- [47] D. Cocco, V. Tola, and G. Cau, "Performance evaluation of chemically recuperated gas turbine (CRGT) power plants fuelled by di-methyl-ether (DME)," vol. 31, pp. 1446–1458, 2006,
- [48] Z. Azizi, M. Rezaeimaneh, T. Tohidian, and M. R. Rahimpour, "Dimethyl ether: A review of technologies and production challenges," *Chem. Eng. Process. Process Intensif.*, vol. 82, pp. 150–172, 2014,
- [49] Balint, "Margarines and Shortenings IAN," *Ullmann's Encycl. Ind. Chem.*, no. group 12, pp. 413–454, 2005,
- [50] K. L. Ng, D. Chadwick, and B. A. Toseland, "Kinetics and modeling of dimethyl ether synthesis from synthesis gas," *Chem. Eng. Sci.*, vol. 54, no. 15–16, pp. 3587–3592, 1999,
- [51] F. Dadgar, R. Myrstad, P. Pfeifer, A. Holmen, and H. J. Venvik, "Direct dimethyl ether synthesis from synthesis gas: The influence of methanol dehydration on methanol synthesis reaction," *Catal. Today*, vol. 270, pp. 76–84, 2016,
- [52] R. Vakili and R. Eslamloueyan, "Optimal design of an industrial scale dual-type reactor for direct dimethyl ether (DME) production from syngas," *Chem. Eng. Process. Process Intensif.*, vol. 62, pp. 78–88, 2012,
- [53] G. Iaquaniello, G. Centi, A. Salladini, E. Palo, S. Perathoner, and L. Spadaccini, "Waste-to-methanol: Process and economics assessment," *Bioresour. Technol.*, vol. 243, pp. 611–619, 2017,
- [54] R. K. D. and H. H. Edwards R. larivé J., Rickeard D., Weindorf W., Godwin S., Hass H., Krasenbrink A., Lonza L., Nelson L. Reid A., "Well-to-tank report version 4.a: Jec well-to-wheels analysis (LD-NA-26237-EN-N)," 2014.
- [55] D. Berkely, "California Dimethyl Ether Multimedia Evaluation Tier I," 2015.
- [56] U. Lee *et al.*, "Well-to-Wheels Emissions of Greenhouse Gases and Air Pollutants of Dimethyl Ether from Natural Gas and Renewable Feedstocks in Comparison with Petroleum Gasoline and Diesel in the United States and Europe," *SAE Int. J. Fuels Lubr.*, vol. 9, no. 3, pp. 546–557, 2016,
- [57] S. Michailos, S. Mccord, V. Sick, G. Stokes, and P. Styring, "Dimethyl ether synthesis via captured CO₂ hydrogenation within the power to liquids concept: A techno-economic assessment," *Energy Convers. Manag.*, vol. 184, no. October 2018, pp. 262–276, 2019,
- [58] M. Bowker, R. A. Hadden, H. Houghton, J. N. K. Hyland, and K. C. Waugh, "The mechanism of methanol synthesis on copper/zinc oxide/alumina catalysts," *J. Catal.*, vol. 109, no. 2, pp. 263–273, 1988,
- [59] P. B. Himelfarb, G. W. Simmons, K. Klier, and R. G. Herman, "Precursors of the copper-zinc oxide methanol synthesis catalysts," *J. Catal.*, vol. 93, no. 2, pp. 442–450, 1985,

- [60] K. C. Waugh, "Methanol Synthesis," *Catal. Today*, vol. 15, no. 1, pp. 51–75, 1992,
- [61] J. F. Edwards and G. L. Schrader, "Infrared spectroscopy of Cu/ZnO catalysts for the water-gas shift reaction and methanol synthesis," *J. Phys. Chem.*, vol. 88, no. 23, pp. 5620–5624, 1984,
- [62] C. Rhodes, G. J. Hutchings, and A. M. Ward, "Water-gas shift reaction: finding the mechanistic boundary," *Catal. Today*, vol. 23, no. 1, pp. 43–58, 1995,
- [63] S. Ghosh, J. Sebastian, L. Olsson, and D. Creaser, "Experimental and kinetic modeling studies of methanol synthesis from CO₂ hydrogenation using In₂O₃ catalyst," *Chem. Eng. J.*, vol. 416, p. 129120, 2021,
- [64] S. Poto, D. Vico van Berkel, F. Gallucci, and M. Fernanda Neira d'Angelo, "Kinetic modeling of the methanol synthesis from CO₂ and H₂ over a CuO/CeO₂/ZrO₂ catalyst: The role of CO₂ and CO hydrogenation," *Chem. Eng. J.*, vol. 435, no. P2, p. 134946, 2022,
- [65] J. F. Portha *et al.*, "Kinetics of Methanol Synthesis from Carbon Dioxide Hydrogenation over Copper-Zinc Oxide Catalysts," *Ind. Eng. Chem. Res.*, vol. 56, no. 45, pp. 13133–13145, 2017,
- [66] H. Graaf, E. J. Stamhuis, and A. A. C. M. Beenackers, "Kinetics of low-pressure methanol synthesis," *Chem. Eng. Sci.*, vol. 43, no. 12, pp. 3185–3195, 1988.
- [67] E. C. F. Iedler, B. Aktiengesellschaft, and F. Republic, "of Germany," 1923,
- [68] R. Raudaskoski, E. Turpeinen, R. Lenkkeri, E. Pongrácz, and R. L. Keiski, "Catalytic activation of CO₂: Use of secondary CO₂ for the production of synthesis gas and for methanol synthesis over copper-based zirconia-containing catalysts," *Catal. Today*, vol. 144, no. 3–4, pp. 318–323, 2009,
- [69] Y. F. Zhao, Y. Yang, C. Mims, C. H. F. Peden, J. Li, and D. Mei, "Insight into methanol synthesis from CO₂ hydrogenation on Cu(1 1 1): Complex reaction network and the effects of H₂O," *J. Catal.*, vol. 281, no. 2, pp. 199–211, 2011,
- [70] S. G. Jadhav, P. D. Vaidya, B. M. Bhanage, and J. B. Joshi, "Catalytic carbon dioxide hydrogenation to methanol: A review of recent studies," *Chem. Eng. Res. Des.*, vol. 92, no. 11, pp. 2557–2567, 2014,
- [71] O. Tursunov, L. Kustov, and A. Kustov, "A Brief Review of Carbon Dioxide Hydrogenation to Methanol Over Copper and Iron Based Catalysts," *Oil Gas Sci. Technol.*, vol. 72, no. 5, 2017,
- [72] C. Federsel, R. Jackstell, and M. Beller, "State-of-the-art catalysts for hydrogenation of carbon dioxide," *Angew. Chemie - Int. Ed.*, vol. 49, no. 36, pp. 6254–6257, 2010,
- [73] R. Guil-López *et al.*, "Methanol synthesis from CO₂: A review of the latest developments in heterogeneous catalysis," *Materials (Basel)*, vol. 12, no. 23, 2019,
- [74] G. Bonura, F. Arena, G. Mezzatesta, C. Cannilla, L. Spadaro, and F. Frusteri, "Role of the ceria promoter and carrier on the functionality of Cu-based catalysts in the CO₂-to-methanol hydrogenation reaction," *Catal. Today*, vol. 171, no. 1, pp. 251–256, 2011,

- [75] F. Arena, G. Mezzatesta, G. Zafarana, G. Trunfio, F. Frusteri, and L. Spadaro, "How oxide carriers control the catalytic functionality of the Cu-ZnO system in the hydrogenation of CO₂ to methanol," *Catal. Today*, vol. 210, pp. 39–46, 2013,
- [76] X. M. Liu, G. Q. Lu, Z. F. Yan, and J. Beltramini, "Recent Advances in Catalysts for Methanol Synthesis via Hydrogenation of CO and CO₂," *Ind. Eng. Chem. Res.*, vol. 42, no. 25, pp. 6518–6530, 2003,
- [77] F. Arena *et al.*, "Solid-state interactions, adsorption sites and functionality of Cu-ZnO/ZrO₂ catalysts in the CO₂ hydrogenation to CH₃OH," *Appl. Catal. A Gen.*, vol. 350, no. 1, pp. 16–23, 2008,
- [78] A. Ateka, I. Sierra, J. Ereña, J. Bilbao, and A. T. Aguayo, "Performance of CuO–ZnO–ZrO₂ and CuO–ZnO–MnO as metallic functions and SAPO-18 as acid function of the catalyst for the synthesis of DME co-feeding CO₂," *Fuel Process. Technol.*, vol. 152, pp. 34–45, 2016,
- [79] G. Bonura, M. Cordaro, C. Cannilla, F. Arena, and F. Frusteri, "The changing nature of the active site of Cu-Zn-Zr catalysts for the CO₂ hydrogenation reaction to methanol," *Appl. Catal. B Environ.*, vol. 152–153, pp. 152–161, 2014,
- [80] M. Lachowska and J. Skrzypek, "Methanol synthesis from carbon dioxide and hydrogen over Mn-promoted copper/zinc/zirconia catalysts," *React. Kinet. Catal. Lett.*, vol. 83, no. 2, pp. 269–273, 2004,
- [81] K. T. Jung and A. T. Bell, "Effects of zirconia phase on the synthesis of methanol over zirconia-supported copper," *Catal. Letters*, vol. 80, no. 1–2, pp. 63–68, 2002,
- [82] K. Chang, T. Wang, and J. G. Chen, "Applied Catalysis B: Environmental Hydrogenation of CO₂ to methanol over CuCeTiO_x catalysts," vol. 206, pp. 704–711, 2017.
- [83] L. Lin *et al.*, "In-situ Characterization of Cu/CeO₂ Nanocatalysts for CO₂ Hydrogenation: Morphological Effects of Nanostructured Ceria on the Catalytic Activity," *J. Phys. Chem. C*, vol. 122, no. 24, pp. 12934–12943, 2018,
- [84] B. Ouyang, W. Tan, and B. Liu, "Morphology effect of nanostructure ceria on the Cu/CeO₂ catalysts for synthesis of methanol from CO₂ hydrogenation," *Catal. Commun.*, vol. 95, pp. 36–39, 2017,
- [85] M. Konsolakis *et al.*, "CO₂ hydrogenation over nanoceria-supported transition metal catalysts: Role of ceria morphology (nanorods versus nanocubes) and active phase nature (Co versus Cu)," *Nanomaterials*, vol. 9, no. 12, 2019,
- [86] L. Spadaro, A. Palella, and F. Arena, "Copper-Iron-Zinc-Cerium oxide compositions as most suitable catalytic materials for the synthesis of green fuels via CO₂ hydrogenation," *Catal. Today*, no. March, 2020,
- [87] R. W. Liu, Z. Z. Qin, H. B. Ji, and T. M. Su, "Synthesis of dimethyl ether from CO₂ and H₂ using a Cu-Fe-Zr/HZSM-5 catalyst system," *Ind. Eng. Chem. Res.*, vol. 52, no. 47, pp. 16648–16655, 2013,
- [88] X. Zhou, T. Su, Y. Jiang, Z. Qin, H. Ji, and Z. Guo, "CuO-Fe₂O₃-CeO₂/HZSM-5 bifunctional catalyst hydrogenated CO₂ for enhanced dimethyl ether synthesis,"

- Chem. Eng. Sci.*, vol. 153, pp. 10–20, 2016,
- [89] L. Zhang, Y. Zhang, and S. Chen, “Effect of promoter SiO₂, TiO₂ or SiO₂-TiO₂ on the performance of CuO-ZnO-Al₂O₃ catalyst for methanol synthesis from CO₂ hydrogenation,” *Appl. Catal. A Gen.*, vol. 415–416, pp. 118–123, 2012,
- [90] J. Yu *et al.*, “Stabilizing Cu⁺ in Cu/SiO₂ catalysts with a shattuckite-like structure boosts CO₂ hydrogenation into methanol,” *ACS Catal.*, vol. 10, no. 24, pp. 14694–14706, 2020,
- [91] H. Yang *et al.*, “Core-shell structured Cu@m-SiO₂ and Cu/ZnO@m-SiO₂ catalysts for methanol synthesis from CO₂ hydrogenation,” *Catal. Commun.*, vol. 84, pp. 56–60, 2016,
- [92] J. et al Graciani, “PCE = 17.76%), and the other was the reference without enhanced reconstruction (V,” *Science (80-.)*, vol. 345, no. 6196, pp. 546–550, 2014.
- [93] K. K. Bando, K. Sayama, H. Kusama, K. Okabe, and H. Arakawa, “In-situ FT-IR study on CO₂ hydrogenation over Cu catalysts supported on SiO₂, Al₂O₃, and TiO₂,” *Appl. Catal. A Gen.*, vol. 165, no. 1–2, pp. 391–409, 1997,
- [94] J. Xiao, D. Mao, X. Guo, and J. Yu, “Effect of TiO₂, ZrO₂, and TiO₂-ZrO₂ on the performance of CuO-ZnO catalyst for CO₂ hydrogenation to methanol,” *Appl. Surf. Sci.*, vol. 338, pp. 146–153, 2015,
- [95] C. Liu, X. Guo, Q. Guo, D. Mao, J. Yu, and G. Lu, “Methanol synthesis from CO₂ hydrogenation over copper catalysts supported on MgO-modified TiO₂,” *J. Mol. Catal. A Chem.*, vol. 425, pp. 86–93, 2016,
- [96] S. Jiang *et al.*, “Dehydration of Methanol to Dimethyl Ether over ZSM-5 Zeolite,” *Bull. Korean Chem. Soc.*, vol. 25, no. 2, pp. 185–189, 2004,
- [97] M. Mollavali, F. Yaripour, H. Atashi, and S. Sahebdelfar, “Intrinsic kinetics study of dimethyl ether synthesis from methanol on γ -Al₂O₃ catalysts,” *Ind. Eng. Chem. Res.*, vol. 47, no. 9, pp. 3265–3273, 2008,
- [98] G. Bonura *et al.*, “Catalytic behaviour of a bifunctional system for the one step synthesis of DME by CO₂ hydrogenation,” *Catal. Today*, vol. 228, pp. 51–57, 2014,
- [99] N. Delgado Otalvaro, G. Sogne, K. Herrera Delgado, S. Wild, S. Pitter, and J. Sauer, “Kinetics of the direct DME synthesis from CO₂rich syngas under variation of the CZA-to- γ -Al₂O₃ratio of a mixed catalyst bed,” *RSC Adv.*, vol. 11, no. 40, pp. 24556–24569, 2021,
- [100] S. Hosseininejad, A. Afacan, and R. E. Hayes, “Catalytic and kinetic study of methanol dehydration to dimethyl ether,” *Chem. Eng. Res. Des.*, vol. 90, no. 6, pp. 825–833, 2012,
- [101] K. W. Jun, H. S. Lee, H. S. Roh, and S. E. Park, “Catalytic dehydration of methanol to dimethyl ether (DME) over solid-acid catalysts,” *Bull. Korean Chem. Soc.*, vol. 23, no. 6, pp. 803–806, 2002,
- [102] G. Bonura *et al.*, “Acidity control of zeolite functionality on activity and stability of hybrid catalysts during DME production via CO₂ hydrogenation,” *J. CO₂ Util.*, vol.

- 24, no. October 2017, pp. 398–406, 2018,
- [103] F. Frusteri, M. Cordaro, C. Cannilla, and G. Bonura, “Multifunctionality of Cu-ZnO-ZrO₂/H-ZSM5 catalysts for the one-step CO₂-to-DME hydrogenation reaction,” *Appl. Catal. B Environ.*, vol. 162, pp. 57–65, 2015,
- [104] M. Cai *et al.*, “Direct dimethyl ether synthesis from syngas on copper-zeolite hybrid catalysts with a wide range of zeolite particle sizes Dedicated to Professor Jean-Pierre Gilson on the occasion of his 60th birthday,” *J. Catal.*, vol. 338, pp. 227–238, 2016,
- [105] F. Frusteri *et al.*, “Direct CO₂-to-DME hydrogenation reaction: New evidences of a superior behaviour of FER-based hybrid systems to obtain high DME yield,” *J. CO₂ Util.*, vol. 18, pp. 353–361, 2017,
- [106] G. F. Froment and K. B. Bischoff, *Chemical Reactor Analysis and Design*, 2nd editio. New York, 1990.
- [107] C. S. Bildea, R. György, C. C. Brunchi, and A. A. Kiss, “Optimal design of intensified processes for DME synthesis,” *Comput. Chem. Eng.*, vol. 105, pp. 142–151, 2017,
- [108] Y. Ohno, H. Yagi, N. Inoue, K. Okuyama, and S. Aoki, “Slurry phase DME direct synthesis technology -100 tons/day demonstration plant operation and scale up study-,” *Stud. Surf. Sci. Catal.*, vol. 167, pp. 403–408, 2007,
- [109] S. Papari, M. Kazemeini, and M. Fattahi, “Mathematical modeling of a slurry reactor for DME direct synthesis from syngas,” *J. Nat. Gas Chem.*, vol. 21, no. 2, pp. 148–157, 2012,
- [110] Z. Wang, J. Wang, J. Diao, and Y. Jin, “The synergy effect of process coupling for dimethyl ether synthesis in slurry reactors,” *Huaxue Fanying Gongcheng Yu Gongyi/Chemical React. Eng. Technol.*, vol. 17, no. 3, pp. 233–237, 2001.
- [111] W. Z. Lu, L. H. Teng, and W. De Xiao, “Simulation and experiment study of dimethyl ether synthesis from syngas in a fluidized-bed reactor,” *Chem. Eng. Sci.*, vol. 59, no. 22–23, pp. 5455–5464, 2004,
- [112] W. Lu, L. Teng, and W. Xiao, “INTERNATIONAL JOURNAL OF CHEMICAL Theoretical Analysis of Fluidized-Bed Reactor for Dimethyl Ether Synthesis from Syngas Theoretical Analysis of Fluidized-Bed Reactor for Dimethyl Ether Synthesis from Syngas,” vol. 1, 2003.
- [113] P. Rodriguez-Vega *et al.*, “Experimental implementation of a catalytic membrane reactor for the direct synthesis of DME from H₂+CO/CO₂,” *Chem. Eng. Sci.*, vol. 234, 2021,
- [114] M. Farsi, A. Hallaji Sani, and P. Riasatian, “Modeling and operability of DME production from syngas in a dual membrane reactor,” *Chem. Eng. Res. Des.*, vol. 112, pp. 190–198, 2016,
- [115] F. Gallucci, *Inorganic Membrane Reactors for Methanol Synthesis*. Elsevier B.V., 2018.
- [116] A. Ateka, J. Ereña, J. Bilbao, and A. T. Aguayo, “Strategies for the Intensification of CO₂ Valorization in the One-Step Dimethyl Ether Synthesis Process,” *Ind. Eng. Chem. Res.*, vol. 59, no. 2, pp. 713–722, 2020,

- [117] M. De Falco, M. Capocelli, and A. Basile, "Selective membrane application for the industrial one-step DME production process fed by CO₂ rich streams: Modeling and simulation," *Int. J. Hydrogen Energy*, vol. 42, no. 10, pp. 6771–6786, 2017,
- [118] N. Diban, A. M. Urriaga, I. Ortiz, J. Ereña, J. Bilbao, and A. T. Aguayo, "Influence of the membrane properties on the catalytic production of dimethyl ether with in-situ water removal for the successful capture of CO₂," *Chem. Eng. J.*, vol. 234, pp. 140–148, 2013,
- [119] J. Wu, M. Saito, M. Takeuchi, and T. Watanabe, "The stability of Cu/ZnO-based catalysts in methanol synthesis from a CO₂-rich feed and from a CO-rich feed," *Appl. Catal. A Gen.*, vol. 218, no. 1–2, pp. 235–240, 2001,
- [120] R. M. Ravenelle *et al.*, "Stability of zeolites in hot liquid water," *J. Phys. Chem. C*, vol. 114, no. 46, pp. 19582–19595, 2010,
- [121] F. Gallucci, A. Basile, and F. I. Hai, *Introduction- A review of membrane reactors*. 2011.
- [122] C. Brencio, M. Maruzzi, and G. Manzolini, "ScienceDirect Butadiene production in membrane reactors : A techno-economic analysis," *Int. J. Hydrogen Energy*, vol. 47, no. 50, pp. 21375–21390, 2022,
- [123] W. Yue, Z. Wan, Y. Li, X. He, J. Caro, and A. Huang, "Synthesis of Cu – ZnO – Pt @ HZSM-5 catalytic membrane reactor for CO₂ hydrogenation to dimethyl ether," *J. Memb. Sci.*, vol. 660, no. July, p. 120845, 2022,
- [124] A. Brunetti, M. Migliori, D. Cozza, E. Catizzone, G. Giordano, and G. Barbieri, "Methanol Conversion to Dimethyl Ether in Catalytic Zeolite Membrane Reactors," 2020,
- [125] L. M. Robeson, "The upper bound revisited," *J. Memb. Sci.*, vol. 320, no. 1–2, pp. 390–400, 2008,
- [126] M. De Falco, M. Capocelli, A. Basile, and C. B. Roma, "ScienceDirect Selective membrane application for the industrial one-step DME production process fed by CO₂ rich streams : Modeling and simulation," *Int. J. Hydrogen Energy*, vol. 42, no. 10, pp. 6771–6786, 2017,
- [127] K. H. Lee, M. Y. Youn, and B. Sea, "Preparation of hydrophilic ceramic membranes for a dehydration membrane reactor," *Desalination*, vol. 191, no. 1–3, pp. 296–302, 2006,
- [128] E. Piera, M. A. Salomón, J. Coronas, M. Menéndez, and J. Santamaría, "Synthesis, characterization and separation properties of a composite mordenite/ZSM-5/chabazite hydrophilic membrane," *J. Memb. Sci.*, vol. 149, no. 1, pp. 99–114, 1998,
- [129] R. Raso *et al.*, "Zeolite membranes: Comparison in the separation of H₂O/H₂/CO₂ mixtures and test of a reactor for CO₂ hydrogenation to methanol," *Catal. Today*, vol. 364, no. September 2019, pp. 270–275, 2021,
- [130] M. P. Rohde, G. Schaub, S. Khajavi, J. C. Jansen, and F. Kapteijn, "Fischer-Tropsch synthesis with in-situ H₂O removal - Directions of membrane development," *Microporous Mesoporous Mater.*, vol. 115, no. 1–2, pp. 123–136, 2008,

- [131] S. Sommer and T. Melin, "Influence of operation parameters on the separation of mixtures by pervaporation and vapor permeation with inorganic membranes. Part 1: Dehydration of solvents," *Chem. Eng. Sci.*, vol. 60, no. 16, pp. 4509–4523, 2005,
- [132] Z. Qiao, Z. Wang, C. Zhang, S. Yuan, Y. Zhu, and J. Wang, "PVAm-PIP/PS composite membrane with high performance for CO₂/N₂ separation," *AIChE J.*, vol. 59, no. 4, pp. 215–228, 2012,
- [133] I. Iliuta, F. Larachi, and P. Fongarland, "Dimethyl ether synthesis with in-situ H₂O removal in fixed-bed membrane reactor: Model and simulations," *Ind. Eng. Chem. Res.*, vol. 49, no. 15, pp. 6870–6877, 2010,
- [134] N. Diban, A. M. Urriaga, I. Ortiz, J. Erenãa, J. Bilbao, and A. T. Aguayo, "Improved performance of a PBM reactor for simultaneous CO₂ capture and DME synthesis," *Ind. Eng. Chem. Res.*, vol. 53, no. 50, pp. 19479–19487, 2014,
- [135] F. Gallucci, L. Paturzo, and A. Basile, "An experimental study of CO₂ hydrogenation into methanol involving a zeolite membrane reactor," *Chem. Eng. Process. Process Intensif.*, vol. 43, no. 8, pp. 1029–1036, 2004,
- [136] M. P. Rohde, D. Unruh, and G. Schaub, "Membrane application in Fischer-Tropsch synthesis to enhance CO₂ hydrogenation," *Ind. Eng. Chem. Res.*, vol. 44, no. 25, pp. 9653–9658, 2005,
- [137] J. Hedlund, F. Jareman, A. J. Bons, and M. Anthonis, "A masking technique for high quality MFI membranes," *J. Memb. Sci.*, vol. 222, no. 1–2, pp. 163–179, 2003,
- [138] R. Lai and G. R. Gavalas, "Surface seeding in ZSM-5 membrane preparation," *Ind. Eng. Chem. Res.*, vol. 37, no. 11, pp. 4275–4283, 1998,
- [139] A. F. Ismail and L. I. B. David, "Future direction of R and D in carbon membranes for gas separation," *Membr. Technol.*, no. 4 APRIL, pp. 4–7, 2003,
- [140] S. C. Rodrigues, M. Andrade, J. Moffat, F. D. Magalhães, and A. Mendes, "Carbon Membranes with Extremely High Separation Factors and Stability," *Energy Technol.*, vol. 7, no. 4, pp. 1–7, 2019,
- [141] A. F. Ismail and L. I. B. David, "A review on the latest development of carbon membranes for gas separation," *J. Memb. Sci.*, vol. 193, no. 1, pp. 1–18, 2001,
- [142] F. Pontzen, W. Liebner, V. Gronemann, M. Rothaemel, and B. Ahlers, "CO₂-based methanol and DME - Efficient technologies for industrial scale production," *Catal. Today*, vol. 171, no. 1, pp. 242–250, 2011,
- [143] P. Applications, "State of the Art and Perspectives of CO₂ Methanation Process Concepts for State of the Art and Perspectives of CO₂ Methanation Process Concepts for Power-to-Gas Applications," no. January, 2014.
- [144] S. M. Saufi and A. F. Ismail, "Fabrication of carbon membranes for gas separation - A review," *Carbon N. Y.*, vol. 42, no. 2, pp. 241–259, 2004,
- [145] A. B. Fuertes, "Adsorption-selective carbon membrane for gas separation," *J. Memb. Sci.*, vol. 177, no. 1–2, pp. 9–16, 2000,

- [146] L. Forster *et al.*, “Tailoring pore structure and surface chemistry of microporous Alumina-Carbon Molecular Sieve Membranes (Al-CMSMs) by altering carbonization temperature for optimal gas separation performance: An investigation using low-field NMR relaxation measurements,” *Chem. Eng. J.*, p. 129313, 2021,
- [147] M. Kiyono, P. J. Williams, and W. J. Koros, “Effect of pyrolysis atmosphere on separation performance of carbon molecular sieve membranes,” *J. Memb. Sci.*, vol. 359, no. 1–2, pp. 2–10, 2010,
- [148] J. B. S. Hamm, A. Ambrosi, J. G. Griebeler, N. R. Marcilio, I. C. Tessaro, and L. D. Pollo, “Recent advances in the development of supported carbon membranes for gas separation,” *Int. J. Hydrogen Energy*, vol. 42, no. 39, pp. 24830–24845, 2017,
- [149] C. W. Jones and W. J. Koros, “Characterization of Ultramicroporous Carbon Membranes with Humidified Feeds,” *Ind. Eng. Chem. Res.*, vol. 34, no. 1, pp. 158–163, 1995,
- [150] A. B. Fuertes, D. M. Nevskaja, and T. A. Centeno, “Carbon composite membranes from Matrimid® and Kapton® polyimides for gas separation,” *Microporous Mesoporous Mater.*, vol. 33, no. 1–3, pp. 115–125, 1999,
- [151] V. C. Geiszler and W. J. Koros, “Effects of polyimide pyrolysis conditions on carbon molecular sieve membrane properties,” *Ind. Eng. Chem. Res.*, vol. 35, no. 9, pp. 2999–3003, 1996,
- [152] J. Gilron and A. Soffer, “Knudsen diffusion in microporous carbon membranes with molecular sieving character,” *J. Memb. Sci.*, vol. 209, no. 2, pp. 339–352, 2002,
- [153] “Transport mechanism of carbon membranes . Carbon-based membr . Sep . Process,” no. 2011, p. 2021, 2021.
- [154] M. A. Llosa Tanco, J. A. Medrano, V. Cechetto, F. Gallucci, and D. A. Pacheco Tanaka, “Hydrogen permeation studies of composite supported alumina-carbon molecular sieves membranes: Separation of diluted hydrogen from mixtures with methane,” *Int. J. Hydrogen Energy*, no. 46.37, pp. 19758-19767, 2020.
- [155] R. J. R. Uhlhorn, K. Keizer, and A. J. Burggraaf, “Gas transport and separation with ceramic membranes. Part I. Multilayer diffusion and capillary condensation,” *J. Memb. Sci.*, vol. 66, no. 2–3, pp. 259–269, 1992,
- [156] K. H. Lee and S. T. Hwang, “The transport of condensible vapors through a microporous vycor glass membrane,” *J. Colloid Interface Sci.*, vol. 110, no. 2, pp. 544–555, 1986.
- [157] T. Horikawa, D. D. Do, and D. Nicholson, “Capillary condensation of adsorbates in porous materials,” *Adv. Colloid Interface Sci.*, vol. 169, no. 1, pp. 40–58, 2011,
- [158] L. Fisher, R. Gamble, and J. Middlehurst, “The Kelvin equation and capillary condensation,” *Nature*, vol. 290, no. April, pp. 575–576, 1981, [Online]. Available: <https://www.nature.com/articles/290575a0.pdf>
- [159] S. Lagorsse, F. D. Magalhães, and A. Mendes, “Aging study of carbon molecular sieve membranes,” *J. Memb. Sci.*, vol. 310, no. 1–2, pp. 494–502, 2008,

CHAPTER 2

Direct conversion of CO₂ to dimethyl ether in a packed bed membrane reactor: influence of membrane properties and process conditions

Abstract

In this chapter, a 1D phenomenological reactor model is developed to evaluate and optimize the performance of a membrane reactor for the direct hydrogenation of CO₂ to dimethyl ether (DME) reaction, otherwise limited by thermodynamic equilibrium and temperature gradients. The cocurrent circulation of a sweep gas stream through the permeation zone promotes both water and heat removal from the reaction zone, thus increasing overall DME yield (from 44% to 64%). The membrane properties in terms of water permeability (i.e., $4 \cdot 10^{-7}$ mol·Pa⁻¹·m⁻²·s⁻¹) and selectivity (i.e., 50 towards H₂, 30 towards CO₂ and CO, 10 towards methanol), for optimal reactor performance have been determined considering, for the first time, non-ideal separation and non-isothermal operation. Thus, this work sheds light into suitable membrane materials for this application. Then, the non-isothermal performance of the membrane reactor was analyzed as a function of the process parameters (i.e., the sweep gas to feed flow ratio, the gradient of total pressure across the membrane, the inlet temperature to the reaction and permeation zone and the feed composition). Owing to its ability to remove 96% of the water produced in this reaction, the proposed membrane reactor outperforms a conventional packed bed for the same application (i.e., with 36% and 46% improvement in CO₂ conversion and DME yield, respectively). The results of this chapter demonstrate the potential of the membrane reactor to make the CO₂ conversion to DME a feasible process.

This chapter is based on the following paper:

Poto, S., Gallucci, F., & Neira d'Angelo, M. F. (2021). Direct conversion of CO₂ to dimethyl ether in a fixed bed membrane reactor: Influence of membrane properties and process conditions. *Fuel*, 302, 121080.

2.1 INTRODUCTION

As described in Chapter 1, the CO₂ conversion to methanol and dimethyl ether is severely limited by the thermodynamic equilibrium. Being water the main reaction by-product as well as often cause for catalyst deactivation, this process could enormously benefit from the in-situ removal of water from the reaction environment. To this scope, membrane reactor has been identified as a promising technology with the ability to couple reaction and product separation in a single unit as a mean to overcome the thermodynamic limitations (*Le Chatelier* principle).

Several studies have been published on the use of both organic and inorganic membranes to enhance the synthesis of methanol. Struis et al. [1], [2] showed that the integration of a Nafion membrane for the selective removal of water in a packed bed reactor has remarkable effects on the CO₂ conversion and methanol yield. However, given the poor thermal stability of the polymeric membranes, most of the recent research interests shifted towards inorganic membranes, which are more thermally stable [3]–[5]. These and other works show that water permeability and selectivity (i.e., H₂O/H₂ and H₂O/CO₂ separation factors) are critical parameters with remarkable impact on the overall process. While the use of membrane technology for the synthesis of methanol is well demonstrated in the literature, and several modeling studies also demonstrate its benefits to enhance the dehydration of methanol to DME [6]–[8], the application of membrane reactors for the direct conversion of CO₂ to DME (i.e., in one step) has gained research attention only very recently. In fact, the direct synthesis of DME from CO₂-rich syngas (i.e., not yet pure CO₂) became a topic of interests in the last decades due to the popularity of biomass gasification technologies. Several works demonstrated the importance of the in-situ water removal, especially when gradually replacing CO with CO₂ [9]–[12]. De Falco et al. [13], [14] showed for the first time that the considerations of a heat management strategy and the operation under non-isothermal conditions are key in this temperature-sensitive process. In view of the increasing interests in CO₂ capture and valorization, very recently the direct synthesis of DME from concentrated CO₂ and H₂ has become a hot topic. The CO₂-to-DME process is even more challenging than the well-studied (CO₂-rich) syngas route, and thus requires dedicated attention, due to the formation of larger amounts of water, leading to more severe thermodynamic limitations and membrane stability issues.

Very recently, the work of Ateka and collaborators [15]–[17], demonstrates the benefits of a packed bed membrane reactor to boost the synthesis of DME starting from CO₂ and CO mixed in different ratios. Their work considers the use of zeolite membranes (i.e., H-SOD type and LTA type), and concludes that the in-situ removal of water leads to improved DME yields and stable catalytic performance with respect to a conventional packed bed. Nevertheless, their work focuses on relatively high temperature operation (i.e., above 275 °C), which limits the membrane separation performance in terms of water permeability and water separation factors [18]. Although these operating conditions lead to attractive DME yields when starting with CO₂/CO_x (with CO_x=CO+CO₂) up to 0.5 (i.e., 65% for pure CO), the

reported DME yields for pure CO₂ feeds remain very low (~5%). Thus, it is evident that the shift in feed composition from (CO₂-rich) syngas to pure CO₂ poses additional demands on the membrane separation, and thus requires further investigation. To this end, it is important to consider a wider temperature range (i.e., especially towards lower temperatures that favor water permeation), as well as the non-ideal behavior of real membranes. Most of the modeling studies reported so far [9]–[14] including the most recent works by Ateka et al. [16], consider zeolite membranes that ideally permeate only the smallest molecules (i.e., H₂O and H₂). However, the likely permeation of other gases such as CO and methanol may significantly reduce the DME yield, and therefore should be taken into account when optimizing membrane properties. Furthermore, the importance of the heat integration in this process should not be underestimated, as temperature enormously affects the product distribution (i.e., reactions limited by thermodynamic equilibrium), as well as the membrane separation properties and stability. Indeed, if an adequate strategy to control the temperature gradients is not adopted, the process would converge into the r-WGS [19].

In this chapter, the performance of a membrane reactor for the direct conversion of CO₂ to DME has been described through a non-isothermal phenomenological 1D reactor model. A reactor configuration in which a sweep gas is fed co-currently with the feed to promote both water and heat removal from the reaction zone is proposed. This work does not focus on a specific membrane material, but rather aims at identifying the required membrane properties (i.e., permeability and selectivity of all the species) which maximize DME yield and CO₂ conversion and uses that as a basis for the identification of a suitable membrane material. Among the available membrane materials, this study pays special attention to porous membranes as they fulfil important pre-requirements concerning hydrophilicity, thermal and mechanical stability and high selectivity [20]. The effect of process parameters (i.e., the sweep gas to feed flow ratio, the gradient of total pressure across the membrane, the inlet temperature to the reaction and permeation zone and the feed composition) on CO₂ conversion and DME selectivity is investigated through parametric studies. Finally, this work provides insights about optimal membrane properties and process conditions that render maximum DME yields.

2.2 REACTOR CONFIGURATION AND MODELING

2.2.1 Description of the reactor configuration

The packed bed membrane reactor considered in this work is sketched in **Figure 2.1** with the properties summarized in **Table 2.1**. The reactor is composed of two coaxial tubes: an inner tubular membrane and an outer reactor shell which hosts the catalyst bed, giving raise to two zones, referred as the permeation and the reaction zone, respectively. This configuration allows for a high mechanical stability of the membrane, and easy optimization of the ratio between the membrane area and catalyst volume. Since the permeation of species depends on the gradient in partial

pressure across the membrane, two different approaches can be considered to promote the removal of water: 1) applying a gradient of total pressure between the reaction and the permeation zone; and 2) feeding a sweep gas through the permeation zone to dilute the permeated water. The first solution leads to more mechanical stress on the membrane, and a higher driving force for the permeation of all the species, leading to the unwanted loss of reactants. On the other hand, using a sweep gas with the same composition of the feed favors the selective removal of water and minimizes reactants loss. In this study, a sweep gas is fed in a cocurrent configuration in order to enhance water removal at the beginning of the reactor, where the reaction rate and water formation are the highest. Additionally, the cocurrent circulation of the sweep gas at a lower temperature favors the removal of the heat of the reaction, optimizing the temperature profile. For an exothermic reaction, a cocurrent circulation of the reaction mixture and the cooling fluid is preferred, because most of the heat is produced at the beginning of the reactor.

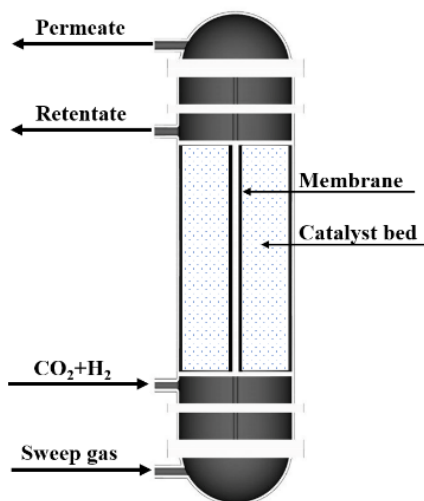


Figure 2.1. Schematic representation of the packed bed membrane reactor

Table 2.1. Main characteristics of the packed bed membrane reactor

Parameter	Value
Reactor shell internal diameter, D_{si} (m)	0.0198
Catalyst bed and membrane length, L (m)	1
Catalyst particle diameter, d_p (m)	$4 \cdot 10^{-4}$
Catalyst density, ρ_c (kg/m^3)	1982
Catalyst bed porosity, ε (-)	0.4
External membrane diameter, D_{mo} (m)	$14 \cdot 10^{-3}$
Internal membrane diameter, D_{mi} (m)	$10 \cdot 10^{-3}$

2.2.2 Modeling equations

The phenomenological reactor model relies on the following assumptions:

1. Steady state conditions
2. 1D ideal plug flow (i.e., axial and radial dispersion is neglected by considering $L/d_p \geq 50$ and $D/d_p \geq 25$, respectively)
3. Kinetic control regime (i.e., the solid and gas phase are described as a single pseudo-homogeneous phase, due to the absence of mass transfer limitations)
4. Negligible pressure drops in the permeation side
5. Kinetics by Lu et al. [21] valid for conventional and membrane reactor
6. Inert membrane material under reaction conditions.

Accordingly, the membrane reactor model consists of mass and energy balances for both the reaction and permeation zone, and a momentum balance for the reaction zone only. For each of the six chemical species that take part in the process (i), the following equations hold:

$$\frac{dF_i^R}{dz} = \rho_c(1 - \varepsilon) \sum_{j=1}^{N_r} (r_j v_{ji}) \frac{\pi}{4} (D_{si}^2 - D_{mo}^2) - J_i \pi D_{mo} \quad (2.1)$$

$$\frac{dF_i^P}{dz} = J_i \pi D_{mo} \quad (2.2)$$

Where J_i is the flux of component i through the membrane, as defined in Eq. 2.3. By definition, J_i is positive when the species permeates from the reaction to the permeation zone.

$$J_i = \wp_i \cdot (P_i^R - P_i^P) \quad (2.3)$$

\wp_i is the permeance of the component i and P_i^R and P_i^P are its partial pressure in the reaction and permeation zone, respectively. The selectivity of water to the permeation (i.e., perm-selectivity) with respect to the component i is defined as follows:

$$S_{H_2O/i} = \frac{\wp_{H_2O}}{\wp_i} \quad (2.4)$$

In this chapter, the dependency of \wp_i on the composition was neglected because the composition of water (i.e., the primarily permeating species) does not change significantly, as confirmed later in Section 2.3.3. In addition, it was assumed that the permeation flux is limited by the transport through the membrane selective layer. Indeed, gas/vapor permeation through porous membranes is usually not affected by concentration polarization phenomena (i.e., resistance to the transport from a bulk phase to the membrane surface) because of the high diffusivity and low permeability of the gases, when compared to liquids [22].

In this chapter, the kinetic model by W. Lu et al. (Eq. 2.5-2.7) for the well-studied CuZnOAl₂O₃/HZSM-5 bifunctional catalyst was considered [21]. This kinetic model neglects the CO hydrogenation to methanol, thus reaction 3 corresponds to the methanol dehydration to DME. The extensive amount of experimental data reported for such catalyst allow to easily validate the kinetic model, as well as its implementation into the reactor model. Nevertheless, other kinetic models have been reported in literature [21], [23]–[29], very recently also for new catalyst types, such as CuO-ZnO-MnO/SAPO-18 [30] and a core shell CuOZnOZrO₂@SAPO-18 [31].

Coke formation and water adsorption (i.e. main causes of catalyst deactivation) are avoided due to the relatively low reaction temperatures and the water removal, respectively. The rate expressions derive from a Langmuir Hinshelwood model, in which the water and methanol adsorption on the catalyst surface are neglected.

$$r_1 = k_1 \frac{P_{\text{CO}_2} P_{\text{H}_2} \left(1 - \frac{1}{K_{p,1}} \frac{P_{\text{H}_2\text{O}} P_{\text{CH}_3\text{OH}}}{P_{\text{CO}_2} P_{\text{H}_2}^3} \right)}{\left(1 + K_{\text{CO}_2} P_{\text{CO}_2} + K_{\text{CO}} P_{\text{CO}} + \sqrt{K_{\text{H}_2} P_{\text{H}_2}} \right)^3} \quad (2.5)$$

$$r_2 = k_2 \frac{\frac{1}{K_{p,2}} \frac{P_{\text{CO}_2} P_{\text{H}_2}}{P_{\text{CO}}} - P_{\text{H}_2\text{O}}}{\left(1 + K_{\text{CO}_2} P_{\text{CO}_2} + K_{\text{CO}} P_{\text{CO}} + \sqrt{K_{\text{H}_2} P_{\text{H}_2}} \right)} \quad (2.6)$$

$$r_3 = k_3 \left(\frac{P_{\text{CH}_3\text{OH}}^2}{P_{\text{H}_2\text{O}}} - \frac{P_{\text{CH}_3\text{OCH}_3}}{K_{p,3}} \right) \quad (2.7)$$

Here P_i is the partial pressure of each component in the reaction zone, calculated as the product between the total pressure and the molar fractions. The kinetics [21], adsorption [32], [33] and equilibrium constants [33] are shown in **Table 2.2**.

Table 2.2. Kinetic parameters of the catalytic hydrogenation of CO₂ to DME

Kinetic parameter	Value
k_1 (kmol/(kg _{cat} · s · bar ²))	$35.45 \cdot \exp\left(-\frac{1.7609 \cdot 10^4}{RT}\right)$
k_2 (kmol/(kg _{cat} · s · bar))	$7.3976 \cdot \exp\left(-\frac{2.0436 \cdot 10^4}{RT}\right)$
k_3 (kmol/(kg _{cat} · s · bar))	$8.2894 \cdot \exp\left(-\frac{5.294 \cdot 10^4}{RT}\right)$
K_{H_2} (bar ⁻¹)	$0.249 \cdot \exp\left(\frac{3.4394 \cdot 10^4}{RT}\right)$
K_{CO_2} (bar ⁻¹)	$1.02 \cdot 10^{-7} \exp\left(\frac{6.74 \cdot 10^4}{RT}\right)$
K_{CO} (bar ⁻¹)	$7.99 \cdot 10^{-7} \exp\left(\frac{5.81 \cdot 10^4}{RT}\right)$
$K_{p,1}$ (bar ⁻²)	$\exp(4213/T - 5.752 \cdot \ln(T) - 1.707 \cdot 10^{-3}T + 2.682 \cdot 10^{-6}T^2 - 7.232 \cdot 10^{-10}T^3 + 17.6)$
$K_{p,2}$ (-)	$\exp(2167/T - 0.5194 \cdot \log(T) + 1.037 \cdot 10^{-3}T - 2.331 \cdot 10^{-7}T^2 - 1.277)$
$K_{p,3}$ (bar ⁻²)	$\exp(4019/T + 3.707 \cdot \ln(T) - 2.783 \cdot 10^{-3}T + 3.8 \cdot 10^{-7}T^2 - 6.56 \cdot 10^4/T^3 - 26.64)$

The energy balance in the reaction and the permeation zone are described in Eq. 2.8 and Eq. 2.9, respectively. These balances assume heat exchange between the reaction and permeation zone, but the reactor is isolated from the external environment to evaluate the thermal effects of feeding cold sweep gas as single cooling strategy.

$$\sum_{i=1}^{N_s} (F_i^R c_{p,i}) \frac{dT^R}{dz} = \rho_c (1 - \varepsilon) \frac{\pi}{4} (D_{si}^2 - D_{mo}^2) \sum_{j=1}^{N_r} r_j (-\Delta H_r(T^R)) + \quad (2.8)$$

$$-U\pi D_{mi}(T^R - T^P) - \pi D_{mo} \sum_{i=1}^{N_s} (J_i c_{p,i}(T^R - T_{mr}))$$

$$\sum_{i=1}^{N_s} (F_i^P c_{p,i}) \frac{dT^P}{dz} = U\pi D_{mi}(T^R - T^P) + \pi D_{mo} \sum_{i=1}^{N_s} (J_i c_{p,i}(T_{mp} - T^P)) \quad (2.9)$$

The global heat transfer coefficient U (2.10) describes three consecutive heat transfer phenomena: 1) the convection in the inner tube, 2) the conduction through the membrane and 3) the convection in the outer tube.

$$\frac{1}{U} = \frac{1}{h_{mi}} + \frac{D_{mi}}{2} \frac{1}{k_m} \ln\left(\frac{D_{mo}}{D_{mi}}\right) + \frac{D_{mi}}{D_{mo}} \frac{1}{h_{mo}} \quad (2.10)$$

The heat transfer coefficient in the permeation zone (h_{mi}) and reaction zone (h_{mo}) are calculated according to the correlations by Dittus-Boelter [34] and Li-Finlayson

[35], respectively (see Appendix A). The temperature at the membrane surface on the reaction (T_{mr}) and permeation side (T_{mp}) are determined by the steady state energy balance around the membrane (Eq. 2.11-2.12)

$$(T_{mp} - T^P)h_{mi} \frac{D_{mi}}{2} = \frac{(T_{mr} - T_{mp})k_m}{\ln\left(\frac{D_{mo}}{D_{mi}}\right)} \quad (2.11)$$

$$(T_{mp} - T^P)h_{mi}D_{mi} = (T^R - T_{mr})h_{mo}D_{mo} \quad (2.12)$$

The pressure drop in the reaction zone is described by the Ergun equation (Eq. 2.13), while the pressure drop along the permeation zone is considered negligible.

$$\frac{dP^R}{dz} = \frac{150\mu(1 - \varepsilon)^2v}{\varepsilon^3d_p^2} + \frac{1.75(1 - \varepsilon)\rho v^2}{\varepsilon^2d_p} \quad (2.13)$$

The above set of equations were implemented in MATLAB R2019a and solved numerically with the *ode15s* function.

2.2.3 Operating conditions and parametric study

Two parametric studies were performed to determine the optimal membrane properties (i.e., \wp_{H_2O} and $S_{H_2O/i}$), that render maximum CO_2 conversion and DME yield. The first parametric study (P1) assumes that only the smallest molecules (i.e., H_2O and H_2) permeates through the membrane, while the other species do not permeate (i.e., ideal membrane assumption). This initial study is used to determine the optimal values \wp_{H_2O} and S_{H_2O/H_2} . The second parametric study (P2) considers a real membrane where all species may permeate, and it is used to find the optimal selectivity of water with respect to the remaining species. Both P1 and P2 were carried out assuming isothermal conditions, and thus the membrane properties refer to the chosen temperature.

Table 2.3. Range of \wp_{H_2O} and $S_{H_2O/i}$ for the parametric study (P1 and P2).

Membrane property	P1: Ideal membrane	P2: Real membrane
\wp_{H_2O} ($mol \cdot Pa^{-1} \cdot m^{-2} \cdot s^{-1}$)	$0 - 1 \cdot 10^{-6}$	Optimal value from P1
S_{H_2O/H_2} (-)	$0.5 - 50$	Optimal value from P1
S_{H_2O/CO_2} (-)	∞	$5 - 50$
$S_{H_2O/CO}$ (-)	∞	$5 - 50$
$S_{H_2O/MeOH}$ (-)	∞	$5 - 10$
$S_{H_2O/DME}$ (-)	∞	∞

The ranges of \wp_{H_2O} and $S_{H_2O/i}$ considered in P1 and P2 are summarized in **Table 2.3**. Typical values of \wp_{H_2O} for porous membranes reported in the literature vary from $6.8 \cdot 10^{-8}$ to $9.7 \cdot 10^{-7}$ $mol \cdot Pa^{-1} \cdot m^{-2} \cdot s^{-1}$ [11]. Thus, this study assesses the effect of \wp_{H_2O} between 0 and $1 \cdot 10^{-6}$ $mol \cdot Pa^{-1} \cdot m^{-2} \cdot s^{-1}$. With respect to the remaining species, it

was considered that water will likely condense in the meso- and micro-pores of the membrane due to the low capillary pressures (e.g., capillary pressure is 10 bar at 200 °C for a pore size of 1 nm in a hydrophilic membrane). This will effectively reduce the pore size, and, consequently, hinder the permeation of non-condensable gases. Therefore, for most cases water has the highest permeance (i.e., $S_{H_2O/i} > 1$). Nevertheless, values of S_{H_2O/H_2} lower than 1 were also considered in this study, to contemplate the possibility of competitive permeation of these two species, with very similar size. In the worst case scenario (i.e., separation dictated by the Knudsen diffusion, usually occurring at higher temperatures within the bigger pores [36]), the Knudsen perm-selectivity of water and H₂ is $S_{H_2O/H_2} = \sqrt{M_{wH_2}/M_{wH_2O}} = 0.33$. Thus, the minimum value of S_{H_2O/H_2} is set to 0.5 (i.e., around 50% higher than the Knudsen perm-selectivity value), although this type of flow is not likely within a hydrophilic membrane. Data from literature [37], [38] show that CO and CO₂ permeances are very similar, due to their comparable molecular size. For this reason, the H₂O/CO₂ and H₂O/CO selectivity was set at the same value. Next, the permeance of methanol is higher than those of non-condensable gases (i.e., $S_{H_2O/MeOH}$ is lower) because methanol may also permeate through capillary condensation. Finally, DME cannot condense under reaction conditions because it exceeds its critical temperature (128 °C) under the operating conditions. DME molecular size is the largest among all the species in this process, which justifies the assumption of an infinite H₂O/DME selectivity. The dissolution of species in the condensed water was assumed negligible in this study, since liquid water only exists inside the (small) pore volume.

Table 2.4 reports the operating conditions evaluated in this study. These were kept constants during P1 and P2, while a third parametric study (P3) aimed to assess the effect of some operating conditions on the reactor performance. An average temperature of 200 °C was set as the target within the reaction zone in order to: 1) avoid catalyst deactivation, which occurs at temperatures greater than 270-300 °C [21], [39], [40]; 2) limit the production of CO, which occurs preferentially at elevated temperatures; 3) guarantee a sufficiently fast water permeation through the membrane, which is enhanced at lower temperatures due to its transport mechanism [41], [42]; and 4) guarantee sufficient catalyst activity, which demands temperatures greater than 190-200 °C [43]. Finally, a total pressure of 40 bar was set in the reaction zone.

Table 2.4. Operating conditions adopted in the simulations

Operating condition	P1	P2	P3
H ₂ :CO ₂ , (mol/mol) ^a	3	3	3 – 10
Φ _{H₂,0} ^R (Nm ³ /h)	0.1	0.1	0.1
T ₀ ^R , (°C)	200	200	200
T ₀ ^P , (°C)	200	200	120-200
P ₀ ^R , (bar)	40	40	40
ΔP (bar) ^b	0	0	0 – 40
SW (-) ^c	3	3	3 – 50

^aThe composition of the feed to the reaction and permeation zone is the same

^bΔP is the gradient in total pressure across the membrane.

^cSW is the sweep gas to feed molar flow ratio

The reactor performance was evaluated in terms of CO₂ conversion, product yield and selectivity, and the amount of water removed. The loss or cofeeding of reactants (i.e., through back-permeation of sweep gas in the reaction zone) was considered in the following definitions [44]:

$$X_{\text{CO}_2} = \frac{F_{\text{CO}_2,0}^{\text{R}} - F_{\text{CO}_2}^{\text{R}} - F_{\text{CO}_2,\text{tmb}}}{F_{\text{CO}_2,0}^{\text{R}} + F_{\text{CO}_2,\text{tmb}}^*} \quad (2.14)$$

$$Y_i = \frac{N_{\text{c},i}(F_i^{\text{R}} + F_i^{\text{P}})}{F_{\text{CO}_2,0}^{\text{R}} + F_{\text{CO}_2,\text{tmb}}^*} \quad (2.15)$$

$$S_i = \frac{Y_i}{X_{\text{CO}_2}} \quad (2.16)$$

$$F_{\text{CO}_2,\text{tmb}} = F_{\text{CO}_2}^{\text{P}} - F_{\text{CO}_2,0}^{\text{P}} \quad \text{CO}_2 \text{ transmembrane flow} \quad (2.17)$$

$$F_{\text{CO}_2,\text{tmb}}^* = 0 \quad \text{if } F_{\text{CO}_2,\text{tmb}} \geq 0 \quad \text{Reactant loss} \quad (2.18)$$

$$F_{\text{CO}_2,\text{tmb}}^* = -F_{\text{CO}_2,\text{tmb}} \quad \text{if } F_{\text{CO}_2,\text{tmb}} < 0 \quad \text{Reactant cofeeding} \quad (2.19)$$

$$\text{WR} = \frac{F_{\text{H}_2\text{O}}^{\text{P}}}{F_{\text{H}_2\text{O}}^{\text{P}} + F_{\text{H}_2\text{O}}^{\text{R}}} \quad (2.20)$$

Where $N_{\text{c},i}$ is the number of carbon atoms in the considered species. The WR is an important key performance indicator that represents the membrane efficiency. This variable was introduced by Battersby et al. [45], who defined the product of the Peclet and Damkohler numbers (DaPe) as a new dimensionless number representing the combined effect of reaction and separation. According to the DaPe definition (Eq. 2.21), a membrane reactor works in optimal conditions when DaPe approaches unity, which means, in our process, that all the water produced is removed through the membrane. However, DaPe = 1 describes a thermodynamic limit that can only be approached. Therefore, when DaPe exceeds 1, water builds-up in the reactor, indicating a poor performance of the membrane reactor.

$$\text{DaPe} = \frac{\text{Maximum reaction rate per unit volume}}{\text{Maximum permeation rate per unit volume}} \quad (2.21)$$

In this work, the WR number represents the reciprocal of the DaPe number.

2.3 SIMULATION RESULTS AND DISCUSSION

This section discusses the validation of the kinetic model and the results of the parametric studies for the optimization of the membrane properties (i.e., P1 and P2) and the process conditions (P3).

2.3.1 Validation of the kinetic model

The validity of the model was assessed by reproducing the experimental results of Ren et al. [46] derived for a CuZnOAl₂O₃/HZSM-5 bifunctional catalyst in a packed bed reactor, where the two functions were mixed in a 1:1 weight ratio. In **Figure 2.2** the results of the simulation related to both CO₂ conversion and DME yield are compared with the experimental data at a pressure of 28 bar, a GHSV of 1215 NL/(kg_{cat}·h) and a H₂/CO₂ molar ratio of 3:1. The model fits quite well the experimental data at lower temperatures (i.e., T ≤ 250 °C), which is the temperature range in which Lu et al. [21] studied the kinetics. Therefore, predictions beyond this temperature range have not been performed in this study. At 220 °C, the divergence between the model prediction and the experimental data is 1.92% for CO₂ conversion, 3.5% for DME yield and 1.05% for CO yield. The difference between the experimental data and the simulated values, which is larger at higher temperature, derives from the different composition of the catalytic bed of the two mentioned studies. However, the kinetic model describes the experimental trend with temperature of both CO₂ conversion and DME yield.

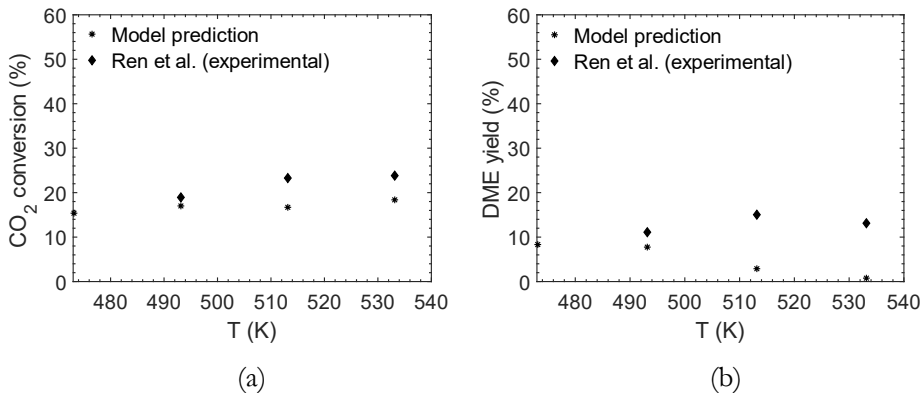


Figure 2.2. Comparison between the experimental data of Ren et al. [46] and the data obtained with the model prediction for a conventional reactor: CO₂ conversion (a) and DME yield (b) as a function of temperature at 28 bar, GHSV of 1215 NL/(kg_{cat}·h) and H₂/CO₂ molar ratio at 3:1.

Furthermore, the correct implementation of the kinetics was assessed by reproducing the theoretical results of a conventional packed bed reactor by Iliuta et al. [9] (see Appendix A, section A.2), with a deviation lower than 2%.

2.3.2 Optimization of membrane properties ($\phi_{\text{H}_2\text{O}}$ and $S_{\text{H}_2\text{O}/i}$)

Results of parametric study

The $\phi_{\text{H}_2\text{O}}$ and $S_{\text{H}_2\text{O}/\text{H}_2}$ were first optimized using the parametric study P1 (i.e., ideal membrane hypothesis holds), since they do not depend on the permeation of the other species. **Figure 2.3a** shows the effect of $\phi_{\text{H}_2\text{O}}$ on the water transmembrane flow, which expectedly increases with greater permeances, reaching a plateau at around $4 \cdot 10^{-7}$ mol/(Pa·m²·s), where the thermodynamic equilibrium between the reaction and the permeation zone is established. Accordingly, increasing permeance leads to improvement on CO₂ conversion (**Figure 2.3c**) and DME yield (**Figure 2.3d**) up to 0.6 and 0.5, respectively, due to a shift in the thermodynamic equilibrium.

In addition, **Figure 2.3** shows the effect of the selectivity of water with respect to H₂ on the same performance indicators (i.e., transmembrane flow of water and H₂, and resulting CO₂ conversion and DME yield). The ideal membrane allows only water and hydrogen to permeate. In principle, an increase in $S_{\text{H}_2\text{O}/\text{H}_2}$ may be considered advantageous to promote the permeation of water with respect to that of H₂ (i.e., a valuable reactant). Loosing H₂ through the membrane would be detrimental for the final DME yield as well as for the economics of the process. In this case, however, the composition of the sweep and feed gas streams are the same, which in facts results in a net back permeation of H₂ from the permeation to the reaction zone regardless of the selectivity. This phenomenon, hereby referred as cofeeding, explains the negative values reported in **Figure 2.3b**, particularly at low $S_{\text{H}_2\text{O}/\text{H}_2}$ values (i.e., poorly selective membranes). In other words, there is no need for a highly selective membrane to prevent H₂ loss when using a sweep gas with the same concentration as the feed mixture.

As shown in **Figure 2.3b** and **2.3c**, H₂ cofeeding is beneficial both for the CO₂ conversion and DME yield, in line with the work of Diban et al. [11]. Interestingly, these results also show that decreasing the H₂O/H₂ selectivity by three orders of magnitude leads to a negligible effect on the reactor performance. The low sensitivity of the process to variations in membrane selectivity is conducive to a very robust reactor concept. However, excessive cofeeding is undesirable because it would require a significant H₂ reintegration in the sweep gas before its recycling. In other words, despite the negligible effects of the perm-selectivity of hydrogen on conversion and yields, it is desirable that the membrane preferentially enhances the separation of water (i.e., relatively high values of $S_{\text{H}_2\text{O}/\text{H}_2}$). In that case, the permeated water can be easily condensed from the outlet of the permeation zone, facilitating direct recirculation of the sweep gas without complex post processing units. Thus, a $S_{\text{H}_2\text{O}/\text{H}_2}$ of 50 was considered for the rest of this study.

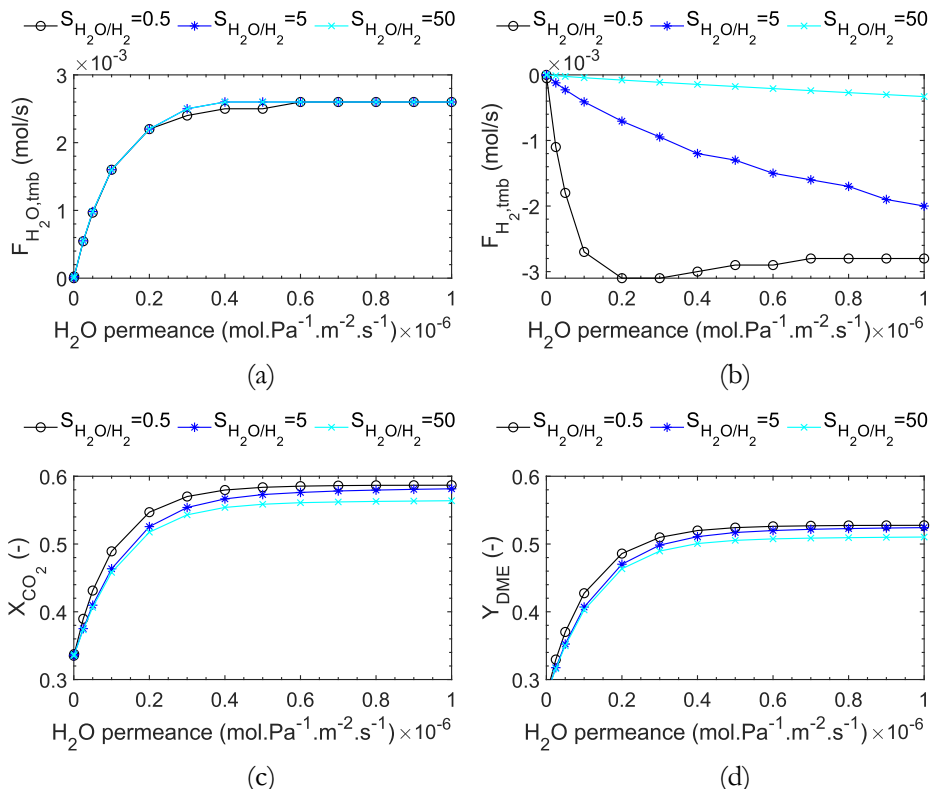


Figure 2.3. Effect of the H₂O permeance and H₂O/H₂ selectivity on the membrane reactor performances in terms of: a) water transmembrane flow ($F_{H_2O,tmb}$), b) hydrogen transmembrane flow ($F_{H_2,tmb}$), c) CO₂ conversion (X_{CO_2}) and d) DME yield (Y_{DME}). In each plot, curves are parametric for the H₂O/H₂ selectivity (S_{H_2O/H_2}).

Afterwards, the $S_{H_2O/CO}$, S_{H_2O/CO_2} and $S_{H_2O/MeOH}$ were optimized with the parametric study P2, which considers a real membrane. **Figure 2.4a** shows the effect of the H₂O/CO_x selectivity (where CO_x refers to either CO₂ or CO, with assumed equal permeance) on CO₂ conversion and products yield. Both CO₂ conversion and DME yield display a very mild increase with greater H₂O/CO_x selectivity, up to a maximum value of 0.60 and 0.42, respectively. On the other hand, methanol and CO yield are nearly unaffected by the H₂O/CO_x selectivity. In principle, increasing the H₂O/CO_x selectivity has two main advantages: 1) both the loss and cofeeding of CO₂ is limited, requiring no adjustment of the CO₂ composition in the sweep gas prior to recirculation, and 2) CO permeation is limited, which minimizes the extent of the reverse water gas shift reaction and thereby improves DME selectivity. However, these results show that the susceptibility of the system to this parameter is negligible, due to the use of a sweep gas with equal concentration as the feed stream, which limits the gases permeation in both ways. Hence, an average value 30 (i.e., a value in the middle of the range explored) is used in the rest of this study.

Figure 2.4b shows a slight negative effect of H₂O/MeOH selectivity on the CO₂ conversion and methanol yield. Expectedly, a greater methanol permeation (i.e., a low selectivity) results in a shift in the thermodynamic equilibrium of the CO₂ hydrogenation reaction (i.e., reaction 1). In this process, such situation is not desired since methanol permeation will limit its further dehydration to DME. For the same reason, when increasing the H₂O/MeOH selectivity, DME yield increases. Likewise in previous cases, the DME yield does not seem very sensitive to a 10-fold increase in the H₂O/MeOH selectivity. Further, **Figure 2.4b** shows that this selectivity has no effect on the CO yield, as expected. Since a higher value of selectivity is not physically expected, the optimal value of H₂O/MeOH selectivity was set to 10.

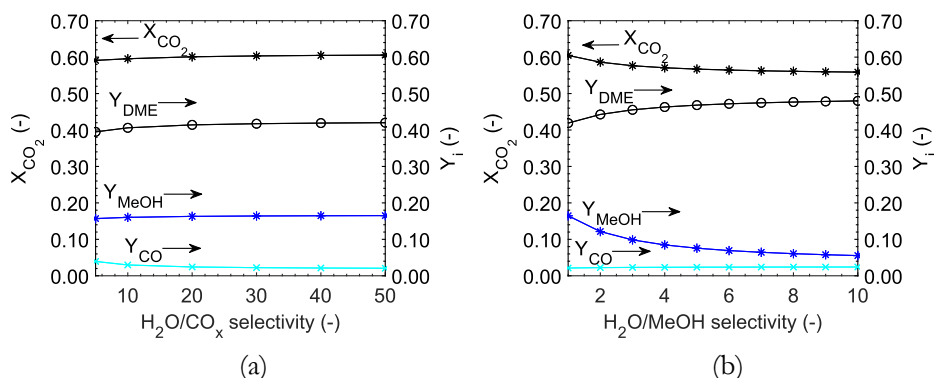


Figure 2.4. Effect of the H₂O/CO_x (a) and H₂O/MeOH selectivity (b) on the membrane reactor performances in terms of CO₂ conversion (X_{CO_2}), DME yield (Y_{DME}), methanol yield (Y_{MeOH}) and CO yield (Y_{CO}).

Finally, the large kinetic diameter of DME and its non-condensable nature under reaction conditions justifies the assumption of infinite H₂O/DME selectivity. However, it should be noted that an infinite value for the H₂O/DME selectivity is not necessarily optimal, since the removal of DME from the reaction environment is expected to enhance its production. Nevertheless, this would also require the recovery of DME from the permeate stream, demanding additional equipment and an energy intensive DME/CO₂ downstream separation track. **Table 2.5** summarizes the optimal membrane permeability properties as determined in the previous parametric studies (P1-P2).

Table 2.5. Optimal membrane properties determined through the parametric studies

Estimated membrane properties	Value
H ₂ O permeance, ϕ_{H_2O} (mol·Pa ⁻¹ ·m ⁻² ·s ⁻¹)	4·10 ⁻⁷
H ₂ O/H ₂ selectivity, S_{H_2O/H_2} (-)	50
H ₂ O/CO ₂ selectivity, S_{H_2O/CO_2} (-)	30
H ₂ O/CO selectivity, $S_{H_2O/CO}$ (-)	30
H ₂ O/MeOH selectivity, $S_{H_2O/MeOH}$ (-)	10
H ₂ O/DME selectivity, $S_{H_2O/DME}$ (-)	∞

Discussion on suitable membrane materials

Based on the results of the parametric studies, it is possible to elucidate on a suitable membrane material for the conversion of CO₂ to DME. To allow the separation of water vapor from a mixture of gases (e.g., H₂ and CO₂) the selected membrane material should be porous and possess affinity to water (i.e., it should be hydrophilic), thus favoring the permeation of water through capillary condensation and hindering that of non-condensable gases. The exact pore size of such material may be tailored as a trade-off between permeation fluxes and selectivity, which will strongly depend on the material itself and its degree of hydrophilicity. Besides its permeation properties, the membrane material should also be mechanically and thermo-chemically stable under process conditions. This is, the membrane should withstand pressures of 10-50 bar and temperature of 200-300 °C in humid environments, while preserving its chemical and porous structure, and associated permeation properties.

Polymeric membranes display adequate separation performance, but they undergo degradation at temperatures above their glass transition point (i.e., usually below 200 °C) and swelling phenomena may occur in too humid environment. The second important category of membranes material are porous ceramic membranes [47], [48] (e.g., alumina, silica, zirconia, titania or a mixture of them). Among them, zeolite membranes have been widely studied for pervaporation [49]. Indeed, several works describe the potential of microporous zeolite membranes for the selective removal of water for different processes such as the methanol synthesis [3]–[5], [20], the Fischer Tropsch process [38], [44] and the DME synthesis as well [10]–[12], [14]–[17]. **Table 2.6** reports the properties of zeolite membranes in terms on ϕ_{H_2O} and $S_{H_2O/i}$ retrieved from a literature survey. Although the reported permeation properties of zeolite membranes look very promising and match with our requirements, their stability in hot humid environments remains a topic of concern within the experimental research [50]. Their high separation factors, especially at high temperature, are still under investigations. In addition, it is difficult to obtain a large crack free zeolite membrane [51][52].

Table 2.6. Summary of the literature review on the properties of zeolite membranes in terms on ϕ_{H_2O} and $S_{H_2O/i}$, in the temperature range of 200-250 °C

Parameter	Value	Reference
ϕ_{H_2O} (mol·Pa ⁻¹ ·m ⁻² ·s ⁻¹)	6.8·10 ⁻⁸ - 1·10 ⁻⁶	[5], [18], [19], [38], [53]–[64]
S_{H_2O/H_2} (-)	2 – 50	[18], [38], [53], [54], [56], [58], [60]–[62]
S_{H_2O/CO_2} (-)	2.45 – 17.7	[38], [55], [57], [65], [66]
$S_{H_2O/CO}$ (-)	3.7 – 19.6	[38], [55], [57], [65], [66]
$S_{H_2O/MeOH}$ (-)	1 – 9	[18], [38], [59], [63], [67], [68]
$S_{H_2O/DME}$ (-)	Not defined	-

Carbon molecular sieve membranes (CMSM) are another interesting category of inorganic porous membranes that could be suitable for this application. Carbon membranes derive from the pyrolysis of a polymeric precursor [69], and according to the conditions of the carbonization process, different groups of atoms are removed from the precursor. The residual functional groups are responsible for the membrane hydrophilicity. Besides, these membranes are stable in both humid and hot environment, as far as the carbonization temperature (e.g. typically above 450 °C) is not overcome. Even if the concept of carbon membranes can be found back in the early 1970 [69], they have only been tested for gas separation processes [70], [71]. Therefore, further investigation is required when concerning the permeation of condensable species, such as water. Owing to its promising features, however, the following section considers the membrane module as an alumina supported carbon molecular sieve membrane [72].

2.3.3 Optimization of the operating conditions

This section discusses the effect of the main operating conditions on the reactor performance. In these simulations, the reactor was no longer considered isothermal. The heat balances were solved by considering an alumina supported carbon molecular sieve membrane material [72], in line with the previous discussion. The permeance and selectivity values of the selected membrane are shown in **Table 2.5**.

Effect of the sweep gas to feed flow ratio (SW) and the gradient of total pressure (ΔP)

The sweep gas to feed flow ratio (SW) and the gradient of total pressure across the membrane (ΔP) are the main parameters regulating the transmembrane driving force. **Figure 2.5a, b and c** show the effect of SW and ΔP on CO₂ conversion, DME yield and water removal (WR), which all increase when both SW and ΔP increase, up to an asymptotic value of 0.63, 0.53 and 0.96, respectively. An increase in both SW and ΔP effectively decreases the partial pressure of water in the permeate zone, and thus increases the driving force for water removal (i.e., greater WR). Therefore, the CO₂ conversion and DME yield, which benefit from the removal of water due to thermodynamic reasons, show the same trend as WR.

All the variables describing the reactor performance reach an asymptotic value when increasing SW and ΔP . In particular, the percentage of water removed from the reaction zone approaches a value slightly lower than 1 (i.e., between 0.94 and 0.96), indicating that most of the water produced in the reaction is effectively removed from the reaction zone. However, complete water removal is not possible due to the thermodynamic equilibrium established between the reaction and permeation zone.

It is interesting to note that WR, and accordingly CO₂ conversion and DME yield, are particularly sensitive to SW, while the effects of ΔP are less significant, especially at high SW. For example, for a SW of 50, an increase of ΔP from 0 to 40 bar leads to the mild increase in CO₂ conversion and DME yield from 0.62 to 0.63 and from 0.52 to 0.53 respectively. On the other hand, increasing the ΔP , also leads to the

undesired loss of reactants or methanol. This is minimized by adjusting the composition of the sweep gas and tuning the membrane properties (i.e., increasing the $S_{\text{H}_2\text{O}/\text{MeOH}}$). These findings are in line with similar results reported in literature [9], [11], [12], [44]. Furthermore, Gorbe et al. [5] reported a decrease in the water/gas separation factors for higher temperatures and ΔP related to the same reason. Therefore, the membrane properties and the compression costs required for the sweep gas will dictate the final choice of ΔP . Since this cost analysis is outside the scope of this study, a value of 5 bar for the ΔP was assumed for the following study.

Figure 2.5c shows the effect of SW and ΔP on CO yield. Upon increasing SW at constant ΔP , CO yield goes through a maximum and then decreases to reach a plateau. The CO transmembrane flow (**Figure A3**) shows the same behavior. Initially absent in the sweep gas stream, both CO and water permeate through the membrane, enhancing the formation of CO via the reverse WGS reaction. Above a certain value of SW – which is lower as higher is the ΔP – the effect of water removal on the methanol synthesis and dehydration reaction becomes less significant. Likewise, the previous trends and following analogous rationale, the CO yield also benefits from increasing ΔP . The ΔP effect on the CO yield is negligible, especially for high values of SW. The asymptotic value of CO yield is 0.06, showing that the DME selectivity is very high under these conditions.

In the proposed reactor concept, the sweep gas also acts as a cooling fluid that helps minimize temperature gradients. The temperature profile of the reaction zone along the reactor shows the typical trend of an exothermic reaction, when a colder fluid – in this case the sweep gas – is circulated in cocurrent mode. The temperature increases up to a maximum (i.e., hot spot) and then decreases to reach an asymptotic value. Therefore, we can identify two characteristic temperatures: 1) the maximum temperature ($T_{\text{max}}^{\text{R}}$) and 2) the asymptotic temperature ($T_{\text{end}}^{\text{R}}$). **Figure 2.6** shows the effect of SW and ΔP on $T_{\text{max}}^{\text{R}}$ and $T_{\text{end}}^{\text{R}}$. While $T_{\text{max}}^{\text{R}}$ is nearly independent on SW, the use of sweep gas seems to be an effective strategy to minimize $T_{\text{end}}^{\text{R}}$. An increase in the SW ratio (i.e., increase the sweep gas flow rate and velocity) increases the heat transfer coefficient (see correlations in Appendix A), improving the heat removal capacity of the sweep gas itself. Besides, larger values of SW lead to higher water transmembrane flows, which contributes to the heat removal as well.

As expected, the ΔP shows no influence on the temperature profile, since it does not influence nor the water transmembrane flow or the heat removal related to convection.

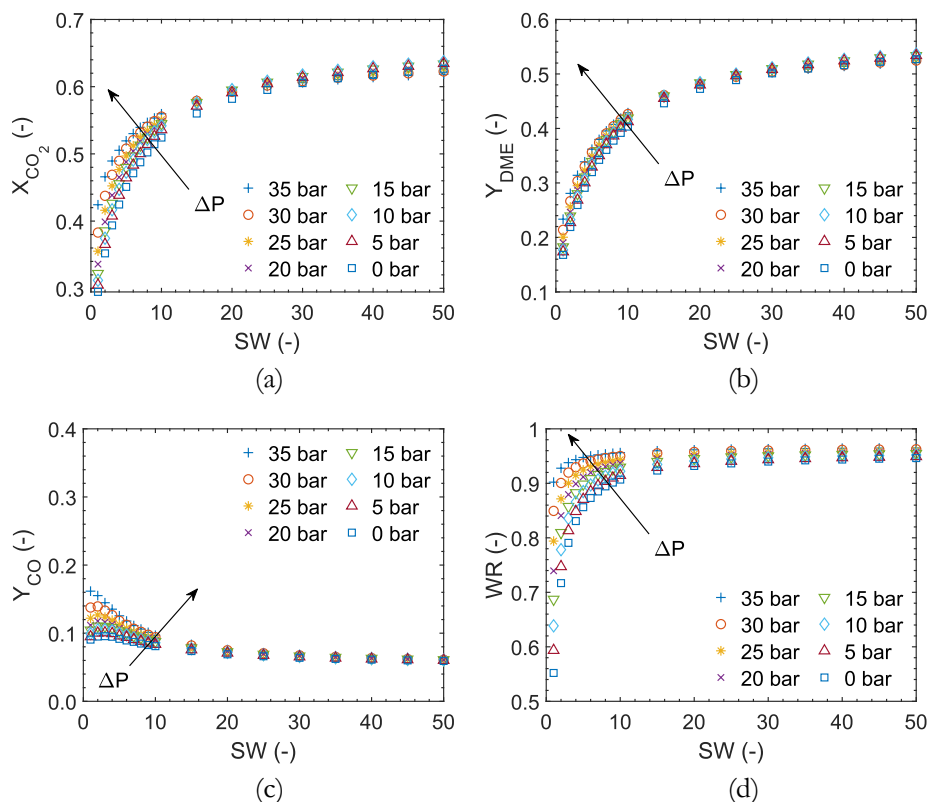


Figure 2.5. Effect of the SW ratio and the ΔP on the reactor performances in terms of a) CO_2 conversion (X_{CO_2}), b) DME yield (Y_{DME}), c) CO yield (Y_{CO}) and d) water removal (WR), ($\text{H}_2:\text{CO}_2 = 3$; $T_0^{\text{P}} = 473$ K, all the other process conditions are reported in Table 2.4 – P3).

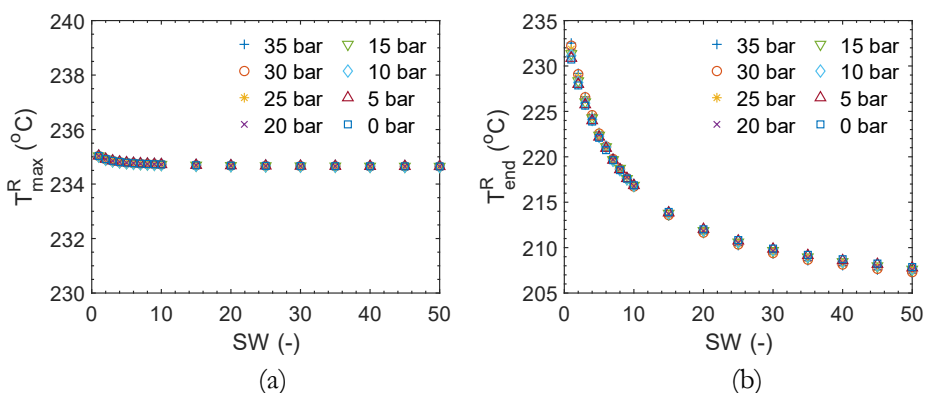


Figure 2.6. Effect of the SW ratio and the ΔP on the reaction zone temperature profile: a) temperature ($T_{\text{max}}^{\text{R}}$) as a function of the SW ratio and ΔP ; b) the asymptotic temperature value ($T_{\text{end}}^{\text{R}}$) as a function of the SW ratio and ΔP ($\text{H}_2:\text{CO}_2 = 3$; $T_0^{\text{P}} = 473$ K, all the other process conditions are reported in Table 2.4 – P3).

According to these results, it can be concluded that for a SW greater than 20 there is no significant improvement in the reactor performance and most of the variables reach their asymptotic value (i.e., an increase of SW from 20 to 30 leads to an insignificant improvement in CO₂ conversion and DME yield lower than 5% and only 1% decrease in $T_{\text{end}}^{\text{R}}$). As mentioned earlier, an average temperature of 200 °C in the reaction zone was selected as a compromise between the reaction kinetics, thermodynamics, catalyst stability and the water separation considerations. Therefore, the sweep gas inlet temperature was adjusted accordingly. The final temperature, $T_{\text{end}}^{\text{R}}$, reaches a value of 200 °C when T_0^{P} is 185 °C, confirming that the sweep gas, in these conditions, has a sufficient heat removal capacity to optimize the reactor temperature profile (see Appendix A, **Figure A4**).

Effect of the feed composition

A key constraint for the methanol and DME production from CO₂+H₂ mixtures is the need of large amounts of expensive H₂. In fact, a large H₂:CO₂ molar ratio favors the CO₂ hydrogenation reactions, both from the kinetic and thermodynamic point of view. **Figure 2.7** shows the effect of the H₂:CO₂ molar ratio on DME yield for either a conventional and a membrane reactor. A high H₂ concentrations increases the DME yields for both the membrane reactor (up to about 0.7) and for a conventional one (up to about 0.4), but it comes at the expense of high operational costs. Thus, a proper optimization of this parameter should result from an economic evaluation. Here, the membrane reactor offers a clear economic advantage to the conventional packed bed reactor, as it achieves greater DME yields, and importantly, it reaches its maximum DME yields at lower H₂:CO₂ ratio (i.e., very close to the stoichiometric value of 3).

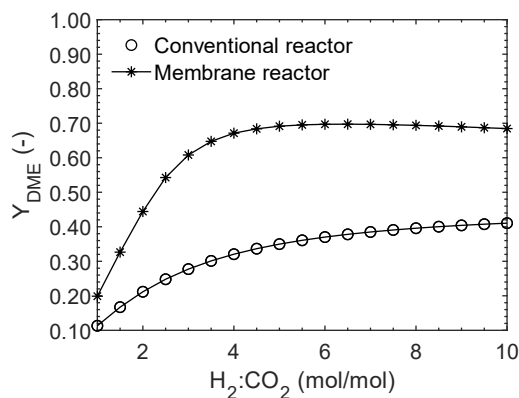


Figure 2.7. Effect of the inlet H₂:CO₂ molar ratio on the DME yield (Y_{DME}) for a membrane reactor with a SW = 20; $\Delta P = 5$ bar; $T_{\text{avg}}^{\text{R}} = 473$ K (all the other process conditions are reported in **Table 2.4 – P3**) and a conventional reactor working at the same conditions in terms of total pressure (i.e., 40 bar) and average temperature (i.e., 473 K).

On the other hand, the proposed membrane reactor configuration, utilizes a CO_2+H_2 stream as sweep gas, with a SW ratio of 20. Such stream contributes only to water and heat removal, thus it could be recirculated back to the reactor with a $\approx 100\%$ recycle ratio. **Figure 2.8** shows the concentration profile of the sweep gas along the reactor. As expected, the main components of this stream are CO_2 and H_2 , with minor amounts of the reaction products (see zoomed in profiles in **Figure 2.8b**). The molar fractions of CO_2 and H_2 in the permeation zone suffer from negligible changes along the reactor. Therefore, the sweep gas can be recycled to the reactor after limited post treatments (i.e., condensation of the permeated water and a make-up of CO_2 and H_2 of 0.13% and 0.0038% of the initial flow rate, respectively). Water is the only species that significantly permeates along the reactor, reaching a WR of 96%. Even then, its concentration in the permeation zone is very low, confirming that the circulation of a sweep gas generates sufficient driving force for water permeation by diluting water in this stream, even if the gradient of total pressure is close to zero. The sweep gas at the outlet of the reactor contains also a small amount of CO (0.018%) and methanol (0.028%), which can be recycled together with CO_2 and H_2 . The presence of methanol and CO in the sweep gas will further avoid the undesired permeation of these species from the reaction side.

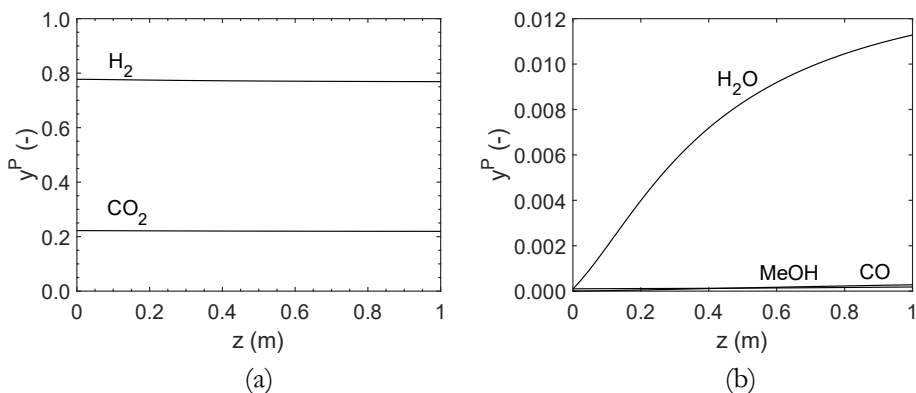


Figure 2.8. Sweep gas (or permeation zone gaseous mixture) concentration profile of a) the main component of the streams (CO_2 and H_2) and b) the permeating species (H_2O , CH_3OH and CO).

2.3.4 Optimized membrane reactor performance vs thermodynamic limitations

This section discusses the performance of the optimized membrane reactor and compares it with the thermodynamic limitations. The optimal operating conditions for the membrane reactor are summarized in **Table 2.7**. **Figure 2.9** shows the profiles of the main reactor variables (i.e., T^R , T^P , $y_{\text{H}_2\text{O}}^R$, $y_{\text{H}_2\text{O}}^P$, X_{CO_2} , Y_{DME}) as a function of the reactor length (z). The temperature profile (**Figure 2.9a**) shows the role of the sweep gas as a cooling agent which minimizes axial temperature profiles in the reaction zone. The water concentration in the reaction zone remains very low along the reactor, which confirms that the membrane reactor has reached its target,

with an efficiency of water separation of 96% (**Figure A5b**). In addition, **Figure 2.9a** also shows that the peak of water concentration is near the reactor inlet, reassuring the choice of the cocurrent operation. Since the reaction rate is the highest in the beginning of the reactor, both heat and water production are maximum at this point. Therefore, in this zone the highest driving force for both the heat and water removal is required.

The pressure drops in the reaction zone are lower than 0.1 bar, under these conditions (**Figure A5a**). This is important to minimize compression costs and to prevent back-permeation of water at the end of the reactor. **Figure 2.9b** shows the membrane reactor performance in terms of CO₂ conversion and DME yield and demonstrate that this reactor configuration clearly overcomes the thermodynamic limitation under these conditions. Indeed, CO₂ conversion and DME yield exceed the thermodynamic values (i.e., best possible performance of a conventional packed bed reactor) by 36.4% and 43.3%, respectively. This result proves that the selective removal of water in a membrane reactor strongly enhances both the methanol production and its dehydration to DME. Therefore, this work proves the use of membrane reactor technology will be key to increase the feasibility of the direct conversion of CO₂ to DME.

Finally, **Figure 2.10** underlines the importance of the heat management in this process by comparing the temperature profiles considering the proposed heat management solution with the corresponding temperature profile under adiabatic conditions. The latter (**Figure 2.10a**) shows a first temperature rise of around 50-60 °C, followed by a decrease in temperature due to the thermodynamically favored endothermic r-WGS reaction. This temperature profile leads to higher CO yield, as shown in **Figure 2.10b** (i.e., CO yield increases from 0.05 to 0.43, whilst DME yield decreases from 0.63 to 0.26).

Table 2.7. Optimal operating conditions for the membrane reactor

Operating condition	Value
Reaction zone inlet temperature, T_0^R (°C)	200
Permeation zone inlet temperature, T_0^P (°C)	185
Reaction zone pressure, P^R (bar)	40
Pressure difference across the membrane, ΔP (bar)	5
Sweep gas to feed flow ratio, SW (-)	20
H ₂ :CO ₂ molar feed ratio (both zones)	3.5
Inlet volumetric flow of H ₂ in the reaction zone, $\Phi_{H_2,0}^R$ (Nm ³ /h)	0.1

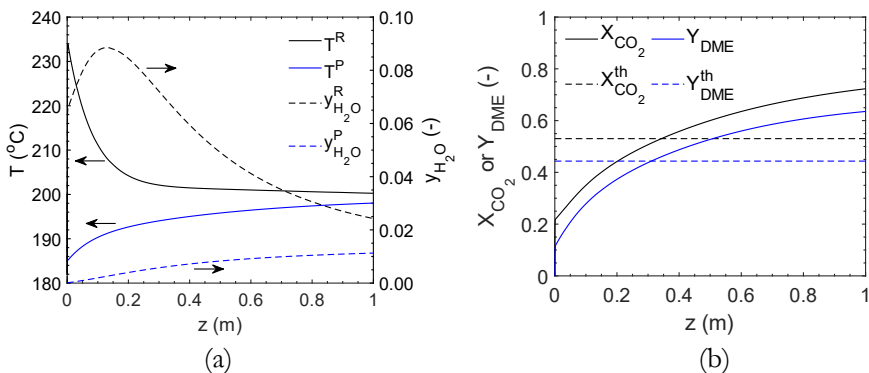


Figure 2.9. Membrane reactor performance: a) temperature and water molar fraction profiles; b) CO_2 conversion and DME yield profile, together with the respective thermodynamic limitations ($X_{CO_2}^{th}$ and Y_{DME}^{th}), calculated at 40 bar and 200 °C. The membrane reactor operating conditions are reported in **Table 2.7**.

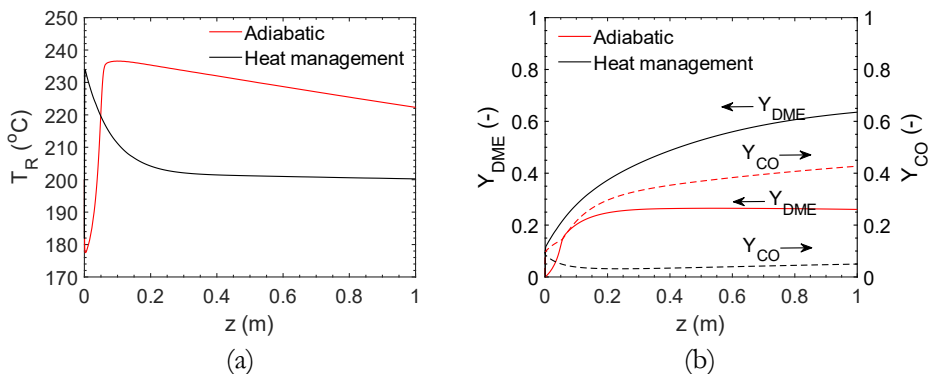


Figure 2.10. Comparison of the membrane reactor performance in adiabatic conditions (red lines) and with the heat management strategy proposed in this work (black lines), in terms of: a) temperature profile in the reaction zone and b) DME yield (solid line) and CO yield (dashed line). The membrane reactor operating conditions are reported in **Table 2.7**.

2.4 CONCLUSIONS

This work demonstrates the possibility of upgrading CO_2 for the production of dimethyl ether, which is an attractive alternative fuel with low environmental impact. A non-isothermal 1D phenomenological reactor model was developed to evaluate and optimize the performance of a membrane reactor for this conversion, otherwise limited by thermodynamic equilibrium and temperature gradients. The credibility of the modeling approach was first assessed, by reproducing experimental results retrieved from literature. Afterwards, the effect of the membrane properties on the reactor performance was studied and a suitable membrane material for this process was accordingly identified. It was concluded that the optimal membrane for this process should have a water permeance of ca. $4 \cdot 10^{-7}$ mol·Pa⁻¹·m⁻²·s⁻¹, a water perm-

selectivity of 50 towards H₂, 30 towards CO₂ and CO, 10 towards methanol and a very large perm-selectivity toward DME, so that its permeation may be neglected. Among the available membrane materials, zeolites show suitable performance, but may pose stability problems under reaction conditions. Carbon membranes, on the other hand, seem promising.

The circulation of a sweep gas (SW=20) in cocurrent mode proved an effective strategy to minimize hot spots and temperature gradients as well as to enhance water removal while avoids water back permeation.

The importance of the heat integration in this process was underlined showing that temperature gradients could enormously affect the product distribution, moving the reactions toward undesired pathways (i.e., production of CO).

The SW ratio showed a higher influence on the reactor performances than the gradient of the total pressure (ΔP), lowering the demands on the membrane mechanical stability. Furthermore, these results proved that the integration of a membrane for the selective water removal in a conventional packed bed reactor lowers the H₂ requirement that maximizes the DME yield, which is key for the industrial attractiveness of the process. With optimal membrane properties and optimal process conditions, the membrane reactor technology shows its potential to overcome the severe thermodynamic limitations of this process. In particular, if 96% of the water produced by the reactions is removed, the CO₂ conversion and DME yield show an improvement of 36% and 43% each, with respect to a conventional packed bed reactor working at the same operating conditions (i.e., 200 °C and 40 bar).

These results show the possibility to easily integrate this reactor in a conventional process scheme, since the sweep gas does not require complex post processing units in order to be recirculated in the permeation zone.

Appendix A

A.1 Physical properties and correlations

The density of the gaseous mixture is calculated via the Peng-Robinson EOS for multicomponent system, by means of the Van der Waals mixing rule [73], based on the critical properties of the species that were retrieved from literature [74]. The binary interaction parameters for the second virial coefficient were derived with the method described by Tarakad and Danner [75].

The viscosity of the gaseous mixture is calculated according to the Wilke method [73]:

$$\mu_{\text{mix}} = \sum_{i=1}^N \left(\frac{\mu_i y_i}{\sum_{j=1}^N y_j \Phi_{ij}} \right) \quad (\text{A.1})$$

$$\Phi_{ij} = \frac{\left[1 + (\mu_i / \mu_j)^{1/2} + (M_i / M_j)^{1/4} \right]^2}{\left[8(1 + M_i / M_j) \right]^{1/2}} \quad (\text{A.2})$$

Where μ_i and M_i are the viscosity and molar mass of each species respectively [74]. The thermal conductivity of the gaseous mixture is calculated according to the Wassiljewa equation [73]:

$$\lambda_{\text{mix}} = \sum_{i=1}^N \frac{\lambda_i \cot(y_i)}{\sum_{j=1}^N A_{ij} (y_i / y_j)} \quad (\text{A.3})$$

The A_{ij} coefficients are calculated according to the Lindsay-Bromley relation [73]:

$$A_{ij} = 0.25 \left\{ 1 + \left[\frac{\mu_i}{\mu_j} \left(\frac{M_i}{M_j} \right)^{3/4} \frac{T + S_i}{T + S_j} \right]^{1/2} \right\} \frac{T + S_{ij}}{T + S_i} \quad (\text{A.4})$$

Where S_i and S_j are the Sutherland constant of pure gases, function of the boiling temperature in normal conditions:

$$S_i = 1.5T_{bi} \quad (\text{A.5})$$

$$S_{ij} = F_S \sqrt{S_i S_j} \quad (\text{A.6})$$

$$S_{ii} = S_i \text{ and } S_{ij} = S_{ji} \quad (\text{A.7})$$

Where F_S is a correction factor, which is 0.735 if at least one of the two species is polar, otherwise its value is 1.

The heat transfer coefficient (h_{mi}) describing the heat transfer due to convection occurring across the gas film forming along the membrane surface area at the permeation side is calculated according to the correlation by Dittus-Boelter [34] (Eq. A.8) and to the Nusselt number (Nu) definition [76] (Eq. A.9):

$$h_{mi} = \frac{\lambda_{\text{mix}} \text{Nu}}{D_{mi}} \quad (\text{A.8})$$

$$\text{Nu} = 0.023 \text{Re}^{0.8} \text{Pr}^{0.4} \quad (\text{A.9})$$

Where Re and Pr are the Reynolds and Prandtl number respectively.

The heat transfer coefficient (h_{mo}) describing the heat transfer due to convection occurring across the gas film forming along the membrane surface area at the reaction side is calculated from according to the Li-Finlayson correlation for packed beds [77]:

$$h_{\text{mo}} = 0.17 \frac{\lambda_{\text{mix}}}{d_p} \left(\frac{\text{Pr}}{0.7} \right)^{1/3} \text{Re}_p^{0.79} \quad (\text{A.10})$$

Where the Reynolds number (Re_p) is calculated using the particle diameter (d_p) as characteristic length.

The conductivity of the membrane was calculated assuming a two layer system: 1) a support made of $\alpha\text{-Al}_2\text{O}_3$ and 2) a pyrolytic carbon layer having a thickness of the order of 1 μm . [74], [78]. The global heat transfer coefficient was calculated according to Eq. A.11 where δ_c is the thickness of the carbon layer.

$$\frac{1}{\bar{U}} = \frac{1}{h_{\text{mi}}} + \frac{D_{\text{mi}}}{2} \left[\frac{1}{k_c} \ln \left(\frac{D_{\text{mi}} + \delta_c}{D_{\text{mi}}} \right) + \frac{1}{k_{\text{Al}}} \ln \left(\frac{D_{\text{mo}}}{D_{\text{mi}} + \delta_c} \right) \right] + \frac{D_{\text{mi}}}{D_{\text{mo}}} \frac{1}{h_{\text{mo}}} \quad (\text{A.11})$$

A.2 Verification of the implementation of the kinetic model

In order to assure the correct implementation of the kinetic model, the simulation results of Iliuta et al. [58] were reproduced. This validation is carried out by reproducing the behavior of a traditional packed bed reactor. The reactor characteristic and the operating conditions are summarized in **Table A1**.

Table A1. Operating conditions used for the model verification

Parameter	Value
Reactor diameter, D (m)	0.026
Catalyst bed length, L (m)	1
Catalyst density, ρ_c (kg/m ³)	1982
Catalyst bed porosity, ε (-)	0.39
Reactor pressure, P (MPa)	5
Reactor temperature, T (°C)	250
Inlet superficial velocity, u_g (m/s)	0.05

Methanol and dimethyl ether selectivity are evaluated according to the following equations:

$$S_{\text{CH}_3\text{OH}} = \frac{\dot{F}_{\text{CH}_3\text{OH}}}{\dot{F}_{\text{CH}_3\text{OH}} + 2\dot{F}_{\text{CH}_3\text{OCH}_3}} \quad (\text{A.12})$$

$$S_{\text{CH}_3\text{OCH}_3} = \frac{\dot{F}_{\text{CH}_3\text{OCH}_3}}{\dot{F}_{\text{CH}_3\text{OH}} + 2\dot{F}_{\text{CH}_3\text{OCH}_3}} \quad (\text{A.13})$$

Figure A1 shows that the model implemented in this work matches with the modeling results found in the literature.

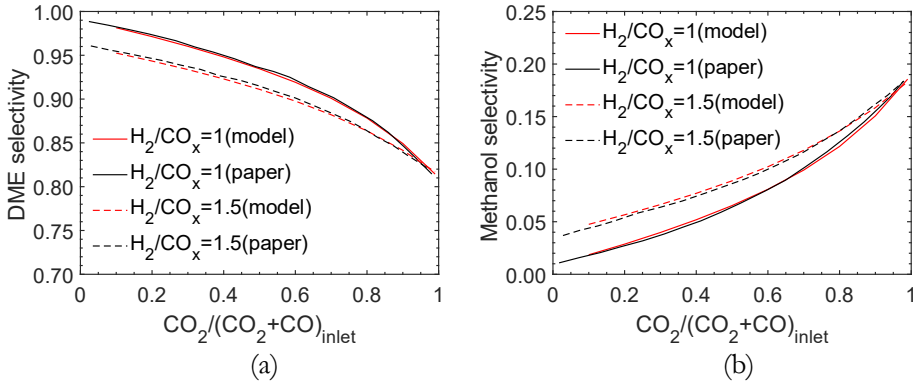


Figure A1. Influence of CO_2 fraction on methanol (a) and DME (b) selectivity at different H_2/CO_x feed ratio. Black lines are derived from Iliuta et al. paper [58], red lines derive from the model solution.

A.3 Variables profile at reactor entrance section

The variables profiles presented in Section 2.3.3 show a very steep curve at the beginning of the reactor. As an example, the CO_2 conversion appears to have a value different from zero at the reactor inlet, which is not the case. A zoom in the first section of the reactor shows the presence of a profile starting from zero (**Figure A2**). The CO_2 conversion shows an initial linear behavior with a very high slope which is related to the fast kinetic. At this very first stage, the membrane is not playing any role, because the amount of water formed is still negligible. When the water removal start to show its influence on the reactions, the CO_2 conversion is interested by an inflection point, after which the slope of the profile decreases. The decrease in the CO_2 profile slope is due to the membrane effect: the water permeation is slowing down the overall rate of the process, because of the alteration of the equilibrium conditions.

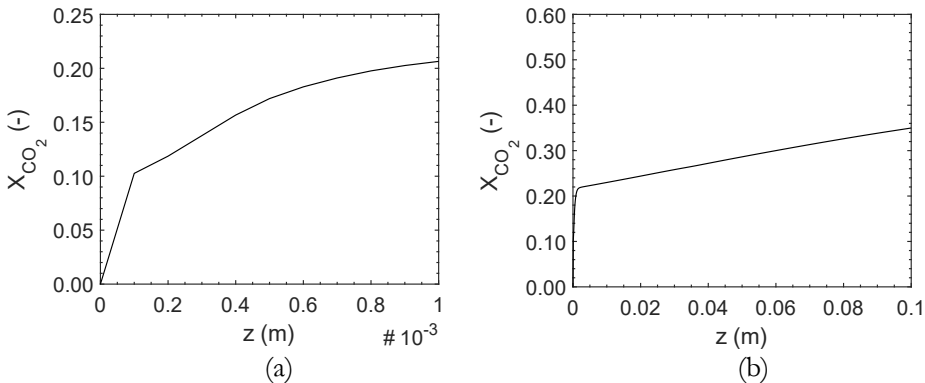


Figure A2. CO_2 conversion profile in the first reactor section for two different scale lengths

A.4 Supplementary figures

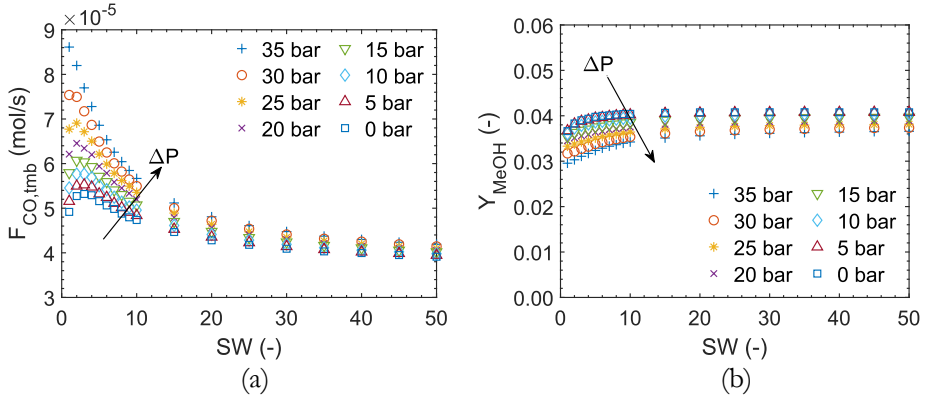


Figure A3. Effect of the SW ratio and the ΔP on the CO transmembrane flow, $F_{CO,tmb}$ (a) and on methanol yield Y_{MeOH} , (b) obtained at $H_2:CO_2 = 3$; $T_0^P = 473$ K, all the other process conditions are reported in **Table 2.4 – P3**.

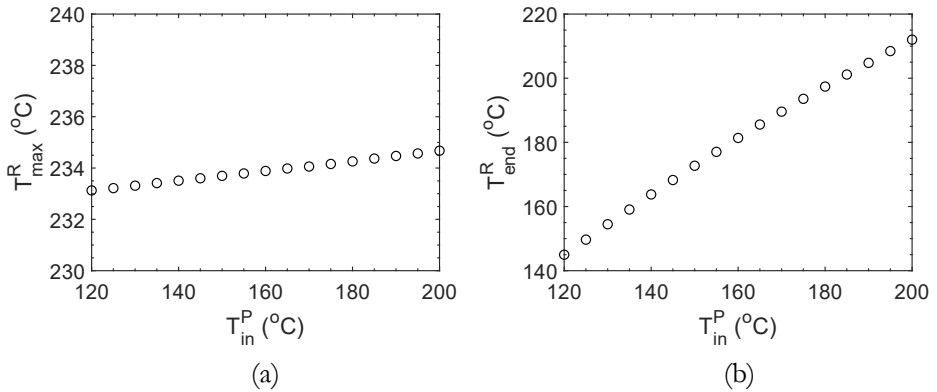


Figure A4. Effect of the inlet sweep gas temperature on the temperature profile of the reaction zone, in term of a) maximum temperature (T_{max}^R) and b) asymptotic temperature (T_{end}^R), ($SW = 20$; $\Delta P = 5$ bar; $H_2:CO_2 = 3.5$; all the other process conditions are reported in **Table 2.4 – P3**).

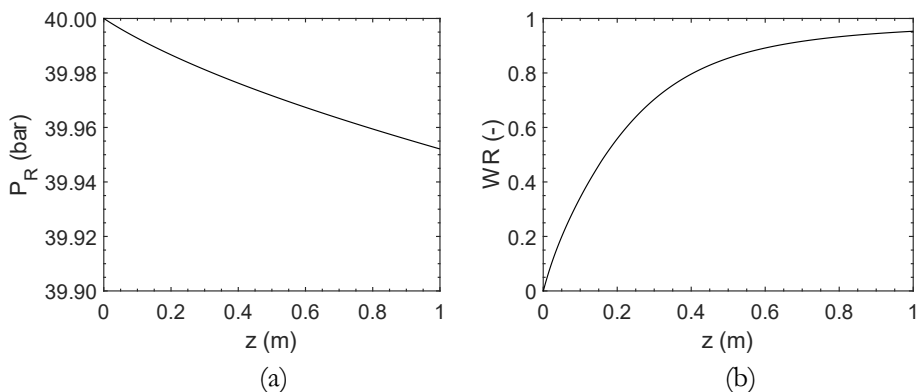


Figure A5. Membrane reactor performance: a) total pressure profile in the reaction zone, b) water removal profile (operating conditions reported in **Table 2.7**).

REFERENCES

- [1] R. P. W. J. Struis, S. Stucki, and M. Wiedorn, "A membrane reactor for methanol synthesis," *J. Memb. Sci.*, vol. 113, no. 1, pp. 93–100, 1996,
- [2] R. P. W. J. Struis and S. Stucki, "Verification of the membrane reactor concept for the methanol synthesis," *Appl. Catal. A Gen.*, vol. 216, no. 1–2, pp. 117–129, 2001,
- [3] F. Gallucci, L. Paturzo, and A. Basile, "An experimental study of CO₂ hydrogenation into methanol involving a zeolite membrane reactor," *Chem. Eng. Process. Process Intensif.*, vol. 43, no. 8, pp. 1029–1036, 2004,
- [4] F. Gallucci and A. Basile, "A theoretical analysis of methanol synthesis from CO₂ and H₂ in a ceramic membrane reactor," *Int. J. Hydrogen Energy*, vol. 32, no. 18, pp. 5050–5058, 2007,
- [5] J. Gorbe *et al.*, "Preliminary study on the feasibility of using a zeolite A membrane in a membrane reactor for methanol production," *Sep. Purif. Technol.*, vol. 200, no. December 2017, pp. 164–168, 2018,
- [6] D. A. Fedosov, A. V. Smirnov, V. V. Shkirskiy, T. Voskoboynikov, and I. I. Ivanova, "Methanol dehydration in NaA zeolite membrane reactor," *J. Memb. Sci.*, vol. 486, pp. 189–194, 2015,
- [7] V. V. Volkov, E. G. Novitskii, G. A. Dibrov, P. V. Samokhin, M. A. Kipnis, and A. B. Yaroslavtsev, "Catalytic conversion of methanol to dimethyl ether on polymer/ceramic composite membranes," *Catal. Today*, vol. 193, no. 1, pp. 31–36, 2012,
- [8] A. Brunetti, M. Migliori, D. Cozza, E. Catizzone, G. Giordano, and G. Barbieri, "Methanol Conversion to Dimethyl Ether in Catalytic Zeolite Membrane Reactors," *ACS Sustain. Chem. Eng.*, vol. 8, no. 28, pp. 10471–10479, 2020,
- [9] I. Iliuta, F. Larachi, and P. Fongarland, "Dimethyl ether synthesis with in-situ H₂O removal in fixed-bed membrane reactor: Model and simulations," *Ind. Eng. Chem.*

- Res.*, vol. 49, no. 15, pp. 6870–6877, 2010,
- [10] M. Farsi, A. Hallaji Sani, and P. Riasatian, “Modeling and operability of DME production from syngas in a dual membrane reactor,” *Chem. Eng. Res. Des.*, vol. 112, pp. 190–198, 2016,
- [11] N. Diban, A. M. Urriaga, I. Ortiz, J. Ereña, J. Bilbao, and A. T. Aguayo, “Influence of the membrane properties on the catalytic production of dimethyl ether with in-situ water removal for the successful capture of CO₂,” *Chem. Eng. J.*, vol. 234, pp. 140–148, 2013,
- [12] N. Diban, A. M. Urriaga, I. Ortiz, J. Ereña, J. Bilbao, and A. T. Aguayo, “Improved performance of a PBM reactor for simultaneous CO₂ capture and DME synthesis,” *Ind. Eng. Chem. Res.*, vol. 53, no. 50, pp. 19479–19487, 2014,
- [13] M. De Falco, M. Capocelli, and G. Centi, “Dimethyl ether production from CO₂ rich feedstocks in a one-step process: Thermodynamic evaluation and reactor simulation,” *Chem. Eng. J.*, vol. 294, pp. 400–409, 2016,
- [14] M. De Falco, M. Capocelli, and A. Basile, “Selective membrane application for the industrial one-step DME production process fed by CO₂ rich streams: Modeling and simulation,” *Int. J. Hydrogen Energy*, vol. 42, no. 10, pp. 6771–6786, 2017,
- [15] P. Rodriguez-Vega *et al.*, “Experimental implementation of a catalytic membrane reactor for the direct synthesis of DME from H₂+CO/CO₂,” *Chem. Eng. Sci.*, vol. 234, 2021,
- [16] A. Ateka, J. Ereña, J. Bilbao, and A. T. Aguayo, “Strategies for the Intensification of CO₂ Valorization in the One-Step Dimethyl Ether Synthesis Process,” *Ind. Eng. Chem. Res.*, vol. 59, no. 2, pp. 713–722, 2020,
- [17] A. Ateka, P. Rodriguez-Vega, T. Cordero-Lanzac, J. Bilbao, and A. T. Aguayo, “Model validation of a packed bed LTA membrane reactor for the direct synthesis of DME from CO/CO₂,” *Chem. Eng. J.*, vol. 408, no. October 2020, 2021,
- [18] M. P. Rohde, G. Schaub, S. Khajavi, J. C. Jansen, and F. Kapteijn, “Fischer-Tropsch synthesis with in-situ H₂O removal - Directions of membrane development,” *Microporous Mesoporous Mater.*, vol. 115, no. 1–2, pp. 123–136, 2008,
- [19] J. Lee, H. G. Park, M. H. Hyeon, B. G. Kim, S. K. Kim, and S. Y. Moon, “Low-temperature CO₂ hydrogenation overcoming equilibrium limitations with polyimide hollow fiber membrane reactor,” *Chem. Eng. J.*, vol. 403, no. July 2020, p. 126457, 2021,
- [20] F. Gallucci, *Inorganic Membrane Reactors for Methanol Synthesis*. Elsevier B.V., 2018.
- [21] W. Lu, L. Teng, and W. Xiao, “Simulation and experiment study of dimethyl ether synthesis from syngas in a fluidized-bed reactor,” vol. 59, pp. 5455–5464, 2004,
- [22] M. Giacinti Baschetti and M. G. De Angelis, *Vapour permeation modeling*. Elsevier Ltd, 2015.
- [23] X. An, Y. Z. Zuo, Q. Zhang, D. Z. Wang, and J. F. Wang, “Dimethyl ether synthesis from CO₂ hydrogenation on a CuO-ZnO-Al₂O₃-ZrO₂/HZSM-5 bifunctional

- catalyst,” *Ind. Eng. Chem. Res.*, vol. 47, no. 17, pp. 6547–6554, 2008,
- [24] K. L. Ng, D. Chadwick, and B. A. Toseland, “Kinetics and modeling of dimethyl ether synthesis from synthesis gas,” *Chem. Eng. Sci.*, vol. 54, no. 15–16, pp. 3587–3592, 1999,
- [25] Z. Nie, H. Liu, D. Liu, W. Ying, and D. Fang, “Intrinsic kinetics of dimethyl ether synthesis from syngas,” *J. Nat. Gas Chem.*, vol. 14, no. 1, pp. 22–28, 2005,
- [26] N. Park, M. J. Park, Y. J. Lee, K. S. Ha, and K. W. Jun, “Kinetic modeling of methanol synthesis over commercial catalysts based on three-site adsorption,” *Fuel Process. Technol.*, vol. 125, pp. 139–147, 2014,
- [27] H. M. Shim, S. J. Lee, Y. D. Yoo, Y. S. Yun, and H. T. Kim, “Simulation of DME synthesis from coal syngas by kinetics model,” *Korean J. Chem. Eng.*, vol. 26, no. 3, pp. 641–648, 2009,
- [28] A. T. Aguayo, J. Ereña, D. Mier, J. M. Arandes, M. Olazar, and J. Bilbao, “Kinetic modeling of dimethyl ether synthesis in a single step on a CuO-ZnO-Al₂O₃/γ-Al₂O₃ catalyst,” *Ind. Eng. Chem. Res.*, vol. 46, no. 17, pp. 5522–5530, 2007,
- [29] C. R. Behloul, J. M. Commenge, and C. Castel, “Simulation of Reactors under Different Thermal Regimes and Study of the Internal Diffusional Limitation in a Fixed-Bed Reactor for the Direct Synthesis of Dimethyl Ether from a CO₂-Rich Input Mixture and H₂,” *Ind. Eng. Chem. Res.*, vol. 60, no. 4, pp. 1602–1623, 2021,
- [30] A. Ateka, J. Ereña, J. Bilbao, and A. T. Aguayo, “Kinetic modeling of the direct synthesis of dimethyl ether over a CuO-ZnO-MnO/SAPO-18 catalyst and assessment of the CO₂ conversion,” *Fuel Process. Technol.*, vol. 181, no. September, pp. 233–243, 2018,
- [31] A. Ateka, M. Sánchez-Contador, A. Portillo, J. Bilbao, and A. T. Aguayo, “Kinetic modeling of CO₂+CO hydrogenation to DME over a CuO-ZnO-ZrO₂@SAPO-11 core-shell catalyst,” *Fuel Process. Technol.*, vol. 206, no. February, p. 106434, 2020,
- [32] K. M. Vanden Bussche and G. F. Froment, “A Steady-State Kinetic Model for Methanol Synthesis and the Water Gas Shift Reaction on a Commercial Cu / ZnO / Al₂O₃ Catalyst,” vol. 10, no. 0156, pp. 1–10, 1996.
- [33] D. Y. Zhang, H. T.; Cao, F. H.; Liu, D. H.; Fang, “Thermodynamic analysis for synthesis of dimethyl ether and methanol from synthesis gas,” *J. ECUST*, vol. 27, pp. 198–201, 2001.
- [34] D. Taler and J. Taler, “Simple heat transfer correlations for turbulent tube flow,” *E3S Web Conf.*, vol. 13, pp. 1–7, 2017,
- [35] C. Engmeermg, *Heat Transfer in Packed Beds*. 1976.
- [36] J. A. Medrano, M. A. Llosa-Tanco, D. A. Pacheco-Tanaka, and F. Gallucci, *Transport mechanism and modeling of microporous carbon membranes*. Elsevier Inc., 2019.
- [37] Y. J. Stark, N. Bend, P. P. Data, and C. Interaction, “(12) United States Patent,” vol. 2, no. 12, 2012.

- [38] R. L. Espinoza, E. Du Toit, J. Santamaria, M. Menendez, J. Coronas, and S. Irusta, "Use of membranes in Fischer-Tropsch reactors," *Stud. Surf. Sci. Catal.*, vol. 130 A, no. 1, pp. 389–394, 2000,
- [39] M. V Twigg and M. S. Spencer, "Deactivation of copper metal catalysts for methanol decomposition, methanol steam reforming and methanol synthesis," vol. 22, no. April, pp. 191–203, 2003.
- [40] H. H. Kung, "Deactivation of methanol synthesis catalysts - a review," *Catal. Today*, vol. 11, no. 4, pp. 443–453, 1992,
- [41] K. I. Okamoto, H. Kita, K. Horii, K. Tanaka, and M. Kondo, "Zeolite NaA membrane: Preparation, single-gas permeation, and pervaporation and vapor permeation of water/organic liquid mixtures," *Ind. Eng. Chem. Res.*, vol. 40, no. 1, pp. 163–175, 2001,
- [42] S. Sommer and T. Melin, "Influence of operation parameters on the separation of mixtures by pervaporation and vapor permeation with inorganic membranes. Part 1: Dehydration of solvents," *Chem. Eng. Sci.*, vol. 60, no. 16, pp. 4509–4523, 2005,
- [43] M. Bukhtiyarova, T. Lunkenbein, K. Kähler, and R. Schlögl, "Methanol Synthesis from Industrial CO₂ Sources: A Contribution to Chemical Energy Conversion," *Catal. Letters*, vol. 147, no. 2, pp. 416–427, 2017,
- [44] M. P. Rohde, D. Unruh, and G. Schaub, "Membrane application in Fischer-Tropsch synthesis to enhance CO₂ hydrogenation," *Ind. Eng. Chem. Res.*, vol. 44, no. 25, pp. 9653–9658, 2005,
- [45] S. Battersby, P. W. Teixeira, J. Beltramini, M. C. Duke, V. Rudolph, and J. C. Diniz da Costa, "An analysis of the Peclet and Damkohler numbers for dehydrogenation reactions using molecular sieve silica (MSS) membrane reactors," *Catal. Today*, vol. 116, no. 1, pp. 12–17, 2006,
- [46] S. Ren *et al.*, "Highly active and selective Cu-ZnO based catalyst for methanol and dimethyl ether synthesis via CO₂ hydrogenation," *Fuel*, vol. 239, no. November 2018, pp. 1125–1133, 2019,
- [47] S. K. Amin, H. A. M. Abdallah, M. H. Roushdy, and S. A. El-Sherbiny, "An overview of production and development of ceramic membranes," *Int. J. Appl. Eng. Res.*, vol. 11, no. 12, pp. 7708–7721, 2016.
- [48] K. P. Lee, T. C. Arnot, and D. Mattia, "A review of reverse osmosis membrane materials for desalination-Development to date and future potential," *J. Memb. Sci.*, vol. 370, no. 1–2, pp. 1–22, 2011,
- [49] S. L. Wee, C. T. Tye, and S. Bhatia, "Membrane separation process-Pervaporation through zeolite membrane," *Sep. Purif. Technol.*, vol. 63, no. 3, pp. 500–516, 2008,
- [50] R. M. Ravenelle *et al.*, "Stability of zeolites in hot liquid water," *J. Phys. Chem. C*, vol. 114, no. 46, pp. 19582–19595, 2010,
- [51] J. Hedlund, F. Jareman, A. J. Bons, and M. Anthonis, "A masking technique for high quality MFI membranes," *J. Memb. Sci.*, vol. 222, no. 1–2, pp. 163–179, 2003,

- [52] R. Lai and G. R. Gavalas, "Surface seeding in ZSM-5 membrane preparation," *Ind. Eng. Chem. Res.*, vol. 37, no. 11, pp. 4275–4283, 1998,
- [53] S. M. Lee *et al.*, "Structure, stability and permeation properties of NaA zeolite membranes for H₂O/H₂ and CH₃OH/H₂ separations," *J. Eur. Ceram. Soc.*, vol. 38, no. 1, pp. 211–219, 2018,
- [54] B. Sea and K. H. Lee, "Methanol synthesis from carbon dioxide and hydrogen using a ceramic membrane reactor," *React. Kinet. Catal. Lett.*, vol. 80, no. 1, pp. 33–38, 2003,
- [55] R. Raso *et al.*, "Zeolite membranes: Comparison in the separation of H₂O/H₂/CO₂ mixtures and test of a reactor for CO₂ hydrogenation to methanol," *Catal. Today*, vol. 364, no. September 2019, pp. 270–275, 2021,
- [56] K. I. Sawamura, T. Shirai, M. Takada, Y. Sekine, E. Kikuchi, and M. Matsukata, "Selective permeation and separation of steam from water-methanol-hydrogen gas mixtures through mordenite membrane," *Catal. Today*, vol. 132, no. 1–4, pp. 182–187, 2008,
- [57] M. A. Salomón, J. Coronas, M. Menéndez, and J. Santamaría, "Synthesis of MTBE in zeolite membrane reactors," *Appl. Catal. A Gen.*, vol. 200, no. 1, pp. 201–210, 2000,
- [58] I. Iliuta, F. Larachi, and P. Fongarland, "Dimethyl Ether Synthesis with in-situ H₂ O Removal in Fixed-Bed Membrane Reactor : Model and Simulations †," pp. 6870–6877, 2010.
- [59] K. Sato, K. Sugimoto, Y. Sekine, M. Takada, M. Matsukata, and T. Nakane, "Application of FAU-type zeolite membranes to vapor/gas separation under high pressure and high temperature up to 5 MPa and 180 °C," *Microporous Mesoporous Mater.*, vol. 101, no. 1-2 SPEC. ISS., pp. 312–318, 2007,
- [60] E. Piera, M. A. Salomón, J. Coronas, M. Menéndez, and J. Santamaría, "Synthesis, characterization and separation properties of a composite mordenite/ZSM-5/chabazite hydrophilic membrane," *J. Memb. Sci.*, vol. 149, no. 1, pp. 99–114, 1998,
- [61] K. Aoki, K. Kusakabe, and S. Morooka, "Gas permeation properties of A-type zeolite membrane formed on porous substrate by hydrothermal synthesis," *J. Memb. Sci.*, vol. 141, no. 2, pp. 197–205, 1998,
- [62] K. Aoki, K. Kusakabe, and S. Morooka, "Separation of gases with an A-type zeolite membrane," *Ind. Eng. Chem. Res.*, vol. 39, no. 7, pp. 2245–2251, 2000,
- [63] C. Algieri, A. Comite, and G. Capannelli, *Zeolite membrane reactors*, vol. 1. 2013.
- [64] M. Andersson, L. Klintberg, and K. Hjort, "CO₂ and H₂O," vol. 26, no. 15, pp. 2–4, 2011.
- [65] J. Gascon, F. Kapteijn, B. Zornoza, V. Sebastián, C. Casado, and J. Coronas, "Practical approach to zeolitic membranes and coatings: State of the art, opportunities, barriers, and future perspectives," *Chem. Mater.*, vol. 24, no. 15, pp. 2829–2844, 2012,
- [66] M. Menendez, E. Piera, J. Coronas, and J. Santamaría, "Zeolite membrane reactor

- for the production of methanol and other alcohols from synthesis gas,” *Oepm*, vol. 2 164 544, pp. 1–6, 1999.
- [67] S. A. S. Rezai, J. Lindmark, C. Andersson, F. Jareman, K. Möller, and J. Hedlund, “Water/hydrogen/hexane multicomponent selectivity of thin MFI membranes with different Si/Al ratios,” *Microporous Mesoporous Mater.*, vol. 108, no. 1–3, pp. 136–142, 2008,
- [68] T. Tomita, R. U. S. A. Data, P. Examiner, and J. M. Greene, “(12) United States Patent,” vol. 2, no. 12, 2010.
- [69] A. F. Ismail and L. I. B. David, “A review on the latest development of carbon membranes for gas separation,” *J. Memb. Sci.*, vol. 193, no. 1, pp. 1–18, 2001,
- [70] S. Fu, E. S. Sanders, S. S. Kulkarni, and W. J. Koros, “Carbon molecular sieve membrane structure-property relationships for four novel 6FDA based polyimide precursors,” *J. Memb. Sci.*, vol. 487, pp. 60–73, 2015,
- [71] D. Naberezhnyi, A. Götzhäuser, and P. Dementyev, “Water-Assisted Permeation of Gases in Carbon Nanomembranes,” *J. Phys. Chem. Lett.*, vol. 10, no. 18, pp. 5598–5601, 2019,
- [72] M. Teixeira, M. C. Campo, D. A. Pacheco Tanaka, M. A. Llosa Tanco, C. Magen, and A. Mendes, “Composite phenolic resin-based carbon molecular sieve membranes for gas separation,” *Carbon N. Y.*, vol. 49, no. 13, pp. 4348–4358, 2011,
- [73] R. C. Reid, T. K. Sherwood, and R. E. Street, *The Properties of Gases and Liquids*, vol. 12, no. 4. 1959.
- [74] B. E. Poling, G. H. Thomson, D. G. Friend, R. L. Rowley, and W. V. Wilding, *Section 2: Physical and Chemical Data*. 2007.
- [75] R. R. Tarakad and R. P. Danner, “An improved corresponding states method for polar fluids: Correlation of second virial coefficients,” *AIChE J.*, vol. 23, no. 5, pp. 685–695, 1977,
- [76] H. C. Hottel, J. J. Noble, A. F. Sarofim, G. D. Silcox, P. C. Wankat, and K. S. Knaebel, *Perry’s Chemical Engineers’ Handbook: Heat and Mass Transfer*. 2008.
- [77] C. Engineering, “Heat Transfer in Packed Beds-a,” 1976.
- [78] I. L. Shabalin, *Ultra-High Temperature Materials I*, I. 2014.

CHAPTER 3

Vapor/gas separation through carbon molecular sieve membranes (CMSM). Part I: boehmite-phenolic resin membranes with improved hydrophilicity

Abstract

In this chapter, composite alumina carbon molecular sieve membranes (Al-CMSM) were prepared from phenolic resin solutions loaded with hydrophilic boehmite (γ -AlO(OH)) nanosheets (0.4-1.4 wt % in solution) which, despite their partial transformation to γ -Al₂O₃ nanosheets upon thermal decomposition of the resin, improve the hydrophilicity and thus the adsorption-diffusion contribution of the H₂O permeation. The boehmite/ γ -Al₂O₃ nanosheets showed no influence on the pore size distribution of the membranes in the range of micropores, but they increased the membrane hydrophilicity. Furthermore, the nanosheets introduce defects in the carbon matrix, increasing the tortuosity of the active layer, as concluded via phenomenological modeling and parametric fitting of the experimental results. Consequently, the water permeability exhibits a maximum with boehmite/alumina content of ca. 0.8 wt %, as the combined effects of increasing hydrophilicity (which favor H₂O permeability) and increasing thickness and tortuosity (which hamper permeability) upon increasing boehmite loading. Similarly, the H₂O/gas perm-selectivity is optimum at 1.2 wt % boehmite loading. The H₂O permeation mechanism was further investigated by modeling the mono- and multi-layer adsorption and capillary condensation of water in microporous media, which result as the main transport mechanisms in the explored conditions.

This chapter is based on the following paper:

Poto, S., Endepoel, J. G., Llosa-Tanco, M. A., Pacheco-Tanaka, D. A., Gallucci, F., & Neira d'Angelo, M. F. (2022). Vapor/gas separation through carbon molecular sieve membranes: Experimental and theoretical investigation. *International journal of hydrogen energy*, 47(21), 11385-11401.

3.1 INTRODUCTION

In Chapter 2, carbon molecular sieve membranes (CMSM) were identified as a potentially attractive candidate to selectively separate H₂O from other gases in the temperature conditions of the CO₂ hydrogenation processes (i.e., 200-400 °C) [1], [2]. CMSMs offer superior thermo-chemical stability in humid and corrosive environments, as well as an excellent balance between gas permeance and perm-selectivity, especially with respect to polymeric membranes [3]–[5].

Carbon-based membranes have emerged as promising material for gas separation processes, with a wide application spectrum, owing to the possibility to tailor the properties of the carbon active layer and thus the governing permeation mechanism to the desired separation. Most of these applications include the separation of mixtures of (dry) gases such as CO₂, N₂, CH₄, H₂ or mixtures of alkane/alkene at relatively low temperature (i.e., 20-80 °C) [5], [6]–[7]. Only very recently they have been demonstrated for water vapor permeation, at temperatures above 150 °C [8]. Carbon membranes derive from the pyrolysis of a thermoset polymeric precursor in inert conditions or vacuum, typically deposited on the surface of a porous ceramic support (e.g., α -Al₂O₃). Depending on the conditions of the carbonization step (e.g., inert atmosphere, temperature, time and heating rate) and on the physicochemical properties of the precursor, their porous structure and degree of hydrophilicity/hydrophobicity can be tuned according to the desired application and its perm-selectivity requirements. Forster et al. [8] have recently reported that an increase in the carbonization temperature causes, on average, a shrinkage of the pore size and, at the same time, a decrease in the affinity to water. Indeed, when the temperature of carbonization is increased above 550 to 650 °C, most of the oxygen-based groups are removed. Upon decomposition of the polymeric precursor, the imperfections in the microcrystalline regions give rise to a porous structure which typically includes ultra-micropores (i.e., $d_p \leq 0.6$ nm) and micropores (i.e., 0.6 nm $\leq d_p \leq 2$ nm) [9], [10]. These are the main responsible for the separation mechanism via molecular sieving (i.e., based on size exclusion) and adsorption diffusion (i.e., based on physicochemical differential interactions between diffusing species and the membrane surface), respectively. Besides the pore structure and surface properties of the membrane, the operating temperature is a well-known parameter that determines the governing permeation mechanism. At higher temperatures, corresponding to higher molecular energy level, the collisions of the molecules with the pore walls are more frequent, slowing down the permeation process. This phenomenon is known as Knudsen diffusion [11]. Therefore, higher temperatures hinder the adsorption phenomena, and the transport mechanism inevitably turns into the molecular sieving or Knudsen diffusion [10], [12]. For each diffusing gas, a specific temperature exists at which the adsorption-diffusion is not relevant anymore. Llosa et al. [13] reported that for temperatures above 180 °C and 80 °C, the adsorption-diffusion mechanism for CO₂ and CH₄, respectively, is negligible. At lower temperatures, on the other hand, when the adsorption-diffusion mechanism is dominant, the diffusing species could reduce the effective pore size of the

membranes, hindering the permeation of the non-diffusing species. Therefore, at low temperatures, higher perm-selectivity values can be achieved.

While most of the literature on CMSM deals with (low temperature) gas separation processes, which are usually described as a combination of molecular sieving and/or adsorption-diffusion, very limited attention has been paid to the separation of mixtures containing condensable species like H₂O. In these cases, an additional transport mechanism via viscous flow of capillary condensate [14]–[16] should be contemplated. Indeed, for wetting systems (e.g., H₂O on a hydrophilic solid surface) the vapor pressure in a capillary is lower than that on a planar surface, as described by the Kelvin's equation [17]. Thus, water can condense in the micropores of the carbon membranes with sufficient hydrophilicity. The viscous flow of capillary condensate is usually slower than the multi- and mono-layer adsorption-diffusion [14], explaining the observed maxima in permeability vs. surface hydrophilicity reported by Forster et al. [8]. In other words, strengthening surface interactions (e.g. by decreasing temperature or tuning surface hydrophilicity/hydrophobicity) does not always render an increase in permeance. Whereas the existence of capillary condensation may be considered as a nuisance (i.e. lower permeability), or even complexing factor that obscures the interpretation of experimental data, it can surely be used for the rational design of a selective membrane if properly understood. When looking at the case of water separation, a hydrophilic carbon membrane is an obvious choice given their well-established affinity to H₂O [42],[50]. Water is known to adsorb on the pores already at ambient conditions, reducing the active pore size of the membranes [19] and thereby increasing the separation factors between water and other gases. Even more, when capillary condensation occurs, water could partially or totally block the pores of the membranes, further suppressing the permeation of the other gases. In processes involving CO₂ hydrogenation, where the focus is the selective separation of H₂O from reactants and products such as H₂, CO₂ and CO, this is for sure an enormous advantage.

In practical terms, the hydrophilicity of the carbon membrane can be tuned not only by selecting the proper polymer precursor and/or the conditions of the carbonization step [8]. Besides, the incorporation of additives like silica [20] or boehmite [21] in the carbon matrix have also proved to affect the gas permeability, due to an alteration of the pore distribution. However, the effect of those fillers on the membrane hydrophilicity has not been investigated yet. In this chapter, the effect of the concentration of boehmite nanosheets into the CMSM on the hydrophilicity of the membrane and its effect on water vapor permeation is assessed. For that purpose, low-cost boehmite nanosheets were incorporated in phenolic resin-based carbon membranes [21]–[23] for the separation of H₂O vapor from H₂, CO₂, CO, N₂ and CH₄ at 150–250 °C and 2–5 bar. The effect of boehmite loading is studied by correlating the membrane properties (assessed by gravimetric studies, morphological analysis such as XRD and XPS, pore size measurement, and cross section analysis via scanning electron microscopy) to performance data (i.e., permeabilities and separation factors). To gain a deeper understanding of the properties-performance correlations, the performance of these membranes is modelled using a

phenomenological model describing the mono- and multi- layer adsorption and capillary condensation of water in microporous media (i.e., transport mechanisms involved in the permeation of pure H₂O-vapor in microporous media). Thus, the insights of this work are key for the rational design of selective CMSM membranes for water vapor separation.

3.2 EXPERIMENTAL

3.2.1 Synthesis of Al-CMSMs

The tubular Al-CMSMs were prepared by the one-dip dry carbonization step method [21]–[23]. The supports are tubular asymmetric α -Al₂O₃ tubes (ID: 7 mm, OD: 10 mm), with a 100 nm average pore size, provided by Inopor[®]. The porous α -Al₂O₃ was attached to the dense Al₂O₃ by using a glass sealant at 1150 °C, leaving an effective length for the deposition of the carbon layer of about 10 cm. One end was closed with the glass seal, while the other end was connected to a standard Swagelok component to allow the flow of the permeate. The supports were dip-coated using a vacuum pump in a solution containing: 13% of Novolac resin, 0.6% of ethylenediamine, 2.4% of formaldehyde, a variable amount of 10% aqueous dispersion of boehmite nanosheets with a particle size of 8-20 nm (*Alumisol* provided by Kawaken fine Chemicals) [21], in order to obtain a boehmite content from 0.4 to 1.4%, and *N*-methyl-2-pyrrolidone (NMP) as solvent. **Table 3.1** reports the boehmite content in the dipping solutions used for the preparation of the Al-CMSMs. The membranes were dried at 90 °C overnight under continuous rotation to guarantee a uniform and defect-free layer of the membrane precursor. Thereafter, the membranes were carbonized at 500 °C in inert atmosphere (i.e., 200 mL·min⁻¹ of N₂). The remaining precursor solutions containing 0.8, 1.0 and 1.4 wt % of boehmite nanosheets were used to prepare unsupported films for XRD and XPS analysis. The solution was placed in a Teflon dish, dried at 90 °C and carbonized following the same procedure described for the supported CMSM.

Table 3.1. Boehmite content in the dipping solutions used to prepare the Al-CMSMs

Membrane ID	Boehmite (wt %)
CM04	0.4
CM06	0.6
CM08	0.8
CM10	1.0
CM12	1.2
CM14	1.4

3.2.2 Permeation experiments

The permeation experiments were carried out in a dedicated setup whose layout is sketched in **Figure 3.1**. The setup is characterized by three main modules: I) the feed module, II) the permeation module and III) the retentate/permeate analysis module. Mass flow controllers from Brook Instruments were used to feed the desired flow rate of H₂, CO₂, CO, CH₄ and N₂ (mL·min⁻¹). Demineralized water was fed with a Controlled Evaporator Mixer (C.E.M.) from Bronkhorst, which requires a minimum flow of N₂ (≥ 150 mL·min⁻¹) to allow the water to reach the reactor. To avoid steam condensation, tracing was installed in all the lines and set at a temperature of 200 °C. The permeation module consists of a stainless-steel vessel where the membrane is connected from the top flange. The vessel is placed in an electrical oven to keep isothermal conditions, controlling the temperature on the outer surface of the membrane. The pressure in the permeate side (i.e., inner tube of the membrane) was kept at 1 bar, while the pressure in the retentate side (i.e., outside of the membrane) was controlled with a back-pressure regulator from Bronkhorst. The analysis module consists of two condensers, a film flow meter (Horiba Stec) and a micro-GC (Agilent Technologies). The two condensers use a synthetic coolant supplied by the Lauda electric unit, to condense and collect liquid water from the retentate and the permeate. Thereafter, the gas flow rate from the permeate line was measured with the film flow meter and then injected to the micro-GC for the analysis of the composition.

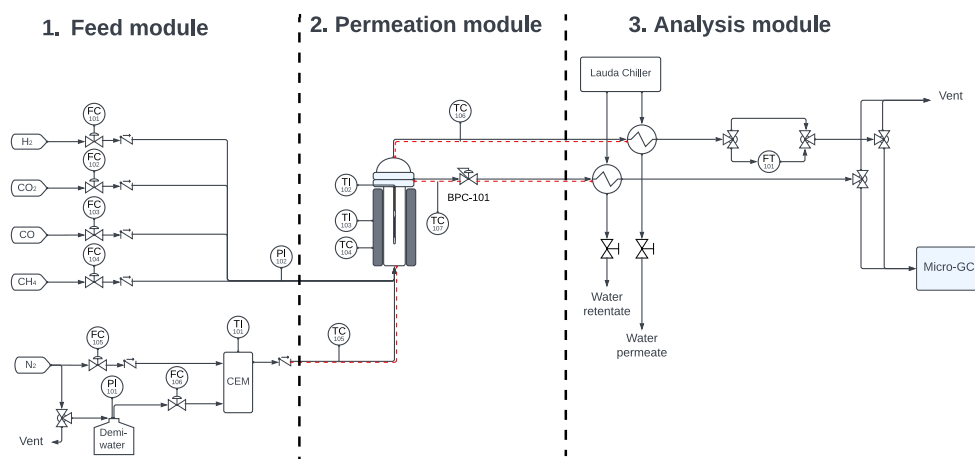


Figure 3.1. Layout of the setup designed for the vapor-gas permeation experiments. The setup is made up of three modules: 1) the feed module; 2) the permeation module and 3) the analysis module. TC, FC and BPC represent the temperature, flow and back-pressure controller. Similarly, TI, FT and PI represent the temperature, flow and pressure transmitters.

Two types of permeation experiments were conducted for: a) pure gas or vapor permeation and b) binary vapor/gas mixture permeation tests. The pure gas/vapor permeation tests were performed at a temperature of 150–240 °C, a pressure gradient

across the membrane of 3 bar and a total feed flow of 1 L·min⁻¹. The membrane was first exposed to a flux of water – containing 7.5 vol. % of N₂ – for 40 minutes to ensure steady state operation. The N₂ permeated flow was measured, and the water was collected and weighted from both the retentate and the permeate. The value of the N₂ flow was used to correct the partial pressures for a more accurate calculation of the water permeance. Afterward, a pure gas flow (H₂, CO₂, CO, CH₄ or N₂) was fed to the membrane section for the pure gas permeation measurement. A vapor permeation test was repeated prior to each gas permeation test, to ensure the same humidity condition of the membrane, which is a parameter that strongly affects the permeation of the gases [24]. These experiments were performed to gain insight into the effect of the alumina nanosheets on the permeation performance of the membranes. Thereafter, the membrane which showed the best performance (i.e., a trade-off of water permeance and water/gas selectivity) was selected for a deeper investigation. In particular, the binary vapor/gas mixture permeation tests were carried out to investigate the effect of the interaction between water and each gas on the water/gas selectivity. These experiments were performed by feeding a mixture of water vapor, N₂ and another gas (H₂, CO₂ and CO) with a concentration of 25-75 vol. % of either H₂, CO₂ or CO, a total feed flow of 1 L·min⁻¹, a temperature of 150-240 °C and a pressure gradient of 3 bar. Lastly, the effect of the pressure gradient across the membrane was investigated at a temperature of 150 °C, with pure gas/vapor permeation tests. The water permeance ($\phi_{\text{H}_2\text{O}}$) and permeability ($\kappa_{\text{H}_2\text{O}}$) were determined according to Eq. 3.1 and Eq. 3.2, respectively.

$$\phi_{\text{H}_2\text{O}} = \frac{W_{\text{H}_2\text{O,permeated}} \cdot M_{\text{w,H}_2\text{O}}^{-1}}{\Delta t \cdot \Delta P_{\text{H}_2\text{O}} \cdot A_m} \quad (3.1)$$

$$\kappa_{\text{H}_2\text{O}} = \phi_{\text{H}_2\text{O}} \cdot l \quad (3.2)$$

Where $W_{\text{H}_2\text{O,permeated}}$ is the weight of the water collected from the permeate, $M_{\text{w,H}_2\text{O}}$ is its molecular weight, Δt indicates the time span of the permeation experiment, A_m and l are the membrane area and thickness, respectively. The $\phi_{\text{H}_2\text{O}}$ accounts for the presence of N₂ in the feed through the gradient of H₂O partial pressure across the membrane ($\Delta P_{\text{H}_2\text{O}}$), defined as follows:

$$\Delta P_{\text{H}_2\text{O}} = y_{\text{H}_2\text{O,ret.}} \cdot P_{\text{ret.}} - y_{\text{H}_2\text{O,perm.}} \cdot P_{\text{perm.}} \quad (3.3)$$

The gas permeance (ϕ_i) was determined according to Eq. 3.4, with $\Phi_{i,\text{perm}}$ the volumetric flow rate of the permeated gas, V_m the standard molar volume of a gas and ΔP_i the gradient of partial pressure across the membrane.

$$\Delta \phi_i = \frac{\Phi_{i,\text{perm}} \cdot V_m^{-1}}{\Delta P_i \cdot A_m} \quad (3.4)$$

The ideal H₂O/gas perm-selectivity ($S_{\text{H}_2\text{O}/i}$) and the H₂O/gas separation factors ($SF_{\text{H}_2\text{O}/i}$) were determined according to Eq. 3.5 and Eq. 3.6, respectively.

$$S_{\text{H}_2\text{O}/i} = \frac{\phi_{\text{H}_2\text{O}}}{\phi_i} \quad (3.5)$$

$$SF_{\text{H}_2\text{O}/i} = \frac{[P_{\text{H}_2\text{O}}/P_i]_{\text{permeate}}}{[P_{\text{H}_2\text{O}}/P_i]_{\text{retentate}}} \quad (3.6)$$

In $SF_{\text{H}_2\text{O}/i}$, the partial pressure of water ($P_{\text{H}_2\text{O}}$) and of the gas species (P_i) in the retentate/permeate, define the degree of separation.

3.2.3 Permporometry experiments

The pore size distribution of the membranes was measured via the permporometry technique, developed by Tsuru et al. [25]. The basic principle of this technique is the capillary condensation of a vapor and the corresponding pore blocking effect on the permeation of a non-condensable gas. This method has the advantage of being able to measure only the pores which are active for the permeation, discarding the dead-end pores. Furthermore, this method does not require the preparation of unsupported carbon films, the pore size distribution could be measured directly on the tubular carbon membranes, leading to a more realistic measurement. The experiments were carried out in a second permeation apparatus, where liquid water was injected via a syringe pump and vaporized in a heating coil; N_2 was used as a carrier gas. The vapor pressure of the stream was controlled by changing the N_2 flow rate. The N_2 permeated flow was measured after removing the water with a cold trap. The experiment was carried out at 70 °C and a ΔP across the membrane of 1 bar. Prior to each experiment, the membrane was dried at 150 °C under N_2 flow, until the N_2 permeance reached a stable value (i.e., corresponding to the membrane dry condition). The different values of water vapor pressure (P_0/P_s) imposed are directly related to the pore radius (r_p), through the Kelvin's equation (Eq. 3.7).

$$RT \ln \left(\frac{P_0}{P_s} \right) = 2v \frac{\sigma \cos(\theta)}{r_p} \quad (3.7)$$

Where v , σ and θ are the molar volume, surface tension and contact angle, respectively. The contact angle was assumed to be 0°, which is a typical assumption for the permporometry experiments [25]. When the vapor pressure of water was stepwise increased, a lower N_2 permeance was measured and the pore size distribution was derived.

3.2.4 Scanning electron microscopy (SEM)

A FEI Quanta scanning electron microscope was used to acquire images of the cross section of the CMSMs, to derive the thickness of the carbon layer. EDX was used to analyze the surface composition of the membranes qualitatively and to assess the uniform distribution of the Al_2O_3 .

3.2.5 X-Ray Diffraction (XRD) and X-Ray photoelectron spectroscopy (XPS) measurements

X-ray diffraction (XRD) analysis in the 2θ range $10\text{--}120^\circ$ was performed on the carbon membrane films samples with a MiniFlex600 machine (*Rigaku*) operating with a Ni β -filtered Cu-K α radiant at 40 kV and 30 mA and a scan step of $0.05^\circ/\text{min}$. The diffraction peaks were identified according to the JCPDS database of reference compounds. XPS measurements were performed using a Kratos AXIS Ultra spectrometer, equipped with a monochromatic X-ray source, and a delay-line detector (DLD). Spectra were obtained using an aluminum anode (Al K α =1486.6eV) operating at 150W. For both the XRD and XPS analyses, the carbon membrane films corresponding to the c-CMSM CM08, CM10 and CM14 were crushed to obtain a fine powder.

3.2.6 Gravimetric analysis

To assess the effect of the alumina content on the hydrophilicity of the CMSMs, the amount of water adsorbed by the membranes was measured via a gravimetric method. The carbon layer was scratched out from the tubular supported membrane and placed in a glass vial which was then kept in a climate chamber at a relative humidity of 99% at room temperature. The weight of the sample was recorded until saturation.

3.3 THEORY OF WATER TRANSPORT THROUGH CMSM

The transport of condensable vapors through porous media is a complex phenomenon involving capillary condensate flow, mono- and multi-layer adsorption, simultaneously. Many efforts have been made in the past years to theoretically describe the combination of these mechanisms [14], [15], [26], [27]. In this work, the *six flows model*, developed by K. H. Lee and S. T. Hwang [15] was implemented to describe the water vapor permeation through the carbon membranes. The objective here was to qualitatively understand which transport mechanism is predominant within the process conditions of this study and to find a correlation with the boehmite/alumina content.

3.3.1 Model description

The permeation through porous media can be categorized in three different types: gas flow, surface flow and capillary condensate flow. The detailed equations describing these mechanisms are reported in Appendix B (section B.1). Understanding the relative contribution of these flow types allows to gain insight on the overall transport mechanisms of water vapor through the membrane. The combination of those flows, together with the blocking effect exerted by the adsorbed layer, give rise to six types of flows (**Figure 3.2**), which can be determined according to: 1) the relative pressure of the permeate (P_2) and the retentate (P_1), with respect to the capillary condensation pressure (P_0) (P_2/P_0 and P_1/P_0 , respectively),

and 2) the relative thickness of the adsorbed layer of water at the permeate (t_2) and retentate (t_1) with respect to the pore radius (r_p) (t_2/r_p and t_1/r_p , respectively).

A detailed description of the phenomena is given below:

1. F_1 : Combination of Knudsen molecular flow (gas flow) and surface flow in the adsorbed phase.
2. F_2 : Capillary condensation occurs at the upstream end of the pore, but not at the downstream end. On the downstream side, gas and adsorbate flows take place.
3. F_3 : The entire pore is filled with a capillary condensate.
4. F_4 : The upstream end of the pore is filled with bulk condensate. Somewhere in the capillary (z) the meniscus is located. There is no curved interphase at the upstream side, therefore no suction force.
5. F_5 : The entire pore is filled with a capillary condensate. Capillary condensation occurs at the downstream side. The upstream end of the pore is filled with bulk condensate.
6. F_6 : The entire pore is filled with a capillary condensate and no meniscus is present in the pore.

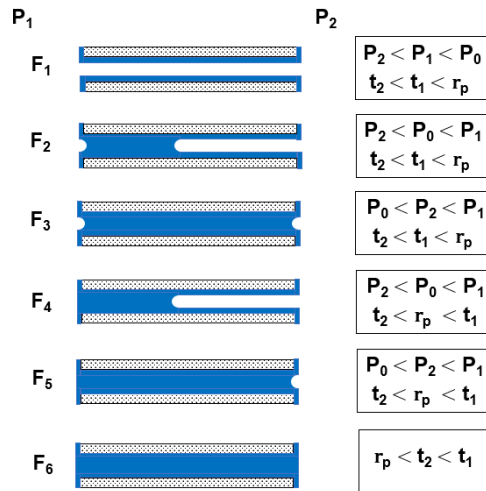


Figure 3.2. Six different flow modes of water permeation with their boundary conditions

Table 3.2. Equations describing the flow rate of water through the pore according to each flow mode.

Flow mode	Equation
1	$F_1 = A_p(Q'_g + Q_s) \frac{\Delta P}{l}$
2	$F_2 = A_p(Q'_g + Q_s) \frac{P_0 - P_2}{l - z}$
3	$F_3 = \frac{A_p K_d \rho RT}{\eta z M} \left[\frac{(r - t_1)^2}{r_p^2} \ln \left(\frac{P_1}{P_0} \right) - \frac{(r - t_2)^2}{r_p^2} \ln \left(\frac{P_2}{P_0} \right) \right]$
4	$F_4 = A_p(Q'_g + Q_s) \frac{P_0 - P_2}{l - z}$
5	$F_5 = \frac{A_p K_d \rho RT}{\eta z M} \frac{(r - t_2)^2}{r_p^2} \ln \left(\frac{P_2}{P_0} \right)$
6	$F_6 = \frac{A_p K_d}{\eta} \frac{P_1 - P_2}{l}$

The equations in **Table 3.2** represent the mathematical expressions to compute the flow rate and the permeance according to each flow type. The physical properties for water vapor were obtained with empirical correlations as a function of temperature and pressure, as reported in Appendix B (section B.1). The pore size distribution of the carbon membrane was accounted for with a fitted Gaussian function and used to determine the total flow rate of the permeate through the membrane as follows:

$$F_t = \int_0^{\infty} f(r) F_r dr \quad (3.8)$$

3.3.2 Model implementation

The six flows model was implemented in MATLAB R2019a. The pore size distribution, the membrane characteristics and the physical properties of water are given as input parameters. The boundary conditions (i.e., temperature and pressures) are defined as those of the permeation experiments. The flow mode is defined for each pore size (r) and Eq. 3.8 is used to calculate the total flow rate and water permeance. Besides the total flow rate and permeance as a function of temperature and pressure, the frequency of the flow modes is given as simulation output, to determine the predominant transport mechanism at each condition. The pore structure constant (K_d), the H₂O film thickness at the retentate and permeate side (i.e., t_1 and t_2 , respectively) and the coefficient of resistance (C_r) could not be measured, so they were fitted comparing the model predictions against the permeability data from the permeation experiments using a least-square non-linear curve fitting algorithm (*lsqcurvefit*). Among these parameters, K_d and C_r are of particular interest since they both reflect the resistance to the flow exerted by the pore structure, which is believed to be influenced by the boehmite content.

3.4 RESULTS AND DISCUSSION

3.4.1 Characterization of the alumina phase in the Al-CMSM

The XRD patterns of the carbon films prepared with 0.8, 1.0 and 1.4 wt % of boehmite are reported in **Figure 3.3a**. The first and higher intensity peak appearing at 22° for the three samples is related to carbon [28]. Besides that, two main broad peaks appear for the 1.0 and 1.4 wt % boehmite samples at 2θ value of 46° and 67° , which are related to the diffraction of the (440) and (400) planes of $\gamma\text{-Al}_2\text{O}_3$, respectively [29]. On the contrary, boehmite ($\gamma\text{-AlO}(\text{OH})$) would have shown peaks centered at 48° and 65° , corresponding to the diffraction of the (200) and (002) planes. However, well dispersed and nanometer size boehmite sheets could not be detected. Indeed, at 0.8 wt % of boehmite, no peaks are observed between 30° and 90° , suggesting that the boehmite/ $\gamma\text{-Al}_2\text{O}_3$ sheets are well dispersed in the carbon matrix, avoiding the crystallization. As the concentration of boehmite increases, clustering of the boehmite nano-sheets takes place, leading to their dehydration: $2\text{AlOOH} \leftrightarrow \gamma\text{-Al}_2\text{O}_3 + \text{H}_2\text{O}$ [30]. As a result, at higher concentration of boehmite, the condensation of some of the nanosheets to the less hydrophilic $\gamma\text{-Al}_2\text{O}_3$ takes place, with no further phase-change towards the hydrophobic $\alpha\text{-Al}_2\text{O}_3$. **Figure 3.3b** displays the Al-region of the XPS pattern measured on the same carbon films. The deconvolution of the Al 2p peak shows the presence of both boehmite ($\text{AlO}(\text{OH})$) and aluminum oxide (Al_2O_3), the former peak being expectedly more pronounced for the 0.8 wt % sample than for the more concentrated samples. Note that the exact amount of $\gamma\text{-Al}_2\text{O}_3$ and/or boehmite in the carbon layer after the carbonization is unknown, so these concentrations refer to the initial boehmite content in the dipping solution. Furthermore, analyzing the Al and C region it can be confirmed that the pyrolysis process did not cause any chemical interaction between them (**Figure B4**). The elemental composition of the carbon films was determined from the XPS spectra and the carbon to aluminum ratio is reported in **Table 3.3**.

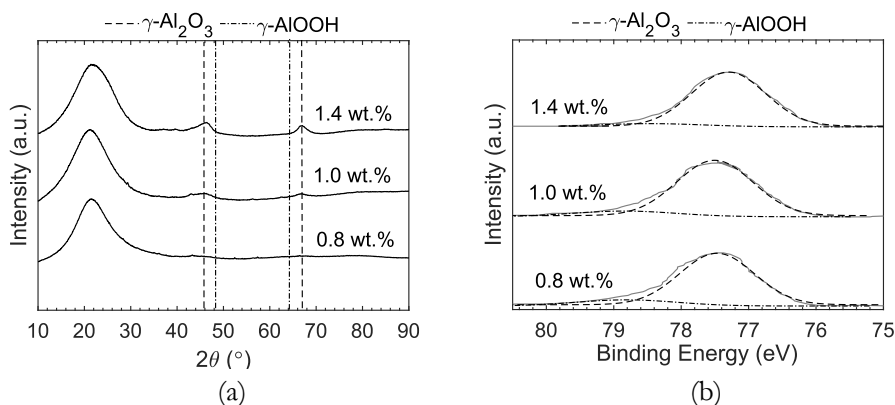


Figure 3.3. XRD pattern (a) and Al-region of the XPS pattern (b) of the carbon films prepared from the dipping solution containing 0.8, 1.0 and 1.4 wt % boehmite.

Table 3.3. Carbon to aluminum ratio of the carbon films determined via the XPS analysis

Initial boehmite content (wt %)	C:Al (weight based)
0.8	27.6
1.0	21.5
1.4	17.6

3.4.2 Effect of alumina content on the Al-CMSMs hydrophilicity

Figure 3.4 shows the effect of the initial boehmite content on the hydrophilicity of the carbon membranes studied by water adsorption experiments. The amount of water adsorbed increases with the boehmite content up to a maximum around 1 wt %, showing then a decrease for the membranes with 1.2 and 1.4 wt %. The membranes without any γ - Al_2O_3 already show a degree of hydrophilicity, as reported elsewhere [8], [18] and confirmed by the water adsorbed by the 0 wt % membrane (**Figure 3.4**). When γ - $\text{Al}_2\text{O}_3/\gamma$ - $\text{AlO}(\text{OH})$ nanosheets are integrated in the carbon matrix, it is clear that an optimum in concentration exists that maximizes the properties of the membrane (i.e., hydrophilicity). Moreover, at higher boehmite contents, the nanosheets of boehmite start to condensate ($2 \text{AlO}(\text{OH}) \leftrightarrow \gamma\text{-Al}_2\text{O}_3 + \text{H}_2\text{O}$) rendering a less hydrophilic cluster. The probability of condensation increases with the boehmite content. The presence of γ - Al_2O_3 is confirmed by the XRD (**Figure 3.3a**).

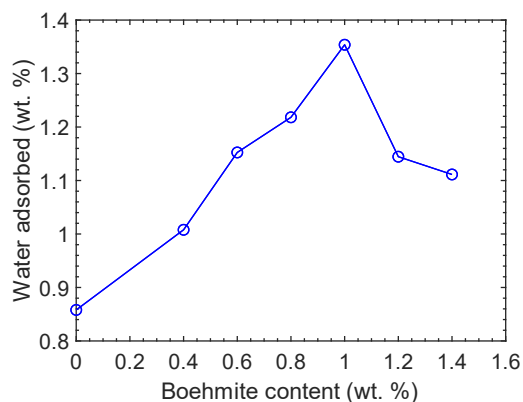


Figure 3.4. Amount of water adsorbed from the Al-CMSMs as a function of their boehmite content.

3.4.3 Effect of the alumina content on the Al-CMSMs pore size distribution

The pore size distributions of the Al-CMSMs are reported in **Figure 3.5**, covering the region of the micropores (i.e., $0.6 \text{ nm} \leq d_p \leq 2 \text{ nm}$), which are more important for transport via adsorption-diffusion [9]. All the membranes have a very similar pore size distribution, with the most frequent size being around 1 nm. Therefore, it can be concluded that the alumina nanosheets do not affect the pore size distribution

of the membranes in the pore size region covered by the N_2 -permporometry technique (i.e. region of the micropores). However, information on the region of ultra-micropores (i.e., $d_p \leq 0.6$ nm), which are responsible of the molecular sieving transport mechanism, are not available. Nevertheless, as later reported in Chapter 4, a carbonization temperature of 500 °C lead to the formation of pores in the micropore region, with negligible number of pores having $d_p \leq 0.6$ nm.

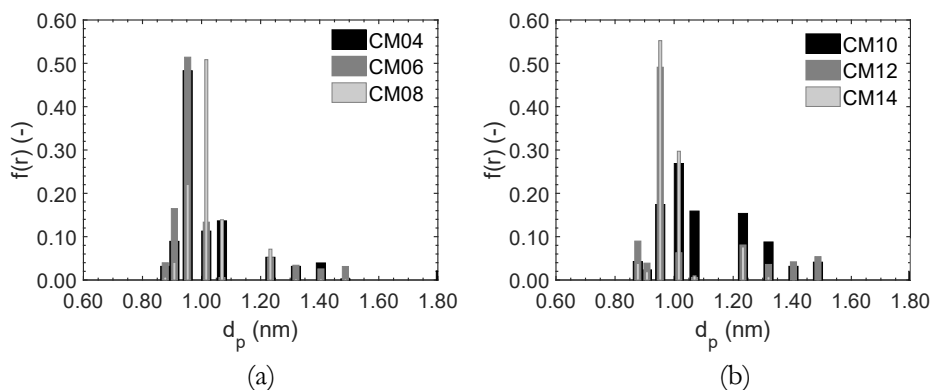


Figure 3.5. Pore size distribution of the c-CMSMs with a boehmite content of 0.4 wt %, 0.6 wt % and 0.8 wt % (a), and of 1.0 wt %, 1.2 wt % and 1.4 wt % (b) derived with the permporometry technique.

3.4.4 Effect of the alumina content on the thickness of the carbon layer

Figure 3.6a and **b** show a representative cross section of the Al-CMSMs prepared with 0.4 wt % and 1.4 wt % of boehmite, respectively, measured by SEM (see the other samples in Appendix B, **Figure B2**). All the membranes were cut in different positions to confirm the uniformity of the layer thickness along the membrane. The average value of at least 3 measurements of the thickness of the composite layer is reported as a function of the initial boehmite content in **Figure 3.7**. The Al-CMSMs show a clear increase in the composite carbon-alumina layer thickness for larger alumina content, although the difference between CM12 and CM14 appear negligible. This is attributed to an increase of the viscosity of the dipping solution, which is a well-known parameter affecting the CMSM layer thickness [31]. Indeed, with higher boehmite concentration, the colloidal mixture becomes more viscous [32]. Note that other parameters that could affect the layer thickness (i.e., the dipping time, the porosity of the support) were kept constant.

Moreover, the sharper increase in the layer thickness at ca. 1.2 wt % of initial boehmite concentration can be attributed to the rheological percolation of the dipping solution containing the boehmite nanosheets (i.e., concentration beyond which the bulk material shows a transition in physical properties, such as viscosity, in this case) [33].

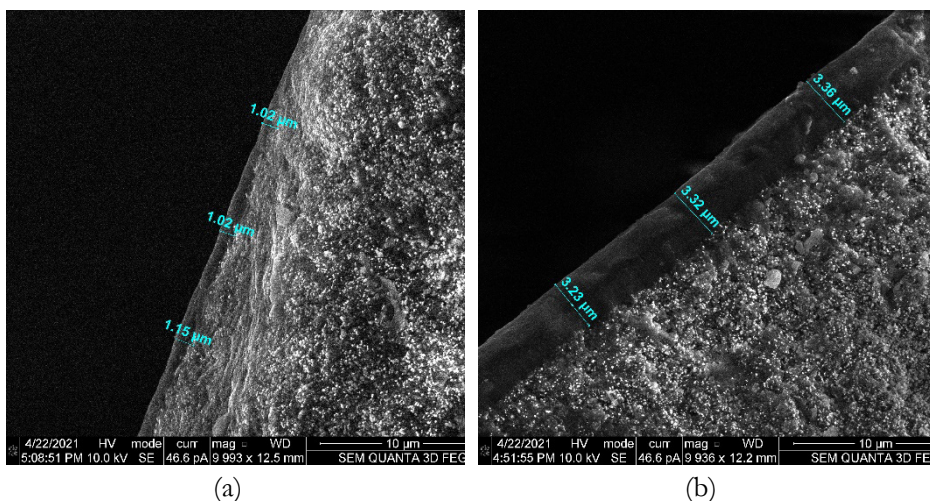


Figure 3.6. Thickness of the carbon layer of the CM04 (a) and CM14 (b) measured on the images of the cross section of the membranes acquired with a FEI Quanta SEM.

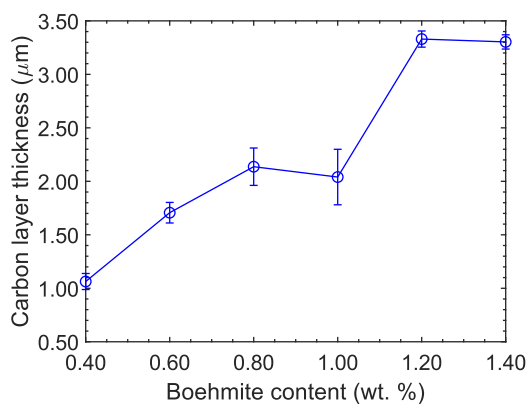


Figure 3.7. Thickness of the carbon layer of the CM04 (a) and CM14 (b) measured on the images of the cross section of the membranes acquired with a FEI Quanta SEM.

3.4.5 Permeation results

The following section focuses on the results of the permeation experiments, first with pure vapor/gas to analyze the effect of the alumina content on the performance of all membranes, and later with binary mixtures, to understand the transport phenomena across a selected membrane.

All the membranes tested in this study did not show any stability issue (i.e., permeance did not change significantly over time). Therefore, no delamination phenomena occur and the boehmite nanosheets did not affect the adherence of the carbon layer to the alumina support.

Effect of the alumina nanosheets on the Al-CMSMs permeation properties

In the field of inorganic membranes, the permeation is frequently reported as permeance (i.e., φ_i in $\text{mol m}^{-2}\text{s}^{-1}\text{Pa}$, defined as the permeated flux normalized by the driving force). However, in this study the water permeation is expressed in permeability (i.e., $\kappa_{\text{H}_2\text{O}} = \varphi_{\text{H}_2\text{O}} \cdot l$, in $\text{mol}\cdot\text{m}^{-1}\text{s}^{-1}\text{Pa}$), to standardize the permeation properties with the membrane thickness, which increases with the boehmite content as discussed earlier (**Figure 3.7**). **Figure 3.8** shows the water permeability ($\kappa_{\text{H}_2\text{O}}$) as a function of temperature and alumina content for the Al-CMSMs. **Figure 3.8a** reveals that $\kappa_{\text{H}_2\text{O}}$ monotonically decreases with temperature for all membranes, suggesting a strong contribution of capillary condensation and multi- and monolayer adsorption diffusion as the main transport mechanisms [14]. Although the alumina content does not seem to influence the type of mechanism governing the water transport, it does show a clear effect on the permeability, as stressed in **Figure 3.8b**. Regardless the operating temperature, a volcano plot for $\kappa_{\text{H}_2\text{O}}$ vs. initial boehmite loading is observed, with a maximum in the $\kappa_{\text{H}_2\text{O}}$ at 0.8 wt % of initial boehmite content. This trend is, to some extent, consistent with the hydrophilicity trends reported in **Figure 3.4**, except that they are peaked at slightly different value of boehmite contents (i.e., 0.8 wt % and 1 wt %, respectively). This suggests a strong hydrophilicity-performance correlation, in line with the expectations for the transport via adsorption-diffusion. Nevertheless, the buildup in boehmite content from membrane CM08 to CM10, however, leads to a lower $\kappa_{\text{H}_2\text{O}}$ despite the increase in the affinity to water. The higher hydrophilicity of these membranes increases the possibility of condensation of water, which render the transport in the pores slower. Note that the effects of layer thickness are normalized in the permeability data, and no major changes were found in the pore size distribution of these membranes, at least in the micropores region. Thus, it is hypothesized that the introduction of boehmite/alumina into the carbon structure induces certain changes into the porous structure of the selective layers (i.e., tortuosity and/or porosity), which may affect the transport of water, particularly at higher boehmite loadings. These effects will be further addressed in Section 3.4.6.

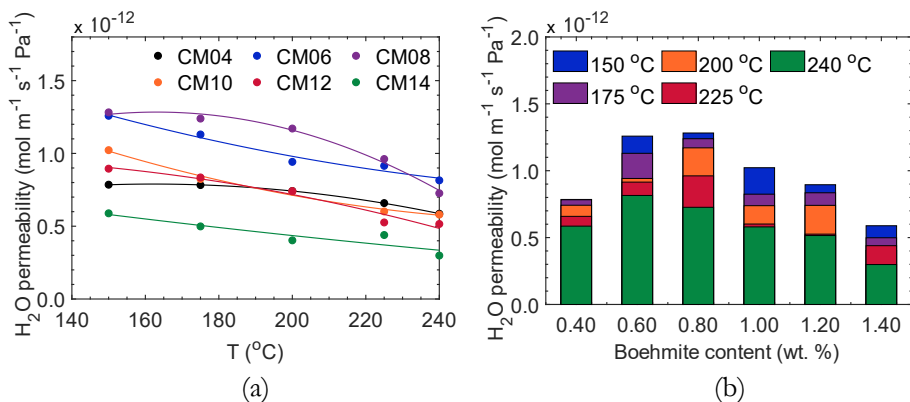


Figure 3.8. Water permeability as a function of the temperature of permeation for the Al-CMSMs prepared with different amount of boehmite (a) and as a function of the boehmite content at 150 °C, 200 °C, 225 °C and 240 °C (b). Other experimental conditions: $\Delta P=3$ bar, 1 L·min⁻¹ feed flow containing 7.5 vol. % N₂.

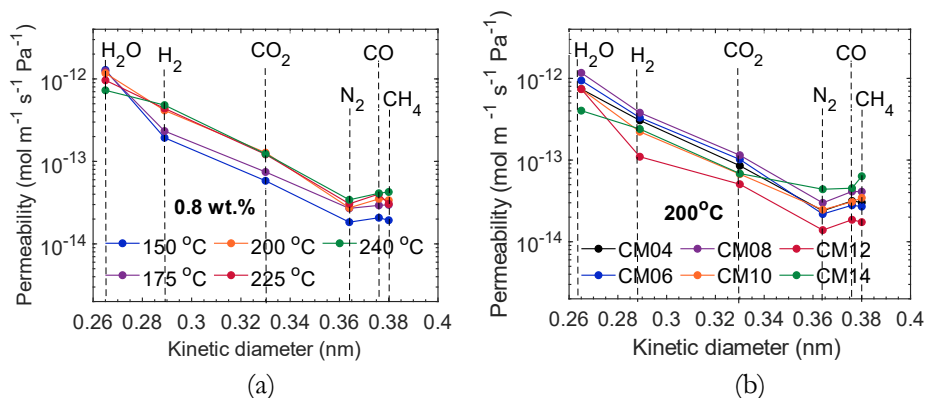


Figure 3.9. Permeability of each component (κ_i) as a function of their kinetic diameter, at various permeation temperatures for the membrane CM08 (a) and at 200 °C for the Al-CMSM containing different amount of boehmite (b).

Next, the study is extended to the permeation of other gases. **Figure 3.9a** shows the permeability (logarithmic scale) as a function of the kinetic diameter of various gases at different temperatures of permeation. The permeability is the highest for the smallest gas (i.e., H₂O) and then it decreases when the kinetic diameter of the gas increases, which is clear indication of molecular sieving being the dominant mechanism for the gas permeation. However, N₂ shows the lowest permeability, being N₂ a molecule with very low polarizability and, as a consequence, not able to interact electrostatically with the hydrophilic pores. On the contrary, CO, despite being bigger than N₂, shows a higher permeability than N₂, due to its polarity. For gases other than water, the permeability increases with the temperature. Similar results were obtained with the other membranes containing 0.4, 0.6, 1.0, 1.2 and 1.4 wt % of boehmite in the dipping solution. **Figure 3.9b** illustrates the permeability as a function of the kinetic diameter at 200 °C of the Al-CMSM with various content

of boehmite. It can be observed that for most of the gases the permeability follows the order $CM08 > CM06 > CM04 > CM10 > CM14 > CM12$. Thus, similarly to water, the gas permeability is also highest at 0.8 wt % of initial boehmite content.

Figure 3.10a, b, c, d and **e** report the ideal perm-selectivity as a function of temperature and of the boehmite content of the pairs H_2O/H_2 , H_2O/CO_2 , H_2O/N_2 , H_2O/CO and H_2O/CH_4 , respectively. The ideal perm-selectivity (H_2O/i) were determined by computing the ratio of the ϕ_{H_2O} and ϕ_i measured at the same temperature and pressure gradient, within the single gas/vapor permeation experiments. In line with the expectations, $S_{H_2O/i}$ generally increases for larger gas molecules, which is a clear indication of molecular sieving. However, the interactions between the permeating gases with the water adsorbed in the pores explain deviations with respect to the simple size-exclusion rationale. For example, the pair H_2O/N_2 shows the highest perm-selectivity (even higher than H_2O/CO and H_2O/CO_2) despite the fact that N_2 is not the largest molecule in this set, due to the lack of polarity. Yet, its relatively large size and low water solubility explain the high S_{H_2O/N_2} . On the other hand, the adsorption diffusion mechanism (i.e., direct gas adsorption on the pore walls) in the temperature range is not likely to occur for each of these gas, as reported in literature [13].

Figure 3.10 also shows that all membranes exhibit a decreasing perm-selectivity with increasing temperature for each H_2O/i pair. As it is typical of molecular sieving [34], the permeability of all the gases (**Figure B3**) shows a slight increase with temperature. Furthermore, when increasing the temperature, the water adsorbed in the pores will gradually desorb, driving to an increase in the active pore size [18], [19], [24]. However, even if ϕ_{H_2O} decreases with temperature, all the perm-selectivity assume values greater than 1 at each experimental condition, being water the most permeating species at all times.

Finally, the H_2O/i perm-selectivity generally increases with the initial boehmite content, displaying a maximum value around 1.2-1.4 wt %. With regards to water permeance, it was shown that the boehmite content has a beneficial effect up to 0.8 wt % due to the strengthening of the water-surface interactions derived from the higher number of hydrophilic sites, as previously established. Greater increase in boehmite loading also leads to lower water permeability, similar to all the other gases, but being water the smallest molecule as well as the most affine to the hydrophilic carbon surface, water permeation is less affected by any obstruction imposed by the structure of the carbon layer. It is also evident that the CM14 (i.e., the membrane with largest boehmite content) does not follow the above trend. It appears that the (limited) hydrophilicity of that sample (**Figure 3.4**) does not provide sufficient water-surface interaction as compared to membranes with the slightly less boehmite, due to the condensation reaction of the molecules of $AlO(OH)$. Thus, it can be concluded that the effect of the boehmite content on the hydrophilicity and on the membrane structure counterbalance each other, resulting again in a maximum in the perm-selectivity for the CM12 (i.e., 1.2 wt % of boehmite).

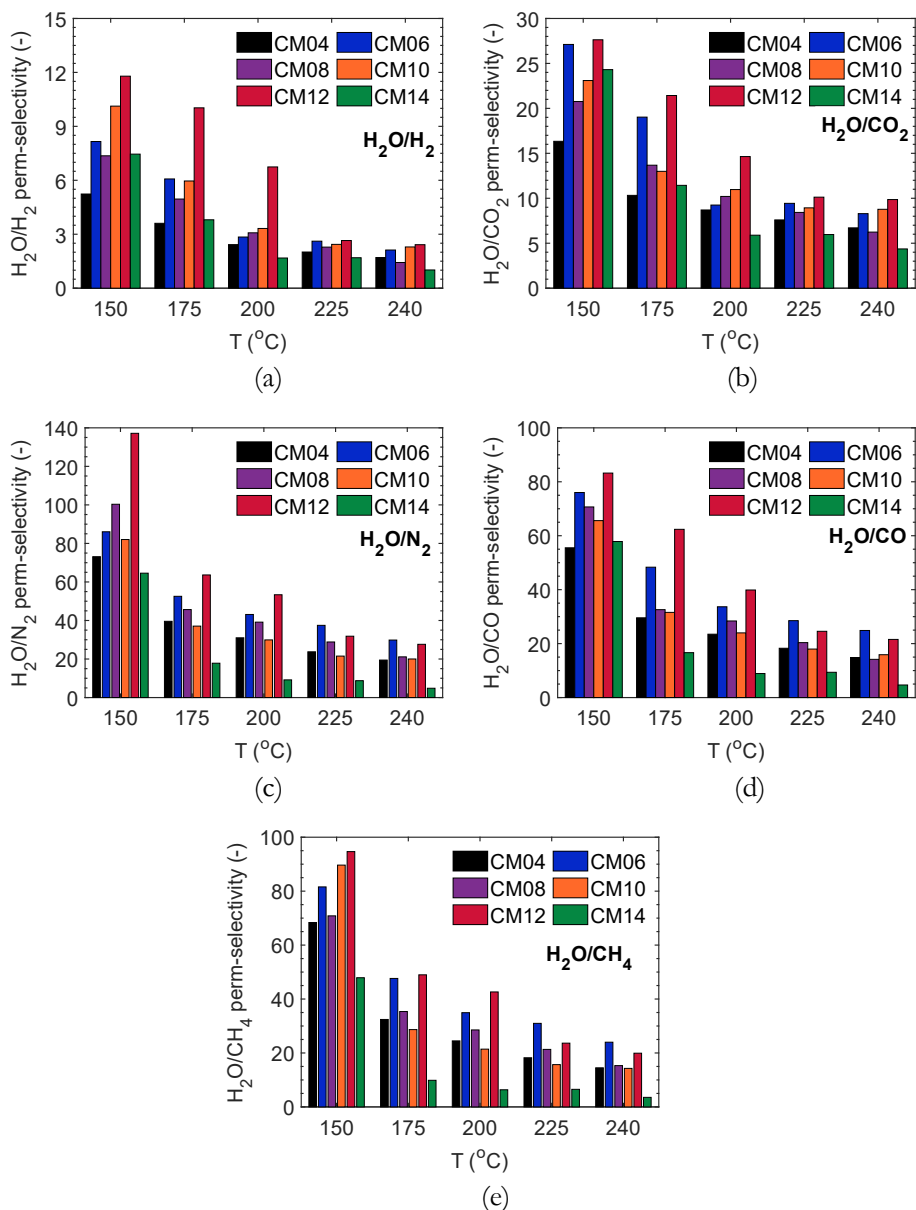


Figure 3.10. Ideal H_2O/H_2 (a) H_2O/CO_2 (b), H_2O/N_2 (c), H_2O/CO (d) and H_2O/CH_4 (e) perm-selectivity as a function of temperature for the Al-CMSMs prepared with different amount of boehmite. Other experimental conditions: $\Delta P=3$ bar, $1 \text{ L}\cdot\text{min}^{-1}$ feed flow of gas. Ideal perm-selectivity were calculated as the ratio of ϕ_{H_2O} and ϕ_i measured at the same temperature and pressure gradient, within the single gas/vapor permeation experiments.

Investigation on the permeation properties of the CM08 membrane

The selection of a membrane material for a specific process always rises from a trade-off between permeability and perm-selectivity [35]. In Chapter 2, given the proposed membrane reactor configuration (i.e., circulation of CO₂-H₂ sweep-gas), it was established that the most important parameter for this application is the $\phi_{\text{H}_2\text{O}}$, so the membrane selected here for a deeper investigation is the CM08.

First, the effect of the gradient in total pressure (ΔP) on the H₂O permeation and perm-selectivity toward H₂, CO₂ and CO (**Figure 3.11**) was investigated at constant temperature (i.e., 150 °C). The $\phi_{\text{H}_2\text{O}}$ increases for larger ΔP , which confirms that the viscous flow of capillary condensate is indeed a main contributor to the transport mechanism. At the same time, ϕ_{H_2} , ϕ_{CO_2} and ϕ_{CO} slightly decrease (i.e., nearly constant) with ΔP (i.e., perm-selectivity increase with ΔP), leading again to the conclusion that the contribution of the adsorption diffusion is negligible in these conditions [37].

Secondly, the separation factors derived from the binary vapor/gas mixture tests (i.e., H₂O/H₂, H₂O/CO₂ and H₂O/CO real perm-selectivity), which are of interests for the reactions involving CO₂ and H₂ with the production of water are analyzed. **Figure 3.12a, b** and **c** show the effect of both temperature and gas/vapor composition in the feed on the separation factors of the pair H₂O/H₂ ($S_{\text{H}_2\text{O}/\text{H}_2}$), H₂O/CO₂ ($S_{\text{H}_2\text{O}/\text{CO}_2}$) and H₂O/CO ($S_{\text{H}_2\text{O}/\text{CO}}$), respectively. The ideal perm-selectivity values are also reported as dashed line, for comparison. Generally, an increase in the gas composition (i.e., H₂, CO₂ or CO) causes a drop in the $S_{\text{H}_2\text{O}/i}$ due to a lower driving force for the permeation of water (i.e., lower H₂O partial pressure gradient across the membrane). Furthermore, a lower separation factor can be interpreted as a result of the “competition” of H₂O and the second species for the hydrophilic sites in the pores. Among all, the $S_{\text{H}_2\text{O}/\text{H}_2}$ is the lowest, as expected considering the kinetic diameter of H₂O and H₂ (i.e., 0.26 and 0.29 nm, respectively). The interaction of a gas with water could be related with its solubility. However, given the constrictions of the pores, water behaves like a molecule rather than bulk water. As a result, it is even more correct to discuss about electrostatic interactions, which, anyway, follow the same trend as the solubility. Since H₂ shows a low solubility in water, especially at these conditions (i.e., lower than 0.001 g_{H₂}/kg_{H₂O}), and water has more affinity with the hydrophilic pores, water either blocks the pores completely where capillary condensation occurs (i.e., in the smallest pores) or it reduces the active pore size, where adsorption diffusion is predominant (i.e., in the slightly larger pores). Therefore, the real $S_{\text{H}_2\text{O}/\text{H}_2}$ is in general higher than the ideal H₂O/H₂ perm-selectivity, while it also decreases with temperature. On the contrary, the $S_{\text{H}_2\text{O}/\text{CO}_2}$ increases with temperature and is lower than the ideal perm-selectivity, particularly at low temperature. This clearly suggests that the high CO₂ solubility in water (ca. 0.5 g_{CO₂}/kg_{H₂O}) facilitates the permeation of CO₂ in the presence of water. As the CO₂ solubility in water (and thus the CO₂ permeation) decreases with temperature the $S_{\text{H}_2\text{O}/\text{CO}_2}$ increases. Lastly, the $S_{\text{H}_2\text{O}/\text{CO}}$ is again

lower than the ideal H₂O/CO perm-selectivity, especially at higher temperature. This behavior can be ascribed to the competitive interaction between CO and water. Indeed, CO, due to its polarity, interacts more strongly with the pores of the membrane than all the other gases considered. In addition, the relatively large size of CO (i.e., 0.376 nm, similar to the size of ultra-micropores) can also cause pore clogging, hindering permeance of water.

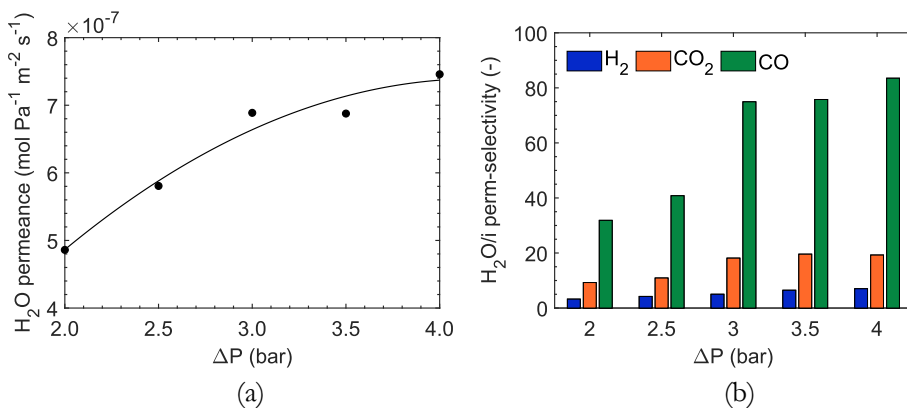


Figure 3.11. Water permeance (a) and ideal H₂O/*i* perm-selectivity (b) as a function of the gradient in total pressure measured at 150 °C for the CM08 membrane.

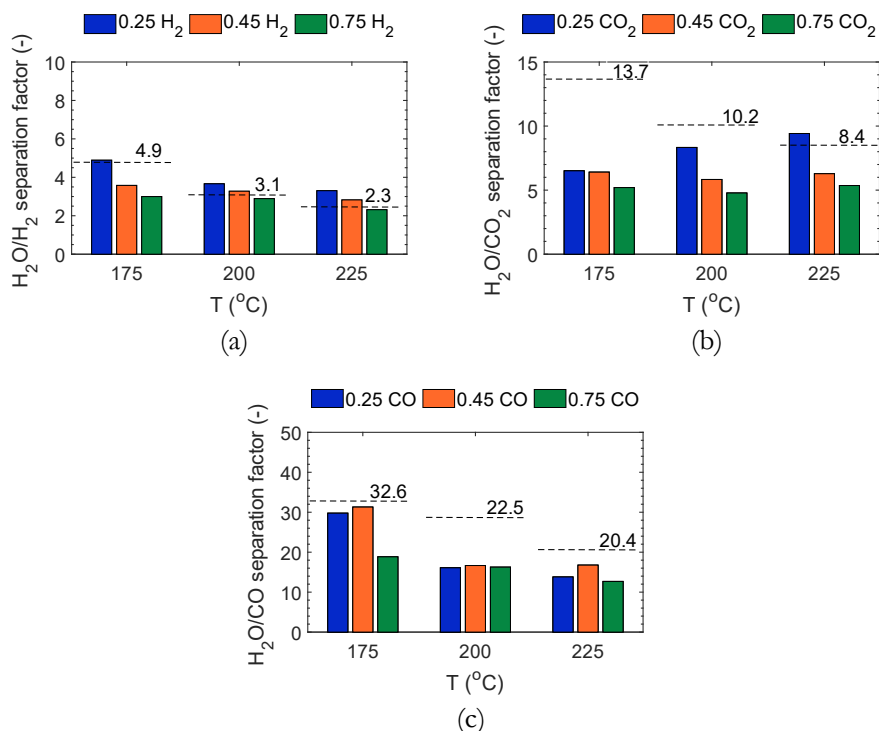


Figure 3.12. Separation factors of: a) the pair H₂O/H₂ (SF_{H_2O/H_2}), b) H₂O/CO₂ (SF_{H_2O/CO_2}) and c) H₂O/CO ($SF_{H_2O/CO}$) as a function of temperature and feed composition. The gradient in total pressure was set at 3 bar and the total flow through the membrane was 1 L·min⁻¹. A 10 % of N₂ was always included in the feed, to ensure the correct functioning of the C.E.M. Dashed lines indicate the ideal perm-selectivity of each H₂O/gas pair, measured at the same temperature.

3.4.6 Modeling results

In this section, the results obtained with the *6 flows model* are discussed. The routine that was implemented in MATLAB allowed to identify the flow mode at each pore size, by imposing the boundary conditions at the upstream and downstream side of the membrane pores (i.e., retentate and permeate) according to the experimental conditions. Therefore, the transport mechanisms of pure water through the pores and their relative occurrence are fully representative of the phenomena occurring at the pore scale. However, parameter fitting on the permeability data was required to derive properties of the complex porous structure of the carbon layer that could not be determined experimentally. First, the water transport phenomena were addressed by fitting the experimental data from the best performing membrane CM08. **Figure 3.13a** shows the result of the curve fitting of the ϕ_{H_2O} as a function of temperature (i.e., data reported in **Figure 3.8**). At 225 °C the curve shows a discontinuity which is ascribed to the evaporation of part of the capillary condensate at the downstream side (i.e., F₂ contribution starts to be relevant). The picture is even clearer when

looking at the frequency of each type of flow as a function of temperature (**Figure 3.13b**). In the lowest temperature range considered (i.e., 120 °C), the entire pore is filled with a capillary condensate and the upstream end of the pore is filled with bulk condensate. (i.e., F_5). As temperature increases from 120 °C to 180 °C, both pore ends are in contact with the bulk vapor phase (i.e., there is no bulk phase condensation of water at these conditions), while the entire pore remains filled with capillary condensate (i.e., F_3). In this case, the viscous flow of the capillary condensate is the dominant transport mechanism. Further increase in temperature above 180 °C shows a gradual transition to F_2 , where capillary condensation only occurs at the upstream end of the pore, while the downstream end contains gas and water adsorbate. Further, the model predicts that for temperature higher than 260 °C, the multi-layer adsorption diffusion (F_1) starts to contribute more significantly, although experimental validation beyond 240 °C is still required. The flow modes F_4 and F_6 do not show any contribution in the conditions explored experimentally (i.e., the conditions defining F_4 and F_6 reported in **Figure 3.2** do not occur). However, predictions beyond the range of the experimental conditions should be validated experimentally. In particular, the model becomes less accurate in predicting the transition to a different type of flow.

Next, the effect of pressure gradient across the membrane (ΔP) was assessed with the same model. To that end, the ϕ_{H_2O} data derived at different ΔP at 150 °C were simulated (**Figure 3.14**). According to the experimental results, no significant changes in the transport mechanism of water is observed in the range of pressure gradients explored in this study (i.e., F_5 is the dominant flow mode). Nevertheless, the model predicts a change in the flow mode when increasing the ΔP beyond 3.8 bar, which is very close to the last experimental point. According to this prediction, the ϕ_{H_2O} is expected to reach an asymptotic value, which unfortunately could not be validated experimentally due to the limitations of the experimental setup.

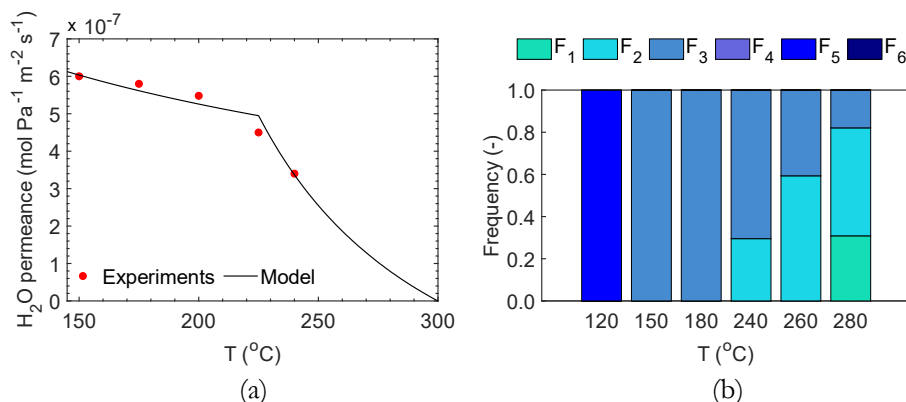


Figure 3.13. Comparison of the modeling and experimental results of the ϕ_{H_2O} as a function of temperature of the CM08 membrane (a). The experimental results reported in **Figure 3.8** (red circles) were fitted with the 6 flows model (continuous black line). The frequency of occurrence of each flow mode as a function of temperature is also reported (b).

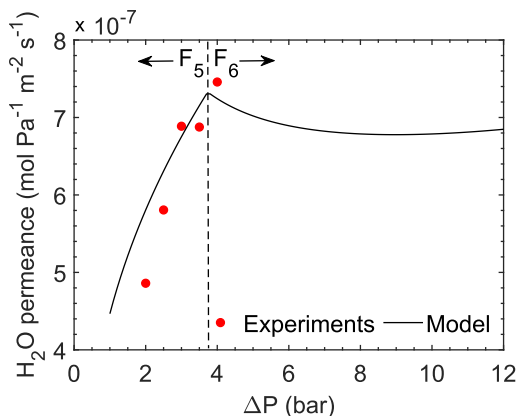


Figure 3.14. Comparison of the modeling and experimental results of the ϕ_{H_2O} as a function of pressure of the CM08 membrane. The experimental results reported in **Figure 3.11** (red circles) were fitted with the 6 flows model (continuous black line). The dominant flow mode is reported in the same figure: flow mode F_5 converge into flow mode F_6 at 3.8 bar (dashed line).

Finally, the ϕ_{H_2O} data as a function of temperature of all the membranes were fitted in the range 150 – 220 °C, where a semi-linear behavior of ϕ_{H_2O} was identified (details in Appendix B, section B.1). An interesting outcome of this curve fitting is the value of K_d , which is a geometrical factor that describes the structure of the porous system (i.e., larger K_d values represent a lower resistance to the transport). In particular, K_d plays a role in the flow mode F_3 (see **Table 3.2**), which is the dominant mechanism in the range of experimental conditions studied in this work.

Figure 3.15 shows the K_d values of all membranes tested, showing a linear inverse correlation with the boehmite content of the carbon membranes. This result support the hypothesis that the boehmite/alumina sheets alter the structure of the porous system, generally hindering the permeation of most of the species as the alumina content increases. Oftentimes this is explained by the formation of defects, which are zones where the permeation decreases because the species are forced to increase the path length (i.e., increase in tortuosity). This finding supports both the decrease in the permeability of the membranes prepared with higher boehmite content and the optimum found in the water permeability and perm-selectivity.

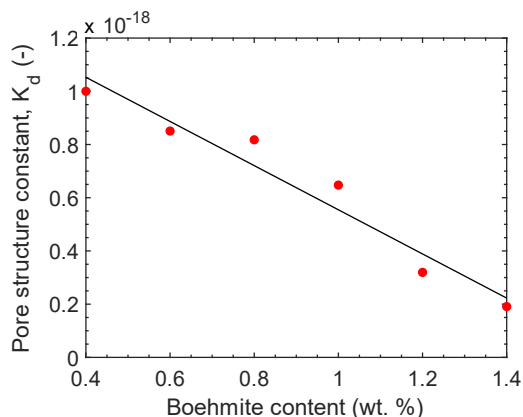


Figure 3.15. Pore structure constant (K_d) derived from the parameter fitting as a function of the boehmite content. Discrete values (red circles) were fitted with a linear regression (black line).

3.5 CONCLUSIONS

In this chapter, several boehmite-phenolic resin composite carbon molecular sieve membranes were prepared by the one dip-dry-carbonization step method, using different boehmite content in the dipping solution (ranging from 0.4 to 1.4 wt %). The membranes were tested in view of their application for the water-vapor separation in membrane reactors. The hydrophilic boehmite nanosheets were used as precursor of γ - Al_2O_3 to increase the adsorption of water and increase its transport mechanism by diffusion. We observed that the alumina content increases the hydrophilicity of the Al-CMSM up to an optimum at c.a. 1.0 wt %. At larger boehmite content the affinity to water decreases because: 1) the probability of boehmite condensation to the less hydrophilic γ - Al_2O_3 is higher and 2) the C:Al ratio corresponding to ca. 1.0 wt % of boehmite content maximizes the membrane properties. The alumina content does not significantly affect the pore size distribution of the membranes, at least in the region of micropores. On the other hand, the cross section of the Al-CMSMs show an increase in the thickness of the composite carbon layer for larger alumina content. The water permeability shows an optimum with the initial boehmite content around 0.8 wt %, which is in line with the increase in hydrophilicity of the membranes. For higher alumina content, the $\kappa_{\text{H}_2\text{O}}$ decreases. This decrease is induced both by a lower hydrophilicity and by a difference in the structure of the porous system (i.e., tortuosity and/or porosity), introduced by the boehmite/alumina sheets. Similarly, the ideal perm-selectivity of H_2O towards H_2 , CO_2 , CO , N_2 and CH_4 increases with the alumina content, showing an optimum with the C:Al ratio (i.e., initial boehmite content of 1.2 wt %). Among all the membranes tested in this study, the CM08 (i.e., membrane prepared with initial boehmite content of 0.8 wt %), show the best combination of H_2O permeability and perm-selectivity. A further investigation on the permeation properties of this membranes revealed that the H_2O /gas interaction plays an

important role in the vapor/gas separation. In particular, the CO₂ electrostatic interaction with water causes lower separation factors when measured from feed containing both H₂O and CO₂ (i.e., real separation factor). On the contrary, the SF_{H₂O/H₂} shows higher values with respect to the corresponding ideal perm-selectivity, due to the pore-blocking effect derived from the water capillary condensation in the pores. Lastly, the SF_{H₂O/CO} displays values lower than the ideal H₂O/CO perm-selectivity, especially at higher temperature. This behavior was ascribed to the possibility of CO to clog some of the pores where water has not yet adsorbed or condensed. In general, it was found that the $\phi_{\text{H}_2\text{O}}$ and H₂O/*i* selectivity decrease with temperature and increase with ΔP . The *6 flows model* indicates that the water vapor flow through the carbon pores transforms from capillary condensation to multi- and monolayer surface flow combined with molecular Knudsen gas flow, as temperature increases. When increasing the applied pressure difference at 150 °C, the water vapor permeance becomes higher, indicating the role of capillary condensation. However, the model predicts an asymptotic behavior for ΔP of approximately 3.8 bar.

In conclusion, this work shows that the composite alumina supported CMSM are promising material for the water separation from gaseous mixtures at relatively high temperatures (i.e., 150-250 °C), conditions which are compatible with the CO₂ conversion to methanol and/or DME reactions. Their separation performance, combined with the high stability of these materials, make these membrane very good candidates for their use in membrane reactors where the in in-situ removal of water is required.

Appendix B

B.1 Theory of water transport through the CMSM

The permeation through porous media can be categorized in three different types: gas flow, surface flow and capillary condensate flow. Details are given in this section.

Gas flow

$$F_g = -\frac{8Nr_p^3}{3\tau\sqrt{2\pi M_w RT}} \frac{dP}{dx} = -\frac{A_p G_1}{\sqrt{2\pi M_w RT}} \frac{dP}{dx} \quad (B.1)$$

Where the number of pores (N), the pore radius (r_p) and tortuosity (τ) are collected in the cross-sectional area of the porous material (A_p) and the geometric constant (G_1). Other parameters include the molecular weight (M_w), the ideal gas constant (R) and the absolute temperature (T). The permeability of the porous material is expressed as:

$$Q_g = \frac{F_g L_p}{A_p \Delta P} = \frac{G_1}{\sqrt{2\pi M_w RT}} \quad (B.2)$$

Where the thickness of the porous medium (L_p) and the pressure difference (ΔP) are included. The reduction of the available pore space decreases the permeability. By defining the gas phase permeability of blocked (Q'_g) and unblocked (Q_g) media, a relation can be derived from an adsorption isotherm:

$$\frac{Q'_g}{Q_g} = \left(\frac{r_e}{r_p}\right)^3 = \left(\frac{r_p - t}{r_p}\right)^3 \quad (B.3)$$

Where the effective pore radius (r_e) represents the radius of a blocked pore of radius r_p , when a film of adsorbed layer of thickness t deposits on the pore walls.

Surface flow

$$F_s = \frac{A_p RT}{C_R S_t} \frac{\rho_{app}}{\tau^2 L_p} \int_{p_2}^{p_1} \frac{x^2}{p_g} dp_g \quad (B.4)$$

Where C_R is the coefficient of resistance, S_t specific surface area of the porous media and ρ_{app} the apparent density of the porous material. The corresponding permeability is defined as follows:

$$Q_g = \frac{F_s L_p}{A_p \Delta P} = \frac{RT \rho_{app}}{C_R S_t \tau^2} \frac{x^2}{p} \quad (B.5)$$

Capillary condensate flow

The capillary condensation pressure (P_t) is calculated from the Kelvin equation:

$$\frac{\rho RT}{M_w} \ln \left(\frac{P_t}{P_s} \right) = - \frac{2\sigma \cos \theta}{r_p} \quad (\text{B.6})$$

The overall hydrostatic pressure (i.e., driving force for the capillary condensate flow), is given by:

$$\Delta P_c = \frac{\rho RT}{M_w} \left[\ln \left(\frac{P_{ret}}{P_s} \right) - \ln \left(\frac{P_{perm}}{P_s} \right) \right] = \frac{\rho RT}{M_w} \ln \left(\frac{P_{ret}}{P_{perm}} \right) \cong \frac{\rho RT}{M_w P_m} \Delta p_g \quad (\text{B.7})$$

Where P_m is the mean gas pressure and Δp_g is the pressure difference across the membrane. The transport of the capillary condensate can be regarded as a viscous flow through the porous media. For this type of flow, Darcy's equation can be applied:

$$F_c = A_p \frac{K_d dP_c}{\eta dl} = A_p \frac{K_d}{\eta} \frac{\rho RT}{M_w P_m} \frac{dp_g}{dl} = Q_c \frac{dp_g}{dl} \quad (\text{B.8})$$

Where K_d is the pore structure constant, η is the viscosity of the condensate and Q_c is the condensate permeability. This expression can only be used when the pore space is completely filled with capillary condensate. When the film thickness of the adsorbed layer is significant with respect to the pore size, a correction must be applied. The effective capillary pressure can be obtained with an "adjusted" Kelvin equation, as follows:

$$P_{c,eff} = \frac{(r_p - t)^2}{r_p^2} \frac{\rho RT}{M_w} \ln \left(\frac{P_t}{P_s} \right) \quad (\text{B.9})$$

The effective capillary pressure drop becomes:

$$\Delta P_{c,eff} = \frac{\rho RT}{M_w} \left[\frac{(r_p - t_1)^2}{r_p^2} \ln \left(\frac{P_{ret}}{P_s} \right) - \frac{(r_p - t_2)^2}{r_p^2} \ln \left(\frac{P_{perm}}{P_s} \right) \right] \quad (\text{B.10})$$

As a consequence, the expression of the "actual" capillary condensate flow becomes:

$$F_c = A_p \frac{K_d}{\eta} \frac{\rho RT}{M_w P_m} \left[\frac{(r_p - t_1)^2}{r_p^2} \ln \left(\frac{P_{ret}}{P_s} \right) - \frac{(r_p - t_2)^2}{r_p^2} \ln \left(\frac{P_{perm}}{P_s} \right) \right] \quad (\text{B.11})$$

Pore size distribution

The pore size distribution of the carbon membranes was fitted with an asymmetric double sigmoidal function (Asym2Sig) described as follows:

$$f(r) = f_0 + \frac{A_f}{1 + \exp \left(\frac{r_p - r_{pc} + w_1/2}{w_2} \right)} \cdot \left(1 - \frac{1}{\exp \left(\frac{r_p - r_{pc} + w_1/2}{w_3} \right)} \right) \quad (\text{B.12})$$

Where A_f , r_{pc} , w_1 , w_2 and w_3 are the parameters for the Asym2Sig fitting.

Water adsorption isotherms

The amount of adsorbed water (x) is an important variable that contributes to the surface flow of water. Water adsorption isotherms were obtained for 80, 150 and 250 °C for the CM08 membrane (the experimental data are not reported in this work). The isotherms were fitted with the following equation (Langmuir-type isotherm):

$$x = \frac{abP^{1-c}}{1 + bP^{1-c}} \quad (\text{B.13})$$

Where the parameters a , b and c fit the H₂O adsorption (x) as a function of pressure (P) at various temperatures. The experimental data, together with the curves obtained from the fitting, are reported in **Figure B1**.

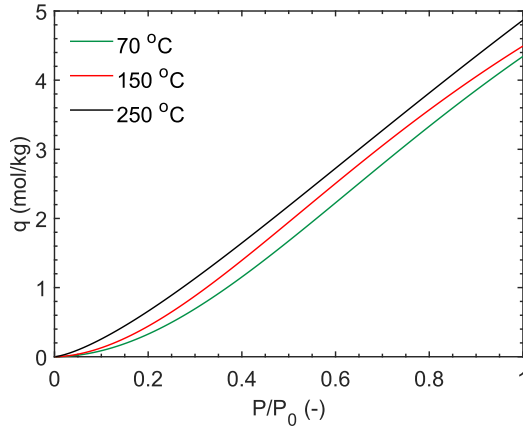


Figure B1. Water adsorption isotherms at 70, 150 and 250 °C of the CM08 represented by Langmuir-type isotherm curves.

Estimation of water physical properties

The saturation vapor pressure of water is given by the following correlation:

$$P_s = \exp(A + BT^{-1} + C \ln(T) + DT^E) \quad (\text{B.14})$$

The surface tension was calculated as follows:

$$\sigma = A(1 - T_r)^{B+CT_r+DT_r^2+ET_r^3} \quad (\text{B.15})$$

Where T_r is the dimensionless temperature, defined as T/T_c , with T_c the critical temperature of water (647.1 K). The vapor density of H₂O was computed as follows:

$$\rho_g = \frac{2 \frac{P}{RT}}{1 + \sqrt{1 + \frac{4PB_2}{RT}}} \quad (\text{B.16})$$

$$B_2 = A + BT^{-1} + CT^{-3} + DT^{-8} + ET^{-9} \quad (\text{B.17})$$

The viscosity of vapor and liquid water were calculated according to Eq. B.18 and B.19, respectively.

$$\eta_v = \frac{AT^B}{1 + \frac{C}{T} + \frac{D}{T^2}} \quad (\text{B.18})$$

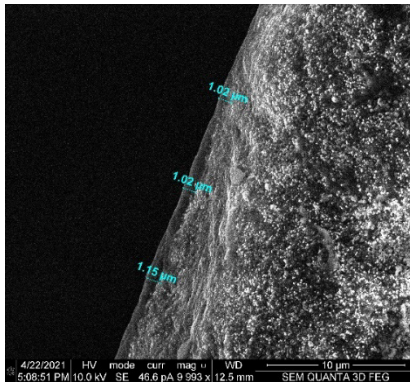
$$\eta_l = \frac{AT^B}{1 + \frac{C}{T} + \frac{D}{T^2}} \quad (\text{B.19})$$

The parameters A, B, C, D and E, used in the correlations are reported in **Table B1**. All the properties determined with these correlations were obtained in the S.I. units.

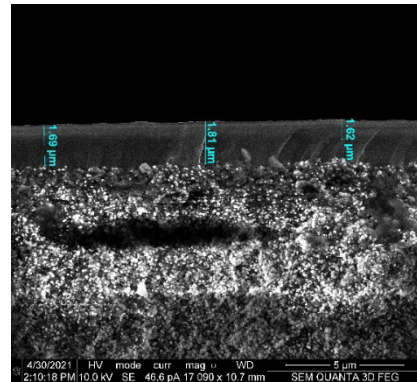
Table B1. Parameters used for the correlations of the physical properties of water.

Correlation	<i>A</i>	<i>B</i>	<i>C</i>	<i>D</i>	<i>E</i>
P_s	73.649	-7258.2	-7.3037	$4.165 \cdot 10^{-6}$	2
σ	0.1776	2.567	-3.3377	1.9699	-
B_2	0.02222	-26.38	$-1675 \cdot 10^4$	$-3.89 \cdot 10^{19}$	$3.13 \cdot 10^{21}$
η_l	-52.843	3703.6	5.866	-5.8810^{-29}	10
η_v	$1.71 \cdot 10^{-8}$	1.1146	-	-	-

B.2 Supplementary figures



(a)



(b)

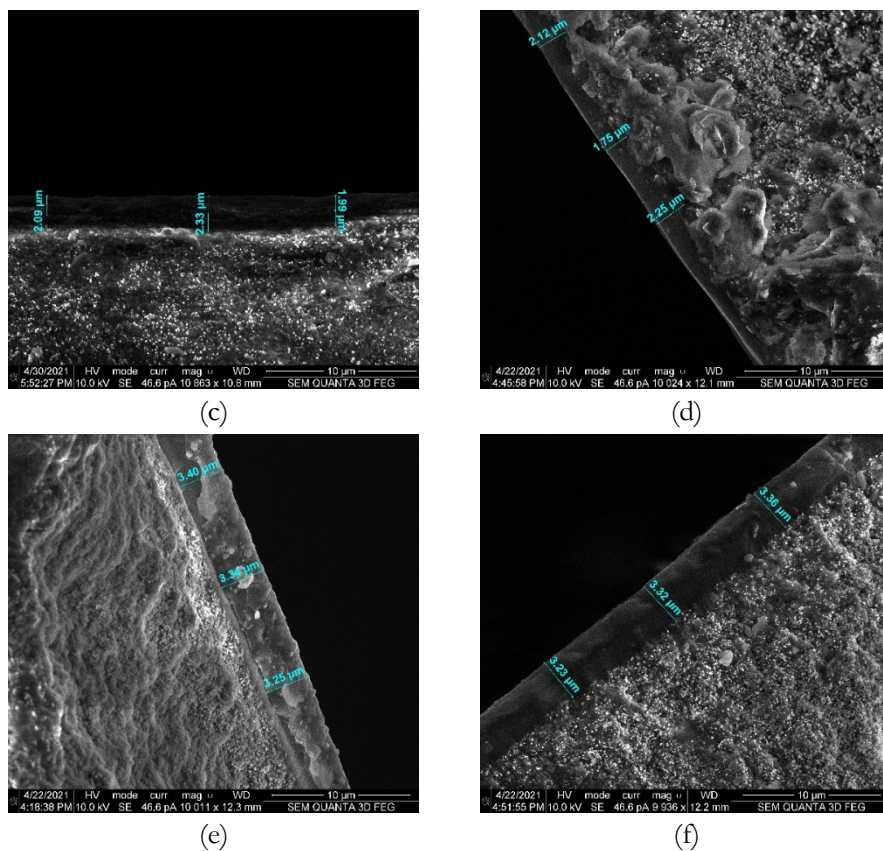
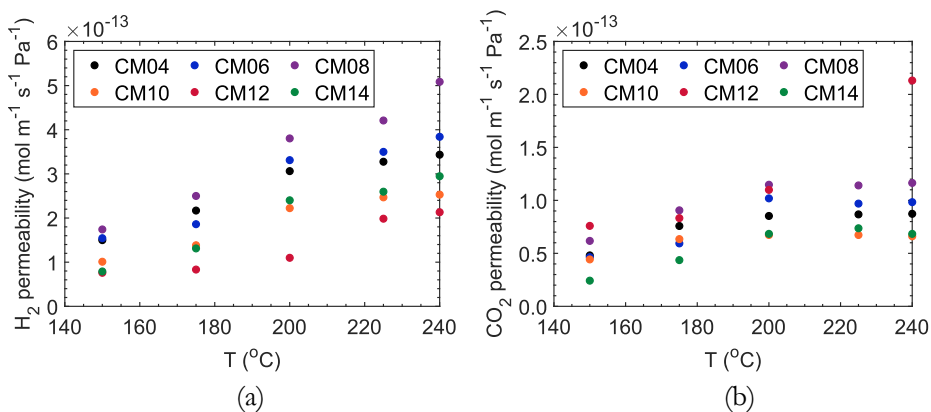


Figure B2. Thickness of the carbon layer of the CM04 (a), CM06 (b), CM08 (c), CM10 (d), CM12 (e) and CM14 (d) measured on the images of the cross section of the membranes acquired with a FEI Quanta scanning electron microscope.



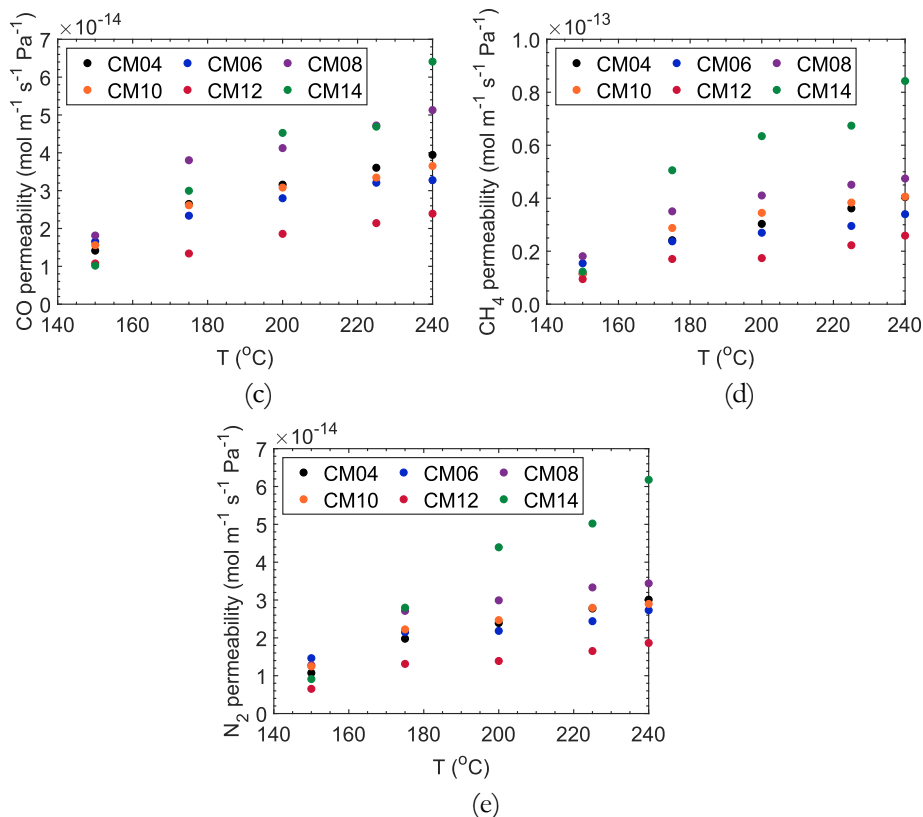


Figure B3. Pure gas permeability of H₂ (a), CO₂ (b), CO (c), CH₄ (d) and N₂ (e) as a function of the temperature of permeation for the Al-CMSMs prepared with different amount of boehmite. Other experimental conditions: $\Delta P=3$ bar, 1 L·min⁻¹ feed flow of pure gas.

The complete XPS spectra of the carbon films prepared with 0.8, 1.0 and 1.4 wt % of boehmite are reported in **Figure B4**, together with the spectra recorder on the carbon film prepared with 0.8 wt % of boehmite, prior to the carbonization, to confirm the absence of any chemical interaction between C and Al during the carbonization.

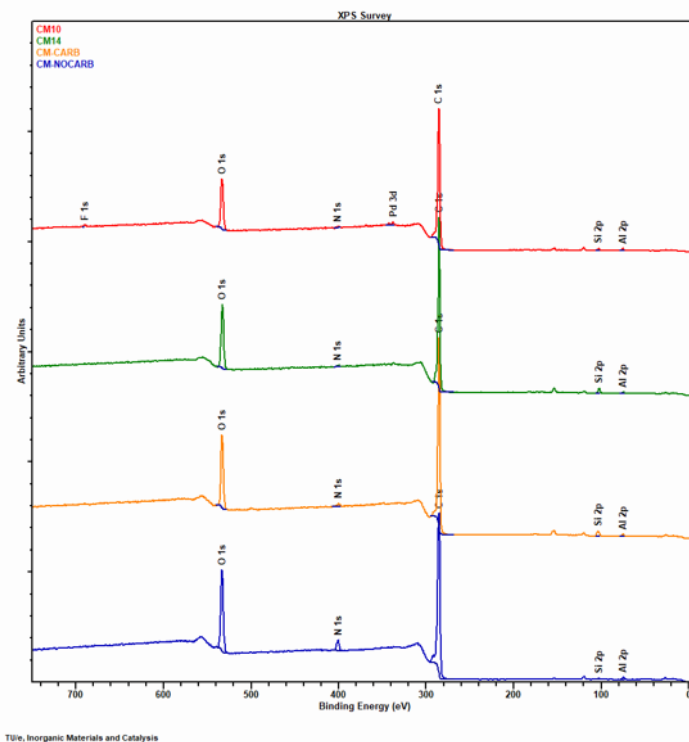


Figure B4. XPS spectra of the carbon film prepared with 1.0 wt% of boehmite (CM10), 1.4 wt% (CM14), 0.8 wt % (CM-CARB) and the corresponding sample prior to the carbonization (CM-NOCARB).

B.3 Permporometry setup

The setup used for the permporometry measurement was developed at the Sustainable Process Engineering group (SPE) of Eindhoven University of Technology (TU/e). The flow diagram of the setup is reported in **Figure B5**. The N_2 gas feed is separated in two lines: 1) the dry gas feed and 2) the “humidified” gas feed, which is meant to push the water in the reactor. The two flows are regulated by two distinct mass flow controller. Liquid demineralized water is injected with a syringe pump to an evaporator cell and pushed to the membrane section via a small N_2 flow (i.e., the “humidified” gas feed). The membrane under study is placed in a double shell reactor tube which is in turn placed in an electrically heated oven. The permeate is cooled down in a condenser, to remove the H_2O vapor. The nitrogen permeate is measured with a film flow meter (HoribaStec). By adjusting the water flow rate from the syringe pump, the relative humidity can be altered. The nitrogen permeation was measured at each relative humidity. When both the water adsorption and desorption is measured with the permporometry setup, the thickness of the adsorbed water layer can be determined with the hysteresis method.

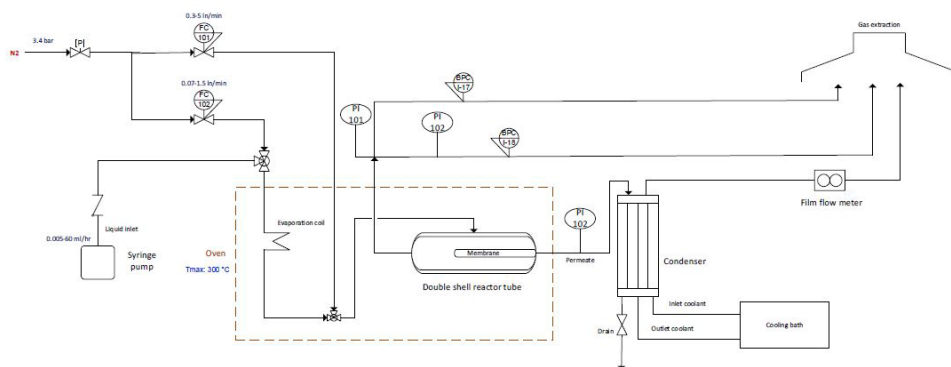


Figure B5. Flow diagram of the permeometry setup developed at SPE group of TU/e

REFERENCES

- [1] F. Pontzen, W. Liebner, V. Gronemann, M. Rothaemel, and B. Ahlers, "CO₂-based methanol and DME - Efficient technologies for industrial scale production," *Catal. Today*, vol. 171, no. 1, pp. 242–250, 2011,
- [2] P. Applications, "State of the Art and Perspectives of CO₂ Methanation Process Concepts for State of the Art and Perspectives of CO₂ Methanation Process Concepts for Power-to-Gas Applications," no. January, 2014.
- [3] A. F. Ismail and L. I. B. David, "Future direction of R and D in carbon membranes for gas separation," *Membr. Technol.*, no. 4 APRIL, pp. 4–7, 2003,
- [4] S. C. Rodrigues, M. Andrade, J. Moffat, F. D. Magalhães, and A. Mendes, "Carbon Membranes with Extremely High Separation Factors and Stability," *Energy Technol.*, vol. 7, no. 4, pp. 1–7, 2019,
- [5] A. F. Ismail and L. I. B. David, "A review on the latest development of carbon membranes for gas separation," *J. Memb. Sci.*, vol. 193, no. 1, pp. 1–18, 2001,
- [6] S. M. Saufi and A. F. Ismail, "Fabrication of carbon membranes for gas separation - A review," *Carbon N. Y.*, vol. 42, no. 2, pp. 241–259, 2004,
- [7] A. B. Fuertes, "Adsorption-selective carbon membrane for gas separation," *J. Memb. Sci.*, vol. 177, no. 1–2, pp. 9–16, 2000,
- [8] L. Forster *et al.*, "Tailoring pore structure and surface chemistry of microporous Alumina-Carbon Molecular Sieve Membranes (Al-CMSMs) by altering carbonization temperature for optimal gas separation performance: An investigation using low-field NMR relaxation measurements," *Chem. Eng. J.*, p. 129313, 2021,
- [9] J. B. S. Hamm, A. Ambrosi, J. G. Griebeler, N. R. Marcilio, I. C. Tessaro, and L. D. Pollo, "Recent advances in the development of supported carbon membranes for gas separation," *Int. J. Hydrogen Energy*, vol. 42, no. 39, pp. 24830–24845, 2017,
- [10] M. Kiyono, P. J. Williams, and W. J. Koros, "Effect of pyrolysis atmosphere on separation performance of carbon molecular sieve membranes," *J. Memb. Sci.*, vol. 359, no. 1–2, pp. 2–10, 2010,
- [11] J. Gilron and A. Soffer, "Knudsen diffusion in microporous carbon membranes with molecular sieving character," *J. Memb. Sci.*, vol. 209, no. 2, pp. 339–352, 2002,
- [12] "Transport mechanism of carbon membranes . Carbon-based membr . Sep . Process," no. 2011, p. 2021, 2021.
- [13] M. A. Llosa Tanco, J. A. Medrano, V. Cechetto, F. Gallucci, and D. A. Pacheco Tanaka, "Hydrogen permeation studies of composite supported alumina-carbon molecular sieves membranes: Separation of diluted hydrogen from mixtures with methane," *Int. J. Hydrogen Energy*, no. xxx, 2020,
- [14] R. J. R. Uhlhorn, K. Keizer, and A. J. Burggraaf, "Gas transport and separation with ceramic membranes. Part I. Multilayer diffusion and capillary condensation," *J. Memb. Sci.*, vol. 66, no. 2–3, pp. 259–269, 1992,

- [15] K. H. Lee and S. T. Hwang, “The transport of condensible vapors through a microporous vycor glass membrane,” *J. Colloid Interface Sci.*, vol. 110, no. 2, pp. 544–555, 1986,
- [16] T. Horikawa, D. D. Do, and D. Nicholson, “Capillary condensation of adsorbates in porous materials,” *Adv. Colloid Interface Sci.*, vol. 169, no. 1, pp. 40–58, 2011,
- [17] L. Fisher, R. Gamble, and J. Middlehurst, “The Kelvin equation and capillary condensation,” *Nature*, vol. 290, no. April, pp. 575–576, 1981, [Online]. Available: <https://www.nature.com/articles/290575a0.pdf>
- [18] C. W. Jones and W. J. Koros, “Characterization of Ultramicroporous Carbon Membranes with Humidified Feeds,” *Ind. Eng. Chem. Res.*, vol. 34, no. 1, pp. 158–163, 1995,
- [19] S. Lagorsse, F. D. Magalhães, and A. Mendes, “Aging study of carbon molecular sieve membranes,” *J. Memb. Sci.*, vol. 310, no. 1–2, pp. 494–502, 2008,
- [20] H. H. Tseng, P. T. Shiu, and Y. S. Lin, “Effect of mesoporous silica modification on the structure of hybrid carbon membrane for hydrogen separation,” *Int. J. Hydrogen Energy*, vol. 36, no. 23, pp. 15352–15363, 2011,
- [21] M. Teixeira *et al.*, “Boehmite-phenolic resin carbon molecular sieve membranes-Permeation and adsorption studies,” *Chem. Eng. Res. Des.*, vol. 92, no. 11, pp. 2668–2680, 2014,
- [22] M. A. Llosa Tanco, D. A. Pacheco Tanaka, S. C. Rodrigues, M. Teixeira, and A. Mendes, “Composite-alumina-carbon molecular sieve membranes prepared from novolac resin and boehmite. Part I: Preparation, characterization and gas permeation studies,” *Int. J. Hydrogen Energy*, vol. 40, no. 16, pp. 5653–5663, 2015,
- [23] M. A. Llosa Tanco, D. A. Pacheco Tanaka, and A. Mendes, “Composite-alumina-carbon molecular sieve membranes prepared from novolac resin and boehmite. Part II: Effect of the carbonization temperature on the gas permeation properties,” *Int. J. Hydrogen Energy*, vol. 40, no. 8, pp. 3485–3496, 2015,
- [24] C. W. Jones and W. J. Koros, “Carbon Composite Membranes;,” pp. 164–167, 1995.
- [25] T. Tsuru, T. Hino, T. Yoshioka, and M. Asaeda, “Permporometry characterization of microporous ceramic membranes,” vol. 186, pp. 257–265, 2001.
- [26] R. J. R. Uhlhorn, K. Keizer, and A. J. Burggraaf, “Gas transport and separation with ceramic membranes. Part II. Synthesis and separation properties of microporous membranes,” *J. Memb. Sci.*, vol. 66, pp. 271–287, 1992.
- [27] H. Rhim and S. tak Hwang, “Transport of capillary condensate,” *J. Colloid Interface Sci.*, vol. 52, no. 1, pp. 174–181, 1975,
- [28] S. López-Romero and J. Chávez-Ramírez, “Synthesis of TiC thin films by CVD from toluene and titanium tetrachloride with nickel as catalyst,” *Matéria (Rio Janeiro)*, vol. 12, no. 3, pp. 487–493, 2007,
- [29] X. Zhang, M. Honkanen, E. Levänen, and T. Mäntylä, “Transition alumina nanoparticles and nanorods from boehmite nanoflakes,” *J. Cryst. Growth*, vol. 310,

- no. 15, pp. 3674–3679, 2008,
- [30] G. Paglia *et al.*, “Boehmite Derived γ -Alumina System. 1. Structural Evolution with Temperature, with the Identification and Structural Determination of a New Transition Phase, γ' -Alumina,” *Chem. Mater.*, vol. 16, no. 2, pp. 220–236, 2004,
- [31] I. Strawbridge and P. F. James, “The factors affecting the thickness of sol-gel derived silica coatings prepared by dipping,” *J. Non. Cryst. Solids*, vol. 86, no. 3, pp. 381–393, 1986.
- [32] P. K. Senapati, B. K. Mishra, and A. Parida, “Modeling of viscosity for power plant ash slurry at higher concentrations: Effect of solids volume fraction, particle size and hydrodynamic interactions,” *Powder Technol.*, vol. 197, no. 1–2, pp. 1–8, 2010,
- [33] *et al.* Abraham, Jiji, “Rheological percolation in thermoplastic polymer nanocomposites,” *Rheol open access*, vol. 1, pp. 1–15, 2017.
- [34] J. A. Medrano, M. A. Llosa-Tanco, D. A. Pacheco-Tanaka, and F. Gallucci, *Transport mechanism and modeling of microporous carbon membranes*. Elsevier Inc., 2019.
- [35] M. P. Rohde, G. Schaub, S. Khajavi, J. C. Jansen, and F. Kapteijn, “Fischer-Tropsch synthesis with in-situ H₂O removal - Directions of membrane development,” *Microporous Mesoporous Mater.*, vol. 115, no. 1–2, pp. 123–136, 2008,
- [36] S. Poto, F. Gallucci, and M. F. Neira, “Direct conversion of CO₂ to dimethyl ether in a fixed bed membrane reactor : Influence of membrane properties and process conditions,” *Fuel*, vol. 302, no. February, p. 121080, 2021,
- [37] J. E. Koresh and A. Soffer, “Mechanism of Permeation through Molecular-sieve Carbon Membrane,” *J. Chem. Soc.*, vol. 82, pp. 2057–2063, 1986.

CHAPTER 4

Vapor/gas separation through carbon molecular sieve membranes (CMSM). Part II: effect of the carbonization temperature

Abstract

This chapter assesses the effect of the carbonization temperature (450-750 °C) on the performance of supported CMSM in terms of vapor/gas separation, in correlation with changes in their surface functionality and porous structure. FTIR spectra showed that the nature of the functional groups changes with the evolution of the carbonization step, leading to a gradual loss in hydrophilicity (i.e., OH stretching disappears at $T_{\text{carb}} \geq 600$ °C). The extent of water adsorption displays an optimum at T_{carb} of 500 °C, with the hydrophilicity decreasing for higher carbonization temperature. However, the pore size distribution was found to strongly influence the water permeance more than the hydrophilicity. At all T_{carb} , adsorption-diffusion (AD) is the dominant transport mechanisms. However, as soon as ultra-micropores appear (T_{carb} : 600-700 °C) molecular sieving (MS) contributes to an increase in the water permeance, despite a loss in hydrophilicity. At $T_{\text{carb}} \geq 750$ °C, MS pores disappear, causing a drop in the water permeance. Finally, similarly to water, the permeance of different gases (N_2 , H_2 , CO , CO_2) is mostly affected by the pore size distribution, with MS being the dominant mechanism over the AD, except for CO_2 . However, the extent and mechanism of gas permeation drastically change as a function of the water content in the feed, indicating that gas/vapor molecules need to compete to access the pores of the membranes.

This chapter is based on the following paper:

Poto, S., Aguirre, A., Huigh, F., Llosa-Tanco, M. A., Pacheco-Tanaka, D. A., Gallucci, F., & Neira d'Angelo, M. F. (2023). Carbon molecular sieve membranes for water separation in CO_2 hydrogenation reactions: effect of the carbonization temperature. *Journal of Membrane Science*, 677, 121613.

4.1 INTRODUCTION

A very important and easy-to-tune parameter in the synthesis procedure of carbon membranes is the carbonization temperature (T_{carb}). Jones and Koros stated that the expansion of the gaseous products of the pyrolysis step causes a rearrangement of the polymeric structure, which corresponds to the formation of the porous system [1]. Fuertes et al. reported the gradual transformation of the porous polymer-carbon structure into dense carbon upon increasing the carbonization temperature [2], [3]. They observed that micropores starts forming at 500 °C. At temperature of 600-700 °C, more pores appear, and some of the previously formed micropores tend to shrink due to sintering, leading to the formation of ultra-micropores. This shift in the nature of the membrane pores led to higher permeability, as well as to lower perm-selectivity for a given separation. When the carbonization temperature is increased even further (i.e., 850-950 °C), the density of the carbon increases due to the graphitization, leading again to lower permeability and higher selectivity [4].

The effect of the carbonization temperature on the pore size distribution of Novolac-based CMSM was studied more recently by Llosa et al. [5]. They found that the membrane carbonized at 450 °C reveals a small number of pores in the range 0.4-0.9 nm, with an average pore size at 0.65 nm. Increasing the T_{carb} to 550 °C results in a larger number of pores and a pore size distribution still centered at 0.65 nm, but narrower (0.45-0.8 nm). The most significant changes occur at 600-650 °C where the number of pores increases significantly with a bi-disperse pore size distribution showing pores both in the MS and AD region. Increasing the T_{carb} even further (i.e., 700-750 °C), the porous system starts to shrink starting from the pores in the AD region. Thus, the membrane carbonized at 750 °C displays less pores, mostly in the MS region (0.35-0.45 nm).

The carbonization temperature has also been proven to affect the hydrophilicity of the membranes. Forster et al. [6] recently reported that when T_{carb} increases above 600 °C, most of the oxygen-based groups are removed, leading to a monotonic decrease of the membrane interaction with the water. However, their analysis did not cover the low carbonization temperature region, where most of the changes in the surface functionalities are expected to occur. Thus, this chapter proposes a detailed investigation of the changes in terms of surface chemistry, hydrophilicity and pore size distribution that phenolic-formaldehyde resin CMSMs undergo with the progression of the carbonization temperatures in the range 450-750 °C. FTIR analysis is used to identify the transformation of the functional groups of the carbon membrane, to gain insights into the pyrolysis mechanism. Thereafter, in-situ FTIR analysis during water adsorption/desorption steps is used to assess the surface interaction with water, as well as the membrane hydrophilicity, as a function of the carbonization temperature. Thermogravimetric analysis is then performed to assess the membrane affinity to different type of gases (i.e., CO₂, CO and H₂). Finally, permeation tests carried out in the range 150-250 °C with H₂O, methanol, H₂, N₂, CO₂ and CO are used to understand the interplay of the hydrophilicity and pore size distribution on the membrane performance. The objective of this chapter is to assess

how the carbonization temperature affects the vapor/gas separation performance of CMSMs, in view of their application in membrane reactors for the in-situ removal of water.

4.2 EXPERIMENTAL

4.2.1 Synthesis of Al-CMSMs

The tubular supported Al-CMSMs were synthesized via the exact same procedure reported in Chapter 3. Tubular asymmetric α -Al₂O₃ tubes (ID: 7 mm, OD: 10 mm), with a 100 nm average pore size from Inopor® were used as support. The dipping solution was prepared with: 13 wt % of Novolac resin, 0.6 wt % of ethylenediamine, 2.4 wt % of formaldehyde, 0.8 wt % of 10 wt % aqueous dispersion of boehmite nanosheets with a particle size of 8-20 nm (*Alumisol* provided by Kawaken fine Chemicals) and *N*-methyl-2-pyrrolidone (NMP) as solvent. The Al-CMSM membranes were dried at 90 °C and carbonized in a temperature range from 450 to 750 °C, following the procedure reported Chapter 3. The remaining precursor solution was used to prepare unsupported membrane films carbonized at different temperatures as the Al-CMSMs, with the same procedure used for the supported membranes.

4.2.2 FTIR analysis

The CMSM surface of as prepared and treated samples was studied by DRIFT spectroscopy to identify the main functional groups which are relevant for the permeation. The adsorption of water was studied using a Harrick DRIFT cell. Time-resolved infrared spectra (up to 1 spectrum/0.39 s) were recorded at a resolution of 4 cm⁻¹ using an FTIR spectrometer (Thermo iS50 with a cryogenic MCT detector). The CO₂ and water vapour contributions from the atmosphere to the spectra were eliminated by purging continuously with purified air (Parker Balston FTIR purge gas generator) on the bench of the spectrometer and the optical path. The gas flow was regulated using mass flow meters (Cole-Parmer). The entrance of the gases was controlled by a flow-through 10-ways valve electronically actuated (Vici-Valco) synchronized with the FTIR. The gas composition at the exit of the cell was analyzed by mass spectrometry (Prisma QMG220, Pfeiffer). Water (2%) in He was obtained from a gas saturator filled with pure water immerse into a thermostatic bath.

The cell was filled with 50 mg of unsupported carbon membrane sample. Before the experiments, the sample was treated by flowing He (300 °C, 1 h, 5 °C/min), and then cooling down to 30 °C. The adsorption of water (2%)/He (50 mL/min) was performed at 30 °C. Next, the desorption of water was studied by changing from 2% water to pure He. After the adsorption/desorption experiments, the samples were heated to 300 °C (5 °C/min).

4.2.3 Thermogravimetric analysis

The adsorption of gases (CO₂, H₂ and CO) by the membrane was studied via thermogravimetric analysis (TGA). The TGA setup (**Figure 4.1**) consists of a microbalance (MK2-5 M from CI-Precision) with a sensitivity of 1 µg. The balance (M) is kept at a constant temperature and in an inert atmosphere (i.e., N₂ is fed at 0.5 L/min via FC101) to prevent any contamination from reactive gases. The balance is attached via a platinum wire to a porous Al₂O₃ basket (0.5 cm d x 1.5 cm l) in which the solid sample can be loaded. The basket is then placed in a ceramic tube (ID 15 mm) which is then surrounded by a stainless-steel vessel and heated via an electric oven. The oven is controlled via thermocouple placed in the proximity of the basket, to guarantee a stable and isothermal operation. The relevant gases are fed from gas cylinders by means of mass flow controllers (FC), while pressure is regulated using a back pressure regulator (BPC) from Bronkhorst. To conduct the analysis ca. 40 mg of unsupported carbon membrane sample were loaded into the basket and placed in the TGA system. Prior to any analysis, a pre-treatment was carried out to remove any adsorbed water from the atmosphere: the sample was heated up to 300 °C, at ambient pressure, under a N₂ flow of 0.5 L/min and kept at these conditions for 1h [7]. After the pre-treatment, the system was cooled down to the desired temperature (i.e., 200 °C) under N₂ flow. Afterwards, the analysis gas was fed at flow rate of 0.5 L/min and the pressure was increased progressively up to 10 bar. An equilibration time of 40 min at each pressure point was guaranteed to allow the sample to achieve stable weight due to the adsorption phenomena. Blank tests were carried out with the empty basket using the same procedure described above, to correct for the buoyance forces exerted by the feeding gases on the basket. During the analysis the weight of the sample and basket was recorded every 5s. However, only steady state values (w_{ss}) were used to determine the weight variation (Δw) related to the adsorption phenomena, as reported in Eq. 4.1-4.2.

$$\Delta w = w_{ss} - w_0 \quad (4.1)$$

$$\Delta w_{\text{corrected}} = \frac{\Delta w_{\text{sample}} - \Delta w_{\text{blank}}}{w_{\text{sample},0}} \cdot 100 \% \quad (4.2)$$

Where w_0 is the initial weight of either the sample (after pre-treatment) or the empty basket and $\Delta w_{\text{corrected}}$ is the net percentage weight increase of the sample due to the adsorption of gases.

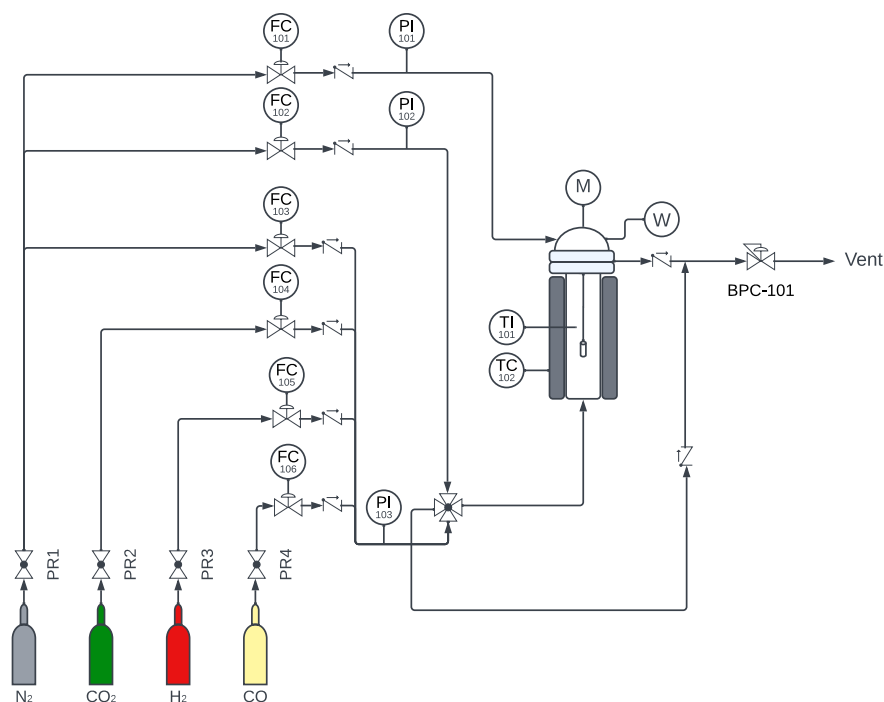


Figure 4.1. Schematic representation of the TGA setup, where FC, PI, TI, TC indicates mass flow controller, pressure meters, temperature indicators and temperature controllers, respectively. BPC represents the back pressure regulator, M the micro-scale and W the weight indicator.

4.2.4 Permeation experiments

The permeation experiments were carried out in a dedicated setup already described in Chapter 3, along with the adopted experimental procedure. All the permeation experiments were carried out at a temperature of 150-250 °C, a pressure gradient across the membrane (ΔP) of 3 bar and a total feed flow of 1 L·min⁻¹.

To derive the water and methanol permeance, the membrane was exposed to a flux of either water or methanol, containing 7.5 vol. % of N₂, as required by the Controlled Evaporator Mixer (C.E.M.). After 40 min (i.e., steady state), the N₂ permeated flow was measured, and the water/methanol was collected and weighted from both the retentate and the permeate side.

The permeance of the gases (i.e., N₂, CO₂, H₂ and CO) was measured in three different conditions: 1) through a humid membrane; 2) through a dry membrane; 3) exposing the membrane to a binary mixture of water and each gas. In the first case, a pure gas flow was fed to the membrane which was prior exposed to water vapor at the same temperature and pressure of the permeation experiment. In the second

case, the membrane was first dried overnight at 250 °C under N₂ flow to remove all the adsorbed water and then exposed to a pure gas flow. In the third case, an equimolar mixture of water vapor and one of the gases of interest was fed to the membrane, with a total feed flow of 1 L·min⁻¹. After 40 min, as in the vapor permeation tests, the gas permeated flow was measured and the water was condensed, collected and weighted from both the permeate and retentate side.

The vapor and gas permeances were calculated as reported in Chapter 3.

4.2.5 Calculation of the activation energy

Adsorption-diffusion and molecular sieving are activated phenomena. As such, they show an exponential dependence with temperature, which is regulated by an activation energy. The permeance due to these mechanisms is commonly described by an Arrhenius-type equation, as follows:

$$\rho_i = \frac{D_i^0}{RT} \exp \left[\frac{-(E_{act,i} - E_{ads,i})}{RT} \right] \quad (4.3)$$

Where D_i^0 is the diffusion coefficient, $E_{act,i}$ is the activation energy of either molecular sieving or adsorption diffusion, and $E_{ads,i}$ is the energy of adsorption. This equation is used to identify and describe the prevailing transport mechanism, looking at the trend of the permeation flux as a function of temperature. In case of molecular sieving, the activation energy for the gas to diffuse into the ultra-micropores is always higher than its adsorption energy, thus leading to an overall activation energy which is positive ($E_{act,MS,i} - E_{ads,i} > 0$). As a result, transport due to molecular sieving is enhanced for increasing temperature. Conversely, the difference in activation and adsorption energy for adsorption-diffusion can be either negative or positive. For gases with high adsorption energy, $E_{act,AD,i} - E_{ads,i} < 0$, meaning that an increase in temperature will result in a decrease in the permeation flux. On the contrary, if the activation energy is lower than the energy for the adsorption-diffusion, the overall term will become positive and an increase in temperature will result in an increase in the permeation flux, as with the molecular sieving [8]. The difference ($E_{act,i} - E_{ads,i}$) will be referred as apparent activation energy ($E_{act,i}^{app}$), which is a parameter that can be determined fitting the permeance data as a function of the operating temperature.

4.3 RESULTS AND DISCUSSION

4.3.1 Insights into the carbonization mechanism and the effect of the carbonization temperature on the CMSM surface chemistry

The FTIR spectra of the as prepared CMSM samples obtained after thermal treatment (i.e., removal of the adsorbed water) is reported in **Figure 4.2**. All the peaks, together with their assignment, are summarized in **Table 4.1**.

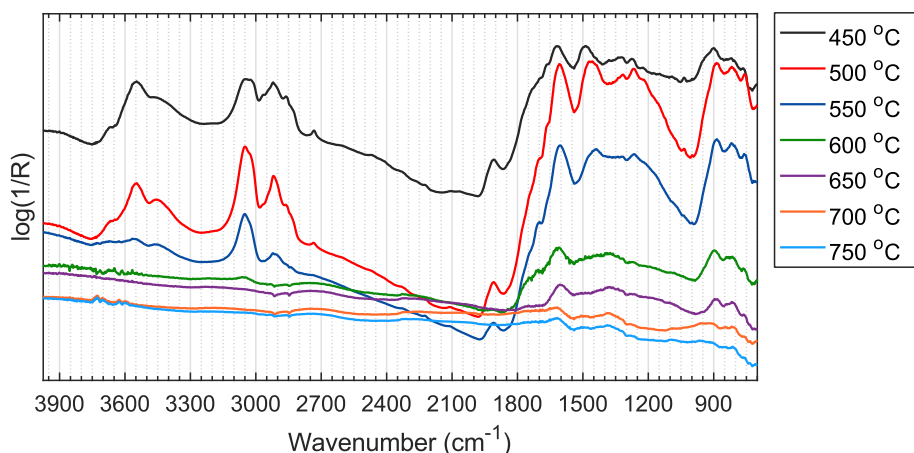


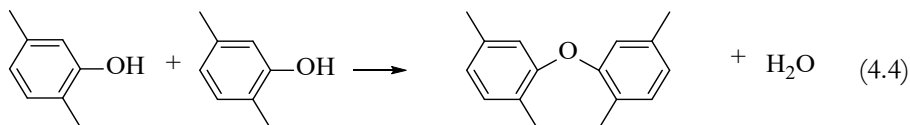
Figure 4.2. FTIR spectra of the as prepared CMSM samples after thermal treatment

Table 4.1. Overview of peak identification of the FTIR samples of the as-prepared CMSM samples carbonized at various temperatures (s = strong, m = medium, w = weak and vw = very weak signal).

T_{carb} (°C)	$\nu(\text{OH})$	$\nu(\text{CH})$ aromatic	$\nu_{\text{as}}(\text{CH})$	$\nu_{\text{s}}(\text{CH})$	$\nu(\text{CH})$ aldehyde
450	3650 m 3545 s 3440 s, b	3047 s 3025 s	2920 s 2860 s	2900 m 2825 m 2730 w	2730
500	3650 s 3545 s 3450 s, b	3050 s 3025 s	2918 s 2855 s	2900 m 2820 m 2735 w	2735
550	3650 s 3545 s 3450 s, b	3050 s 3025 s	2918 s 2855 s	2900 m 2820 w 2735 vw	2735
600	-	3055 m 3025 m	-	-	-
650	-	-	-	-	-
700	-	-	-	-	-
750	-	-	2958 w 2927 w 2855 w	-	-
T_{carb} (°C)	$\nu(\text{C}=\text{O})$	Tetra- substituted benzene ring	$\nu(\text{C}-\text{C})$ aromatic	$\nu(\text{C}-\text{C})$ aromatic and $\delta(\text{CH})$ of CH_2 and CH_3	$\nu(\text{CO})$ diphenyl ether structure
450	1705 s	1700-1730 m	1616 s 1585 m	1485 s 1440 s	1300-1200 s (1270 & 1225)
500	1705 s	1700-1730 m	1605 s 1585 m	1460 s 1430 s	1300-1200 s (1270 & 1225)

550	1705 s	1700-1730 m	1605 s 1585 m	1442 1430 s	1300-1200 s (1270 & 1225)
600	1705 s	1700-1730 m	1624 s 1585 m	1440 w 1400-1300 w	1270 m
650	-	-	1600 s 1585 m	1440 w 1400-1300 m	1270 m
700	-	-	1600 m 1585 w	1400-1350 w	-
750	-	-	1600 m 1585 w	1400-1350 w	-
T_{carb} (°C)	$\delta(\text{OH})$	Benzene ring substitution			
450	1200-1000	888 s, 823 s, 760 s			
500	-	883 s, 820 s, 754 s			
550	-	880 s, 820 s, 756 s			
600	-	893 m, 820 w, 760 w			
650	-	885 m, 820 w, 760 w			
700	-	900 w			
750	-	-			

In the region 3700-3100 cm^{-1} , the OH stretching signals ($\nu(\text{OH})$) for the samples carbonized at 450, 500 and 550 °C, are observed. The samples treated at 600 °C and higher temperatures do not show any signal in this band, which is in agreement with literature [9] (see integrated OH bands in **Figure 4.3a**). Indeed, Morterra et al. reported that for temperatures above 550 °C, the resin undergoes drastic changes. In this band, we can identify three main peaks: 1) a shoulder at 3650 cm^{-1} which corresponds to free or unbridged OH groups [10], 2) a stronger peak at 3545 cm^{-1} that corresponds to the bridged OH groups from the phenols of the Novolac resin [9], [11], [12] and 3) a strong and broad polymeric OH peak at 3450 cm^{-1} that is ascribed to the intense intra-molecular OH-OH interactions [9], [10]. When comparing the area of the bridged and free OH band with those of the bridged and polymeric band, via the integrated $\text{OH}_{3550}/\text{OH}_{3650}$ and $\text{OH}_{3550}/\text{OH}_{3450}$ (**Figure 4.3b**) ratios, respectively, it is clear that increasing the carbonization temperature from 450 to 550 °C causes better polymer crosslinking via condensation reactions of the OH groups of the phenol rings, forming diphenyl ethers (Eq. 4.4).



As a result, some of the bridged OH groups of the phenols disappear due to the formation of the ether linkage. At the same time, this reaction could lead to the formation of more free OH (i.e., water produced via condensation), which explains the faster decrease in the ratio $\text{OH}_{3550}/\text{OH}_{3650}$. Furthermore, the condensation reaction seems to influence the intra-molecular interaction between the remaining phenol groups to a lesser extent, evidenced by the little influence of carbonization temperature on the $\text{OH}_{3550}/\text{OH}_{3450}$ ratio. This could also indicate an increase in crosslinking via intra-molecular interaction [12].

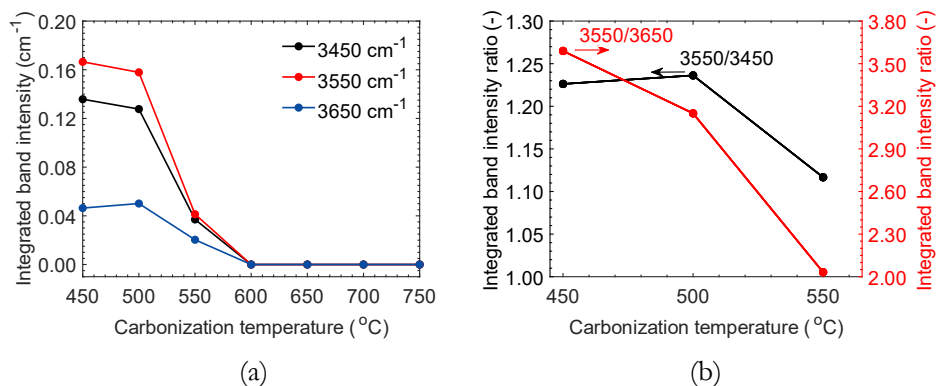
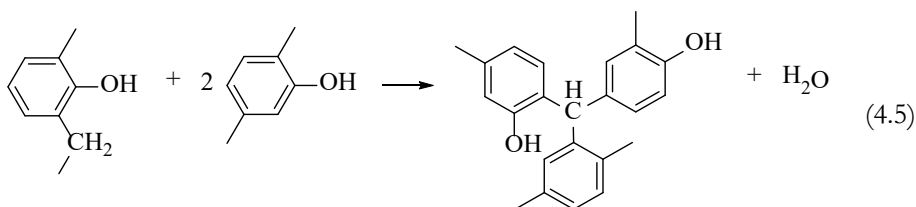


Figure 4.3. Integrated OH_{3450} , OH_{3550} and OH_{3650} (a) and $\text{OH}_{3550}/\text{OH}_{3650}$ and $\text{OH}_{3550}/\text{OH}_{3450}$ integrated bands ratio (b) as a function of the carbonization temperature, derived from the spectra in **Figure 4.2**.

In the region 3100-2700 cm^{-1} the CH stretching vibration ($\nu(\text{CH})$) is observed. First, the sample carbonized at 450 °C displays two clear aromatic CH bands at 3047 and 3025 cm^{-1} . With the increase in the pyrolysis temperature, the first band shifts to higher wavenumbers (i.e., 3055 for the sample carbonized at 600-650 °C), and the intensity of both bands gradually decreases to medium (600 °C) and weak (650 °C), to completely disappear for temperatures above 650 °C. However, the aliphatic CH bands, typically found in the region below 3000 cm^{-1} , disappear first. In the aliphatic region, the CH_3 , CH_2 and aldehyde ($\text{C}=\text{OH}$) stretching can be identified. The CH_3 stretching bands (2920 and 2860 cm^{-1}) corresponding to the $\nu_{\text{as}}(\text{CH})$ lose their intensity with the carbonization temperature. As a matter of fact, Trick et al. [12] proved that the aliphatic bands first increase and then decrease with the progression of the pyrolysis reactions. This is linked to the transformation that the resin undergoes especially in the region 500-520 °C, where Morterra et al. suggests the scheme reported in Eq. 4.5 [9]. However, all the bands related to the aliphatic CH groups completely disappear at 600 °C, which is in agreement with literature [9].



The relative signal intensity and position change with the pyrolysis temperature. **Figure 4.4** shows the $\text{CH}_{\text{alkyl}}/\text{CH}_{\text{aromatic}}$ ratio as function of the carbonization temperature, from which is clear that the relative amount of alkyl CH decreases with temperature much faster than the aromatic bands. At temperatures above 650 °C, no CH stretching vibrations are observed.

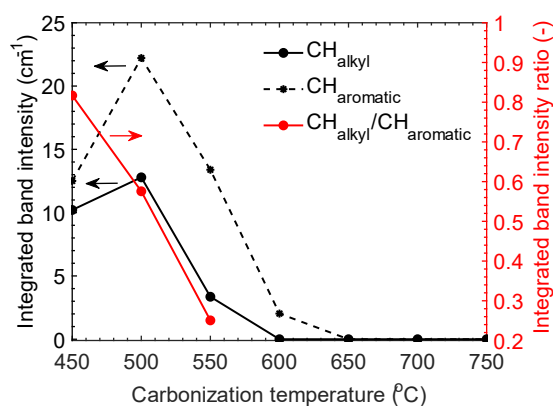


Figure 4.4. Integrated CH_{alkyl} and $\text{CH}_{\text{aromatic}}$ bands on the left and $\text{CH}_{\text{alkyl}}/\text{CH}_{\text{aromatic}}$ integrated band ratio as a function of the carbonization temperature, derived from the spectra in **Figure 4.2**.

An additional signal is observed at 2730 cm^{-1} for temperatures below 550 °C. This signal can be assigned to the $\nu(\text{CH})$ of aldehyde-like species $[(\text{R}-\text{C}=\text{O})-\text{H}]$.

The region between 2000 and 1000 cm^{-1} corresponds to the fingerprint region of this material, where a series of intense, overlapped and broad bands are observed. The peak at 1705 cm^{-1} corresponds to the stretching of the carbonyl group $\nu(\text{C}=\text{O})$. The base location of this peak is 1720 cm^{-1} , but the presence of benzene rings in the surrounding molecular structure increases the dipolar character of the $\text{C}=\text{O}$, leading to a shift of ca. 20 cm^{-1} towards lower wavenumbers [12]. The $\nu(\text{C}=\text{O})$ is not observed for temperature higher than 600 °C.

The C-C stretching of aromatic rings are observed at ca. 1600, 1585 and 1450 cm^{-1} . These peaks decrease their intensity at higher carbonization temperatures. On the other hand, the CH deformation ($\delta(\text{CH})$) of aliphatic bridges CH_3 and CH_2 are observed at 1485 and 1400 cm^{-1} . A shift in the peak position, as well as a change in

weaker adjacent peaks are indications of changes in the nature of the aliphatic bridges [12].

The region $1300\text{--}1200\text{ cm}^{-1}$ is assigned to the stretching of the C-O bond ($\nu(\text{CO})$). In particular, two signals at 1270 and 1225 cm^{-1} are observed, which indicate the C-O stretching of the diphenyl ether structure, formed via condensation reaction of two phenol groups (see Eq. 4.4), and of the phenol group, respectively. These signals are absent for the samples carbonized at temperatures higher than $650\text{ }^{\circ}\text{C}$.

For all the signals in the fingerprint region, their intensity increases with pyrolysis temperature from 450 to $500\text{ }^{\circ}\text{C}$ and then decrease. At temperatures higher than $650\text{ }^{\circ}\text{C}$ only a broad signal at 1350 cm^{-1} remains, which is also indicative of the $\delta(\text{CH})$ of aliphatic bridges.

Finally, signals in the range of $1200\text{--}1000$ represents bending of the OH group ($\delta(\text{OH})$), which are only visible for the sample carbonized at $450\text{ }^{\circ}\text{C}$, in line with what we observed with the OH stretching $\nu(\text{OH})$.

The range below 1000 cm^{-1} is usually attributed to the deformation of the CH bond ($\delta(\text{CH})$) of aromatics. Changes in the relative heights of these peaks indicate ring substitution reactions, in line with what found in literature [12]. The shift from lower (760 cm^{-1}) to higher (890 cm^{-1}) wavenumber, represent an increase in the ring substitution related to the increase in carbonization temperature (**Figure 4.5**), which overall leads to a decrease in H free atoms (i.e., OH and alkyl groups substitution).

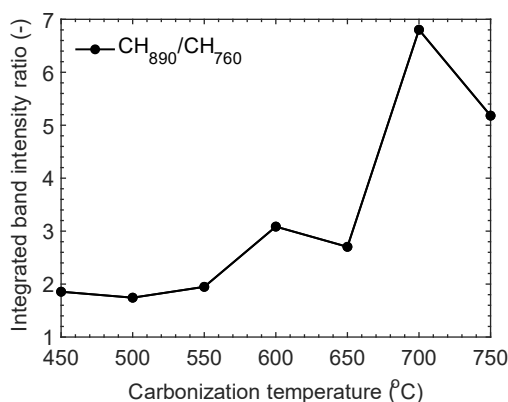


Figure 4.5. Integrated $\text{CH}_{890}/\text{CH}_{760}$ band ratio (indication of ring substitution) as a function of the carbonization temperature, derived from the spectra in **Figure 4.2**.

The evolution of the bands is in agreement with the study of Trick et al. [12] carried out via the analysis of the gas evolution. To summarize, we can identify four main steps in the carbonization:

- *Step 1*: crosslinking of the cured resin (R) via the formation of the CH and O (ether) links (R_{CH} and R_O , respectively), as described via Eq. 4.5 and Eq. 4.4, respectively. This step leads to a loss in C-OH and alkyl groups.
- *Step 2*: stripping of the previously formed CH crosslinks, as well as of the methylene crosslinks from the original cured resin. The aliphatic CH concentration decreases with respect to the ring-related CH bonds. This step leads to the formation of C-crosslinked char (Ch_C).
- *Step 3*: reaction with gaseous products leads to the formation of direct aromatic-aromatic link (Ch_{Ar}).
- *Step 4*: splitting of the H atoms directly bonded to the benzene nuclei, to form the final char structure (Ch) with coalesced rings.

The evolution of the char structure as described in step 2, 3 and 4 is sketched in **Figure 4.6**.

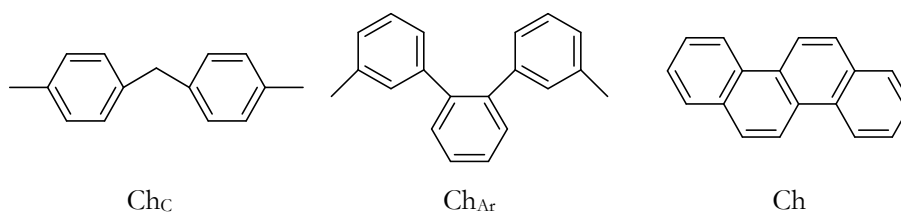


Figure 4.6. Evolution of the structure of the char from carbon crosslink (Ch_C) to aromatic crosslink (Ch_{Ar}) and to coalesced rings (Ch).

The Novolac-based dipping solution used in this study for the preparation of the carbon membranes includes two additives: 0.6 wt % of ethylenediamine ($C_2H_8N_2$) and 0.8 wt % of 10% aqueous dispersion of boehmite nanosheets. The NH stretching vibrations occur in the same range of the OH vibrations, but they are usually much weaker. Primary amines show some deformation peaks related to the NH_2 bond at ca. 1650 cm^{-1} , which were not detected. On the other hand, secondary amines ($R-NH-R'$) show deformation vibration at ca. 1600 cm^{-1} , which would overlap with the aromatic $C=C$ stretching. However, it should be kept in mind that the nitrogen content found in the carbonized samples via elemental analysis (see Appendix C, **Figure C1**) is ca. 1-1.5 wt %, which indicates that any peak related to this element is in general less significant (i.e., comparable to the noise of the measurement) than the peaks related to the C, H and O bonds. As a result, the N-related bonds do not contribute much to the FTIR spectra of these samples.

Furthermore, in Chapter 3, the absence of any Al-C interaction was proved. Therefore, boehmite contributes to the FTIR spectra in the free OH bands, although, likewise the N-bonds, this contribution is very little when compared to the bands linked to the carbon skeleton of the resin.

In conclusion, the analysis of the FTIR spectra with the carbonization temperature in a wider range ($450\text{-}750\text{ }^\circ\text{C}$) shows that the resin undergoes drastic changes in the

range 450-550 °C, where functional groups transformation occurs prior to their disappearance (i.e., formation of char structures). Therefore, the functional groups formed in this range could be either less or more hydrophilic than the ones from the original cured resin. However, it is expected that above 600-650 °C the hydrophilicity is gradually lost, as reported elsewhere [13]. The affinity of the samples carbonized at different temperatures to water will be addressed in the following section.

4.3.2 Water adsorption/desorption on the CMSM surface studied via in-situ FTIR

The membrane carbonized at 500 °C is used as example to qualitatively analyze the evolution of the FTIR spectra with time during the water adsorption (**Figure 4.7a**) and desorption step (**Figure 4.7b**). When the membrane sample is exposed to 2 vol. % water, the FTIR signal displays a development and subsequent increase of intensity of peaks in the band region of the OH stretching, and to a milder extent, of the OH bending (see Appendix C, **Figure C2**). In particular, in the OH stretching region, 4 peaks can be identified [14]: the peaks at ca. 2990 cm⁻¹, 3320 cm⁻¹ and 3490 cm⁻¹, all representing the monolayer of water adsorbed to the hydrophilic pores via the formation of strong, medium-strong and weak H-bonds, respectively. The peak at ca. 3560 cm⁻¹ can be ascribed to the free or unassociated water, which means isolated water molecules that are either physically adsorbed onto the membrane surface or interacting with the strongly adsorbed water. **Figure 4.7a** shows that after ca. 30 min, the system achieves a steady state condition and the FTIR spectra stabilizes. However, when the water is removed and the sample is only exposed to a He environment at the same temperature and pressure (i.e., 30 °C and ambient pressure) – **Figure 4.7b** – the membrane surface cannot restore its initial (dry) status, as reported in **Figure 4.2**, even when achieving steady state condition. Indeed, some water is still bonded to the membrane surface. This indicates that the water adsorption/desorption phenomena displays a hysteresis behavior. To restore the initial status of the membrane surface, the membrane needs to be exposed to an inert atmosphere (i.e., N₂) at 300 °C for 1h.

The high intensity peaks (i.e., in the region 3700-3100 cm⁻¹) characterizing both the water adsorption and desorption spectra were integrated and normalized with the maximum integrated band intensity (i.e., steady state), as shown in **Figure 4.8a** and **Figure 4.8b**, respectively. During the water adsorption, all the peaks achieve a steady state condition with the same rate. However, during the desorption step, only the free water molecules completely desorb and at a higher rate. On the other hand, the water molecules bonded to the membrane surface via H-bonds do not desorb completely, showing a residual peak area which is larger for the medium-strong than for the weak H-bonds. Therefore, the water directly adsorbed onto the membrane pores (i.e., via H-bonds) appears to be responsible for the hysteresis behavior.

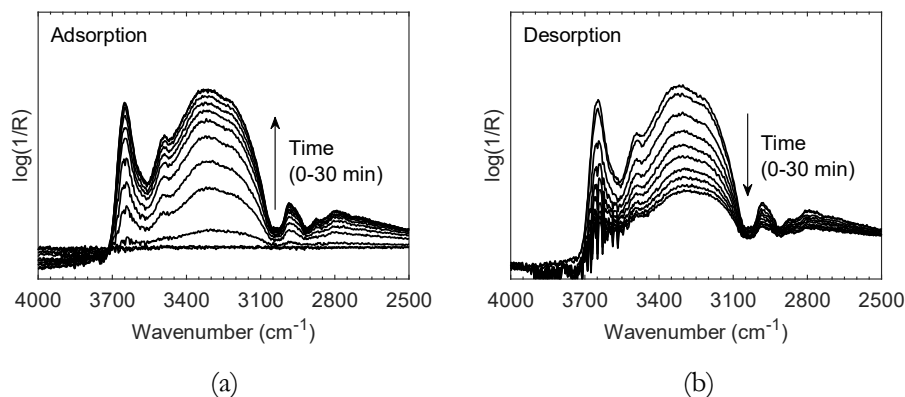


Figure 4.7. FTIR spectra obtained when exposing the membrane carbonized at 500 °C to a 2 vol% water/He environment (a – water adsorption) and to a He environment (b – water desorption) at 30 °C and ambient pressure, as a function of time.

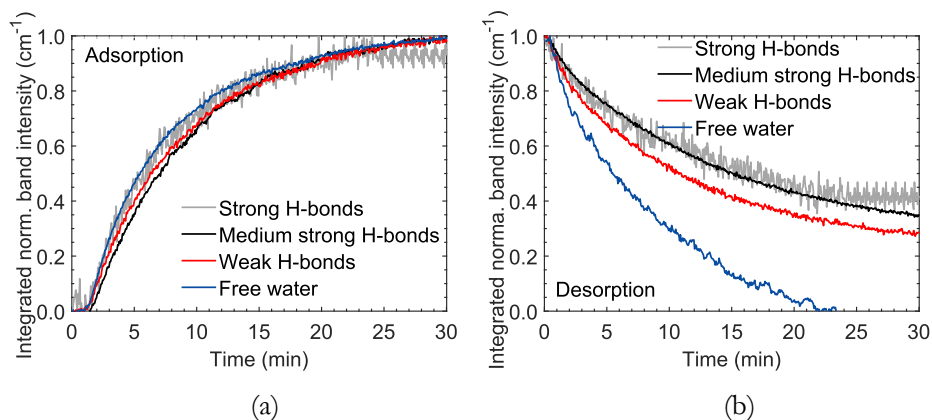


Figure 4.8. Integrated normalized band intensity corresponding to the strong H-bonds (2990 cm^{-1}), medium strong H-bonds (3320 cm^{-1}), weak H-bonds (3490 cm^{-1}) and to the free water (3560 cm^{-1}) as a function of time during the water adsorption (a) and desorption (b) step, obtained from the FTIR spectra of **Figure 4.7** (membrane sample carbonized at 500 °C)

The same water adsorption/desorption experiment was carried out on all the membrane samples carbonized at different temperatures (i.e., 450-750 °C). **Figure 4.9** displays the FTIR spectra obtained after subtracting the spectra of the dry membrane (**Figure 4.2**) from the steady state water adsorption spectra. For the samples carbonized at temperatures higher than 550 °C, the signal is much weaker and the peaks corresponding to strongly adsorbed water via medium and strong H-bonds disappear (i.e., peaks at lower wavenumber), while the peak representing mainly weak bonded or free water is much broader. As a matter of fact, at 600 °C and 650 °C, the membrane surface loses the hydroxyl and carbonyl groups,

respectively, which are the most polar functional groups able to form hydrogen bonds with water.

Analyzing the low carbonization temperature region (i.e., 450-550 °C), it is clear that the sample carbonized at 500 °C adsorbs the highest amount of water, followed by the sample carbonized at 550 and 450 °C. The higher hydrophilicity of the 500 °C-carbonized sample is believed to be linked to the C-O, C=O, aromatic and aliphatic CH groups (corresponding to the signals in the region 2000 and 1000 cm^{-1} that display a peak at 500 °C), which all increase the probability of the water to adsorb onto the membrane surface.

When zooming into the high carbonization temperature region (see Appendix C, **Figure C3**) we observe that the signal is quite weak and noisy. However, it is clear that the hydrophilicity tendentially decreases for $T_{\text{carb}} \geq 600$ °C.

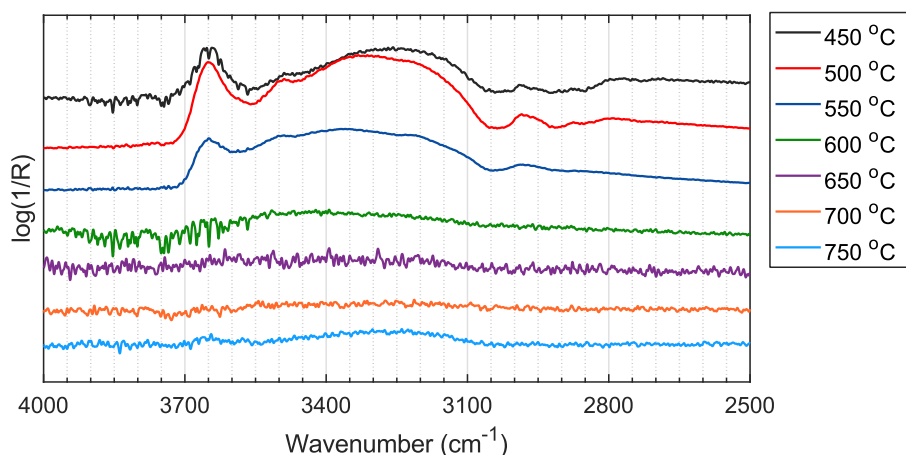


Figure 4.9. FTIR spectra of the carbon membrane samples carbonized at different temperatures, obtained after subtraction of the characteristic dry membrane spectra (**Figure 4.2**) from the steady state spectra obtained when exposing each membrane sample to a 2 vol% water/He environment at 30 °C and ambient pressure (water adsorption experiment).

4.3.3 Gas adsorption properties derived via thermogravimetric analysis

To assess whether the adsorption diffusion is a relevant transport mechanism for gas permeation, the affinity of the membranes carbonized at different temperatures to the gas of interests (i.e., CO_2 , H_2 and CO) was studied via thermogravimetric analysis (TGA). As shown in the previous section, the membrane carbonized at 500 °C displays the highest adsorption capacity for water vapor, being the pores walls rich in functional groups. Therefore, this membrane sample was used again as a reference for further studies. It was found that the adsorption of CO and H_2 at temperatures relevant to the permeation (i.e., 200 °C) can be neglected, at least in the pressure range of 1-10 bar. The only gas showing affinity to the membrane

surface is CO₂. Therefore, the CO₂ adsorption was systematically studied for all the membrane samples. For all membranes, the amount of CO₂ adsorbed increases as a function of pressure, following a Dubinin-Astakhov type of isotherm, as reported elsewhere [7]. Furthermore, **Figure 4.10** shows that the weight variation associated to the CO₂ adsorption generally increases with the carbonization temperature, with the membrane carbonized at 650 °C being the only one out of the trend. Indeed, the sample carbonized at 650 °C displays a lower adsorption capacity than those carbonized at 600 and 700-750 °C, in agreement with what found with the water adsorption. This finding implies that although no noteworthy differences can be observed in the FTIR spectrum among the carbonized membranes produced at temperatures of 600 °C and 700-750 °C, when compared to the membrane obtained at 650 °C, the latter displays a lower surface area. This reduction results in fewer functional groups being available to expose to the gaseous atmosphere for the adsorption of CO₂.

The increase in the CO₂ adsorption with the carbonization temperature can be ascribed to two reasons: the change in the surface chemistry and 2) the change in the surface area with the carbonization temperature. The surface functionality of the membranes was studied via FTIR, where no bands related to N-containing group were detected, due to the very little concentration (i.e., 0.6 wt%) of the ethylenediamine (C₂H₈N₂) in the Novolac-based dipping solution that was used for the preparation of the membranes. On the other hand, any transformation of the amine group involving the incorporation of the nitrogen atom in the aromatic ring cannot be excluded, leading to the formation of pyridine/pyridone structures within the pyrolysis process. L. Geunsik et al. [15] proved via DFT calculation that the binding energy of CO₂ to pyridine/pyridone groups is stronger than for amine groups, which could explain the increase in the CO₂ uptake with the carbonization temperature. Secondly, the porous structure (i.e., pore size, pore size distribution and surface area) of these membranes, has been proven to be affected by the carbonization temperature [5], [16]. As reported in Section 4.1, the membrane carbonized at 450 °C has few pores, mostly in the range 0.4-0.9 nm. Thus, at 450 °C the membrane has a small pore volume, combined with relatively large pores, which also translate into a small surface area. At intermediate T_{carb} (600-650 °C), the membranes display a bimodal distribution, with MS and AD pores. These membranes are expected to have the largest surface area. Finally at higher T_{carb}, the porous system shrinks, leaving most of the pores in the MS region. As a result, the surface area of the membranes is expected to display an optimum with the carbonization temperature, which is something that does not reoccur in the CO₂ uptake (**Figure 4.10**). Thus, the results suggest that at low carbonization temperature, the increase in the CO₂ adsorption is linked to the increase in the surface area with the carbonization temperature. At higher T_{carb}, despite the shrinkage of the porous structure, the CO₂ adsorption continue to increase due to the transformation of the amine group into the pyridine/pyridone structure, due to the pyrolysis process. This theory agrees with the lower CO₂ adsorption capacity

found at 650 °C, where the effect of the surface area prevails on the surface chemistry.

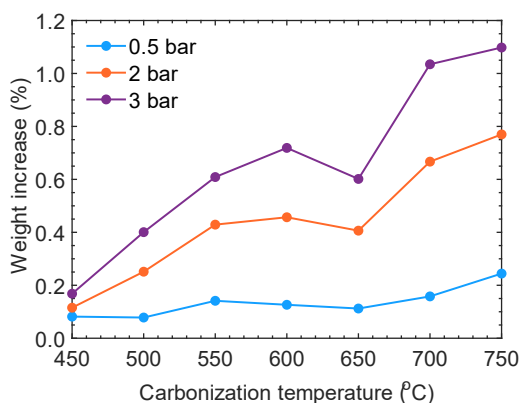


Figure 4.10. Weight increase (%) recorded during the CO₂ TGA test at 200 °C as a function of the carbonization temperature for three values of pressure (0.5, 2 and 3 barg).

Water adsorption tests via thermogravimetric analysis were not carried out due to setup limitations. However, the water adsorption was studied at low temperature and pressure (i.e., 30 °C, 2 vol. % water in He and ambient pressure) via in-situ FTIR analysis (section 4.3.2). The same type of experiment was repeated replacing water by CO₂. No signal due to the CO₂ adsorption was detected, as CO₂ seems to require higher pressures to adsorb onto the membrane surface. Thus, although it was not possible to quantify the water adsorption at conditions relevant for the permeation (i.e., 200 °C), it is expected that it would be even more relevant than the CO₂ adsorption. This is also confirmed by the characteristic functional groups of the surface of the membranes (Section 4.3.1), which interact more with water than CO₂.

4.3.4 Permeation properties of the supported Al-CMSMs

This section focuses on the permeation properties of the tubular supported Al-CMSM. First, the effect of the carbonization temperature is assessed through the analysis of the single vapor (water and methanol) and single gas permeance through humidified membranes. Then, gas and gas/vapor permeation through both a humid and a dry membrane will be discussed in order to elucidate the permeation mechanism.

Effect of the carbonization temperature on the vapor/gas permeation properties

The permeance of N₂ (ρ_{N_2}), CO (ρ_{CO}) and H₂ (ρ_{H_2}) measured at 200 °C is reported in **Figure 4.11a** as a function of the carbonization temperature. The permeance of these gases shows a first increases with the carbonization temperature, displaying an optimum in the region 600-700 °C, to decrease again at 750 °C. The same trend

repeats at all the operating temperatures in the range 150-250 °C (see Appendix C, **Figure C4**). In the optimum region, two peaks are identified: one at 600 °C and one at 700 °C. This could imply either that the permeance of all gases at 650 °C is lower than expected or that the permeance at 600 or 700 °C is unexpectedly higher, breaking the volcano-shape trend.

Being the affinity of N₂ to the membrane surface, as well as its interaction with the water adsorbed on the surface of the pores negligible, it is possible to conclude that the ϕ_{N_2} trend with T_{carb} solely depends on the changes introduced by the carbonization temperatures in the porous structure, both in terms of pore size distribution and porosity of the membranes. As a result, on one hand, the trend of ϕ_{N_2} with T_{carb} can be explained with the information already available on the pore size distribution of these membranes. On the other hand, the ϕ_{N_2} can be used to elucidate even more on the effect that the carbonization temperature has on the pore size distribution of the membranes. All the techniques used for measuring the pore size distribution have some limitations: 1) physisorption techniques measure also dead-end pores, which are not active for the permeation, 2) perm-porometry techniques are based on capillary condensation phenomena, which requires strong hypothesis, especially for pore diameter below 1 nm. Therefore, using the permeation flux of inert species through the membrane is an effective way to have an indication of the properties of the porous system which are relevant for the permeation.

For this scope, it would be ideal to use, as a reference, the smallest inert gas of the system, which would have the possibility to access even smaller pores. In the previous section, it was found that H₂ does not interact with the membrane surface as its adsorption capacity measured via thermogravimetric analysis is negligible. Indeed, ϕ_{H_2} displays the exact same trend of ϕ_{N_2} vs T_{carb} , as well as of ϕ_{CO} , which was also proved to be inert with respect to the membrane surface. As a result, each of these gases could be used to gain insights into the pore size distribution of the membranes.

Combining the information on the pore size distribution measured on unsupported carbon films from previous study and the trend reported in **Figure 4.11a**, it can be stated that initially, ϕ_{N_2} increases with T_{carb} due to an increase in the porosity of the membranes and to the gradual development of pores in the MS region. At intermediate T_{carb} (600-700 °C), ϕ_{N_2} is the highest due to the large fraction of pores, especially in the MS region. At 650 °C, the ϕ_{N_2} is slightly lower, which could indicate that the membrane could also display some differences in terms of pore size distribution (i.e., a lower porosity or a shift in the average pore size to lower values). Finally, as soon as the porous structure starts to shrink (750 °C) also the ϕ_{N_2} decreases.

As it was shown in the previous section, these species do not adsorb on the membrane pores, thus molecular sieving is the dominant transport mechanism. At all carbonization temperatures, their permeance monotonically increases with the

operating temperature, as reported in **Figure 4.12a** for the membrane carbonized at 550 °C. This observation makes even clearer that, when the membranes display a high portion of pores in the MS region (i.e., T_{carb} in the range 600-700 °C), the gas permeance is also the highest.

The permeance of all species with a proved (i.e., water and CO₂) or expected (methanol) affinity to the membrane surface, is reported in **Figure 4.11b** as a function of the carbonization temperature. Surprisingly, $\rho_{\text{H}_2\text{O}}$, ρ_{CO_2} and ρ_{MeOH} show the same trend with T_{carb} as for the inert gases. However, **Figure 4.12b** shows that $\rho_{\text{H}_2\text{O}}$ and ρ_{MeOH} monotonically decrease when the operating temperature decreases, which is a clear indication of the adsorption diffusion being the dominant transport mechanism, as it was found in Chapter 3 for $\rho_{\text{H}_2\text{O}}$. Capillary condensation could also play a role, especially at lower temperatures. However, when using the information of the pore size distribution to estimate the capillary condensation pressure, it can be concluded that this phenomenon could play a role only at 150 °C.

CO₂ permeance (ρ_{CO_2}), instead, displays an optimum at ca. 200 °C, which is also typical of adsorption diffusion. Indeed, since CO₂ permeance was measured through a humid membrane, some water molecules are adsorbed on the pore walls. This results in a reduced accessibility for the CO₂ to its adsorption sites, as well as in a lower active pore size, which make molecular sieving the dominant transport mechanism for ρ_{CO_2} . Moreover, when water is adsorbed on the pore walls, CO₂ can interact with it via dipole-quadrupole interactions in the larger AD pores. As temperature increases (i.e., above 200 °C), water progressively desorbs and adsorption diffusion becomes the dominant mechanism for ρ_{CO_2} as well.

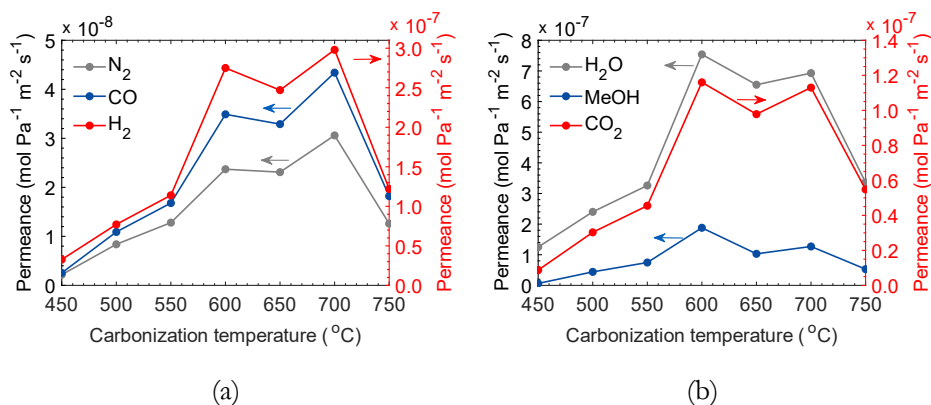


Figure 4.11. Permeance of gases and vapors as a function of the carbonization temperature: (a) N₂, CO and H₂ (b) H₂O, methanol and CO₂, measured at 200 °C and a total pressure gradient of 3 bar.

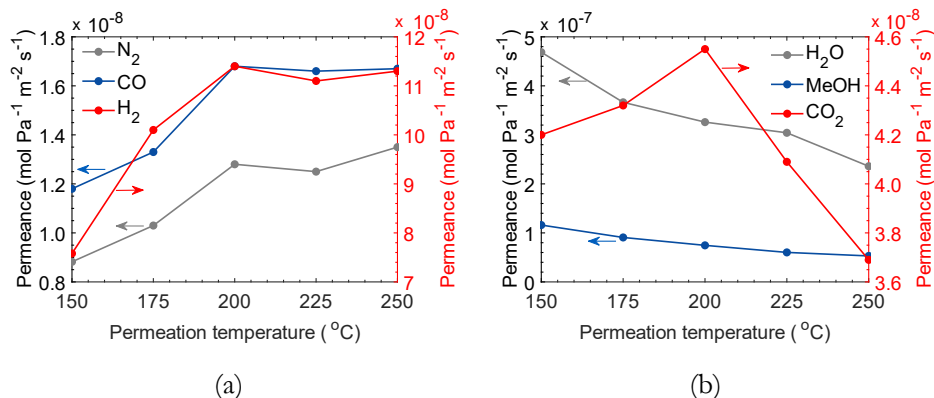


Figure 4.12. Permeance of gases and vapors as a function of the permeation temperature: (a) N₂, CO and H₂ (b) H₂O, methanol and CO₂, measured at a total pressure gradient of 3 bar for the membrane carbonized at 550 °C.

These observations lead to the conclusion that the trend induced in the permeance of each species by the carbonization temperature solely depends on the characteristics of the porous structure of the membranes. On the other hand, the trend of the permeance of each species as a function of the operating temperature is strongly influenced by the dominant transport mechanism.

The trend of ϕ_i with the permeation temperature is qualitatively the same for all the membranes carbonized at different temperatures. However, as the permeation of water or methanol vapor are concern, the $\phi_{i,vapor}$ decrease with a different slope for different T_{carb} . In other words, the apparent activation energy (E_{act}^{app}) for both methanol and water (**Figure 4.13**) is negative, which means that both species have a high adsorption energy ($E_{act}^{app} = E_{act,AD} - E_{ads} < 0$) and that adsorption diffusion is the dominant mechanism. However, when increasing the carbonization temperature, E_{act}^{app} increases, becoming less negative, assuming the highest value at ca. 600-700 °C, to then decrease again at 750 °C, thus showing a similar trend to the ϕ_i vs T_{carb} curves.

The only reason for the activation energy to increase is because of the interplay of two transport mechanisms, one being the adsorption diffusion, with a negative E_{act}^{app} , and the other molecular sieving, with a positive E_{act}^{app} . As a result, for the membranes carbonized in the range 600-700 °C, molecular sieving plays a relevant, although not dominant, contribution also in the permeation of water, methanol and CO₂. In conclusion, this is a further confirmation that MS pores appears gradually in the membrane porous structure and that a T_{carb} of 600-700 °C induces the formation of a large fraction of pores in the MS region, which subsequently shrinks for higher carbonization temperatures.

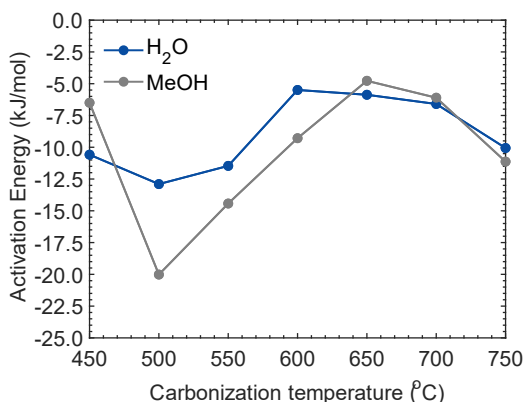


Figure 4.13. Apparent activation energy as a function of the carbonization temperature for both methanol and water.

Insights into the gas permeation mechanism

In this section, the membrane carbonized at 600 °C is used as model to discuss the mechanisms involved in the permeation of the gases of interests, with a specific focus on how the presence of water affects the interplay of the transport phenomena.

Firstly, it is observed that when ϕ_{H_2} (**Figure 4.14a**) and ϕ_{CO} (**Figure 4.14b**) are measured through a humid membrane and via a H₂/H₂O or CO/H₂O mixture, the permeance increases with the operating temperature with a similar slope, which indicates that molecular sieving is still dominant. However, both ϕ_{H_2} and ϕ_{CO} are higher when measured via pure gas permeation tests through a humid membrane. This indicates that when the gas/water mixture is fed to the membrane, water adsorbs on the pore walls, reducing the active pore size, thus partially or totally blocking some of the pores, hindering gas permeation.

On the other hand, when the membrane undergoes a thermal treatment which removes the adsorbed water from the surface, the pores will be bigger and the absence of water in the pores, makes the gases to collide with the walls of the pores increasing the path length behaving as Knudsen (microporous Knudsen) [17]. The Knudsen diffusivity depends on $T^{1/2}$, which means that the gas permeance ($\propto T^{-1/2}$) decreases with temperature when Knudsen diffusion is the dominant mechanism. As a matter of fact, when ϕ_{H_2} and ϕ_{CO} are measured through a dry membrane, ϕ_{H_2} slightly decreases with temperature, while ϕ_{CO} increases with temperature with a much lower slope than the previous cases. This means that when the membrane is dry, microporous Knudsen diffusion becomes the dominant transport mechanism for the H₂ permeation and it contributes to the permeation of CO, with molecular sieving being still dominant. Indeed, the mean free path of H₂ is larger than for CO, which explains the different contribution of the Knudsen flow for the two gases.

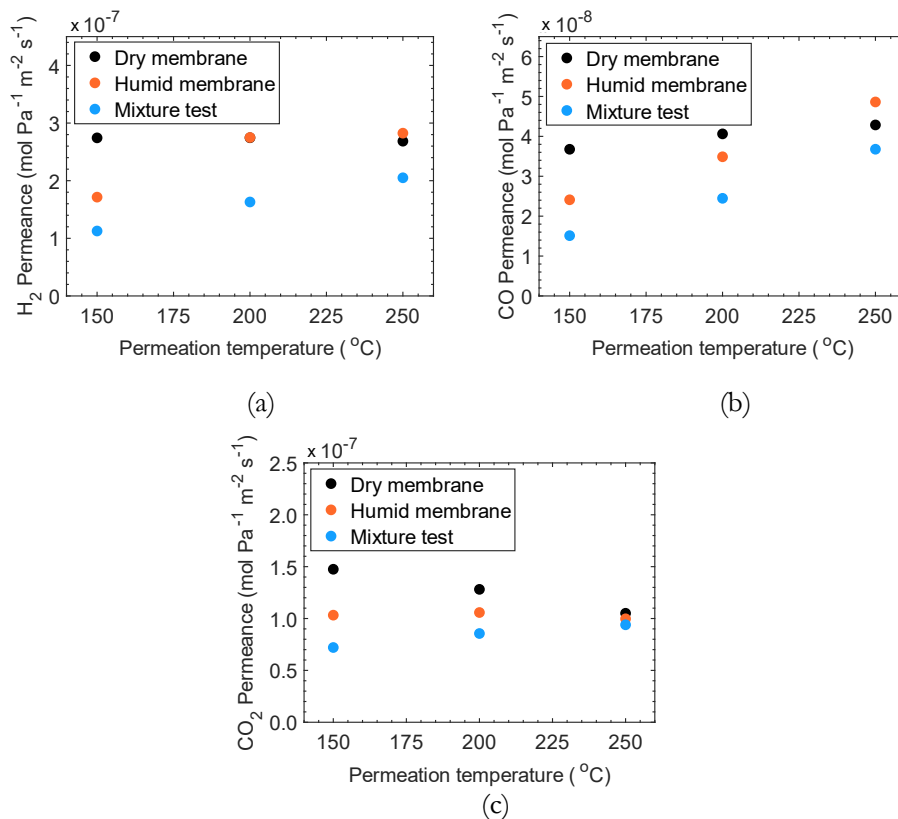


Figure 4.14. H₂ permeance (a), CO permeance (b) and CO₂ permeance (c) as a function of the permeation temperature measured through a dry and humid membrane and in gas/vapor mixtures for the membrane carbonized at 600 °C.

As discussed above, \wp_{CO_2} is affected by both molecular sieving and adsorption diffusion. In **Figure 4.14c**, it can be observed that when water is adsorbed on the membrane pores (i.e., humid membrane) or it is fed together with CO₂ (i.e., mixture test), \wp_{CO_2} displays an increase with the operating temperature, indicating molecular sieving as dominant mechanism. As a matter of fact, as seen in **Figure 4.12**, free water molecules reduce the accessibility of the adsorption sites for CO₂. As soon as this water is being removed from the pores, the pore size increases and adsorption diffusion becomes more relevant, to finally control the CO₂ transport when the membrane is dry. Indeed, \wp_{CO_2} measured in dry conditions displays a negative activation energy, as clearly visible from **Figure 4.14c**. The decreasing trend of \wp_{CO_2} with temperature recorded in dry conditions is not linked to the Knudsen diffusion. Indeed, the H₂O/CO₂ selectivity is 5.89 at 200 °C, which is ca. 4 times higher than the value of the Knudsen selectivity for the same gas/vapor pair (i.e., $\sqrt{Mw_{\text{CO}_2}/Mw_{\text{H}_2\text{O}}} = 1.56$).

The same experiments were carried out also for the membranes carbonized at 450 and 700 °C (see Appendix C, **Figure C5** and **Figure C6**), which belong to the low porosity region, as seen in previous sections. Overall, it can be confirmed that, even when removing the water via the thermal treatment (i.e., dry membrane), the permeance of the gases display the same trend with the carbonization temperature as in **Figure 4.11**. On the contrary, the presence/absence of water in the membrane pores affect the relative contribution of the transport mechanism, which results in a different behavior of the permeance with the operating temperature.

Effect of the carbonization temperature on the vapor/gas perm-selectivity

The ideal perm-selectivity of water towards each of the gases and methanol ($S_{H_2O/i}$) were determined using the ϕ_i obtained via pure gas (via humid membrane) and pure vapor permeation tests. The behavior of $S_{H_2O/i}$ with respect to the gases (i.e., H₂, CO₂, CO, N₂) confirms what was found in Chapter 3: $S_{H_2O/i}$ generally increases with the kinetic size and decreases with the permeation temperature for the gas showing molecular sieving behavior (i.e., H₂, CO and N₂). S_{H_2O/CO_2} , instead, is barely affected by the operating temperature, given the contribution of the adsorption diffusion in both CO₂ and water permeation mechanism.

Expectedly, all the perm-selectivity display the same trend as a function of T_{carb} , as for the ϕ_i . As example, **Figure 4.15** depicts the S_{H_2O/H_2} vs T_{carb} measured in the temperature range 150-250 °C. At all operating temperatures, S_{H_2O/H_2} assumes the lowest values for the most permeable membranes (i.e., 600-700 °C). As a matter of fact, in membrane technology it is well known that a trade-off always exists between permeability and perm-selectivity, for a given separation. However, the trend is more marked at lower permeation temperatures (i.e., 150-175 °C), where capillary condensation phenomenon is more likely to contribute to the water permeation mechanism. This results in a higher probability for the water to partially or totally block some of the membrane hydrophilic pores, hindering the permeation of other gases. At 250 °C, the carbonization temperature barely affects the perm-selectivity.

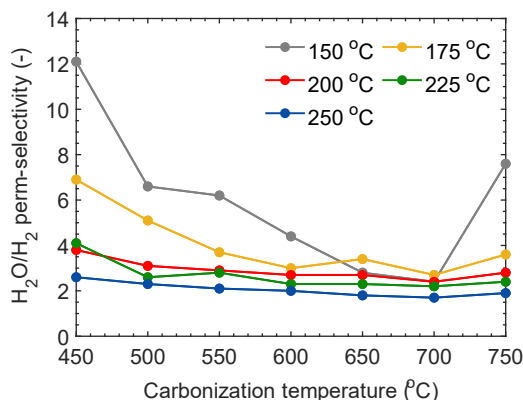


Figure 4.15. $\text{H}_2\text{O}/\text{H}_2$ perm-selectivity as a function of the carbonization temperature measured at operating temperatures in the range 150-250 °C

The water/methanol perm-selectivity ($S_{\text{H}_2\text{O}/\text{MeOH}}$) is also an important parameter when the scope of the membrane is to enhance reaction performance such as for the synthesis of MeOH or dimethyl ether (DME). When methanol is the desired product, a low value of $S_{\text{H}_2\text{O}/\text{MeOH}}$ is preferred, in such a way that the equilibrium of the methanol synthesis is even more shifted to the products side. On the other hand, when methanol is the intermediate product, such as in the methanol to gasoline (MTG) process or in the DME synthesis, $S_{\text{H}_2\text{O}/\text{MeOH}}$ needs to be as high as possible, to keep the methanol in the reaction side. **Figure 4.16** displays the values of the $S_{\text{H}_2\text{O}/\text{MeOH}}$ determined for the membranes with different carbonization temperatures. $S_{\text{H}_2\text{O}/\text{MeOH}}$ displays the same trend with T_{carb} as seen for the water/gas pair. Furthermore, it is observed that for most of the membranes, $S_{\text{H}_2\text{O}/\text{MeOH}}$ is not much affected by the operating temperature, given the very similar average dipolar moment (2.64 and 2.95 D for methanol and water, respectively) and activation energy of water and methanol. $S_{\text{H}_2\text{O}/\text{MeOH}}$ ranges from 3 to 6.4, except for the membrane carbonized at 450 °C which shows a selectivity of 19.9-16.5. Indeed, at T_{carb} of 450 °C, the membrane combines a high hydrophilicity with a relatively low porosity, which results in a much higher permeance of the water than of methanol.

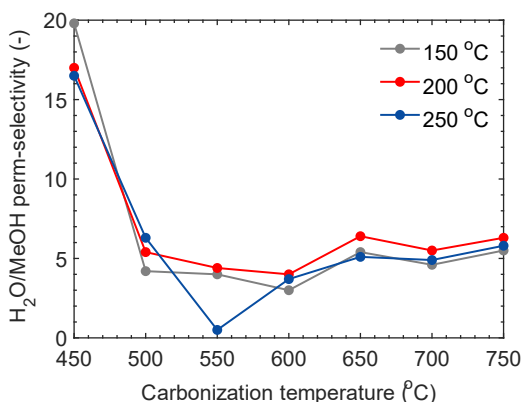


Figure 4.16. Water/methanol perm-selectivity for the membranes carbonized at different temperatures, measured at 150, 200 and 250 °C

Finally, when the permeation properties are measured feeding a mixture of gas and vapor, ϕ_{H_2O} decreases with a similar extent to what we observed for the gas permeance in **Figure 4.14** (see Appendix C, **Figure C7**). As a result, the separation is not significantly affected by the gas/vapor interactions, which means that the molecules need to compete for their transport through the membrane pores, despite the high affinity of the membrane to the water. This suggests that the competition between water and a second species occurs prior to the access of any molecule to the pores. Then, once water enters the pores, its transport is influenced by the interaction with the hydrophilic surface. This lead overall to lower separation factors than ideal selectivity, as seen in Chapter 3. However, it must be noted that the separation factor is calculated differently than the ideal selectivity and that comparing permeances measured via pure gas/vapor or mixture test gives a clearer indication on the separation performance in real conditions.

4.4 CONCLUSIONS

In this study, boehmite-phenolic resin carbon molecular sieve membranes were prepared, based on a previously optimized composition (Chapter 3), carbonizing the membranes in the temperature range 450-750 °C. Both supported and unsupported membranes were tested to assess how the carbonization temperature affects the vapor-gas separation performance, in view of their potential application in membrane reactors, to enhance CO₂ hydrogenation reactions.

First, the transformation occurring in terms of the surface chemistry of the membranes as soon as the pyrolysis step progresses was elucidated via FTIR analysis. It was found that the OH groups disappear at $T_{carb} \geq 600$ °C. At the same temperature, the membrane also loses the aliphatic CH groups. The aromaticity, instead, disappear at higher temperature (700-750 °C), with the resin gradually transforming into a char-like structure.

The hydrophilicity of the membranes was first assessed via in-situ FTIR analysis, carried out when exposing the membrane to water vapor at ambient conditions. It was found that two types of water adsorb onto the membrane surface: one directly bonded to the hydrophilic pores via H-bonds and the other free or weakly bonded, mostly interacting with the already adsorbed water (i.e., water monolayer). The membrane affinity to water initially increases with T_{carb} , with the sample carbonized at 500 °C being the most hydrophilic. Then, hydrophilicity tendentially decreases as hydrophilic functional groups are being removed.

The results of the thermogravimetric analysis revealed that the membrane is inert with respect to H₂, CO and N₂. On the other hand, CO₂ adsorption cannot be neglected and the affinity of the membrane to CO₂ generally increases with T_{carb} , due to a combination of a higher surface area and the possible transformation of the amine group into a pyridine/pyridone structure, which display stronger affinity to CO₂.

The permeance of all gases and vapors tested shows the same behavior with the carbonization temperature: ρ_i first increases, displaying an optimum in the region 600-700 °C – with a slightly lower value at 650 °C – to decrease again at 750 °C. This result suggests that the trend induced by T_{carb} solely depends on the pore size distribution and porosity of the membranes. Indeed, the membranes carbonized in the range 600-750 °C display a bi-modal pore size distribution, with the majority of the pores in the MS region, which was confirmed also by the higher activation energy calculated for water and methanol.

On the other hand, the trend of ρ_i with the operating temperature is strongly influenced by the transport mechanisms. Water, methanol and CO₂ permeate mostly via adsorption diffusion mechanism. The inert gases (i.e., H₂, CO and N₂), instead, permeates mostly via molecular sieving. However, when the permeance of such gases is measured through a dry membrane, microporous Knudsen diffusion starts to play a relevant role. Therefore, the presence/absence of water in the membrane pores affect the relative contribution of the transport mechanism, as well as the extent of the permeation flux: ρ_i decreases for higher water content. Furthermore, when the permeance is measured via gas/vapor mixture, also the ρ_{H_2O} decreases, indicating that all molecules, despite their affinity to the membrane surface, compete for accessing and interacting with the pores of the membranes.

Finally, it was observed that all the perm-selectivity display the same trend as a function of T_{carb} , as for the ρ_i , with the lowest values in the region 600-700 °C, corresponding to the highest permeabilities. This trend is more visible at low operating temperatures (i.e., 150-175 °C), where water condensation is more likely to occur and block some of the pores.

Appendix C

C.1 Supplementary figures

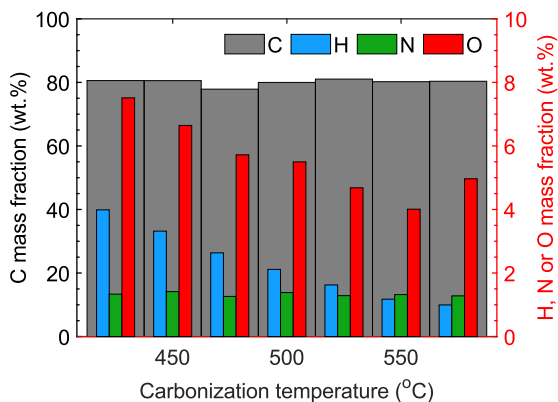


Figure C1. Elemental composition of the CMSM in terms of carbon (C), hydrogen (H), nitrogen (N) and oxygen (O) mass fraction determined using a Thermo Scientific, Flash Smart – CHNS/O, Waltham, MA, USA analyzer.

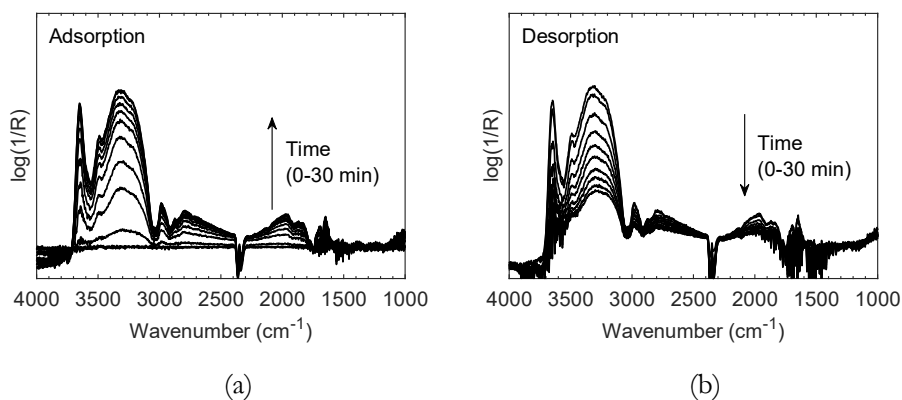


Figure C2. FTIR spectra obtained when exposing the membrane carbonized at 500 °C to a 2 vol% water/He environment (a – water adsorption) and to a He environment (b – water desorption) at 30 °C and ambient pressure, as a function of time.

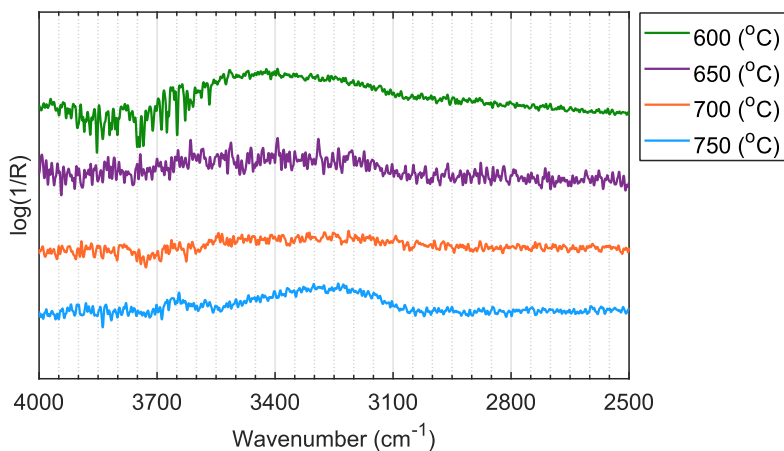
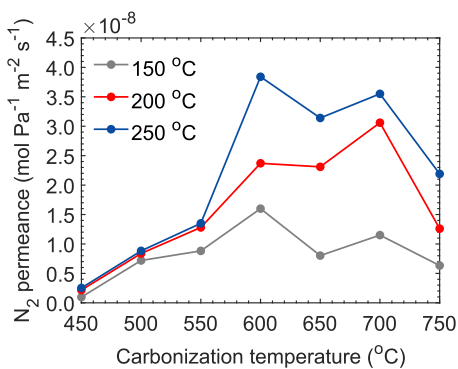
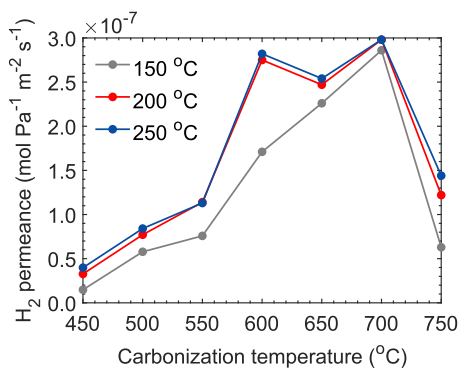


Figure C3. FTIR spectra of the carbon membrane samples carbonized at different temperatures in the range 600-750 °C, obtained after subtraction of the characteristic dry membrane spectra (**Figure 4.2**) from the steady state spectra obtained when exposing each membrane sample to a 2 vol% water/He environment at 30 °C and ambient pressure (water adsorption experiment).



(a)



(b)

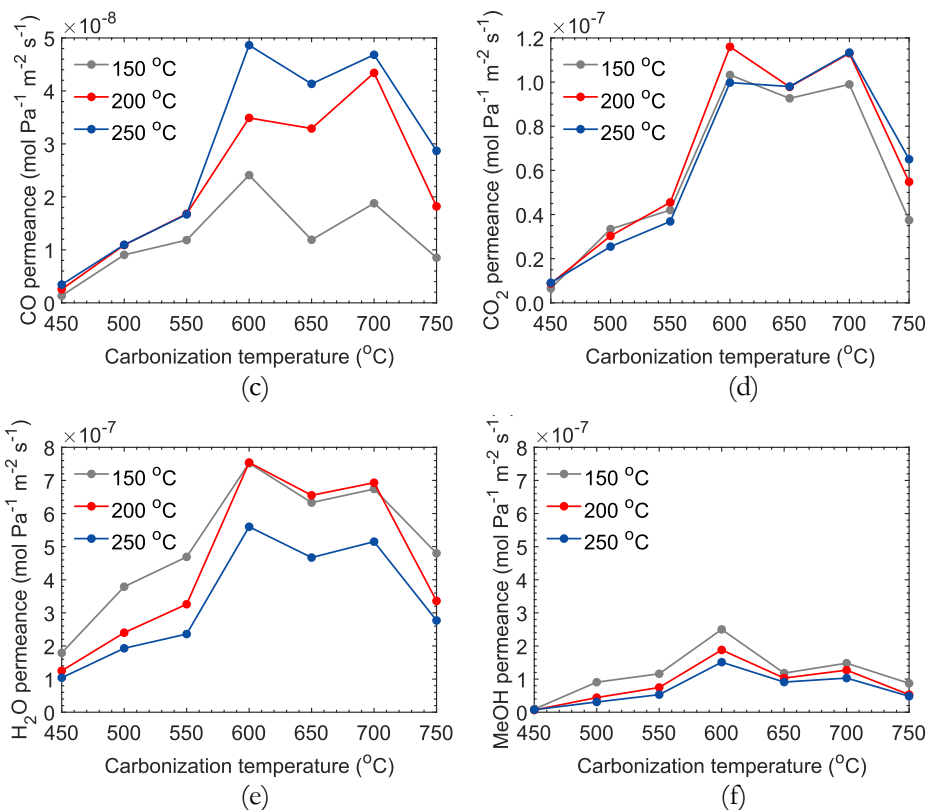
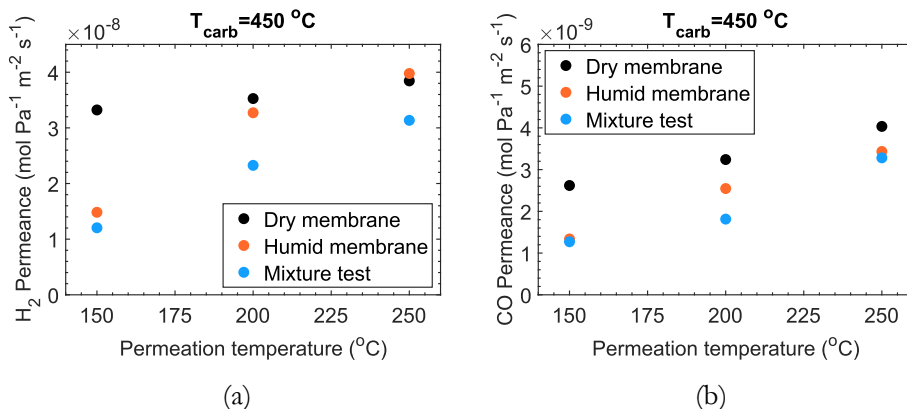


Figure C4. Permeance of gases and vapors as a function of the carbonization temperature measured at 150, 200 and 250 °C and a total pressure gradient of 3 bar.



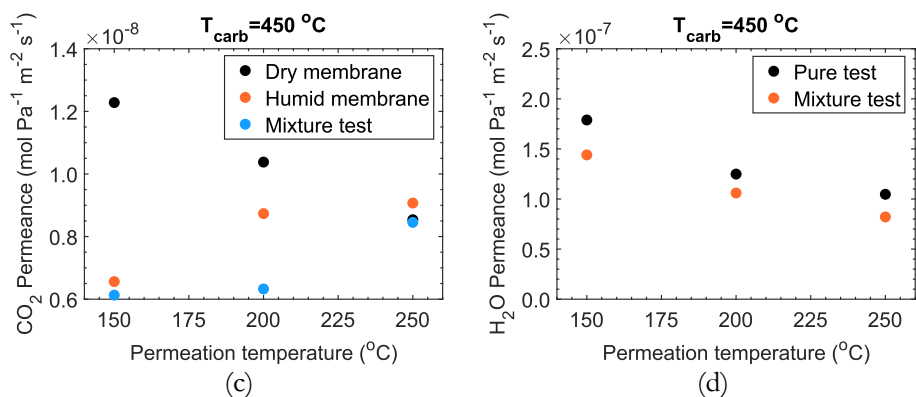
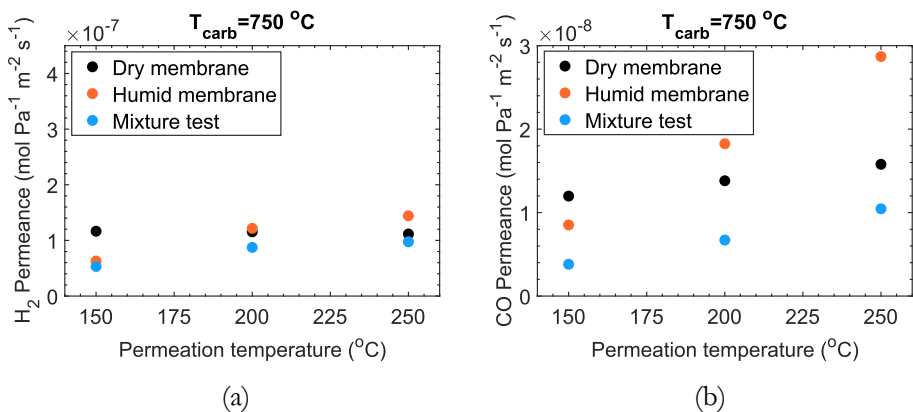


Figure C5. H₂ permeance (a), CO permeance (b), CO₂ permeance (c) as a function of the permeation temperature measured through a dry and humid membrane and in gas/vapor mixtures for the membrane carbonized at 450 °C. Water permeance (d) measured for the same membrane as a function of the permeation temperature via a pure vapor permeation test and via gas/vapor mixture test (as average obtained with H₂, CO₂ and CO) for the membrane carbonized at 450 °C



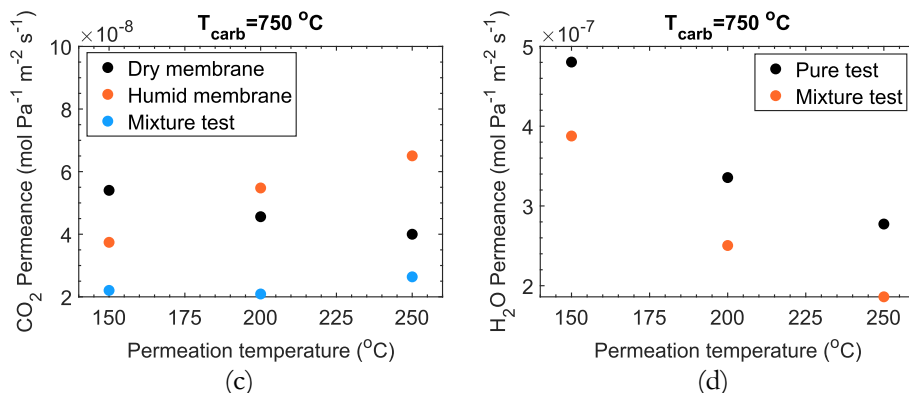


Figure C6. H₂ permeance (a), CO permeance (b), CO₂ permeance (c) as a function of the permeation temperature measured through a dry and humid membrane and in gas/vapor mixtures for the membrane carbonized at 750 °C. Water permeance (d) measured for the same membrane as a function of the permeation temperature via a pure vapor permeation test and via gas/vapor mixture test (as average obtained with H₂, CO₂ and CO) for the membrane carbonized at 750 °C

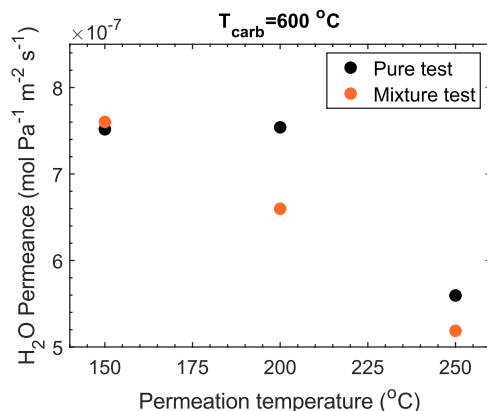


Figure C7. Water permeance measured for the same membrane as a function of the permeation temperature via a pure vapor permeation test and via gas/vapor mixture test (as average obtained with H₂, CO₂ and CO) for the membrane carbonized at 600 °C

REFERENCES

- [1] C. W. Jones and W. J. Koros, "Characterization of Ultramicroporous Carbon Membranes with Humidified Feeds," *Ind. Eng. Chem. Res.*, vol. 34, no. 1, pp. 158–163, 1995,
- [2] A. B. Fuertes, D. M. Nevskaja, and T. A. Centeno, "Carbon composite membranes from Matrimid® and Kapton® polyimides for gas separation," *Microporous Mesoporous Mater.*, vol. 33, no. 1–3, pp. 115–125, 1999,
- [3] T. A. Centeno and A. B. Fuertes, "Carbon molecular sieve membranes derived from a phenolic resin supported on porous ceramic tubes," *Sep. Purif. Technol.*, vol. 25, no. 1–3, pp. 379–384, 2001,
- [4] V. C. Geiszler and W. J. Koros, "Effects of polyimide pyrolysis conditions on carbon molecular sieve membrane properties," *Ind. Eng. Chem. Res.*, vol. 35, no. 9, pp. 2999–3003, 1996,
- [5] M. A. Llosa Tanco, D. A. Pacheco Tanaka, and A. Mendes, "Composite-alumina-carbon molecular sieve membranes prepared from novolac resin and boehmite. Part II: Effect of the carbonization temperature on the gas permeation properties," *Int. J. Hydrogen Energy*, vol. 40, no. 8, pp. 3485–3496, 2015,
- [6] L. Forster *et al.*, "Tailoring pore structure and surface chemistry of microporous Alumina-Carbon Molecular Sieve Membranes (Al-CMSMs) by altering carbonization temperature for optimal gas separation performance: An investigation using low-field NMR relaxation measurements," *Chem. Eng. J.*, p. 129313, 2021,
- [7] M. L. V. Nordio, J. A. Medrano, M. Van Sint Annaland, D. A. P. Tanaka, M. L. Tanco, and F. Gallucci, "Water adsorption effect on carbon molecular sieve membranes in H₂-CH₄ mixture at high pressure," *Energies*, vol. 13, no. 14, 2020,
- [8] J. A. Medrano, M. A. Llosa-Tanco, D. A. Pacheco-Tanaka, and F. Gallucci, *Transport mechanism and modeling of microporous carbon membranes*. Elsevier Inc., 2019.
- [9] C. Morterra and M. J. D. Low, "I.R. studies of carbons - VII. The pyrolysis of a phenol-formaldehyde resin," *Carbon N. Y.*, vol. 23, no. 5, pp. 525–530, 1985.
- [10] C. J. Mitchell, G. R. Yang, and J. J. Senkevich, "Adhesion aspects of poly(p-xylylene) to SiO₂ surfaces using γ -methacryloxypropyltrimethoxysilane as an adhesion promoter," *J. Adhes. Sci. Technol.*, vol. 20, no. 14, pp. 1637–1647, 2006,
- [11] H. Kumar, S. K. Tripathi, S. Mistry, and G. Bajpai, "Synthesis, characterization and application of coatings based on epoxy novolac and liquid rubber blend," *E-Journal Chem.*, vol. 6, no. 4, pp. 1253–1259, 2009,
- [12] K. A. Trick and T. E. Saliba, "Mechanisms of the pyrolysis of phenolic resin in a carbon/phenolic composite," *Carbon N. Y.*, vol. 33, no. 11, pp. 1509–1515, 1995,
- [13] L. Forster *et al.*, "Tailoring pore structure and surface chemistry of microporous Alumina-Carbon Molecular Sieve Membranes (Al-CMSMs) by altering carbonization temperature for optimal gas separation performance: An investigation using low-field NMR relaxation measurements," *Chem. Eng. J.*, vol. 424, no. December 2020, p. 129313, 2021,

- [14] “Fourier Transform Infrared Spectroscopy Studies of Water Uptake in Chemically Amplified Photoresists,” pp. 1–22.
- [15] G. Lim, K. B. Lee, and H. C. Ham, “Effect of N-Containing Functional Groups on CO₂ Adsorption of Carbonaceous Materials: A Density Functional Theory Approach,” *J. Phys. Chem. C*, vol. 120, no. 15, pp. 8087–8095, 2016,
- [16] M. A. Llosa Tanco, D. A. Pacheco Tanaka, S. C. Rodrigues, M. Teixeira, and A. Mendes, “Composite-alumina-carbon molecular sieve membranes prepared from novolac resin and boehmite. Part I: Preparation, characterization and gas permeation studies,” *Int. J. Hydrogen Energy*, vol. 40, no. 16, pp. 5653–5663, 2015,
- [17] J. Gilron and A. Soffer, “Knudsen diffusion in microporous carbon membranes with molecular sieving character,” vol. 209, pp. 339–352, 2002

CHAPTER 5

Experimental investigation of a packed bed membrane reactor for the direct conversion of CO₂ to dimethyl ether

Abstract

In this chapter, the performance of a packed bed membrane reactor (PBMR) based on carbon molecular sieve membranes for the one-step CO₂ conversion to dimethyl ether (DME) is experimentally compared to that of a conventional packed bed reactor (PBR) using a CuO-ZnO-Al₂O₃/HZSM-5 bifunctional catalyst. The PBMR outperforms the PBR in most of the experimental conditions. The benefits were greater at lower GHSV (i.e., conditions that approach thermodynamic equilibrium and water formation is more severe), with both X_{CO₂} and Y_{DME} improvements of +35-40% and +16-27%, respectively. Larger sweep gas-to-feed (SW) ratios increase the extent of water removal (ca. 80% at SW=5), and thus the performance of the PBMR. Nevertheless, alongside the removal of water, a considerably high amount of all products are removed as well, leading to a greater improvement in the CO yield (+122%) than the DME yield (+66%). Higher temperatures (>200 °C) selectively improve the rWGS reaction, leading to a lower Y_{DME} with respect to the PBR at 260 °C, due to the significant loss of methanol. Furthermore, larger transmembrane pressures (ΔP) were not beneficial for the performance of the PBMR due to the excess reactant loss (i.e., 98-99% at $\Delta P=3$ bar). Finally, the reactor models developed in Chapter 2 and 6 accurately describe the performance of both the PBR and PBMR in the range of tested conditions. This result is of high relevance, since the reactor models could be used for further optimization studies and to simulate conditions which were not explored experimentally.

This chapter is based on the following paper:

Poto, S., Llosa-Tanco, M. A., Pacheco-Tanaka, D. A., Gallucci, F., & Neira d'Angelo, M. F.. Experimental investigation of a packed bed membrane reactor for the direct conversion of CO₂ to dimethyl ether. *Submitted to Journal of CO₂ utilization*

5.1 INTRODUCTION

In Chapter 2, the state of the art membrane reactor technologies for the in-situ removal of water during methanol and dimethyl ether (DME) production has been extensively discussed. According to literature, it is clear that the one-step DME synthesis has gained more attention only very recently, with most of the studies focusing on the use of CO₂-rich syngas, rather than on pure CO₂ feeds. However, the removal of water becomes even more important as the CO₂ content in the feed increases [1]–[4]. To date, most of the work aimed at demonstrating the potential of the in-situ removal of water to enhance the DME synthesis follows a modeling approach, while only the group of Ateka and collaborators has proved the improved performance of the membrane reactor experimentally [5], [6]. In these studies, the authors validated their previously developed reactor model by testing, at laboratory scale, an LTA (i.e., zeolite type A) membrane reactor using feedstocks containing CO₂/CO_x (with CO_x=CO₂+CO) in different proportions. However, the reported DME yield for pure CO₂ feeds remains very low (~5%), given the very high temperature (i.e., 275-325 °C) adopted in this study. Given the stronger thermodynamic limitation of the CO₂-to-DME process, lower temperature operation would be preferred to achieve higher DME yields which would, as a consequence, lead to the production of more water. This poses higher demands on the selection of the membrane material, especially in terms of stability. The LTA membrane proposed by Ateka et al. shows a water permeance in the order of 10⁻⁸ mol·m⁻²·s⁻¹·Pa⁻¹ and separation factors very close to (or sometimes lower than) those measured with the carbon molecular sieve membranes (CMSM) in this thesis (i.e., S_{H₂O/H₂} of 1.1, S_{H₂O/CO} of 2.4, S_{H₂O/CO₂} of 0.56 and S_{H₂O/MeOH} of 1.8 for the LTA membrane at 275 °C). Thus, zeolite membranes display similar separation performance than CMSM, but with lower permeabilities. Besides, CMSM present improved stability with respect to zeolites in presence of water at high temperatures [7], which highlights the potential for CMSM for this application, especially when using pure CO₂ feeds that lead to larger production of water.

Carbon membranes have already been proposed in the past for their application in membrane reactors, mostly to enhance dehydrogenation reactions. Indeed, given their molecular sieving character, if the pore size of these membranes is finely tuned, H₂ (i.e., one of the smallest molecules) can be selectively separated from the reaction mixture. Itoh and Haraya developed one of the first carbon membrane reactor (CMR) to enhance the dehydrogenation of cyclohexane. Their CMR, made of a bundle of 20 carbon fibers, exceeded the equilibrium conversion at 195 °C and ambient pressure [8]. Later on, Hirota et al. improved the properties of the carbon membrane by controlling the pore size through activation with different gas/vapor atmosphere, which lead to better performance of the CMR for the dehydrogenation of methylcyclohexane in the range 200-260 °C [9]. Szejner and Sheintuch tested, for the first time, a CMR for the dehydrogenation of isobutene at very high temperature (i.e., 450-500 °C). The conversion of isobutene was significantly improved due to the H₂ removal, which was rendered even more effective thanks to the circulation of a N₂-containing sweep gas (i.e., H₂ dilution in the sweep gas as a way to increase

its driving force for the permeation flux) [10]. Zhang et al. proposed a CMR to enhance the methanol steam reforming (SRM) via the in-situ removal of H₂. The authors measured a few percentage improvement in the methanol conversion and H₂ yield with respect to a conventional reactor in the range 200-250 °C, even when using N₂ as a carrier gas for the H₂ dilution [11]. Later, Sá et al investigated, first via a numerical study, the use of either Pd or carbon membrane to enhance the SRM and to recover pure H₂ in the permeate stream. Carbon membranes were identified as a cheaper alternative to the Pd counterpart, allowing for a higher H₂ recovery, but with lower purity [12]. The same authors, few years later, experimentally investigated the use of CMR for the SRM, and found that the low H₂/H₂O perm-selectivity (i.e., 0.4 at 200 °C) caused steam depletion from the reaction zone, thus a decrease in the performance of the CMR, and higher production of CO (i.e., methanol decomposition). To solve this issue, they proposed the circulation of steam as a sweep gas to prevent its permeation from the reaction zone. In this configuration, back-permeation of water allowed to achieve higher performance with lower steam/methanol ratios in the feed [13]. This last application anticipates the challenges encountered in this study, where water has to be separated and H₂ retained in the reaction zone. Finally, to underline the wide range of application of carbon membranes, Dubé et al. used a relatively large pore size carbon membrane (i.e., in the range of 0.05 to 1.4 μm), to obtain pure biodiesel via the transesterification of canola oil in a CMR [14], [15].

Thus, the concept of using carbon membranes in membrane reactors is not new. Nevertheless, in all the applications mentioned, the CMR operates at relatively low pressure and was mostly demonstrated for H₂ separation. This underlines the challenges and novelty of this study, where keeping H₂ in the reaction zone is essential to obtain high methanol and DME selectivity, especially at high pressure and temperature (i.e., 40 bar and 200-260 °C).

In this chapter, a carbon membrane reactor is demonstrated for the one-step CO₂ conversion to DME. As already discussed in Chapter 2, the cocurrent circulation of a sweep gas containing the reactants (i.e., H₂ and CO₂) is proposed as a way to prevent reactant loss through the membrane. At the same time, this configuration allows to operate at relatively low pressure gradient across the membrane (ΔP), since the driving force for the water separation is given by its dilution in the sweep gas. However, in Chapter 2, this reactor configuration was explored via a modeling study, where also a target for optimal membrane properties was defined. Here, a CMSM is prepared based on the inputs of Chapter 3 and 4, and is then integrated in a conventional CuO-ZnO-Al₂O₃/HZSM-5 bifunctional catalyst bed. The as-obtained packed bed membrane reactor (PBMR) was tested in different conditions to investigate the effect of the main operational parameters, such as GHSV, temperature, sweep gas ratio (SW) and pressure gradient across the membrane (ΔP). The performance of the PBMR was compared to a PBR tested in the same conditions. Finally, the reactor model initially developed in Chapter 2 and then improved in Chapter 6 (i.e., implementation of new kinetic models) was validated with the experimental data gathered in this study. This result is of very high

relevance, given that reactor model is a powerful tool for reactor design and optimization, as well as for scale-up and integration at process level.

5.2 EXPERIMENTAL

5.2.1 Catalyst material and characterization

The bifunctional catalyst used in this study is a physical mixture of a CuO/ZnO/Al₂O₃ (CuZA) catalyst and a HZSM-5, with a mass ratio of 1. The composition of the commercial CuO/ZnO/Al₂O₃ is reported in **Table 5.1**. The catalyst was provided in cylindrical pellets (5.4x3.6 mm) and was crushed and sieved to produce 50-125 μm particle size, to be used for the characterization techniques and reaction tests.

Table 5.1. Composition of the commercial CuO/ZnO/Al₂O₃

Component	Composition (wt %)
CuO	52
ZnO	30
Al ₂ O ₃	17
Act. Charcoal	1

Typically, the γ -Al₂O₃ and the HZSM-5 are the acid catalysts used for the methanol dehydration function [16], [17]. Several works have proved that the γ -Al₂O₃ suffers from strong and fast deactivation with high concentration of water in the reaction medium. Indeed, the selectivity to DME drastically decreases when the CO₂ content in the syngas feed is increased [18]. The poor activity of the CuO-ZnO-Al₂O₃/ γ -Al₂O₃ bifunctional catalyst for the one-step DME synthesis from CO₂ and H₂ has also been proved in this chapter, using commercial γ -Al₂O₃ provided by Thermo Scientific™ (see Appendix D, **Figure D1**). On the other hand, several studies proved that the HZSM-5 has higher activity for the DME synthesis, given the Brønsted acidity and higher stability with water [19], [20]. In particular, zeolites are characterized by both Lewis and Brønsted acid sites and their balance is influenced by the SiO₂:Al₂O₃ (SAL) molar ratio. Better selectivity to DME have been measured with SAL between 20 and 40 [16], [20]. Thus, HZSM-5 with a SAL of 23 was used in this study. The fine powder ZSM-5 zeolite was provided in ammonium form from Thermo Scientific™. The proton form (HZSM-5) was obtained after calcination of the NH₄-ZSM-5 at 550 °C for 5h under N₂ atmosphere [21]. The HZSM-5 powder was then pelletized, crushed and sieved to produce 50-125 μm particle size, to be used for the characterization techniques and reaction tests.

The specific surface area (S.A.) and pore volume (P.V.) of both catalysts were determined via the BET and BJH elaboration of the N₂ adsorption-desorption isotherms at -196 °C, obtained using a Micromeritics ASAP 2020 gas adsorption device. Before the measurement, the sample was degassed at 250 °C for 2 h. The

catalyst density (ρ_{cat}) was measured using an automatic gas pycnometer instrument (Ultrapyc 1200e).

The CuZA catalyst reducibility was studied via temperature programmed reduction (TPR) analysis performed using a Micromeritics AutoChem 2920 equipment with a TCD detector. The analysis was carried out in the range 50-400 °C with a heating rate of 10 °C·min⁻¹, feeding 50 mL·min⁻¹ of a 10% H₂/Ar mixture. Prior to the TPR analysis, the sample was outgassed under inert conditions as for the N₂ physisorption.

X-ray diffraction (XRD) analysis in the 2 θ range 10-120° was performed on the reduced CuZA catalyst and on the HZSM-5 with a MiniFlex600 (*Rigaku*) operating with a Ni β -filtered Cu-K α radiant at 40 kV and 30 mA and a scan step of 0.05°/min. The diffraction peaks were identified according to the JCPDS database of reference compounds.

The acidity of the HZSM-5 was characterized via NH₃-temperature programmed desorption (TPD), carried out with the same equipment used for the TPR. Prior to the analysis, the sample was cleaned with He at 250 °C for 2 h. Thereafter, the temperature was reduced to 100 °C and the sample was saturated with a flow of 50 mL·min⁻¹ of a 5% NH₃/He mixture for 1 h. Then, the sample was purged with He until a constant baseline was measured. The TPD analysis was finally carried out increasing the temperature to 700 °C with a heating rate of 10 °C·min⁻¹ under 25 mL·min⁻¹ of pure He flow.

Prior to the packed bed membrane reactor experiments, the bifunctional CuO-ZnO-Al₂O₃/HZSM-5 catalyst was tested to prove its activity and stability for the CO₂ hydrogenation to DME and to validate the kinetic model described in Chapter 6. The catalytic tests were carried out in a stainless-steel reactor (d_{int} , 10 mm), loaded with 0.25 g of catalyst, diluted with 0.75 g of silicon carbide (SiC), to ensure isothermal operation and prevent sintering phenomena. The catalyst and the SiC used for dilution were introduced in the reactor with the same particle size of 50-125 μm . Larger SiC particles were used as pre-heating bed, separated from the catalytic bed with c.a. 1 cm³ of quartz-wool. The reactor was placed in an electric oven and precisely heated via a heating mantle. The temperature was measured with two thermocouples, one at the beginning of the catalytic bed and one placed at the exit of the gases. The reaction mixture was analysed with a compact gas chromatograph (Global Analyzer Solution™, G.A.S.) equipped with a TCD detector and two packed columns (HayeSep Q 60-80 mesh and 5A molecular sieve) for the analysis of permanent gases (i.e., H₂, CO₂, CO and N₂) and an FID detector with capillary columns (Rtx-1, MTX-1 and MTX-QBond) for the analysis of the hydrocarbons. The experimental setup is sketched in **Figure 5.1**.

Prior to the reaction tests, the catalyst was reduced in-situ at 280 °C, with 50 mL·min⁻¹ of a 50% H₂/N₂ mixture for 4 h. The reaction tests were performed in a range of temperature and pressure of 200-260 °C and 30-40 bar, respectively. The

feed contained $\text{H}_2/\text{CO}_2/\text{N}_2$ mixtures in different proportion to have a $\text{H}_2:\text{CO}_2$ molar ratio of 3 or 5, and a GHSV ranging from 1700-15000 $\text{NL kg}_{\text{cat}}^{-1} \text{h}^{-1}$. The full carbon balance in the reaction was achieved with a maximum error of 3%. The catalyst stability was observed with a 40 h time-on-stream test at 250 °C, 30 bar, $\text{H}_2:\text{CO}_2$ molar ratio of 3 and a GHSV of 11000 $\text{NL kg}_{\text{cat}}^{-1} \text{h}^{-1}$.

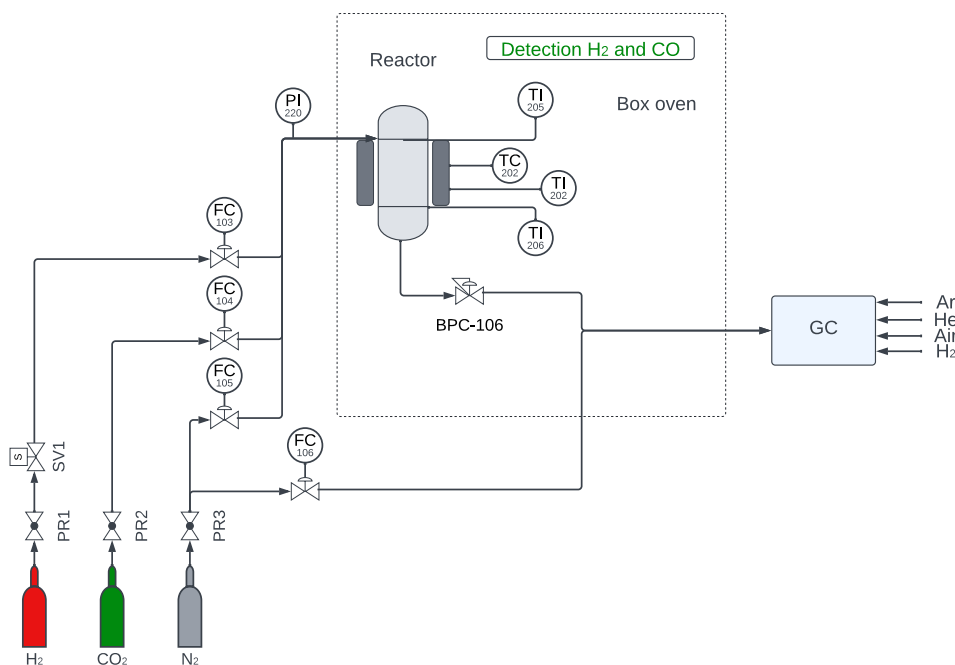


Figure 5.1. Schematic representation of the experimental setup used for the catalytic tests. Gases (H_2 , CO_2 and N_2) are fed from bottles (Linde). FC indicates mass flow controllers, TI and TC represent thermocouples and controllers, respectively. Pressure is controlled via a back pressure control system (BPC).

5.2.2 Membrane material and characterization

The carbon molecular sieve membrane (CMSM) was prepared following the procedure described in Chapter 3 (i.e., one-dip dry carbonization step method). To ensure a good balance between water permeance and selectivity, the dipping solution was prepared with a boehmite content of 0.8 wt % and the carbonization temperature was set to 600 °C (in line with the results of Chapter 3-4). In addition, to guarantee a better adherence of the carbon layer to the ceramic support, a 1:1 dilution of the dipping solution with the NMP solvent was applied in this case. This dilution resulted in a decrease in viscosity, and thus a thinner carbon layer, as proved in Chapter 3. As a result, a higher water permeance and lower vapor/gas selectivity than those reported in previous chapters are to be expected.

Although the prepared CMSM does not correspond to the optimized membrane, as identified in the previous chapters, this study aims at proving the concept of the packed bed membrane reactor technology and, at the same time, at validating the reactor model described in Chapter 6 and later used in Chapter 7 for the reactor scale-up and process design.

The membrane was cut and sealed using two metallic tubes: 1) a dead end tube and 2) a tube welded to a Swagelok connection. The tubes were connected to the membrane with a hydraulic crimping machine (FINN-POWER), applying a pressure of 20 psi and using graphite tape for the deformation as well as to protect the membrane. After sealing, a CMSM with total active length of 3.7 cm was obtained, as shown in **Figure 5.2**.



Figure 5.2. Carbon molecular sieve membrane sealed with a dead end metallic tube from one side, and a metallic tube with a Swagelok connection on the other side.

Prior to the reaction tests, the membrane permeation properties were tested. The permeation tests were carried out with the same procedure and experimental setup described in Chapter 3 and 4. Vapor/gas separation performance were derived via binary mixture tests, exposing the membrane to an equimolar mixture of H₂O and one of each gas (i.e., H₂, CO₂, CO and DME). The permeance of methanol was derived via pure vapor permeation tests. The tests were carried out with a total pressure gradient (ΔP) across the membrane of 3 bar and in the temperature range of 200-260 °C, which is relevant for the reaction.

5.2.3 Packed bed membrane reactor setup and testing

A schematic representation of the setup used for the packed bed membrane reactor (PBMR) tests is given in **Figure 5.3**. The membrane reactor is a stainless-steel vessel (OD 28.5 mm, L 150 mm) with a top flange for the connection of the membrane tube. Both a sweep gas and a permeate line are connected to the inner side of the membrane via the top flange. The catalyst bed is placed in the outer space. Gases (H₂, CO₂ and N₂) are fed via mass flow controller (FC) from Bronkhorst, from gas cylinders (Linde). N₂ is only fed during the reduction protocol (FC105) and during reaction tests as external standard (FC106), to dilute both the retentate and permeate stream, via a three-way valve (3WV). H₂ and CO₂ are fed both in the reaction zone (FC103 and FC104), and in the sweep gas (FC101 and FC102), to limit the permeation of reactants, as proposed in Chapter 2. The pressure in the reaction and permeation zone is regulated via two back pressure controllers BPC106 and BPC107, respectively, and measured via pressure indicators PI110 and PI220,

upstream the reactor. The membrane reactor is heated via an external jacket through the temperature control system TC202-TI202. The reactor is then placed in an electric oven to also preheat the feed lines. Temperature is measured inside the membrane tube (TI205), at the entrance of the catalytic bed (TI207) and at the exit of the catalytic bed (TI206), in order to monitor whether the operation is isothermal. The retentate and the permeate lines can be sent to the analysis section via a six-way valve (6WV), after dilution with the N₂ stream, as described above. Both the retentate and permeate mixture were analyzed with the same compact gas chromatograph described in Section 5.2.1.

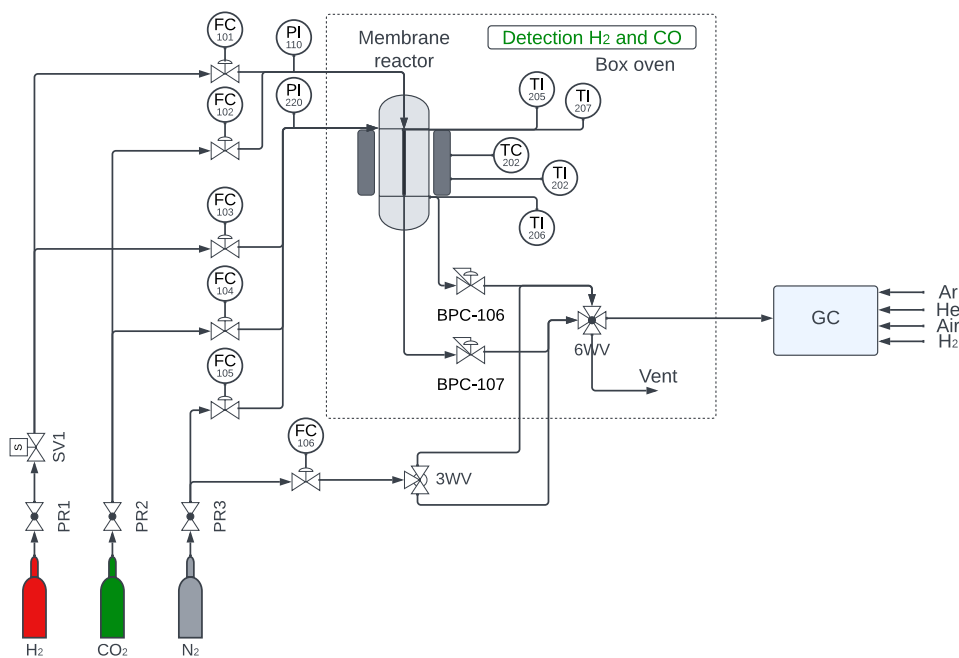


Figure 5.3. Schematic representation of the experimental setup used for the PBMR tests. Gases (H₂, CO₂ and N₂) are fed from bottles (Linde). FC indicates mass flow controllers, TI and TC represent thermocouples and controllers, respectively. Pressure is controlled via a back pressure control system (BPC). 3WV and 6WV corresponds to the 3-way and 6-way valves respectively.

Once connected the membrane to the top flange, the reactor was closed and packed via a funnel, as follows (from bottom to top):

1. A layer of quartz wool (ca. 5 mL).
2. 25 g (ca. 15 mL) of SiC (100-150 μm), to fill the volume corresponding to the bottom metallic connection of the membrane.
3. 20 mL of catalyst bed, composed of: 1.5 g of CuO/ZnO/Al₂O₃, 1.5 g of HZSM-5 and 25 g of SiC, with an average particle size of 100-150 μm .
4. 25 g (ca. 15 mL) of larger (250 μm) SiC, to fill the volume corresponding to the top metallic connection of the membrane and to function as a preheating bed, given the high thermal conductivity of SiC.

In this configuration, the catalyst is only in contact with the membrane active layer, while inert material (SiC) is used to dilute the catalyst to prevent hot spots formation and, at the same time, to ensure the desired aspect ratio of the catalyst bed.

To properly compare the two reactor technologies under the same conditions, the packed bed reactor (PBR) experiments were repeated using the configuration shown in **Figure 5.3** and packing procedure described above, but replacing the membrane with a stainless steel tube with the same size of the CMSM.

Prior to the reaction tests, the catalyst was reduced in-situ at 280 °C with a mixture of 100 mL/min 50 vol. % H₂ in N₂ for 24h. In the PBMR configuration, 100 mL/min of H₂ was also fed in the sweep gas, to prevent H₂ permeation. Thereafter the reaction tests were carried out in the temperature range 200-260 °C, a pressure of 40 bar, H₂:CO₂ molar ratio of 3 both in the feed to the reaction zone and in the sweep gas, a GHSV in the range 400-2600 NL kg_{cat}⁻¹ h⁻¹. The ΔP was varied from 0 to 3 bar and a sweep gas ratio (SW) ranging from 1 to 5 was used. An overview of the experiments carried out is given in **Table 5.2**. Prior to each experiment, the PBMR_1 test was repeated to confirm that either the membrane or the catalyst were stable. A stability test was finally performed in the conditions of PBMR_5 for 120 h.

Table 5.2. Overview of the PBMR and PBR experiments carried out with the corresponding operating conditions.

ID (-)	GHSV (NL kg _{cat} ⁻¹ h ⁻¹)	T (°C)	P ^R (bar)	ΔP (bar)	SW (-)	(H ₂ :CO ₂)* (-)
PBMR_1	400	200	40	0	1	3
PBMR_2	1300	200	40	0	1	3
PBMR_3	2600	200	40	0	1	3
PBMR_4	400	200	40	0	3	3
PBMR_5	400	200	40	0	5	3
PBMR_6	400	220	40	0	5	3
PBMR_7	400	240	40	0	5	3
PBMR_8	400	260	40	0	5	3
PBMR_9	2600	200	40	1.5	1	3
PBMR_10	2600	200	40	3	1	3
PBR_1	400	200	40	-	-	3
PBR_2	1300	200	40	-	-	3
PBR_3	2600	200	40	-	-	3
PBR_4	400	220	40	-	-	3
PBR_5	400	240	40	-	-	3
PBR_6	400	260	40	-	-	3

*In the PBMR tests, the same H₂:CO₂ was used for both the reaction zone feed and the sweep gas

The reaction performance in terms of CO₂ conversion (X_{CO_2}) and product yield (Y_i), were determined using the methodology reported in Chapter 2. The removal of water was quantified for each PBMR experiment, along with the removal of each product (i.e., MeOH, DME, CO), generalizing the formula reported in Chapter 2 (WR) according to Eq. 5.1 (R_i).

$$R_i = \frac{F_i^P}{F_i^P + F_i^R} \quad (5.1)$$

The loss (L_i) or cofeeding (CoF_i) of reactants (i.e., CO₂ and H₂), was calculated as follows:

$$L_i = \frac{F_{i,tmb}}{F_{i,0}^R} \quad \text{if } F_{CO_2,tmb} \geq 0 \quad \text{Reactant loss} \quad (5.2)$$

$$CoF_i = \frac{-F_{i,tmb}}{F_{i,0}^R} \quad \text{if } F_{CO_2,tmb} < 0 \quad \text{Reactant cofeeding} \quad (5.3)$$

Where the transmembrane flow ($F_{i,tmb}$) for the reactants was calculated as reported in Chapter 2.

5.3 MODELING

The 1D-pseudo homogeneous PBR and PBMR reactor model described in section 6.6 (Chapter 6) were used to simulate the experiments carried out in this chapter. Being the catalyst particle size in the order of 50-125 μm , internal mass transfer limitations were neglected. Furthermore, in all experimental conditions, temperature gradients along the catalyst bed, as well as between reaction and permeation zone, were found negligible. Thus, the model was considered isothermal. Finally, the concentration polarization phenomena was accounted for by implementing the correlation developed in Chapter 6 (section 6.7).

First, the kinetic model of Portha et al. [22] for the methanol synthesis, combined with the kinetic model of Ortega et al. [23] for the methanol dehydration, were validated with the experimental data obtained with the differential reactor (section 5.2.1). This validation is reported in Appendix E (**Figure E1**).

Thereafter, the permeance of each species as a function of temperature derived experimentally for the CMSM were fitted with an Arrhenius law (see Appendix D, **Figure D7**), similarly to what is done in Chapter 6 and 7, in order to implement the membrane properties in the reactor model.

5.4 RESULTS AND DISCUSSION

5.4.1 Catalyst properties and activity tests

The physical properties of the CuO/ZnO/Al₂O₃ (CuZA) and HZSM-5 catalyst are summarized in **Table 5.3**. The apparent density of the catalyst ($\rho_{\text{b,cat}}$) was calculated via the catalyst porosity (ϵ_{cat}), determined from the N₂ physisorption analysis.

The TPR profile of the CuZA catalyst (see Appendix D, **Figure D2**) exhibits three peaks after deconvolution at 212 °C, 228 °C and 242 °C. No further reduction of the support, due for example to H₂ spillover, was measured. Therefore, a reduction temperature of 280 °C, as suggested also in literature [24], is believed to be sufficient to reduce all the CuO prior to the reaction tests. The XRD pattern on the calcined and reduced catalyst (see Appendix D, **Figure D3**) show the typical diffraction peaks of CuO at 2θ of 35.5° and 38.7°, and those of Cu at 2θ of 43.3° and 50.4°, respectively. Note that CuO crystals smaller than 3-5 nm as well as the Cu that is in contact with the Zn phase cannot be detected. Thus, the disappearance of the CuO peak in the XRD pattern of the reduced sample does not necessarily exclude the presence CuO crystals. The average diameter of the Cu-crystals (d_{Cu}), estimated via the Scherrer's equation, was 11.7 nm. According to literature, Cu crystals larger than 8.5 nm minimize CO formation during methanol synthesis, and methanol formation does not depend on the Cu-size when $8.5 \text{ nm} \leq d_{\text{Cu}} \leq 37.3 \text{ nm}$ [25].

The NH₃-TPD profile of the HZSM-5 catalyst (see Appendix D, **Figure D4**) consists of two characteristic desorption peaks: the low temperature (LT) peak at 213 °C and the high temperature (HT) peak at 414 °C, corresponding to weak and

strong acid sites, respectively [26], [27]. The amount of acid sites derived from the TPD curve is reported in **Table 5.4**.

Table 5.3. Physical properties of the CuO/ZnO/Al₂O₃ (CuZA) and HZSM-5 catalyst

Property	CuZA	HZSM-5
Surface area, <i>S. A.</i> (m ² /g)	112.1	204.9
Pore volume, <i>P. V.</i> (cm ³ /g)	0.2576	0.1306
Average pore diameter, <i>P. D.</i> (nm)	7.06	0.55
Catalyst solid density, ρ_{cat} (g/cm ³)	1.926	1.201
Catalyst apparent density, $\rho_{b,cat}$ (g/cm ³)	1.300	0.720

Table 5.4. Characteristic of the NH₃-TPD profile of the HZSM-5

Temperature peak (°C)		NH ₃ uptake (μmol/g)		
LT-peak	HT-peak	Weak	Strong	Total
213	414	344	319	664

The DME (Y_{DME}), methanol (Y_{MeOH}) and CO yield (Y_{CO}) as a function of temperature at 40 bar, measured with a GHSV of 3400 NL kg_{cat}⁻¹ h⁻¹ and a feed composition of CO₂/H₂/N₂ = 3/9/1 is depicted in **Figure 5.4a**. The yield of all products expectedly increases with temperature, since the operation is kinetically limited (i.e., thermodynamic equilibrium is not yet achieved) at the tested GHSV. The Y_{DME} and Y_{CO} show a crossover behaviour at 220 °C. In particular, for a $T \leq 220$ °C, $Y_{DME} > Y_{CO}$ (i.e., DME selectivity larger than 70%); for a $T \geq 220$ °C, the situation is reversed. At the same time, Y_{MeOH} is limited, indicating that methanol is effectively converted to DME. The same trend repeats at all pressures and H₂:CO₂ ratios (see Appendix D, **Figure D5** and **Figure D6**). However, both pressure and H₂ concentration affect positively the CO₂ conversion (X_{CO_2}) and the DME selectivity, leading to a shift in the Y_{DME} - Y_{CO} crossover point towards higher temperatures.

Besides DME, methanol and CO, no other products were detected, and full carbon balance was closed with a maximum error of 3%. Thus, the experiments do not reveal any evidence of side reactions (e.g., methanol to gasoline).

In addition, the product yield measured at 250 °C (**Figure 5.4b**) did not show any significant changes within 40 h of time on stream, indicating that, in these conditions and timespan, catalyst deactivation appears to be negligible.

Finally, the experimental data obtained in this study were used to validate the kinetic model described in Chapter 6 (see Appendix E, section E.1). The alignment between kinetic predictions and experimental data further supports the absence of deactivation or any other phenomena that would otherwise alter kinetic activity of the catalyst upon operation.

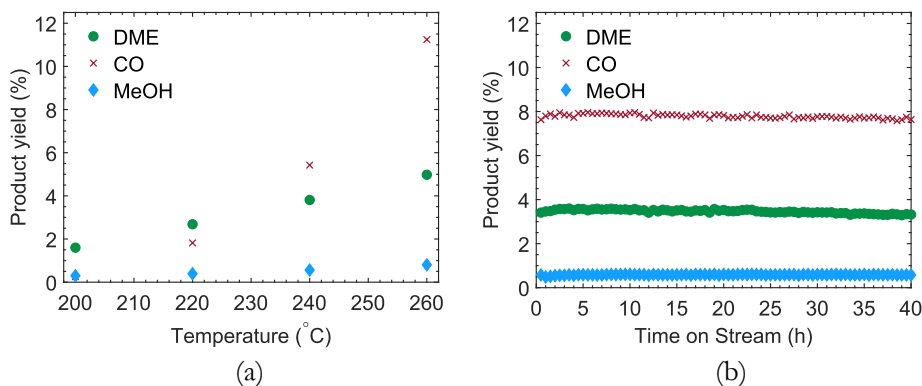


Figure 5.4. DME, Methanol and CO yield as a function of temperature (a) and as a function of the time on stream at 250 °C (b) measured at $3400 \text{ ML kg}_{\text{cat}}^{-1} \text{ h}^{-1}$ and a feed composition of $\text{CO}_2/\text{H}_2/\text{N}_2 = 3/9/1$.

5.4.2 Separation performance of the CMSM

The membrane properties in terms of water permeance ($\phi_{\text{H}_2\text{O}}$) and perm-selectivity ($S_{\text{H}_2\text{O}/i}$) derived at 200 °C are reported in **Table 5.5**. For comparison, the average properties of the membranes studied in Chapter 3 and 4, as well as the target properties set via the optimization study presented in Chapter 2 are also reported. It is clear that the target $\phi_{\text{H}_2\text{O}}$ was successfully achieved in the membranes studied in Chapter 3-4, while the targets in $S_{\text{H}_2\text{O}/i}$ were in most cases not achieved. With respect to the new membrane prepared in this chapter, it evidently has a much greater permeance (i.e., $\phi_{\text{H}_2\text{O}}$ in the order of $10^{-6} \text{ mol}\cdot\text{Pa}^{-1}\cdot\text{m}^{-2}\cdot\text{s}^{-1}$), and a consequently lower selectivity (i.e., $S_{\text{H}_2\text{O}/i}$, especially for the $\text{H}_2\text{O}/\text{CO}_2$, $\text{H}_2\text{O}/\text{CO}$ and $\text{H}_2\text{O}/\text{MeOH}$ pairs) than the previous membranes. This is in line with the decrease in carbon layer thickness of this new membrane with respect to the previous, as discussed in section 5.2.2. Nevertheless, an improvement of the separation properties (i.e., increase in selectivity) could be obtained by depositing one or more carbon layers on top of the first one, using the same synthesis method described in previous chapters.

In general, the highest $\phi_{\text{H}_2\text{O}}$ corresponds to the lowest $S_{\text{H}_2\text{O}/i}$ in the range reported in **Table 5.5**. For all membranes, $S_{\text{H}_2\text{O}/\text{H}_2}$ is always the smallest perm-selectivity, due to the very similar size of the two molecules. Indeed, despite capillary condensation phenomena, H_2O and H_2 are believed to compete for their access to the molecular sieving pores, as discussed in previous chapters. Furthermore, $S_{\text{H}_2\text{O}/\text{CO}}$ is always greater than $S_{\text{H}_2\text{O}/\text{CO}_2}$, since CO_2 shows significant affinity to the membrane surface, favoring adsorption diffusion over molecular sieving for some membranes. On the other hand, $S_{\text{H}_2\text{O}/\text{CO}}$ and $S_{\text{H}_2\text{O}/\text{MeOH}}$ show the expected behavior, based on the predictions of Chapter 2, and the corresponding values achieve the target in most of the cases.

Given the challenges in working with DME in a laboratory setting (due to its vapor/gas equilibrium at room conditions), the permeance of DME through CMSM could not be measured in previous chapters of this thesis. Nevertheless, this parameter was believed to be less relevant for the optimization/selection of the CMSM, as already explained in Chapter 2. For the first time in this thesis, the permeance of DME is measured in this work. Interestingly, ρ_{DME} was found to decrease strongly with temperature (see Appendix D, **Figure D7**), indicating that adsorption diffusion is the dominant transport mechanism for DME. Its activation energy is quite large when compared to CO_2 (i.e., -163 vs -4.09 $\text{kJ}\cdot\text{mol}^{-1}\text{K}^{-1}$) and the $S_{\text{H}_2\text{O}/\text{DME}}$ spikes from 2.61 to 237 when temperature increases from 200 to 260 °C. This means that DME adsorbs more strongly on the CMSM surface, such that its transport due to surface diffusion is more limited at higher temperatures.

Table 5.5. Properties of the membrane of this work compared to the average properties of the CMSM studied in Chapter 3 and 4 and to the target set via the optimization proposed in Chapter 2. All membrane properties are reported at 200 °C

Membrane property	Target	CMSM Chapter 3-4	CMSM of this Chapter
$\rho_{\text{H}_2\text{O}}$ ($\text{mol}\cdot\text{Pa}^{-1}\text{m}^{-2}\text{s}^{-1}$)	$4\cdot 10^{-7}$	$(1.25\text{-}7.54)\cdot 10^{-7}$	$1.39\cdot 10^{-6}$
$S_{\text{H}_2\text{O}/\text{H}_2}$ (-)	50	1.68-6.74	2.06
$S_{\text{H}_2\text{O}/\text{CO}_2}$ (-)	30	5.33-14.6	2.37
$S_{\text{H}_2\text{O}/\text{CO}}$ (-)	30	8.90-49	3.99
$S_{\text{H}_2\text{O}/\text{MeOH}}$ (-)	10	4.01-17	2.39
$S_{\text{H}_2\text{O}/\text{DME}}$ (-)	—	—	2.61

More details on the permeation properties of this membrane as a function of temperature are reported in Appendix D.

5.4.3 Packed bed membrane reactor performance and model validation

Effect of the GHSV

The reactor model describes quite accurately the performance of both the PBR and PBMR as a function of the GHSV in terms of CO_2 conversion (**Figure 5.5a**) and product yield (**Figure 5.5b**). As displayed in **Figure 5.5**, the PBMR outperforms the PBR in the entire range of GHSV explored, with greater improvement as the GHSV decreases (i.e., closer to thermodynamic equilibrium), as reported in **Table 5.6**. At lower GHSV, the concentration of water in the reaction zone is higher, which makes its removal via the CMSM more effective.

Nevertheless, the improvement in the Y_{DME} is considerably lower than the increase in the Y_{CO} . This is partly explained by a relatively low concentration of methanol in the reaction zone, which limits the extent of DME synthesis. Indeed, despite CO and DME removal being quite similar (i.e., 45% and 47% at GHSV of 400 $\text{NL kg}_{\text{cat}}^{-1} \text{h}^{-1}$, respectively), methanol is being removed as much as water (i.e., 52 and 49% at GHSV of 400 $\text{NL kg}_{\text{cat}}^{-1} \text{h}^{-1}$, respectively). This behavior is also discussed in

Chapter 7, where it is observed that even for large $S_{H_2O/MeOH}$ (ca. 5), the methanol loss through the membrane notably decreases the Y_{DME} in the PBMR.

Severe removal of CO, as measured within the PBMR experiments, is detrimental for this process because, together with water removal, it enhances the rWGS reaction considerably, leading to unselective CO_2 and H_2 consumption. At the same time, the permeated CO cannot be further converted to methanol (i.e., via the CO hydrogenation). This explains the higher selectivity to CO obtained in the PBMR with low $S_{H_2O/CO}$ (i.e., 26.3% vs 35% obtained at a GHSV of $400 \text{ NL kg}_{cat}^{-1} \text{ h}^{-1}$ with the PBR and PBMR, respectively).

An effective solution to prevent methanol permeation is the recirculation of permeated methanol in the sweep gas together with H_2 and CO_2 , as a way to decrease the driving force across the membrane. However, this solution could not be tested experimentally due to the setup limitations (i.e., the setup does not have a recirculation loop, and no feeding system for methanol).

In principle, this solution could be adopted also to prevent CO permeation. Nevertheless, according to the PBMR modeling predictions (see Chapter 6 and 7) with the membrane properties discussed in Chapter 3-4 (i.e., which met the target set in Chapter 2 for $S_{H_2O/CO}$), the removal of CO is not relevant. Thus, in such condition, the improvement in DME yield becomes similar to the those in CO_2 conversion, meaning that the product distribution is not much affected with respect to the PBR.

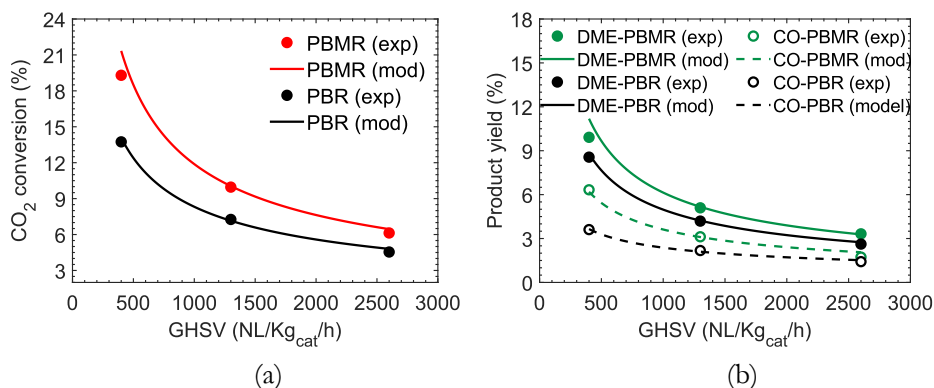


Figure 5.5. CO_2 conversion (a) and DME and CO yield (b) as a function of the GHSV for both the PBR and PBMR derived experimentally (markers) and via simulations (continuous lines). Other operating conditions: $P^R=40$ bar, $T=200$ °C and a feed composition of $H_2/CO_2 = 3$; a $SW=1$ and $\Delta P=0$ bar were used for the PBMR.

Table 5.6. Improvement of the reaction performance (CO₂ conversion, DME yield and CO yield) of the PBMR with respect to the PBR evaluated experimentally.

Reaction performance	Improvement determined at GHSV of:		
	400 NL kg _{cat} ⁻¹ h ⁻¹	1300 NL kg _{cat} ⁻¹ h ⁻¹	2600 NL kg _{cat} ⁻¹ h ⁻¹
CO ₂ conversion	+40.5%	+37.3%	+34.9%
DME yield	+26.8%	+21.8%	+15.8%
CO yield	+75.3%	+43.1%	+21.8%

Effect of the SW ratio

As thoroughly studied in Chapter 2 using modeling tools, **Figure 5.6a** demonstrates experimentally that large SW ratios indeed increase the reaction performance (i.e., CO₂ conversion and product yield). Greater SW ratios remarkably increase the extent of product removal (**Figure 5.6b**). Indeed, the water removal (R_{H_2O}) increases from 52% to 80% along with the removal of all the other products, from 45-47% to 65-68%, upon increasing SW from 1 to 5, respectively, with the R_{DME} being the lowest. As already discussed, this leads to a larger improvement in the CO rather than the DME formation with respect to the PBR (i.e., 66% and 112% improvement for Y_{DME} and Y_{CO} , respectively, at SW of 5).

Furthermore, as also observed via the model prediction in Chapter 2, a low S_{H_2O/H_2} and/or S_{H_2O/CO_2} , in this particular reactor configuration (i.e., circulation of a sweep gas containing the reactants), leads to the back-permeation of reactants from the permeation to the reaction zone. Indeed, larger SW ratios leads to a more efficient removal of the water, which, as a consequence, increases CO₂ and H₂ conversion. As a result, the CO₂ and H₂ concentration in the reaction zone decreases axially, while their concentration in the permeation zone is barely affected due to the high dilution of the permeating species in the sweep gas. Thus, given their transmembrane concentration gradient, the CO₂ and H₂ permeate towards the reaction zone (i.e., CO₂ and H₂ cofeeding).

However, **Figure 5.6b** shows that the extent of CO₂ and H₂ cofeeding (CoF_{CO_2} and CoF_{H_2}) is not significantly affected by the SW ratio in this range (i.e., SW of 1-5). This could be attributed to the significantly high ϕ_{CO_2} and ϕ_{H_2} for this CMSM, which leads to a significant CoF_{CO_2} and CoF_{H_2} of ca. 28% and 19%, respectively, already at SW of 1.

Finally, **Figure 5.6a** shows that the PBMR model developed in Chapter 2 and 6 describes very well the reaction performance, including the effect of SW ratio. Nevertheless, the model slightly underpredicts the Y_{CO} and Y_{MeOH} , while it estimates a slightly higher Y_{DME} . This discrepancy is explained by the fact that the membrane properties have been measured with binary mixture (i.e., vapor/gas), rather than with a multicomponent system. Thus, interactions among the species are neglected also in the model. However, given its large kinetic diameter, DME is expected to

permeate less when competing with the other species in the system, which could explain the lower Y_{DME} measured experimentally.

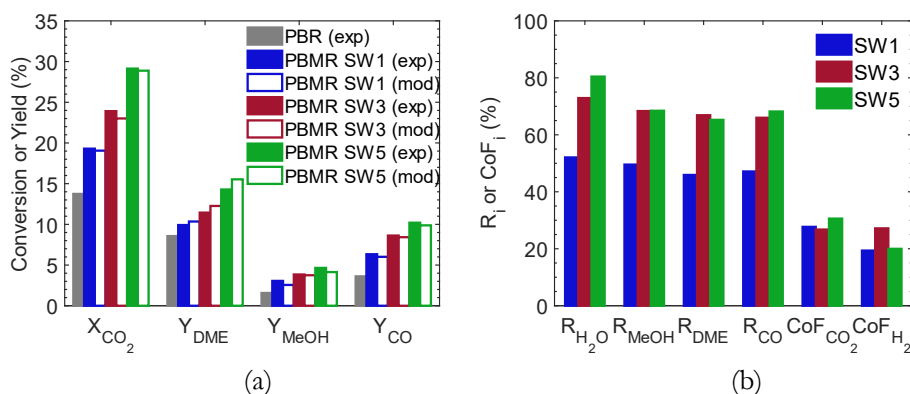


Figure 5.6. CO_2 conversion and product yield (a) and product removal/reactant cofeeding (b) for the PBMR at different SW ratios (1,3, and 5) derived experimentally and via simulations, in comparison with the reaction performance of the PBR obtained in the same conditions. Other operating conditions: $P^{\text{R}}=40$ bar, $T=200$ °C, a GHSV of $400 \text{ ML kg}_{\text{cat}}^{-1} \text{ h}^{-1}$ and a feed composition of $\text{H}_2/\text{CO}_2 = 3$; $\Delta P=0$ bar were used for the PBMR.

Effect of temperature

The effect of temperature on the reaction performance is depicted in **Figure 5.7**, where the thermodynamic limit is also reported for comparison. In these experiments, a SW of 5 was used given the results reported in the previous paragraph. The PBMR and PBR models accurately describe also the effect of temperature on the CO_2 conversion and product yield, predicting a slightly higher Y_{DME} and lower Y_{CO} and Y_{MeOH} for the PBMR, with respect to their experimental values, as previously discussed.

Given the low GHSV used in these experiments, the system is more affected by the thermodynamic equilibrium, especially at high temperature, which corresponds to faster reaction rates. Indeed, CO_2 conversion and product yield of the PBR achieve their thermodynamic limit at 260 °C (i.e., continuous line in **Figure 5.7**). It should be noted that the Y_{CO} of the PBR is slightly larger than its thermodynamic value for temperatures below 260 °C. Since CO is not only a product in this reaction network, but also a reactant for the methanol synthesis (i.e., reversible reactions in series), a Y_{CO} beyond the thermodynamic curve indicates that the extent of CO conversion to methanol is not at its maximum value (i.e., CO hydrogenation has not achieved equilibrium). More details on this observation are given in Appendix D. As a matter of fact, the profile of Y_{CO} in a conventional PBR is characterized by a maximum, after which CO starts to react to form methanol and finally achieves thermodynamic equilibrium.

The behavior of the PBMR with temperature is more complex than that in the PBR, due to the alteration of the thermodynamic equilibrium caused by the

product/reactant separation. Nevertheless, since the membrane removes products more effectively when their concentration in the reaction zone is higher (i.e., closer to the thermodynamic equilibrium), the PBMR trend with temperature resembles that of the PBR.

From **Figure 5.7a**, it is clear that the introduction of the membrane enhances the CO₂ conversion in the entire temperature region explored (i.e., 200–260 °C), exceeding thermodynamic equilibrium for temperatures greater than 220 °C. As a matter of fact, water is the main reaction by-product of both the rWGS and CO₂ hydrogenation to methanol and DME, which means that the in-situ removal of water, and any other products, positively affects CO₂ conversion.

However, a higher X_{CO₂} does not necessarily mean a higher selectivity to the desired product. Indeed, **Figure 5.7b** clearly shows that the improvement in Y_{DME} becomes negligible for temperature higher than 200 °C, dropping from 67% to 8.7% at 260 °C. This indicates that at the highest tested temperature, the PBMR leads to a lower Y_{DME} than the PBR. This behavior is explained by the extremely high extent of product removal obtained in these conditions. Indeed, for temperatures above 200 °C, R_i achieves ca. 98–99% for all products, indicating that all methanol is being removed from the reaction zone and cannot be effectively converted to DME. As a consequence, Y_{DME} never exceeds its thermodynamic limit in these conditions.

At the same time, as temperature increases, the PBMR considerably improves the performance of the rWGS reaction well above its thermodynamic equilibrium, leading to a Y_{CO} ca. 2.7 times higher than the PBR at 260 °C (**Figure 5.7c**). Indeed, CO formation is favored by high temperature, given the endothermicity of the reaction. In addition, due to the reaction stoichiometry, the rWGS requires a lower H₂:CO₂ ratio than the methanol synthesis, which makes it even faster and favored in these conditions, where H₂ is being removed more than CO₂ (see ϕ_1 trend vs temperature in Appendix D, **Figure D7**). All this explains why, given the similar extent of methanol and CO removal, the CO formation is favored over methanol synthesis (**Figure 5.7c and d**).

It should be noted that thermodynamic limitations are altered by the presence of the membrane. However, qualitative thermodynamic considerations are still valid, since the presence of the membrane alters the composition of the system, which corresponds to a different chemical equilibrium (i.e., dynamic equilibrium) [28].

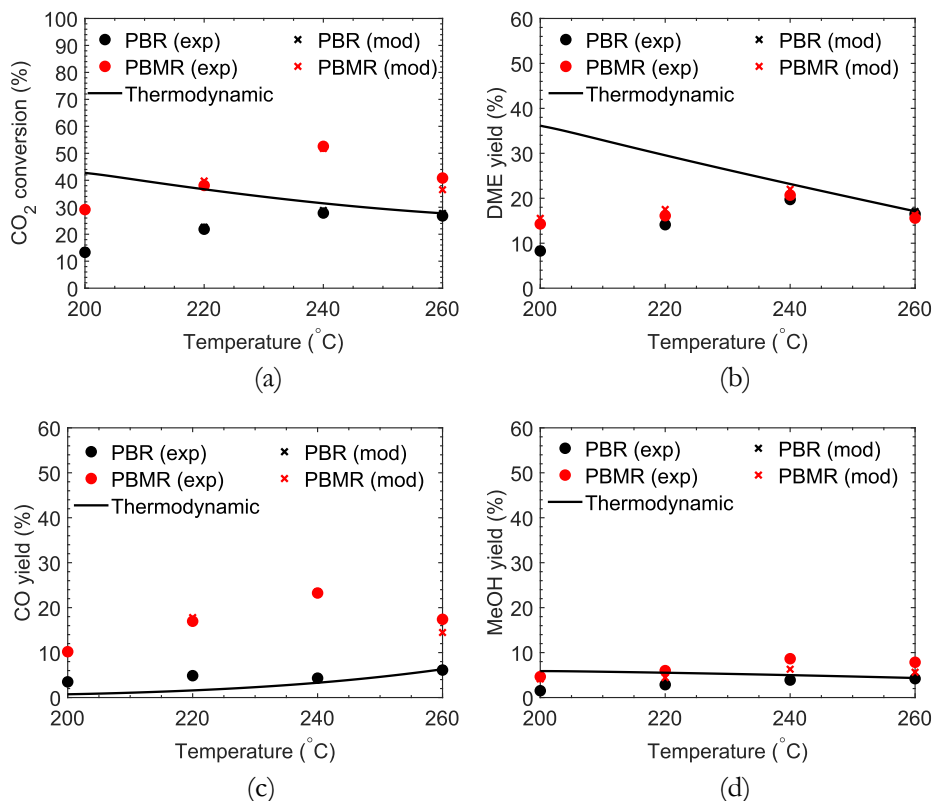


Figure 5.7. CO₂ conversion (a), DME yield (b), CO yield (c) and methanol yield (d) as a function of temperature for the PBMR and PBR derived experimentally and via simulations. Other operating conditions: $P^R=40$ bar, a GHSV of $400 \text{ ML kg}^{-1} \text{ h}^{-1}$ and a feed composition of $\text{H}_2/\text{CO}_2 = 3$; $\text{SW}=5$ and $\Delta P=0$ bar were used for the PBMR.

As already anticipated, the product removal increases to ca. 98-99% for all products as temperature increases above 200 °C, despite both $\phi_{\text{H}_2\text{O}}$ and ϕ_{MeOH} decrease with temperature, due to their permeation mechanism. However, as shown in Chapter 2, once the target permeance has been achieved, its effect on the reaction performance, including product removal, is not relevant. Given the very high permeance of the CMSM used in this work, also at the highest temperature (i.e., 260 °C), $\phi_{\text{H}_2\text{O}}$ is 2.6 times higher than its target value determined in Chapter 2. In addition, given the fast reaction rates at higher temperatures, a large gradient in the driving force across the membrane develops for all products, favoring their removal from the reaction zone.

Alongside the increase in the product removal, at higher temperature also the reactant cofeeding becomes consistently higher, with CoF_{CO_2} and CoF_{H_2} achieving ca. 130%. Note that values higher than 100% are possible due to the circulation of the sweep gas (i.e., for $\text{SW}=1$, the maximum cofeeding is 100%, which corresponds to the situation in which all the CO₂ and/or H₂ back-permeate to the reaction zone). Reactant cofeeding is also not highly beneficial to the PBMR performance. When

either CO₂ or H₂ are introduced in the reaction zone at a specific length of the catalytic bed, their residence time is lower than if they were introduced at the reactor inlet. Therefore, they do not have enough contact time with the catalyst, which overall leads to a lower conversion/yield (see Eq. 5.4-5.8).

$$X_{\text{CO}_2} = \frac{F_{\text{CO}_2,0}^{\text{R}} - F_{\text{CO}_2}^{\text{R}} - F_{\text{CO}_2,\text{tmb}}}{F_{\text{CO}_2,0}^{\text{R}} + F_{\text{CO}_2,\text{tmb}}^*} \quad (5.4)$$

$$Y_1 = \frac{N_{\text{c,i}}(F_1^{\text{R}} + F_1^{\text{P}})}{F_{\text{CO}_2,0}^{\text{R}} + F_{\text{CO}_2,\text{tmb}}^*} \quad (5.5)$$

$$F_{\text{CO}_2,\text{tmb}} = F_{\text{CO}_2}^{\text{P}} - F_{\text{CO}_2,0}^{\text{P}} \quad \text{CO}_2 \text{ transmembrane flow} \quad (5.6)$$

$$F_{\text{CO}_2,\text{tmb}}^* = 0 \quad \text{if } F_{\text{CO}_2,\text{tmb}} \geq 0 \quad \text{Reactant loss} \quad (5.7)$$

$$F_{\text{CO}_2,\text{tmb}}^* = -F_{\text{CO}_2,\text{tmb}} \quad \text{if } F_{\text{CO}_2,\text{tmb}} < 0 \quad \text{Reactant cofeeding} \quad (5.8)$$

Effect of the ΔP

Experiments with a ΔP larger than 0 were particularly difficult to conduct, given the very high permeability of the CMSM used in this work. Indeed, as soon as a slightly positive ΔP is imposed, even with no reaction, all the gas permeates from the reaction to the permeation zone, leading to a drop in the retentate pressure (P^{R}), until it equilibrates with the permeate pressure (P^{P}). To prevent this situation, a high flow rate had to be used as feed to the reaction zone (i.e., GHSV of 2600 $\text{NL kg}_{\text{cat}}^{-1} \text{h}^{-1}$), to ensure that enough gas was left in the reaction zone to keep the pressure.

Given this initial consideration, the extent of product removal and reactant loss expectedly achieves ca. 98-99% for a $\Delta P=3$ bar (**Figure 5.8b**), which leads to very poor performance of the PBMR (i.e., CO₂ conversion 16% lower than the PBR). This was also confirmed by the simulations, where already at a length of 1.86 cm (i.e., in the middle of the PBMR), the CO₂ and H₂ flow in the reaction zone becomes zero. A similar situation applies at $\Delta P=1.5$ bar, where CO₂ and H₂ flow becomes zero at the outlet of the reaction zone (see flow profiles in Appendix D, **Figure D8** and **Figure D9**).

Thus, for a $\Delta P > 0$, the PBR outperform the PBMR both in terms of CO₂ conversion and product yield (**Figure 5.8a**). This is also predicted by the PBMR model. The slightly lower accuracy of the PBMR model in these conditions can be ascribed to the fact that when the CO₂ and H₂ concentration approaches zero, the model becomes unstable (i.e., the denominator of the kinetic rate expressions depends on these nearly zero CO₂ and H₂ partial pressures).

Better performance are expected for SW ratios larger than 1, which could not be tested due to the limitation of the MFCs.

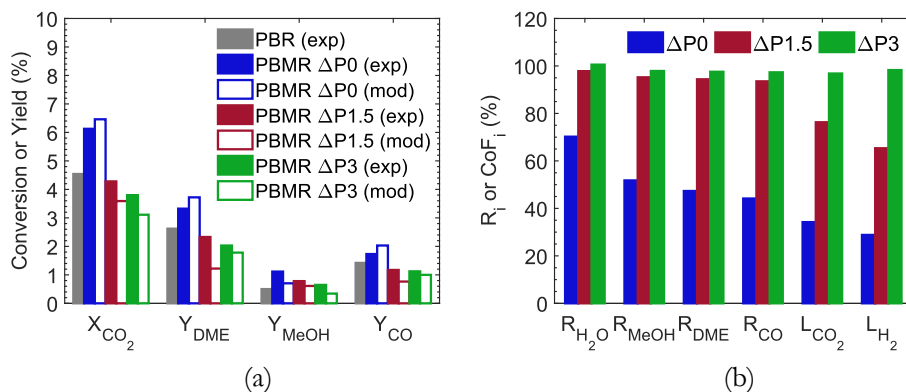


Figure 5.8. CO_2 conversion and product yield (a) and product removal/reactant cofeeding (b) for the PBMR at different ΔP (0, 1.5, and 3) derived experimentally and via simulations, in comparison with the reaction performance of the PBR obtained in the same conditions. Other operating conditions: $P^R=40$ bar, $T=200$ °C, a GHSV of $2600 \text{ NL kg}_{\text{cat}}^{-1} \text{ h}^{-1}$ and a feed composition of $H_2/CO_2 = 3$; $SW=1$ bar were used for the PBMR.

Stability test

The productivity of the PBMR in terms of DME flow rate in both retentate (F_{DME}^R) and permeate (F_{DME}^P) streams was recorded with time during the stability test (Figure 5.9). The DME flow in the permeate stream allows to identify three regions:

1. In the first region, the F_{DME}^P increases up to a maximum since the CMSM is desorbing the water previously adsorbed during the catalyst reduction step (i.e., $CuO_{(s)} + H_{2(g)} \rightarrow Cu_{(s)} + H_2O_{(g)}$). As water desorbs from the membrane pores, the active pore size increases, which corresponds to a higher DME permeance.
2. In the second region, the F_{DME}^P decreases, since the CMSM is stabilizing with the humidity content of the reaction zone. Indeed, the separation performance of carbon membranes are very sensitive to the humidity conditions, as discussed in Chapter 4. Different level of humidity corresponds to a different active pore size, which can significantly affect the extent of gas permeation and its mechanism.
3. In the third and last zone, the PBMR performance stabilize to the values reported in the previous section for this experimental conditions. Both F_{DME}^R and F_{DME}^P achieves a constant value, which leads to an overall DME yield of 14.3%.

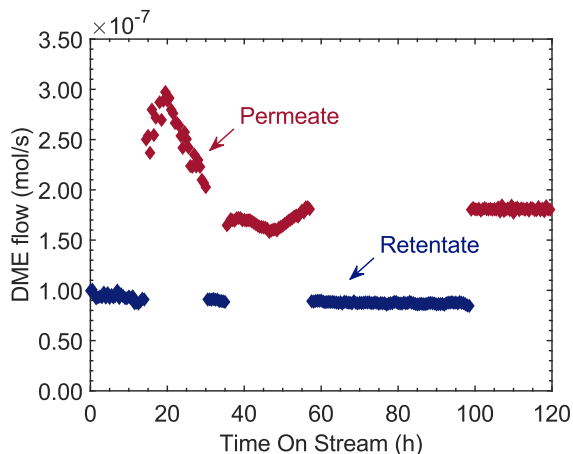


Figure 5.9. DME flow in the retentate (blue symbols) and permeate (red symbols) stream as a function of the time on stream, monitored during the stability test carried out at $P^R=40$ bar, $T=200$ °C, GHSV of $400 \text{ ML kg}_{\text{cat}}^{-1} \text{ h}^{-1}$, $SW=5$, $\Delta P=0$ and a feed composition of $\text{H}_2/\text{CO}_2 = 3$.

It should be noted that a full carbon balance was respected at all times, also during the dynamic (first and second) regions. When more DME is produced, less methanol is detected.

From this experiment, it is possible to conclude that the PBMR performance are stable in these conditions and that no deactivation phenomena are observed for neither the membrane nor the catalyst.

The PBMR performance reported in the previous sections correspond to their steady-state value (i.e., region 3). Indeed, after the reduction step, the membrane was first stabilized at the reaction temperature and under inert flow (N_2), to remove the extra water adsorbed. Thereafter, reaction was started and the performance were analysed after ca. 12 h.

5.5 CONCLUSIONS

This study demonstrates, at laboratory scale, that the incorporation of carbon molecular sieve membranes in conventional packed bed reactors allows for an improvement, in most of the cases, in the performance of the one-step CO_2 conversion to DME.

In order to demonstrate the PBMR technology, the activity of the $\text{CuO-ZnO-Al}_2\text{O}_3/\text{HZSM-5}$ bifunctional catalyst for the CO_2 hydrogenation to DME was first assessed in a PBR. The catalyst was found to be active and stable for this reaction. Furthermore, the kinetic model developed in Chapters 2 and 6 describes well the reaction performance in the range of conditions of interest for this study (i.e., 10-40 bar and 200-260 °C).

Due to small modification in the membrane preparation procedure (i.e., dilution of the dipping solution), the CMSM used in this work showed a much higher water permeance with respect to the membranes studied in the previous chapters (i.e., $\phi_{\text{H}_2\text{O}}$ one order of magnitude larger) and a consequently lower vapor/gas selectivity, especially for the $\text{H}_2\text{O}/\text{CO}_2$, $\text{H}_2\text{O}/\text{CO}$ and $\text{H}_2\text{O}/\text{MeOH}$ pairs. Despite the permeance of this CMSM not matching with the target set in Chapter 2, the PBMR was found to outperform the PBR in most of the experimental conditions. In particular, the CO_2 conversion was found to be 35%-40% higher than the PBR, for a $\text{SW}=1$ and $\Delta\text{P}=0$. Lower GHSV led to larger improvement, due to the system approaching its thermodynamic equilibrium (i.e., higher concentration of water). Nevertheless, the PBMR improves CO formation more than DME (i.e., Y_{DME} and Y_{CO} improve of 27% and 75% at a GHSV of $400 \text{ ML kg}_{\text{cat}}^{-1} \text{ h}^{-1}$, respectively), due to the considerably large extent of both CO and methanol removal from the reaction zone. Better membrane performance and the recirculation of the permeated methanol in the sweep gas would prevent this problem.

Expectedly, the SW ratio was found to have a positive effect on the reaction performance, with the removal of water achieving ca. 80% at $\text{SW}=5$. Also in this case, due to the removal of methanol and CO (ca. 70%), Y_{DME} and Y_{CO} increase of 66% and 122%, respectively, for a $\text{SW}=5$. Temperatures higher than 200 °C were found to improve the rWGS reaction more than the DME synthesis, such that at 260 °C, the Y_{DME} of the PBMR is lower than for the PBR. This is because at higher temperature, given the fast reaction rates, product removal achieves ca. 98-99% for all species, due to the very large driving force. Thus, methanol cannot be converted to DME, while the removal of CO improves the rWGS. Finally, given the high permeability of this CMSM, higher ΔP were not beneficial on the reaction performance, due to the excessive loss of reactants (98-99% for a $\Delta\text{P}=3$ bar).

The stability of the PBMR was also tested for ca. 120 h, from which it was observed that the membrane needs some equilibration time to stabilize with the humidity condition of the reaction environment, after which the reaction performance are constant over time.

The reactor model developed in Chapter 6 was found to describe the performance of both the PBR and PBMR very accurately in the range of tested conditions. Nevertheless, in some cases, the model slightly underpredicts the Y_{CO} and Y_{MeOH} , while it estimates a slightly higher Y_{DME} than the experimental value. This difference can be ascribed to the CMSM permeation properties implemented in the model, which do not account for the interactions of the species in a multicomponent system.

In conclusion, although this study was not carried out with the optimal membrane as defined in previous chapters, the improved performance of PBMR technology for the CO_2 hydrogenation to DME was demonstrated. Most importantly, the reactor models developed and extensively used in other chapters, were hereby validated. This means that, with optimal membrane properties, even better performance are to be expected. Nevertheless, as also concluded in Chapter 2, the

PBMR conditions, especially in terms of SW and ΔP , can be further optimized as a function of a specific set of membrane properties, for example to address poor perm-selectivity/high permeability issues. This guarantees robust and effective operation of the PBMR.

Appendix D

D.1 Supplementary figures

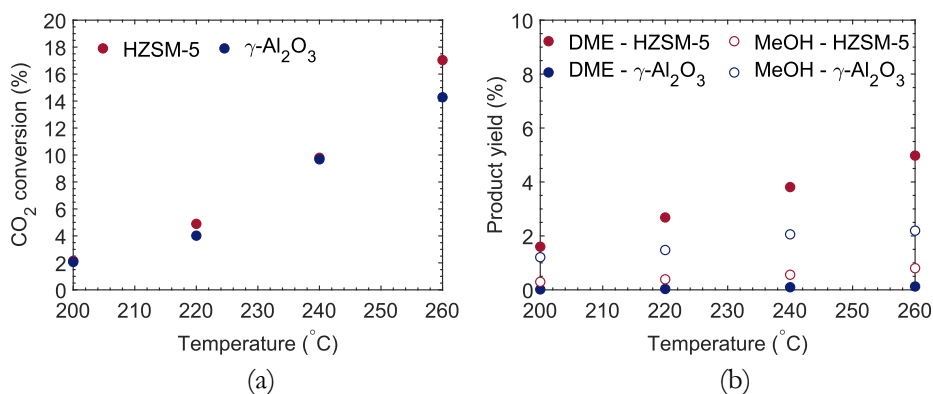


Figure D1. CO₂ conversion (a) and DME and methanol (MeOH) yield (b) as a function of temperature at 40 bar, 11630 NL kg_{cat}⁻¹ h⁻¹ and a feed composition of CO₂/H₂/N₂ = 3/9/1 measured using HZSM-5 and γ -Al₂O₃ as acid function in of the bifunctional catalyst (CuZA and acid function physically mixed with a 1:1 mass ratio).

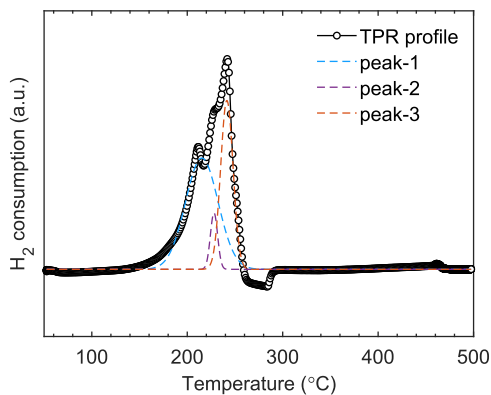


Figure D2. H₂ consumption profile of the CuO/ZnO/Al₂O₃ catalyst as a function of temperature obtained via TPR analysis. Black circles represents experimental points, while the three dashed lines result from the deconvolution.

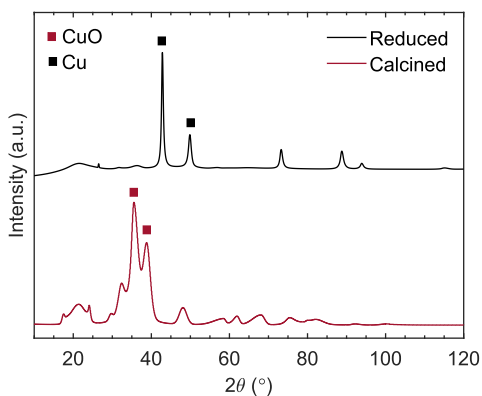


Figure D3. XRD spectra of the calcined (red line) and reduced (black line) CuO/ZnO/Al₂O₃ catalyst.

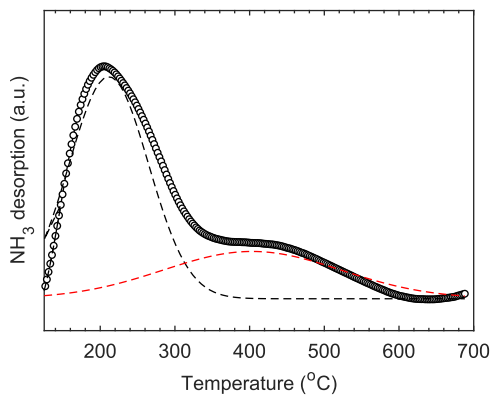


Figure D4. NH₃ desorption profile of the HZSM-5 catalyst as a function of temperature obtained via TPD analysis. Black circles represent experimental points, while the two dashed lines result from the deconvolution.

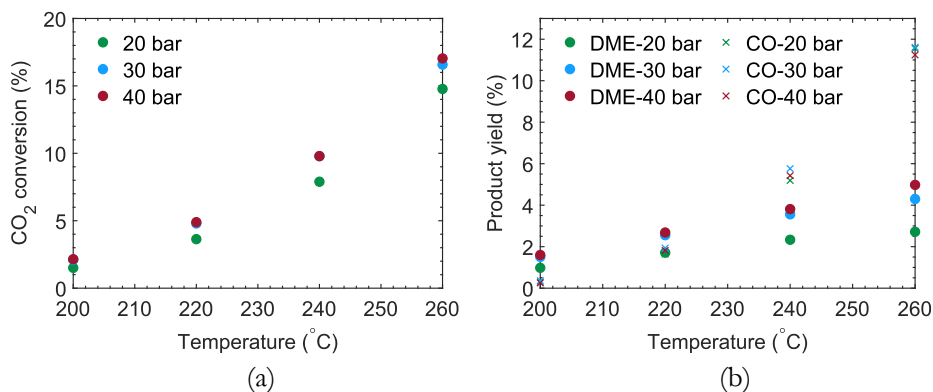


Figure D5. CO₂ conversion (a) and DME and CO yield (b) as a function of temperature at different total pressure, measured for the CuZA/HZSM-5 at a GHSV 11630 $NL\ kg_{cat}^{-1}\ h^{-1}$ and a feed composition of CO₂/H₂/N₂ = 3/9/1.

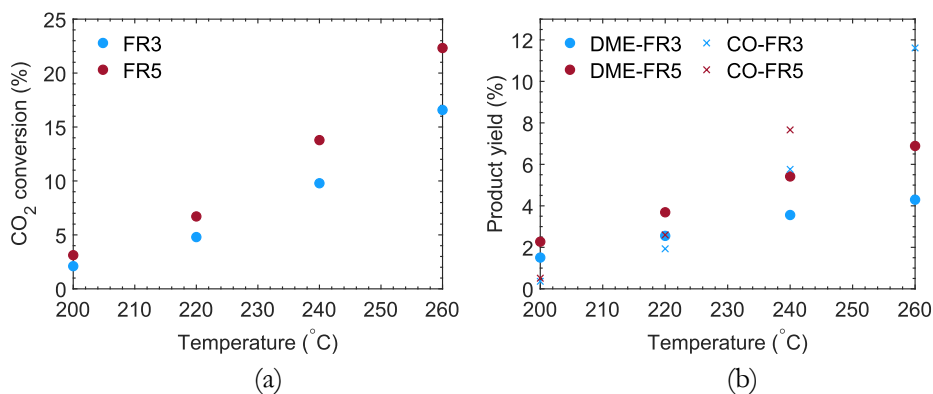


Figure D6. CO₂ conversion (a) and DME and CO yield (b) as a function of temperature at different H₂:CO₂ ratios (FR), measured for the CuZA/HZSM-5 at a GHSV 11630 $NL\ kg_{cat}^{-1}\ h^{-1}$ and a total pressure of 30 bar.

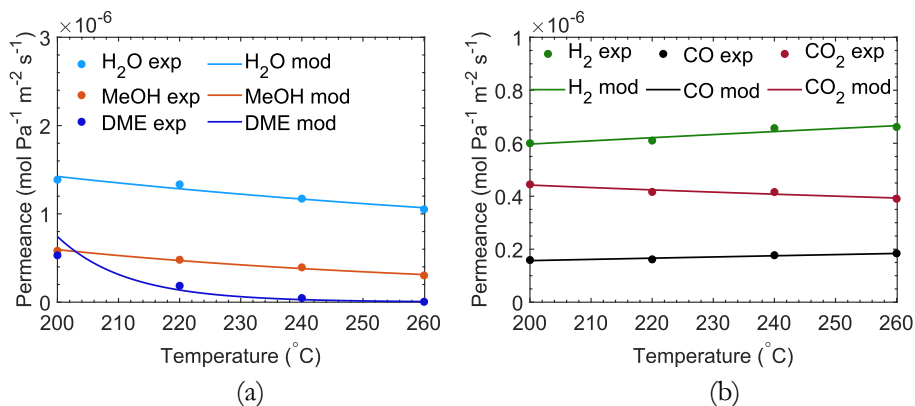


Figure D7. Membrane properties of the CMSM used in this study in terms of water, methanol and DME permeance (a) and H₂, CO and CO₂ permeance (b): markers and lines represent experimental and simulated data, respectively.

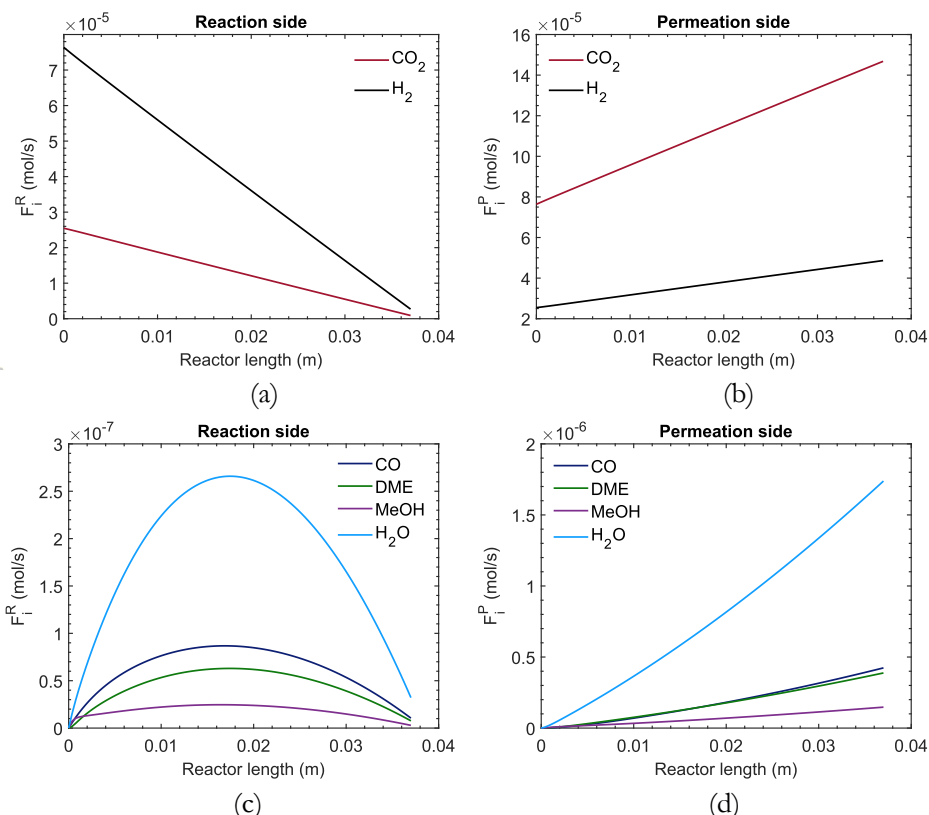


Figure D8. Flow profile of reactants in the reaction (a) and permeation zone (b) and of products in the reaction (c) and permeation zone (d) as a function of the reactor length as predicted by the PBMR model at $\Delta P=1.5$ bar, $SW=1$, $P^R=40$ bar, $T=200$ $^{\circ}\text{C}$, a GHSV of $2600 \text{ NL kg}_{cat}^{-1} \text{ h}^{-1}$ and a feed composition of H₂/CO₂ = 3.

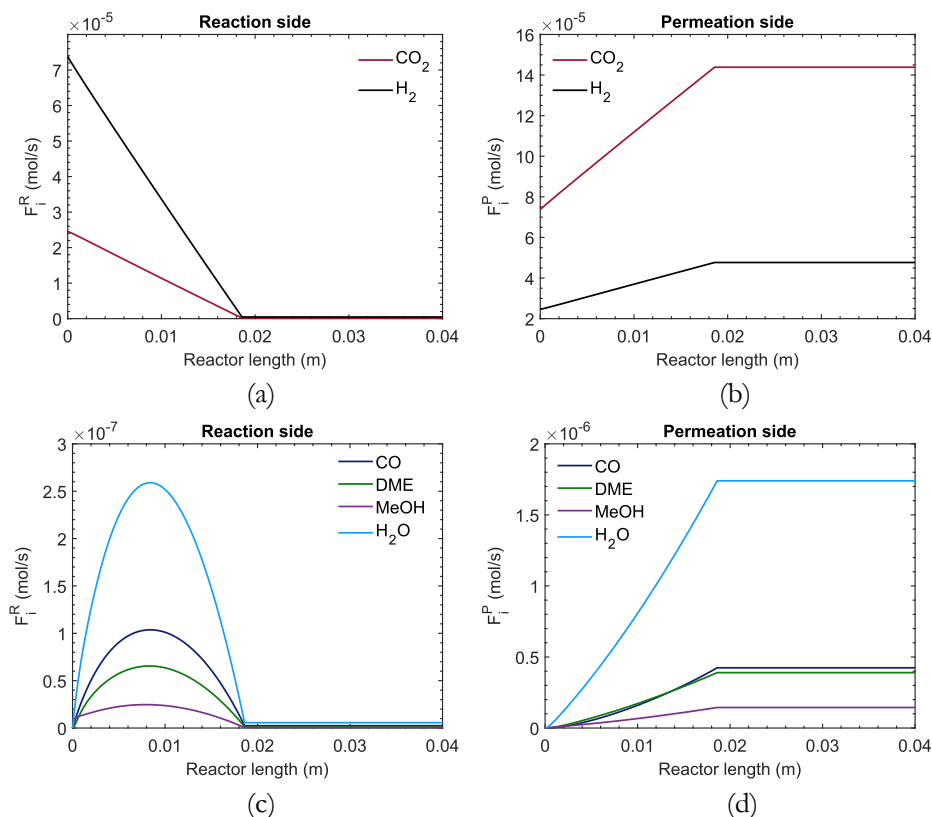


Figure D9. Flow profile of reactants in the reaction (a) and permeation zone (b) and of products in the reaction (c) and permeation zone (d) as a function of the reactor length as predicted by the PBMR model at $\Delta P=3$ bar, $SW=1$, $P^R=40$ bar, $T=200$ °C, a GHSV of $2600 \text{ NL kg}_{cat}^{-1} \text{ h}^{-1}$ and a feed composition of $\text{H}_2/\text{CO}_2 = 3$.

D.2 Thermodynamic equilibrium of intermediate products

The concentration profile along the reactor obtained for successive reversible reactions depends on the ratio of the reaction rates [29]. Nevertheless, the concentration of all species, for a sufficiently long reactor, will approach thermodynamic equilibrium. Considering the following general system:



Where A convert to R with a reaction rate r_A , and R converts to S with a reaction rate r_R . If $r_A/r_R \gg 1$, the concentration of R displays a maximum vs the reactor length to then decrease and approach its equilibrium value. This scenario represents a build-up of the concentration of the intermediate product/reactant (R), before its after conversion rate (r_R) can become significant and achieve equilibrium.

In this specific system (CO_2 -to-DME), two situations can be identified: 1) CO formation (r_2) and its hydrogenation (r_1) to methanol and 2) methanol formation

($r_1 + r_3$) and its subsequent dehydration ($2r_4$). The ratio r_2/r_1 , calculated near the reactor entrance, varies from 1492 to 47 in the temperature range 200–260 °C. This explains the higher CO concentration measured with respect to its equilibrium value at lower temperatures. On the contrary, the ratio between methanol synthesis and dehydration rate is always close to 1, which means that methanol concentration does not achieve any maximum along the reactor.

REFERENCES

- [1] I. Iliuta, F. Larachi, and P. Fongarland, “Dimethyl ether synthesis with in-situ H₂O removal in fixed-bed membrane reactor: Model and simulations,” *Ind. Eng. Chem. Res.*, vol. 49, no. 15, pp. 6870–6877, 2010,
- [2] M. Farsi, A. Hallaji Sani, and P. Riasatian, “Modeling and operability of DME production from syngas in a dual membrane reactor,” *Chem. Eng. Res. Des.*, vol. 112, pp. 190–198, 2016,
- [3] N. Diban, A. M. Urtiaga, I. Ortiz, J. Ereña, J. Bilbao, and A. T. Aguayo, “Influence of the membrane properties on the catalytic production of dimethyl ether with in-situ water removal for the successful capture of CO₂,” *Chem. Eng. J.*, vol. 234, pp. 140–148, 2013,
- [4] N. Diban, A. M. Urtiaga, I. Ortiz, J. Ereña, J. Bilbao, and A. T. Aguayo, “Improved performance of a PBM reactor for simultaneous CO₂ capture and DME synthesis,” *Ind. Eng. Chem. Res.*, vol. 53, no. 50, pp. 19479–19487, 2014,
- [5] A. Ateka, P. Rodriguez-Vega, T. Cordero-Lanzac, J. Bilbao, and A. T. Aguayo, “Model validation of a packed bed LTA membrane reactor for the direct synthesis of DME from CO/CO₂,” *Chem. Eng. J.*, vol. 408, no. October 2020, 2021,
- [6] P. Rodriguez-Vega *et al.*, “Experimental implementation of a catalytic membrane reactor for the direct synthesis of DME from H₂+CO/CO₂,” *Chem. Eng. Sci.*, vol. 234, 2021,
- [7] R. M. Ravenelle *et al.*, “Stability of zeolites in hot liquid water,” *J. Phys. Chem. C*, vol. 114, no. 46, pp. 19582–19595, 2010,
- [8] N. Itoh and K. Haraya, “A carbon membrane reactor,” *Catal. Today*, vol. 56, no. 1–3, pp. 103–111, 2000,
- [9] Y. Hirota, A. Ishikado, Y. Uchida, Y. Egashira, and N. Nishiyama, “Pore size control of microporous carbon membranes by post-synthesis activation and their use in a membrane reactor for dehydrogenation of methylcyclohexane,” *J. Memb. Sci.*, vol. 440, pp. 134–139, 2013,
- [10] G. Szejner and M. Sheintuch, “Application of a carbon membrane reactor for dehydrogenation reactions,” *Chem. Eng. Sci.*, vol. 59, no. 10, pp. 2013–2021, 2004,
- [11] X. Zhang, H. Hu, Y. Zhu, and S. Zhu, “Methanol steam reforming to hydrogen in a carbon membrane reactor system,” *Ind. Eng. Chem. Res.*, vol. 45, no. 24, pp. 7997–8001, 2006,

- [12] S. Sá, H. Silva, J. M. Sousa, and A. Mendes, "Hydrogen production by methanol steam reforming in a membrane reactor: Palladium vs carbon molecular sieve membranes," *J. Memb. Sci.*, vol. 339, no. 1–2, pp. 160–170, 2009,
- [13] S. Sá, J. M. Sousa, and A. Mendes, "Steam reforming of methanol over a CuO/ZnO/Al₂O₃ catalyst part II: A carbon membrane reactor," *Chem. Eng. Sci.*, vol. 66, no. 22, pp. 5523–5530, 2011,
- [14] M. A. Dubé, A. Y. Tremblay, and J. Liu, "Biodiesel production using a membrane reactor," *Bioresour. Technol.*, vol. 98, no. 3, pp. 639–647, 2007,
- [15] C. Peigang, A. Y. Tremblay, M. A. Dubé, and K. Morse, "Effect of membrane pore size on the performance of a membrane reactor for biodiesel production," *Ind. Eng. Chem. Res.*, vol. 46, no. 1, pp. 52–58, 2007,
- [16] H. Li, S. He, K. Ma, Q. Wu, Q. Jiao, and K. Sun, "Micro-mesoporous composite molecular sieves H-ZSM-5/MCM-41 for methanol dehydration to dimethyl ether: Effect of SiO₂/Al₂O₃ ratio in H-ZSM-5," *Appl. Catal. A Gen.*, vol. 450, pp. 152–159, 2013,
- [17] A. García-Trenco, E. R. White, M. S. P. Shaffer, and C. K. Williams, "A one-step Cu/ZnO quasi-homogeneous catalyst for DME production from syn-gas," *Catal. Sci. Technol.*, vol. 6, no. 12, pp. 4389–4397, 2016,
- [18] N. Delgado Otalvaro, G. Sogne, K. Herrera Delgado, S. Wild, S. Pitter, and J. Sauer, "Kinetics of the direct DME synthesis from CO₂rich syngas under variation of the CZA-to- γ -Al₂O₃ratio of a mixed catalyst bed," *RSC Adv.*, vol. 11, no. 40, pp. 24556–24569, 2021,
- [19] T. Takeguchi, K. I. Yanagisawa, T. Inui, and M. Inoue, "Effect of the property of solid acid upon syngas-to-dimethyl ether conversion on the hybrid catalysts composed of Cu-Zn-Ga and solid acids," *Appl. Catal. A Gen.*, vol. 192, no. 2, pp. 201–209, 2000,
- [20] V. Vishwanathan, K. W. Jun, J. W. Kim, and H. S. Roh, "Vapour phase dehydration of crude methanol to dimethyl ether over Na-modified H-ZSM-5 catalysts," *Appl. Catal. A Gen.*, vol. 276, no. 1–2, pp. 251–255, 2004,
- [21] A. S. Zambare, J. Ou, D. S. Hill Wong, C. W. Yao, and S. S. Jang, "Controlling the product selectivity in the conversion of methanol to the feedstock for phenol production," *RSC Adv.*, vol. 9, no. 41, pp. 23864–23875, 2019,
- [22] S. Ghosh, J. Sebastian, L. Olsson, and D. Creaser, "Experimental and kinetic modeling studies of methanol synthesis from CO₂ hydrogenation using In₂O₃ catalyst," *Chem. Eng. J.*, vol. 416, p. 129120, 2021,
- [23] C. Ortega, M. Rezaei, V. Hessel, and G. Kolb, "Methanol to dimethyl ether conversion over a ZSM-5 catalyst: Intrinsic kinetic study on an external recycle reactor," *Chem. Eng. J.*, vol. 347, no. April, pp. 741–753, 2018,
- [24] J. F. Portha *et al.*, "Kinetics of Methanol Synthesis from Carbon Dioxide Hydrogenation over Copper-Zinc Oxide Catalysts," *Ind. Eng. Chem. Res.*, vol. 56, no. 45, pp. 13133–13145, 2017,

- [25] A. Karelavic and P. Ruiz, "The role of copper particle size in low pressure methanol synthesis via CO₂ hydrogenation over Cu/ZnO catalysts," *Catal. Sci. Technol.*, vol. 5, no. 2, pp. 869–881, 2015,
- [26] L. Rodríguez-González, F. Hermes, M. Bertmer, E. Rodríguez-Castellón, A. Jiménez-López, and U. Simon, "The acid properties of H-ZSM-5 as studied by NH₃-TPD and 27Al-MAS-NMR spectroscopy," *Appl. Catal. A Gen.*, vol. 328, no. 2, pp. 174–182, 2007,
- [27] N. Katada and M. Niwa, "Analysis of acidic properties of zeolitic and non-zeolitic solid acid catalysts using temperature-programmed desorption of ammonia," *Catal. Surv. from Asia*, vol. 8, no. 3, pp. 161–170, 2004,
- [28] F. Gallucci and A. Basile, "A theoretical analysis of methanol synthesis from CO₂ and H₂ in a ceramic membrane reactor," *Int. J. Hydrogen Energy*, vol. 32, no. 18, pp. 5050–5058, 2007,
- [29] O. Levenspiel, *Chemical reaction engineering*, vol. 38, no. 11. 1999.

CHAPTER 6

Evaluation of the relevant mass and heat transfer phenomena in a packed bed membrane reactor for the direct conversion of CO₂ to dimethyl ether

Abstract

This chapter investigates the relevant heat and mass transfer phenomena occurring at the different scales in a packed bed (membrane) reactor for the direct conversion of CO₂ to dimethyl ether (DME) via the implementation of heterogeneous 2D reactor models. Intra-particle diffusion limitations were found to be relevant for particle diameters larger than 1 mm and temperature above 220 °C, with the catalyst efficiency dropping up to 50% and 5% for the Cu/ZnO/Al₂O₃ and the HZSM-5, respectively. A Thiele modulus-efficiency correlation was developed based on the results of the rigorous particle model. This correlation shows the typical behavior reported in literature for power law kinetics and accurately predicts the reaction performance with deviation of less than 5% for values of the Thiele modulus lower than 2. In the packed bed membrane reactor (PBMR), the concentration polarization (CP) also showed to affect the reactor performance. The concentration of water at the surface of the membrane selective layer was found to be up to 64% lower than the concentration in the bulk phase, hindering the effectiveness of the membrane separation. To account for this phenomenon via a simplified approach, a Sherwood-type correlation was developed to determine a CP mass transfer coefficient, based on the results obtained via the rigorous 2D PBMR model. Such correlation showed to predict with high accuracy (i.e., errors lower than 5%) the effect of the CP on the PBMR performance.

This chapter is based on the following paper:

Poto, S., van den Bogaard, H.L., Gallucci, F., & Neira d'Angelo, M. F.. Evaluation of the relevant mass and heat transfer phenomena in a packed bed membrane reactor for the direct conversion of CO₂ to dimethyl ether. *Submitted to Fuel*

6.1 INTRODUCTION

Reactor modeling is an essential tool for the design and scale-up of different reactor technologies but can be also used to identify the relevant transport phenomena occurring in the reactor. The latter scope is key to identify the bottlenecks of the system and to consequently propose solutions and reaction intensification strategies.

At the very first stage, a reactor model is developed based on the most simplistic hypotheses, which often include an ideal flow pattern, combined with a kinetic regime (see chapter 2), often analyzed under isothermal and isobaric conditions. These hypotheses are valid under certain conditions, which usually verify at laboratory scale, where the size of the system is such that deviation from ideality can be neglected and unwanted phenomena (i.e., heat/mass transfer limitation) can be easily avoided by properly selecting the operating conditions [1], [2]. Nevertheless, when such hypotheses fail, more rigorous reactor models, which include the interplay of multiscale heat and mass transfer phenomena become essential. In the majority of the cases, these models have to deal with multiple phases (i.e., heterogeneous model) and are described by a complex non-linear system of equations [3]. Thus, rigorous reactor modeling requires specifically developed software and is usually computationally expensive, requiring long simulation times and a significantly larger memory allocation space. Therefore, evaluating the relevance of the heat and mass transfer at different reactor scales is crucial to identify the phenomena which affect the reactor behavior and that, as a consequence, must be accounted for. This is even more important when it comes to investigate novel technologies, such as membrane reactors, coupled with relatively complex reaction schemes, such as CO₂ utilization pathways.

In this chapter, the mass and heat transfer phenomena in a packed bed (membrane) reactor for the direct conversion of CO₂ to dimethyl ether are investigated at different scales. To that end, the work uses a bifunctional catalysts based on the physical mixture of Cu/ZnO/Al₂O₃ and HZSM-5.

A particle model was developed to assess the extent of intra-particle mass and heat transfer limitations in relevant reaction conditions, as well as their impact on the performance of the packed bed reactor, with and without the membrane (i.e., PBR and PBMR, respectively). The choice of the catalyst particle diameter in fixed/packed bed reactors is crucial. Large particles inhibit severe pressure drops, but, at the same time, induce significant internal mass transfer limitations. These limitations are often neglected and not quantified in literature, given the complexity of this reaction system. Indeed, simulation results often led to unrealistic values in terms of catalyst efficiency [4], [5]. More recently, Chakib et al. developed a heterogeneous reactor model to study the pore-diffusion limitations involved in the one-step DME synthesis from CO₂-rich feedstocks, using bifunctional catalyst based on Cu/ZnO/Al₂O₃ and γ -Al₂O₃ [6]. In this study, it was found that the internal mass transfer limitation are significant for particle diameter larger than 2 mm, while the maximum temperature difference in the particle is never above 1 °C. However, in the aforementioned study, there's no distinction between the methanol synthesis and

dehydration catalyst particles. Furthermore, γ -Al₂O₃ is used instead of zeolites. The γ -Al₂O₃ has usually pores between 5-20 nm, while HZSM-5 is known for its microporous structure, as well as for enhancing the DME formation rate [7], which are two features that could render the effect of pore-diffusion even more limiting. Furthermore, in literature, rigorous heterogeneous models have been developed and solved to account for internal mass/heat transfer limitations. In this work, once identified the relevance of these phenomena using a rigorous modeling approach, a Thiele modulus-efficiency correlation was developed for the calculation of the effective reaction rate via a short-cut method, which does not require to couple reactor and particle model. This method was developed from the more rigorous particle model and later verified comparing the results of the heterogeneous and pseudo-homogeneous reactor model.

Thereafter, the particle-fluid interphase was investigated, to assess the relevance of any external mass or heat transfer limitation, which means the presence of concentration and temperature gradients from the bulk fluid phase to the surface of the catalyst particle (i.e., in the particle boundary layer). In laminar systems, with little mixing or low superficial velocities, these gradients can be significant. However, these phenomena do not add much complexity to the reactor modeling, and can be accounted for using state-of-the-art correlations to define heat and mass transfer coefficients. Indeed, several empirical Sherwood/Nusselt type correlations have been developed in the past, based on physical properties of the fluid and characteristics of the packed bed (e.g., particle size, bed porosity, etc.) [2], [8].

Packed bed reactors are usually modeled as plug flow reactors (PFRs), based on the assumption of no mixing in the axial direction. However, in real conditions, mixing can be relevant due to the diffusion, the turbulent flow around the solid particles or to the presence of radial velocity profiles [2]. In this work, deviations from the ideal plug flow behavior were analyzed via the implementation of the axial dispersion model. Similarly to the external mass/heat transfer phenomena, a state-of-the-art correlation was used to determine the axial dispersion coefficient [9].

The introduction of the membrane in the packed bed reactor adds more complexity to the transport phenomena. Indeed, concentration gradients can develop in the radial direction giving rise to a phenomenon which in membrane separation is known as concentration polarization (CP). CP occurs when the concentration of a species increases or decreases in the proximity of the membrane surface (i.e., in the boundary layer) due to the species permeation, thus affecting the overall rate of permeation. This phenomenon is analogue to the fluid-particle mass transfer. Thus, different types of correlations based on either Sherwood or Peclet number have been empirically developed in the past, mostly for gas separation processes (i.e. no reaction and absence of catalytic bed) [10], [11]. Specific correlations for this system have never been developed and such phenomenon has often been neglected, especially for porous membranes and for vapor permeation. Therefore, a 2D packed bed membrane reactor model was developed in this study to evaluate the relevance of the radial concentration gradients generated by the presence of the membrane.

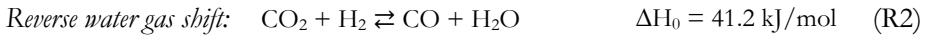
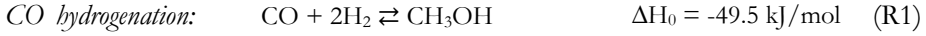
From the simulations results of the 2D model, a Sherwood-type correlation was developed to account for the CP phenomena via a simplified approach. Indeed, the CP mass transfer coefficient allows to correct the driving force for the permeation flux, without the need to solve 2D equations.

Finally, solutions to mitigate the effect of these mass and heat transfer limitations on the performance of both the PBR and PBMR were proposed, together with alternative reactor designs to complement the work reported in chapter 7.

6.2 METHODOLOGY AND NUMERICAL IMPLEMENTATION

6.2.1 Reaction scheme and kinetic model

The direct hydrogenation of CO₂ to DME is described by the following reaction scheme:



The reactions R1, R2, R3 are assumed to be carried out over a Cu/ZnO/Al₂O₃ (CuZA) following the kinetic of Portha et al. [12], while reaction R4 occurs over a HZSM-5 catalyst, according to the kinetic of Ortega et al. [13]. The reaction rates expressions are reported in Eq. 6.1-6.4.

$$r_1 = k_1 b_{\text{CO}} \left\{ \frac{P_{\text{CO}} P_{\text{H}_2}^{3/2} - \frac{P_{\text{CH}_3\text{OH}}}{P_{\text{H}_2}^{1/2} K_1}}{(1 + b_{\text{CO}} P_{\text{CO}} + b_{\text{CO}_2} P_{\text{CO}_2}) \left[P_{\text{H}_2}^{1/2} + \left(\frac{b_{\text{H}_2\text{O}}}{b_{\text{H}_2}^{1/2}} \right) P_{\text{H}_2\text{O}} \right]} \right\} \quad (6.1)$$

$$r_2 = k_2 b_{\text{CO}_2} \left\{ \frac{P_{\text{CO}_2} P_{\text{H}_2} - \frac{P_{\text{CO}} P_{\text{H}_2\text{O}}}{K_2}}{(1 + b_{\text{CO}} P_{\text{CO}} + b_{\text{CO}_2} P_{\text{CO}_2}) \left[P_{\text{H}_2}^{1/2} + \left(\frac{b_{\text{H}_2\text{O}}}{b_{\text{H}_2}^{1/2}} \right) P_{\text{H}_2\text{O}} \right]} \right\} \quad (6.2)$$

$$r_3 = k_3 b_{\text{CO}_2} \left\{ \frac{P_{\text{CO}_2} P_{\text{H}_2}^{3/2} - \frac{P_{\text{CH}_3\text{OH}} P_{\text{H}_2\text{O}}}{P_{\text{H}_2}^{3/2} K_3}}{(1 + b_{\text{CO}} P_{\text{CO}} + b_{\text{CO}_2} P_{\text{CO}_2}) \left[P_{\text{H}_2}^{1/2} + \left(\frac{b_{\text{H}_2\text{O}}}{b_{\text{H}_2}^{1/2}} \right) P_{\text{H}_2\text{O}} \right]} \right\} \quad (6.3)$$

$$r_4 = k_4 \left\{ \frac{(b_{\text{CH}_3\text{OH}} P_{\text{CH}_3\text{OH}})^2 [1 - P_{\text{H}_2\text{O}} P_{\text{DME}} / (P_{\text{CH}_3\text{OH}}^2 K_4)]}{(1 + b_{\text{CH}_3\text{OH}} P_{\text{CH}_3\text{OH}} + b_{\text{H}_2\text{O}}^* P_{\text{H}_2\text{O}})^2} \right\} \quad (6.4)$$

Where P_i is the partial pressure of each component in the reaction zone. The kinetic constants (k_i), the adsorption constants (b_i) and the equilibrium constants (K_i) are reported in Appendix E. The kinetic model was validated with experimental data obtained with a physical mixture of 50 wt % Cu/ZnO/Al₂O₃ and 50 wt % HZSM-5 (see Appendix E, section E.1).

6.2.2 Properties of the membranes used

The membranes used for the PBMR are alumina supported carbon molecular sieve membranes (Al-CMSM). The permeation properties of these membranes are reported in Chapter 3 (CM08). The permeance of each species as a function of temperature derived experimentally was fitted with an Arrhenius law and the resulting equations are reported in **Table 6.1** (see quality of the fit in Appendix E, **Figure E2**). DME permeance was assumed to be 50 times lower than the H₂O permeance, which is a common assumption in literature [14].

Table 6.1. Permeation properties of the membrane CM08 (Chapter 3) fitted with an Arrhenius law.

Permeance	Expression	Units
$\phi_{\text{H}_2\text{O}}$	$\exp\left(-17.15 + \frac{1232.45}{T}\right)$	$\text{mol m}^{-2}\text{s}^{-1}\text{Pa}^{-1}$
ϕ_{H_2}	$\exp\left(-10.27 - \frac{2549.20}{T}\right)$	$\text{mol m}^{-2}\text{s}^{-1}\text{Pa}^{-1}$
ϕ_{CO}	$\exp\left(-13.06 - \frac{2254.52}{T}\right)$	$\text{mol m}^{-2}\text{s}^{-1}\text{Pa}^{-1}$
ϕ_{CO_2}	$\exp\left(-13.73 - \frac{1489.84}{T}\right)$	$\text{mol m}^{-2}\text{s}^{-1}\text{Pa}^{-1}$
$\phi_{\text{CH}_3\text{OH}}$	$\exp\left(-24.87 + \frac{3770.59}{T}\right)$	$\text{mol m}^{-2}\text{s}^{-1}\text{Pa}^{-1}$

6.2.3 Reactor performance indicators

The CO₂ conversion, product yield and selectivity, as defined in Chapter 2 were used as performance indicators for both the PBR and PBMR. Indeed, when the membrane is not incorporated in the reactor, the trans-membrane flux of all the species is set to zero and the model is used to assess the performance of a PBR.

6.2.4 Numerical method

The governing equations used to derive the concentration, pressure, temperature and velocity profiles have a non-linear character, due to the reaction kinetics. Furthermore, 2nd order derivatives must be simultaneously solved, due to convection and dispersion, complicating the system even further. Thus, given the non-linearity and complexity of the system, the Newton Raphson scheme was implemented to solve the system numerically.

Discretization grid and grid-size analysis

The continuous steady-state governing equations were discretized and evaluated at set points in space. A central differencing scheme was adopted, which consists in defining the concentrations, pressure and temperature at the centers of the grid cells and the gradients at the faces of the grid cells.

As a consequence of the chosen discretization system, velocities were also defined at the faces of the grid cells. Being the convective terms defined by the product of velocity and concentration, a first-order upwind discretization was used, meaning that the concentration at the face of a grid cell is considered equal to the concentration at the center of the downstream grid cell.

The conditions and gradients at the first and last grid point of the domain are generally defined by mixed or Robin boundary conditions, which also require discretization. This was done with a second order Lagrange interpolation near the boundary of the grid cell where the boundary condition is imposed.

To determine the optimal size of the grid cell in each domain (i.e., particle and reactor), a grid size analysis was carried out in the conditions producing the steepest gradients. The optimal size was chosen setting the maximum error relative to the largest grid size of 10^{-5} .

In some cases, the grid size is not uniform along the domain, since a refined grid is required only in the region with steeper gradients. As an example, in the proximity of the reactor outlet and at the reactor walls, profiles are expected to be fully developed and less grid points are required. This optimization was done to minimize the computation time and the memory allocation space.

Model verification

The models verification was carried out at two stages:

- 1) Checking the conservation of the total mass in the reactor.
- 2) Comparing the solution of the numerical model to an analytical solution of a simplified system (i.e., first order irreversible and elemental reaction $A \rightarrow B$). The relative error of the solution of the numerical model with respect to the analytical solution was defined acceptable when in the order of 10^{-5} , indicating the correct implementation of the numerical model.

6.3 HEAT AND MASS TRANSFER PHENOMENA AT PARTICLE SCALE

The heat and mass transfer phenomena were investigated at the particle scale, to assess their relevance at realistic reaction conditions.

The simplified Thiele modulus approach is commonly implemented in pseudo-homogeneous reactor models to account for intra-particle diffusion limitations without rigorously modeling the concentration profile in the particle [1], [3].

However, this method is not directly applicable to this system because of: 1) the dependency of the reaction rates on both kinetic and adsorption phenomena (i.e., Langmuir-Hinshelwood rate equations) and 2) the complexity of the reaction scheme (i.e., involving multicomponent reactions, as well as parallel and consecutive reversible reactions).

Similarly, the presence of internal heat transfer limitations cannot be evaluated a priori, using simplified approaches such as the Prater number, being its derivation based on the assumption of 1st order kinetic [15].

As a result, the mass and heat transfer phenomena were investigated by modeling the concentrations and temperature profiles inside the catalyst particle explicitly.

6.3.1 Governing equations and boundary conditions

The governing equations describing the mass (Eq. 6.5) and heat (Eq. 6.6) conservation in the catalyst particle are reported in **Table 6.2** with the corresponding boundary conditions. The equations are derived for a spherical particle with a radius R_p . In Eq. 6.5 and 6.6, r_i''' and r_j''' are the reaction rate of component i and of reaction j , respectively, based on the volume of the catalyst pellet. The effective diffusivity of each component ($D_{eff,i}$) is assumed to be based on the Knudsen and molecular diffusion in the pores of the catalyst pellet, accounting also for the tortuosity and porosity of the particle (see Appendix E) [6]. The effective thermal conductivity inside the particle (λ_{eff}), is based on the equation of Coté and Konrad developed for porous media (see Appendix E) [16]. At the center of the particle ($r = 0$), the concentration/temperature gradient is set to zero, given the symmetry of the system. At the surface of the particle ($r = R_p$), the concentration/temperature is the same as in the bulk fluid, assuming the absence of any external (i.e., fluid-particle) heat and mass transfer limitations, at this stage.

Table 6.2. Governing equations for mass and heat conservation in the spherical catalyst particle with radius R_p and the corresponding boundary conditions (B.C.)

Equation	B.C. $r = 0$	B.C. $r = R_p$
$\frac{1}{r^2} \frac{\partial}{\partial r} \left(D_{eff,i} \cdot r^2 \frac{\partial C_i}{\partial r} \right) + r_i''' = 0$ (6.5)	$\frac{\partial C_i}{\partial r} = 0$	$C_i = C_{i,bulk}$
$\frac{1}{r^2} \frac{\partial}{\partial r} \left(\lambda_{eff} \cdot r^2 \frac{\partial T}{\partial r} \right) + \sum_{j=1}^{N_r} r_j''' (-\Delta H_r(T^R)) = 0$ (6.6)	$\frac{\partial T}{\partial r} = 0$	$T = T_{bulk}$

The direct conversion of CO₂ to DME requires a bifunctional catalyst, which in this system was assumed to be a physical mixture of two types of catalyst: 1) the Cu/ZnO/Al₂O₃ (CuZA or Methanol catalyst) and 2) the HZSM-5 (DME catalyst). The two catalysts have different properties (see Appendix E and Chapter 5) as well as a different reaction scheme, thus, the concentration of species and temperature is different in the two particles. As a result, the equations were solved for the two

particles, separately, computing two different values per each C_i and T . The bulk concentrations and temperature are the same for both particles. The particles have the same radius as well as the same radial discretization.

6.3.2 Simulation results and discussion

To assess the relevance of the intra-particle diffusion phenomena, the concentration profiles in the catalyst particles were first determined in a limiting case. Thus, simulations were run with a particle diameter of 10 mm and at a reaction temperature of 270 °C to guarantee a longer diffusion path and fast reaction rates, respectively. In this scenario, in both catalyst particles, the concentration gradients of products and reactant are quite significant, particularly for the DME catalyst (**Figure 6.1**). Indeed, the HZSM-5 particles have very small pores (i.e., average pore size of ca. 3 nm), which explain the lower diffusion rates. Furthermore, the methanol dehydration reaction is faster than methanol synthesis, which makes the diffusion step more limiting, thus leading to steeper concentration gradients. As a result, internal mass transfer phenomena can become limiting in realistic conditions (i.e., particle size relevant to industrial applications and at higher temperatures, which can easily develop in non-isothermal operation). Thus, these phenomena must be included in the reactor model to obtain more reliable predictions of the reaction performance.

On the contrary, internal temperature gradients were found negligible even when simulated in a limiting condition (i.e., fast heat production due to the fast reaction rate and slow heat diffusion rate). The maximum temperature difference between the center and the surface of the particle was found to be ca. 0.1 °C for both catalysts (see Appendix E, **Figure E3**), which corresponds to a relative difference of less than 0.01%. This result is in agreement with literature, since the absence of internal heat transfer limitations is often observed in similar systems [15]. Being the temperature gradients not significant even in a critical situation, the catalyst particles can be considered isothermal.

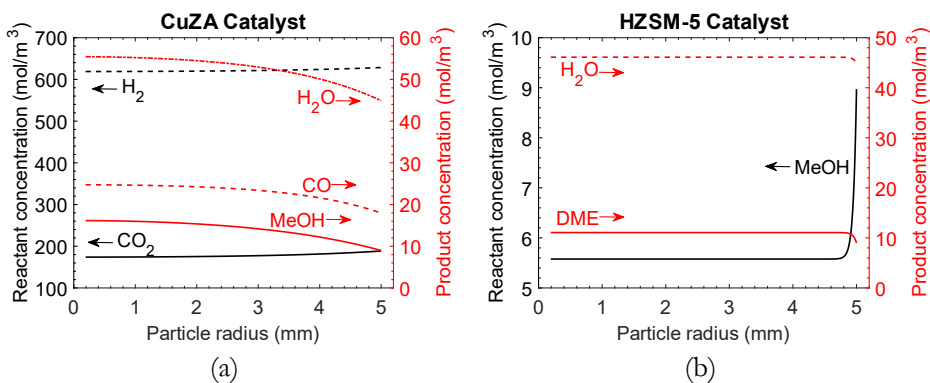


Figure 6.1. Concentration of reactants (left axis) and products (right axis) in the CuZA (a) and HZSM-5 catalyst (b) particles ($T_{\text{surf}}=270$ °C, $P=40$ bar, $d_p=10$ mm).

To account for pore-diffusion limitations at reactor scale, at each position of the reactor, the concentration profiles in the particles should be explicitly modeled (i.e., heterogeneous reactor model), which is computationally expensive. As a result, a simplified approach which resemble the Thiele modulus-effectiveness factor would increase the efficiency of the computation significantly. Since none of the state-of-the-art short-cut methods are applicable to this system, here a specific correlation is proposed to estimate the catalyst efficiency from parameters which are known at reactor scale. A component-specific Thiele modulus (φ_i) and the corresponding effectiveness factor (η_i) are defined as reported in Eq. 6.7 and 6.8, respectively. The Thiele modulus compares the maximum reaction rate (i.e., reaction at the surface of the catalyst particle, $r_{i,\text{surf}}'''$) with the maximum diffusion rate. For a reversible reaction, the maximum/minimum concentration at the center of the particle corresponds to its thermodynamic equilibrium value ($C_{i,\text{eq}}$). Thus, the maximum diffusion rate is proportional to the difference $C_{i,\text{eq}} - C_{i,\text{surf}}$. The effectiveness factor – or efficiency – (η_i) is defined as the ratio of the observed – or actual – reaction rate ($r_{i,\text{obs}}'''$) in the catalyst particle and the reaction rate determined at the surface conditions ($r_{i,\text{surf}}'''$).

$$\varphi_i = \frac{V_{\text{cat}}}{A_{\text{cat}}} \sqrt{\frac{r_{i,\text{surf}}'''}{D_{\text{eff},i}(C_{i,\text{surf}} - C_{i,\text{eq}})}} \quad (6.7)$$

$$\eta_i = \frac{r_{i,\text{obs}}'''}{r_{i,\text{surf}}'''} \quad (6.8)$$

To assess whether a correlation exists between φ_i and η_i for this system, several simulations were carried out with the rigorous diffusion-reaction model, varying the particle characteristic size (0.1-20 mm), the temperature (200-270 °C), the pressure (30-40 bar), the catalyst geometry (slab, cylinder, sphere) and the surface compositions. The φ_i and η_i evaluated from the simulation results correlates in a similar way as for 1st order kinetic reactions, as depicted in **Figure 6.2a** and **b** for the methanol and DME catalyst, respectively. However, this correlation does not hold for CO, which is not reported here (see Appendix E, **Figure E4**). CO is an intermediate product of the methanol synthesis, meaning that its profile in the methanol catalyst particle is not monotonically increasing/decreasing vs the radius of the particle. On the contrary, it displays a maximum or minimum value, according to the temperature conditions. This means that CO could diffuse in multiple directions in the catalyst particle, which is something that it is not taken into account in the definition of the Thiele modulus. Nevertheless, the methanol synthesis requires only two independent components, which means that the efficiency of CO can be eventually derived via mass balance, as follows:

$$2 \eta_{\text{CO}} r_{\text{CO},\text{surf}}''' = \eta_{\text{H}_2} r_{\text{H}_2,\text{surf}}''' - 3 \eta_{\text{CO}_2} r_{\text{CO}_2,\text{surf}}''' \quad (6.9)$$

To check if the correlations displayed in **Figure 6.2** is general, the same analysis was carried out using different kinetic models describing the methanol synthesis, such as the kinetics from Bussche & Froment [17], Graaf et al. [18], Henkel [19], Park [19]

and the kinetic derived by us in a previous study [20]. It was found that the correlation still holds even when considering different kinetics.

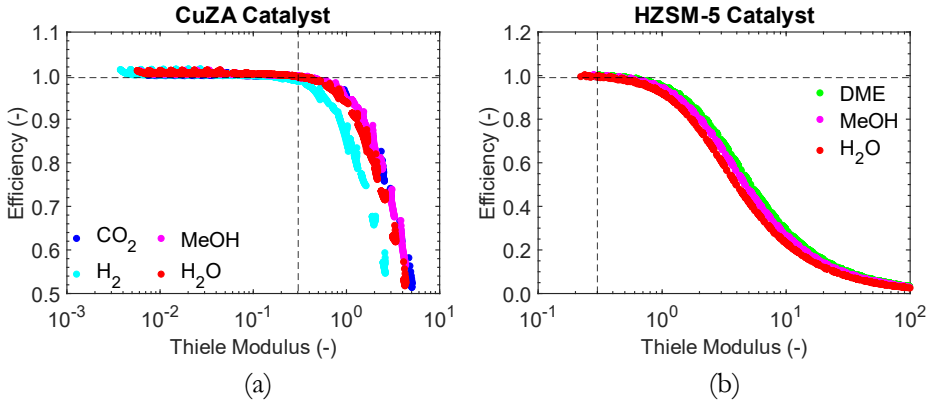


Figure 6.2. Catalyst efficiency (η_i) as a function of the Thiele modulus (ϕ_i) for the different species in both methanol catalyst (a) and DME catalyst (b) for systems with varying particle geometry (slab, cylinder, sphere), temperature (200-270 °C), pressure (30-40 bar), particle size (0.1-20 mm) and surface compositions. Dashed lines indicate the point of significant deviation of η_i from 1.

To mathematically describe this correlation, the following function can be defined:

$$\eta_i = \frac{1}{(1 + a \phi_i^2)^b} \quad (6.10)$$

According to Eq. 6.10, η_i approaches 1 for small values of ϕ_i (i.e., kinetic limiting regime), and approaches 0 for very large values of ϕ_i (i.e., diffusion limiting regime), which is the expected physical behavior. The values of a and b were derived via parametric fitting of the curves displayed in **Figure 6.2** with Eq. 6.10, per each component (excluding CO) and for the two catalysts (**Table 6.3**).

The fitted value of b is close to 0.5 independently of the component, catalyst and particle geometry. This value indicates that for larger value of ϕ_i , such that $a \phi_i^2 \gg 1$, η_i scales linearly with $1/\phi_i$. This behavior is also observed with the effectiveness factor analytically derived for 1st order reaction.

The parameter a changes significantly per component and catalyst type, but it does not depend on the particle geometry. In particular, the value of the parameter a was found to be equal to the ratio $D_{\text{eff},i}/D_{\text{eff},\text{lim}}$, where $D_{\text{eff},\text{lim}}$ is the diffusivity of the slowest diffusing component in each catalyst particle. Thus, the formula for the component-specific efficiency proposed here is the following:

$$\eta_i = \frac{1}{\left(1 + \frac{D_{\text{eff},i}}{D_{\text{eff},\text{lim}}} \phi_i^2\right)^{0.5}} \quad (6.11)$$

The dependency of η_i on the $D_{\text{eff,lim}}$ is also physically reasonable, since the reactive system is more affected by the slowest diffusing species. The parity plot representing the quality of the fit of Eq. 6.10 with respect to the efficiency derived via the rigorous particle model are reported in **Figure 6.3** for both catalyst particles.

Table 6.3. Coefficients a and b for Eq. 6.10 and dependency of a on the effective diffusivity.

Component	Catalyst	a	b	$10^6 \cdot D_{\text{eff},i}$	$10^6 \cdot a/D_{\text{eff},i}$	$a \cdot D_{\text{eff,lim}}/D_{\text{eff},i}$
<i>Spherical geometry</i>						
CO ₂	CuZA	1.09	0.47	1.07	1.02	0.99
H ₂	CuZA	3.07	0.50	2.76	1.11	1.08
MeOH	CuZA	0.89	0.54	0.97	0.92	0.89
H ₂ O	CuZA	1.56	0.46	1.36	1.15	1.11
DME	HZSM-5	1.03	0.48	0.42	2.45	1.03
MeOH	HZSM-5	1.28	0.48	0.53	2.41	1.01
H ₂ O	HZSM-5	1.80	0.48	0.74	2.43	1.02
<i>Cylindrical geometry</i>						
CO ₂	CuZA	0.86	0.50	1.07	0.80	0.91
H ₂	CuZA	2.63	0.52	2.76	0.95	1.08
MeOH	CuZA	0.86	0.55	1.13	0.76	0.86
H ₂ O	CuZA	1.22	0.50	1.36	0.90	1.01
DME	HZSM-5	1.00	0.51	0.42	2.38	1.00
MeOH	HZSM-5	1.08	0.51	0.45	2.34	1.01
H ₂ O	HZSM-5	1.51	0.51	0.64	2.35	0.99
<i>Slab geometry</i>						
CO ₂	CuZA	1.00	0.53	1.07	0.94	0.91
H ₂	CuZA	2.74	0.54	2.76	0.99	0.97
MeOH	CuZA	0.96	0.55	0.97	0.99	0.96
H ₂ O	CuZA	1.40	0.53	1.36	1.03	1.00
DME	HZSM-5	0.96	0.53	0.42	2.27	0.96
MeOH	HZSM-5	1.03	0.53	0.45	2.27	0.96
H ₂ O	HZSM-5	1.45	0.53	0.64	2.28	0.96

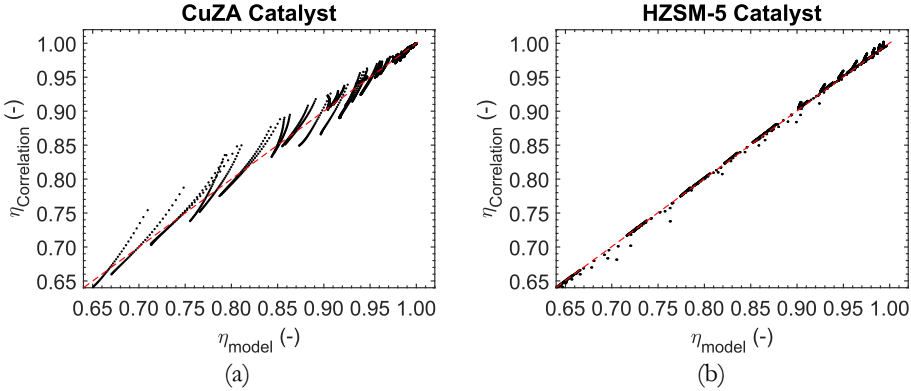


Figure 6.3. Catalyst efficiency derived solving the rigorous particle model (η_{model}) vs efficiency derived via the correlation proposed in Eq. 6.10 ($\eta_{\text{Correlation}}$) for both methanol catalyst (a) and DME catalyst (b) corresponding to the data of **Figure 6.2**.

6.4 HEAT AND MASS TRANSFER PHENOMENA AT THE PARTICLE-FLUID INTERPHASE

This section discusses the relevance of the mass and heat transfer phenomena at the particle-fluid interphase (i.e., from the bulk fluid phase to the catalyst particle). These phenomena are commonly referred as film or external mass/heat transfer [1].

6.4.1 Governing equations

Section 6.3.2 showed that intra-particle diffusion limitations are significant in some cases, while the temperature gradient inside the catalyst particle are negligible. Furthermore, the pore diffusion effects can be accounted for via a simplified approach (i.e., Thiele modulus-efficiency), which does not require solving the complex particle model. As a result, the film mass/heat transfer phenomena were studied setting a mass/heat balance around the catalyst particles, as follows:

$$\eta_i \rho_{\text{cat}}^{\text{app}} r_{i,\text{surf}}''' - k_{i,\text{ext}} \cdot (C_{i,\text{bulk}} - C_{i,\text{surf}}) = 0 \quad (6.12)$$

$$\Delta H_{r2} r_{\text{CO}_2,\text{surf}}''' \eta_{\text{CO}_2} \rho_{\text{cat1}}^{\text{app}} - \Delta H_{r3} r_{\text{MeOH},\text{surf}}''' \eta_{\text{MeOH}} \rho_{\text{cat1}}^{\text{app}} - h_{\text{ext}} \cdot (T_{\text{bulk}} - T_{\text{surf},1}) = 0 \quad (6.13)$$

$$-\Delta H_{r4} r_{\text{DME},\text{surf}}''' \eta_{\text{DME}} \rho_{\text{cat2}}^{\text{app}} - h_{\text{ext}} \cdot (T_{\text{bulk}} - T_{\text{surf},2}) = 0 \quad (6.14)$$

Eq. 6.12 (i.e., mass balance) was solved separately for the CuZA and HZSM-5 particles, which have different surface concentrations ($C_{i,\text{surf}}$), despite sharing the same bulk conditions ($C_{i,\text{bulk}}$). Eq. 6.12 was only solved for the independent components (i.e., for CO_2 and H_2 for the CuZA and for methanol for the HZSM-5). For all the other species, the concentration at the surface of the two catalyst particles was determined via the reaction stoichiometry. The particle-fluid (external) mass transfer coefficient ($k_{i,\text{ext}}$) is also component specific and was determined via

the correlation of Dwivedii, developed for packed bed reactors [8] (see Appendix E).

Eq. 6.13 and 6.14 represent the heat balance for the CuZA and HZSM-5 particle, respectively. Due to the definition of the component-specific efficiency (η_i), the observed reaction rate can be determined per component, rather than per each reaction. Thus, to simplify the calculation of the heat generated in the CuZA particle, it was considered that all the CO₂ reacts to CO and that all the methanol is produced via CO hydrogenation. The particle-fluid (external) heat transfer coefficient (h_{ext}) was determined via the correlation developed by Gupta et al. [21] (see Appendix E).

6.4.2 Simulation results and discussion

As for the intra-particle heat and mass transfer phenomena, also the relevance of the film mass and heat transfer was first evaluated in a limiting scenario. These phenomena could be limiting in a scenario with fast kinetic (i.e., high reaction temperature) combined with large catalyst particle and low superficial velocity (u_{sf}). As a result, simulations were first run at 270 °C, with a particle diameter of 10 mm and varying the superficial velocity in the range 0.001-10 m/s. The results are reported in terms of normalized surface concentration ($C_{i,\text{surf}}/C_{i,\text{bulk}}$) and temperature ($T_{\text{surf}}/T_{\text{bulk}}$), as a function of u_{sf} (**Figure 6.4a** and **b**, respectively). The two reference lines displayed in **Figure 6.4** represent a 1% deviation from 1, which corresponds to the scenario in which the external mass and heat transfer phenomena are fast enough, thus not limiting. **Figure 6.4a** shows that at low superficial velocity (i.e., below 0.2 m/s), the external mass transfer has a significant effect, with surface concentration deviating up to 6% from the concentration in the bulk phase.

On the contrary, the temperature gradients are, once again, not significant, with $T_{\text{surf}}/T_{\text{bulk}}$ approaching 1 even for very low velocities (**Figure 6.4b**). Usually, in gas phase reactions with solid porous catalysts, the external heat transfer is slower than the external mass transfer, due to the very low thermal conductivity of the gases [2]. However, H₂ has a relatively high thermal conductivity (i.e., in the order of 0.2 W/m/K) with respect to other gases (i.e., in the order of 0.03 W/m/K). This explains the absence of any film ΔT even in a limiting situation. As a matter of fact, when the H₂ thermal conductivity is artificially set as the conductivity of CO₂, the simulation results show that the temperature gradients in the particle-fluid interphase can be significant (see Appendix E, **Figure E5**).

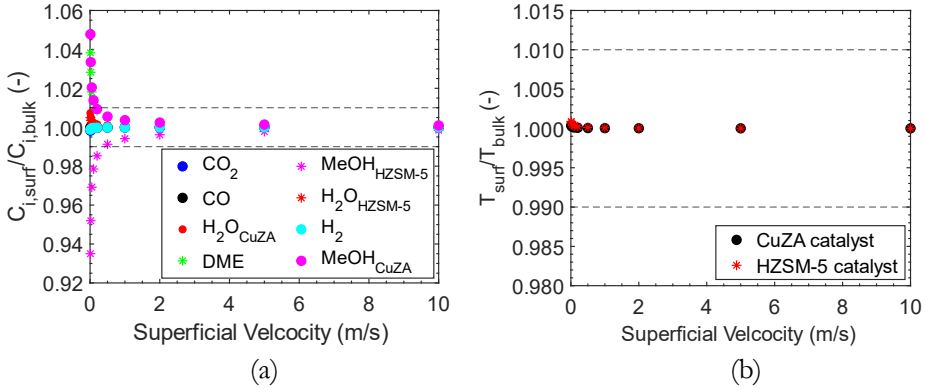


Figure 6.4. Normalized surface concentration ($C_{i,surf}/C_{i,bulk}$) for the different components (a) and normalized surface temperature (T_{surf}/T_{bulk}) (b) of the CuZA (circles) and HZSM-5 (stars) catalysts as a function of the superficial gas velocity determined at a bulk temperature of 270 °C, a pressure of 40 bar and a particle diameter of 10 mm. The dashed lines represent a 1% deviation from 1.

In literature, the Mears criterion is often used to check a priori whether the external mass transfer is limiting the reaction rate and therefore must be considered when modeling reactor performance [2]. Such criterion consists in calculating a dimensionless number, commonly known as Carberry number (Ca), defined in Eq. 6.15 as the ratio of the maximum reaction rate (including the reaction order n), over the maximum external mass transfer flux. For values of $Ca < 0.15$, the difference between the concentration at the surface of the particle and in the bulk phase is less than 5% (i.e., $(C_{i,bulk} - C_{i,surf})/C_{i,bulk} < 0.05$), so film concentration gradients are considered negligible [22].

$$Ca = \frac{r'_{i,obs} R_p |n|}{k_{ext} C_{bulk}} \quad (6.15)$$

However, once again, this criterion has been developed for simple reaction schemes and for a 1st – and generalized for n^{th} – order reaction. Nevertheless, the applicability of this criterion to this system was assessed by calculating rigorously the relative concentration difference, $(C_{i,bulk} - C_{i,surf})/C_{i,bulk}$ and the Ca (with n equal to 1, for simplicity) using the simulation results obtained for different particle sizes (1-20 mm), pressures (30-40 bar), temperatures (200-270 °C), surface compositions and superficial gas velocities (0.001-1 m/s). **Figure 6.5** shows that for $Ca < 0.15$, $(C_{i,bulk} - C_{i,surf})/C_{i,bulk} < 0.05$ holds for both catalyst particles, which means that this criterion is applicable also to this system, despite its complexity.

As a result, the Mears criterion could be implemented in the reactor model, to evaluate a priori whether the film concentration gradient is significant and must be taken into account. Nevertheless, the implementation of Eq. 6.12, together with the

Thiele-modulus approach does not add significant complexity to the reactor model, thus this phenomenon could be considered regardless of its relevance.

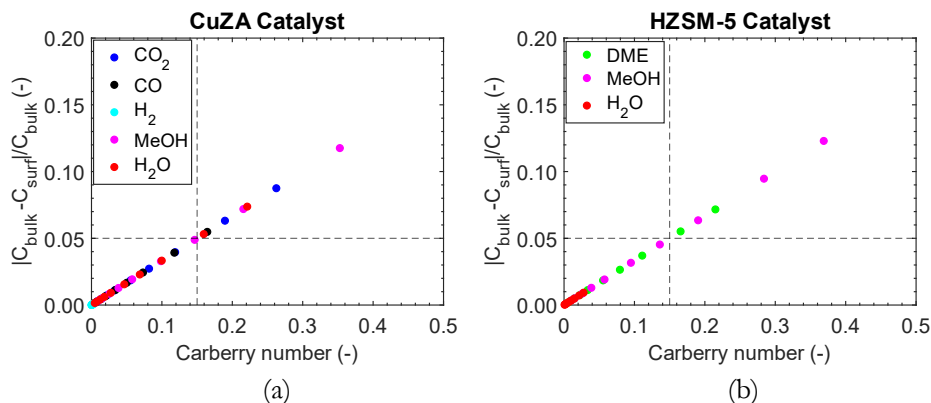


Figure 6.5. Relative concentration difference between the catalyst surface and the bulk fluid as a function of the Carberry number obtained for different particle sizes (1-20 mm), pressures (30-40 bar), temperatures (200-270 °C), surface compositions and superficial gas velocities (0.001-1 m/s). The vertical dashed line corresponds to $\text{Ca} = 0.15$, the horizontal dashed line corresponds to $(C_{i,\text{bulk}} - C_{i,\text{surf}})/C_{i,\text{bulk}} = 0.05$ (i.e., Mears criterion).

6.5 1D PACKED BED REACTOR MODEL: HETEROGENEOUS VS PSEUDO-HOMOGENEOUS MODEL AND DEVIATION FROM PLUG FLOW BEHAVIOR

In this section, the effect of the internal (i.e., intra-particle) and external (i.e., fluid-particle) mass transfer is discussed at reactor scale, to assess the relevance of these phenomena on the reaction performance (i.e., CO_2 conversion and product selectivity). At this stage, the membrane is not yet incorporated in the reactor. Thus, the results showed here were obtained via a 1D packed bed reactor (PBR) model.

In particular, the results obtained via the heterogeneous (i.e., including the particle model) and pseudo-homogeneous (i.e., no internal diffusion limitations or Thiele-modulus approach) PBR model are first compared, based on the hypothesis of ideal plug flow. Thereafter, deviations from the ideal plug flow pattern are evaluated, implementing the axial dispersion model.

6.5.1 Governing equations and boundary conditions

The governing equations describing the mass and heat conservation as well as the continuity equation (i.e., total mass conservation) in the packed bed reactor are summarized in **Table 6.4**. Eq. 6.18 describes the component specific mass balance in the PBR, derived with the hypothesis of plug flow and steady-state. When the plug flow hypothesis is removed, an axial dispersion term is added on the left side of Eq. 6.18, as shown in Eq. 6.19, where $D_{\text{ax},i}$ is the axial dispersion coefficient, determined via a Peclet number correlation (Pe_{ax}) based on the work of Gunn [9], [23] (see Appendix E). The heat balance reported in Eq. 6.20 represents a generic

reactor with heat exchange (Q). Eq. 6.20 does not change when the hypothesis of plug flow is removed, since axial heat dispersion was not considered in this work. This term seldom significant and often neglected in literature [24]. Eq. 6.21 represents the continuity equation which was used to determine the pressure drops ($\partial p/\partial z$) along the reactor. In the axial dispersion model, the continuity equation is represented by Eq. 6.22.

The friction factor (β) of Eq. 6.21 and 6.22 was calculated via the Ergun equation (Eq. 6.16), where μ_f is the fluid viscosity (see Appendix A), ρ_f is the fluid density, calculated via the Peng-Robinson equation of state (see Appendix A) and D_p is the particle diameter. The velocity of the gas mixture (v) in the packed bed varies along the reactor axis (z) according to the Darcy equation (Eq. 6.17).

$$\beta = 150 \frac{(1-\varepsilon_{bed})^2 \mu_f}{\varepsilon_{bed}^3 D_p^2} + 1.75 \frac{\rho_f (1-\varepsilon_{bed}) |v|}{\varepsilon_{bed}^2 D_p} \quad (6.16)$$

$$v = -\frac{1}{\beta} \frac{\partial p}{\partial z} \quad (6.17)$$

Table 6.4 also reports the boundary conditions for Eq. 6.18-6.22. For the mass and heat balance we set: 1) the composition and the temperature at the entrance of the reactor ($z = 0$), and 2) a null gradient for both concentration and temperature at the exit of the reactor ($z = L$). For the continuity equation, an inlet velocity (v_{in}) and a pressure at the outlet (p_{out}) were set.

The equation describing the reaction term (R_i) depends on the mass transfer phenomena considered and the approach used to model them. All the scenarios are summarized in **Table 6.5**:

- Pseudo-homogeneous model kinetically limited: Eq. 6.23 is used when both intra-particle diffusion and fluid-particle mass transfer phenomena are neglected. Thus, the gas and solid phase are described as a single pseudo-homogeneous phase.
- Pseudo-homogeneous model (Thiele modulus approach): R_i is described by Eq. 6.24 when the Thiele modulus approach developed in section 6.3.2 is used to describe the internal mass transfer phenomena. In this case, the concentration of each species at the surface of the catalyst particle ($C_{i,surf}$) can be different from the concentration in the bulk ($C_{i,bulk}$), due to the film mass transfer phenomena, which is described via a mass balance around the catalyst particle (Eq. 6.12). The model is still pseudo-homogeneous, since the mass balance inside the catalyst particle is not explicitly solved.
- Heterogeneous model: in this case, the concentration profile in the catalyst particle is modeled rigorously by explicitly solving the mass balance as described in Eq. 6.5. Thus, the model becomes heterogeneous and the particle and reactor model are coupled via the diffusion flux determined at

the surface of the catalyst particle (Eq. 6.25). In this last case, the external mass transfer is accounted for in the boundary condition of the particle mass balance, imposing the mass transfer flux at the surface of the catalyst particle.

In all cases, it is important to distinguish between the two catalyst particles in the reaction term (R_i), where $x_{\text{cat}1}$ and $x_{\text{cat}2}$ are the volume fraction of the CuZA and HZSM-5 in the catalytic bed, respectively. Furthermore, to prevent hot spots, the catalyst bed was assumed to be diluted with inert particles (SiC), with a volumetric dilution factor (D_{cat}).

Table 6.4. Mass, heat and momentum balance equations and corresponding boundary conditions for both ideal PFR and axial dispersion model.

Equation	Boundary conditions
Mass balance – Ideal plug flow (PFR)	
$\frac{\partial(vC_{i,\text{bulk}})}{\partial z} = R_i \quad (6.18)$	$z=0$ $C_{i,\text{bulk}} = C_{i,\text{bulk}}^{\text{IN}}$
Mass balance – Axial dispersion	
$\frac{\partial}{\partial z}(vC_{i,\text{bulk}} - D_{\text{ax},i} \frac{\partial C_{i,\text{bulk}}}{\partial z}) = R_i \quad (6.19)$	$z=0$ $z=L$ $C_{i,\text{bulk}} = C_{i,\text{bulk}}^{\text{IN}}$ $\frac{\partial(C_{i,\text{bulk}})}{\partial z} = 0$
Heat balance (valid with both Eq. 6.18 and 6.19)	
$\frac{\partial}{\partial z} \left(v \sum_{i=1}^{N_s} (C_{pi} C_{i,\text{bulk}}) T_{\text{bulk}} \right) = \sum_{i=1}^{N_s} R_i (-\Delta H_r) - Q \quad (6.20)$	$z=0$ $T_{\text{bulk}} = T_{\text{bulk}}^{\text{IN}}$
Continuity equation – Ideal plug flow (PFR)	
$-\frac{\partial}{\partial z} \left(\rho_f \frac{1}{\beta} \frac{\partial p}{\partial z} \right) = \sum_{i=1}^{N_s} M_i R_i \quad (6.21)$	$z=0$ $z=L$ $\frac{\partial p}{\partial z} = \beta_0 v_{\text{in}}$ $p = p_{\text{out}}$
Continuity equation – Axial dispersion	
$-\frac{\partial}{\partial z} \left(\rho_f \frac{1}{\beta} \frac{\partial p}{\partial z} \right) = \sum_{i=1}^{N_s} M_i R_i + \sum_{i=1}^{N_s} M_i \frac{\partial}{\partial z} D_{\text{ax}} \frac{\partial C_{i,\text{bulk}}}{\partial z} \quad (6.22)$	$z=0$ $z=L$ $\frac{\partial p}{\partial z} = \beta_0 v_{\text{in}}$ $p = p_{\text{out}}$

Table 6.5. Reaction term for Eq. 6.18-6.22 for three cases: 1) pseudo-homogeneous reactor model kinetically limited; 2) pseudo-homogeneous reactor model accounting for internal (MT_{INT}) and external (MT_{EXT}) mass transfer via the Thiele-modulus approach; 3) heterogeneous reactor model (particle model solved for MT_{INT} and MT_{EXT} included in its boundary condition).

Internal mass transfer	External mass transfer	R_i for Eq. 6.18-6.22
Pseudo-homogeneous reactor model (kinetic limiting regime)		
Neglected	Neglected	$D_{cat}(1-\varepsilon_{bed})(x_{cat1}\rho_{cat1}r_{i,cat1}'''+x_{cat2}\rho_{cat2}r_{i,cat2}''')$ (6.23)
Pseudo-homogeneous reactor model (MT_{INT} + MT_{EXT})		
Thiele modulus (Eq. 6.7 and 6.11 for φ_i and η_i)	Eq. 6.12 for $C_{i,surf,cat1}$ and $C_{i,surf,cat2}$	$D_{cat}(1-\varepsilon_{bed})(x_{cat1}\rho_{cat1}\eta_{icat1}r_{i,surf,cat1}'''+x_{cat2}\rho_{cat2}\eta_{icat2}r_{i,surf,cat2}''')$ (6.24)
Heterogeneous reactor model (MT_{INT} + MT_{EXT})		
Particle model (Eq. 6.5) with B.C.:		$D_{cat}(1-\varepsilon_{bed})\frac{3}{R_p}\cdot$ $\cdot\left(x_{cat1}D_{eff,i,cat1}\frac{\partial C_{i,cat1}}{\partial r}\Big _{r=R_p}+x_{cat2}D_{eff,i,cat2}\frac{\partial C_{i,cat2}}{\partial r}\Big _{r=R_p}\right)$ (6.25)
$r = 0$	$\frac{\partial C_i}{\partial r} = 0$	
$r = R_p$	$D_{eff,i}\frac{\partial C_i}{\partial r} = k_{i,ext}(C_{i,bulk} - C_{i,surf})$	

6.5.2 Simulation results and discussion

To assess the effect of the internal diffusion limitations on the packed bed reactor performance, simulations were run under isothermal conditions, and in two scenarios: 1) at 270 °C, varying the particle diameter in the range 0.25-20 mm; and 2) using a particle diameter of 10 mm, varying the temperature in the range 200-270 °C. The analysis was done at a relatively high space velocity (i.e., GHSV of 500 h⁻¹), to prevent the system to achieve thermodynamic equilibrium. This corresponds to a situation where both the kinetics and mass transfer do not affect the performance anymore. **Figure 6.6a** and **c** show that at large catalyst particle diameter (≥ 1 mm) and at high temperature (≥ 220 °C), the CO₂ conversion determined via the heterogeneous reactor model (i.e., solving the particle model) deviates significantly from the conversion determined under the hypothesis of kinetically limited regime (i.e., without internal mass transfer, MT_{INT}) up to a maximum of 5%. Similarly, the selectivity towards DME (**Figure 6.6b** and **d**) decreases when the system is affected by the pore diffusion rate. At the same time, methanol selectivity increases, which indicates that the HZSM-5 catalyst is more affected by internal diffusion, as previously observed. Furthermore, **Figure 6.6** shows that the Thiele modulus approach (circles) predicts with high accuracy the trend in CO₂ conversion and product selectivity computed via the heterogeneous reactor model (stars) in the range of $D_p = 0-3$ mm and $T = 200-250$ °C.

In severely diffusion limited regime (i.e., particle diameter larger than 5 mm and temperature above 250 °C), the Thiele modulus approach tends to overestimate the effect of internal mass transfer, resulting in a lower conversion compared to that obtained when solving the heterogeneous model. The product selectivity, instead, is predicted with high accuracy over the entire range of explored conditions. Nevertheless, it must be noted that the largest deviations observed in the CO₂ conversion correspond to the least realistic conditions. Indeed, in industry, particle size of ca. 3 mm are commonly used, while temperatures above 250 °C corresponds to very low DME selectivity (i.e., rWGS favored).

The relative error between the solution of the heterogeneous (i.e., particle-reactor) and of the pseudo-homogeneous (i.e., Thiele modulus approach) model was determined in all the conditions. Such error was found to exceed 5% for the CO₂ conversion, when the maximum Thiele modulus in the system is larger than 2. This situation corresponds to an effectiveness factor of ca. 90%.

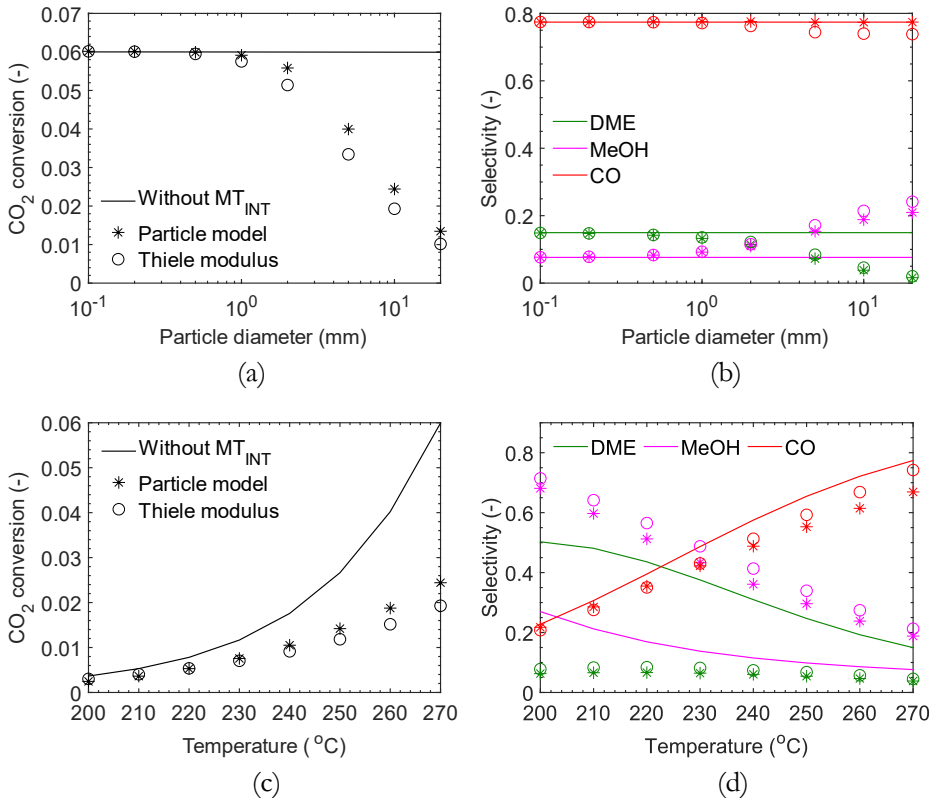


Figure 6.6. CO₂ conversion (a) and product selectivity (b) as a function of the particle diameter, at a reaction temperature of 270 °C and CO₂ conversion (c) and product selectivity (d) as a function of the reaction temperature, with a particle diameter of 10 mm. Other conditions are: $P_{in}^R = 40$ BAR, $(C_{H_2}/C_{CO_2})_{IN,BULK} = 3$, $GHSV = 500$ h⁻¹, $w_{cat1} = 0.5$.

The effect of the external mass transfer was assessed in a similar way, carrying out isothermal reactor simulations at the same conditions of section 6.4.2 and with a GHSV of 500 h⁻¹. It can be observed that the CO₂ conversion and product selectivity are barely affected by the velocities in the range 0.001-10 m/s. Indeed, at the lowest velocity, a maximum deviation in the DME selectivity and methanol yield of 3.5% (see Appendix E, **Figure E6**) was calculated. As a consequence, considering that an inlet superficial velocity of 0.001 m/s, a temperature of 270 °C and a particle diameter of 10 mm are not common for this system, it is concluded that the film concentration gradients are not relevant at reactor scale. Thus, also the external mass transfer phenomena can be neglected.

The relevance of the axial dispersion was also assessed running isothermal simulations in a limiting condition (i.e., high axial dispersion coefficient, D_{ax}). D_{ax} depends on the molecular diffusivity, particle diameter and fluid velocity, similarly to the external mass transfer coefficient (see Appendix E, section E.3). In particular, D_{ax} increases for larger particle diameters and becomes more relevant as the superficial gas velocity increases. Thus, simulations were run with a particle diameter of 10 mm and varying the superficial gas velocity. Furthermore, a temperature of 270 °C was selected to ensure fast reaction rates

However, in all the explored conditions, conversion and selectivity did not show significant deviations from the results obtained under the assumption of plug flow (see Appendix E, **Figure E7**). Therefore, this phenomenon can be neglected and plug flow will be considered a valid assumption for the rest of this study.

6.6 1D PSEUDO-HOMOGENEOUS PACKED BED MEMBRANE REACTOR MODEL: EFFECT OF DIFFUSION LIMITATIONS ON A LARGE SCALE PBR AND PBMR

Given the results from previous sections, a 1D pseudo-homogeneous plug flow packed bed membrane reactor (PBMR) model was developed, proposing a specific heat management solution (i.e., specifying the term Q of Eq. 6.20), and implementing the Thiele modulus approach to account for the pore diffusion effects (i.e., pseudo-homogeneous model). All the phenomena which were found irrelevant for the PBR, such as fluid-particle heat and mass transfer, intra-particle heat transfer and axial dispersion, as shown in the previous sections, were not modeled here.

In this section, the effect of intra-particle diffusion phenomena on the performance of the PBR and PBMR is discussed at relevant operating conditions (i.e., temperature, pressure) and at a space velocity which is compatible with industrial scale (i.e., which guarantees approach to thermodynamic equilibrium). Reaction conditions were selected based on preliminary simulations (e.g. Chapter 2), carried out with simplified models, which do not consider any effect of internal/external mass and heat transfer phenomena.

6.6.1 Governing equations and boundary conditions

As shown in Chapter 2, in the PBMR two zones can be identified: the reaction (i.e., outer reactor shell hosting the catalytic bed) and the permeation zone (i.e., the inner tubular membrane). As a result, all the variables, such as concentration, temperature, pressure and velocity, assume a different value in the two zones. To distinguish the variables of the reaction and permeation zone, the superscripts R and P were used, respectively.

Table 6.6 summarizes the mass and heat balance equations, with the corresponding boundary conditions. The mass balance of the reaction zone (Eq. 6.26) is based on Eq. 6.18, with the term $\phi_i(P_i^R - P_i^P)$ representing the permeation flux ($J_{\text{perm},i}$) of the species through the membrane. In Eq. 6.26, the a_{memb} represents the membrane area per reactor volume. The membrane was considered to be placed all along the reactor, thus $L_M = L_R$.

The mass balance of the permeation zone (i.e., where sweep gas is circulated), reported in Eq. 6.27, accounts only for the permeation flux (i.e., no reaction).

To remove the heat produced by the reactions and keep isothermal conditions, the circulation of boiling water in an external cooling mantle was selected as a heat management strategy. As a result, heat is removed from the reactor via the evaporation of water (i.e., latent heat exchange) at constant temperature (T_w).

During the lab-scale membrane reactor tests discussed in Chapter 5, the temperature in the reaction and permeation zone was found to be the same in all experimental conditions, suggesting a fast heat transfer between the membrane and the catalytic bed. However, the lab-scale tests are not fully representative of large scale reactors, where radial temperature gradients between the bulk phase of the reaction and permeation zone could develop. Nevertheless, in practice, these gradients could be avoided by placing multiple smaller membranes in parallel. Furthermore, the inlet temperature for both the permeation and reaction zone is the same. As a result, the temperature profile in the two zones is the same (i.e., $T^R = T^P = T$) and an overall heat balance can be formulated, as in Eq. 6.28, where a_{heat} is the heat transfer area per reactor volume and U is the global heat transfer coefficient (see Appendix E).

The reaction term (R_i) is described via Eq. 6.24 (**Table 6.5**), with $C_{i,\text{surf}}^R = C_{i,\text{bulk}}^R$ and with the Thiele modulus-efficiency from Eq. 6.7 and 6.11.

The gas velocity profile in the reaction zone (v^R) was modeled as in section 6.5, combined with the continuity equation reported in **Table 6.6** (Eq. 6.29) which accounts also for the transport of species through the membrane. The continuity equation for the permeation zone (Eq. 6.30) was used to determine the velocity profile (v^P). The total pressure (P^P) in the permeation zone was assumed constant. Indeed, due to the absence of solid particles, the pressure drop of the gas flowing in the membrane tube is negligible.

When the PBR was modeled instead of the PBMR, the permeance of each species was set to zero (i.e., no permeation flux in Eq. 6.26), Eq. 6.27 was not implemented and the energy balance was solved only for the reaction zone ($v^P = \mathbf{0}$ was set at zero in Eq. 6.28).

Table 6.6. Mass and heat balance equations and boundary conditions for the permeation and reaction zone of the 1D pseudo-homogeneous PBMR model.

Equation	Boundary condition
Mass balance – Reaction zone	
$\frac{\partial(v^R C_i^R)}{\partial z} = R_i - a_{\text{memb}} \cdot \phi_i(p_i^R - p_i^P) \quad (6.26)$	$z = \mathbf{0}$ $C_i^R = C_i^{R,IN}$
Mass balance – Permeation zone	
$\frac{\partial(v^P C_i^P)}{\partial z} = a_{\text{memb}} \cdot \phi_i(p_i^R - p_i^P) \quad (6.27)$	$z = \mathbf{0}$ $C_i^P = C_i^{P,IN}$
Heat balance – Reaction/Permeation zone	
$\begin{aligned} \frac{\partial}{\partial z} \left(\sum_{i=1}^{N_s} (v^R C_i^R + v^P C_i^P) C_{pi} T \right) = \\ = \sum_{i=1}^{N_s} R_i (-\Delta H_r(T^R)) - a_{\text{heat}} \cdot U \cdot (T - T_w) \end{aligned} \quad (6.28)$	$z = \mathbf{0}$ $T = T^{IN}$
Continuity equation – Reaction zone	
$-\frac{\partial}{\partial z} \left(\rho_f \frac{1}{\beta} \frac{\partial p^R}{\partial z} \right) = \sum_{i=1}^{N_s} (M_i R_i - a_{\text{memb}} \cdot J_{\text{perm},i}) \quad (6.29)$	$z = \mathbf{0}$ $z = \mathbf{L}$ $\frac{\partial p^R}{\partial z} = \beta_0 v_{in}^R$ $p^R = p_{out}^R$
Continuity equation – Permeation zone	
$\frac{\partial}{\partial z} (\rho_f v^P) = \sum_{i=1}^{N_s} (a_{\text{memb}} \cdot J_{\text{perm},i}) \quad (6.30)$	$z = \mathbf{0}$ $v^P = v_{in}^P$

6.6.2 Simulation results and discussion

The reaction conditions used to simulate the PBR and PBMR are reported in **Table 6.7**. A total pressure of 40 bar and a H₂:CO₂ molar feed ratio of 3 were selected for the reaction zone, based on the work reported in Chapter 2. An average temperature of 220 °C for the reaction zone was found to lead to an adequate trade-off between CO₂ conversion and DME selectivity (see Chapter 7). Thus, the boiling water temperature, for both the PBR and PBMR, was optimized to guarantee an average reaction temperature of 220 °C (i.e., T_w of 190 °C and 178 °C for the PBR and PBMR, respectively). A GHSV of 32.11 h⁻¹ is sufficient to approach the thermodynamic equilibrium in the PBR for a catalytic bed composed of 50 wt % of HZSM-5. The mass fraction of zeolite has often been found to not significantly influence the overall reaction performance, being the system limited by the methanol synthesis. Thus, values between 33-50% are often proposed in literature (i.e., CuZA/HZSM-5 ratio between 1 and 2) [25]–[27].

As reported in Chapter 2, a relatively low gradient in total pressure ($\Delta P = 5$ bar) between the reaction and permeation zone, together with the circulation of a sweep gas containing the reactants (i.e., CO₂, H₂ with H₂:CO₂ of 3 mol/mol) was selected to ensure the selective removal of water while retaining the reactants in the reaction zone of the PBMR. The inlet flow rate to the permeation zone is linked to the inlet flow rate to the reaction zone, via the sweep gas ratio (SW), as defined in Chapter 2. In Chapter 2, it was found that a SW value of 20 maximizes the simultaneous removal of water and heat from the reaction zone. However, to minimize the H₂ requirement, in this study a SW value of 1 is proposed, which is sufficient to promote the selective removal of water. Once this parameters were set, the optimal value of a_{memb} was determined to be $0.0659 \text{ m}_{memb}^2/\text{m}_{\text{reac}}^3$.

Details on the optimization and sizing procedure adopted for the PBR and PBMR are reported in Chapter 7.

Table 6.8 reports the corresponding reactor performance for both the PBR and PBMR evaluated both with a simplified model (i.e., model which does not account for internal mass transfer phenomena, MT_{INT}) and with the model described in section 6.6. From these results, it can be observed that the intra-particle diffusion phenomena have no significant effect on the performance of both reactors in these conditions.

These results were obtained assuming a particle size which is typically employed in industry for these system (i.e., 3 mm). Interestingly, even when increasing the D_p to 10 mm, the reduction in the CO₂ conversion and DME yield is less than 0.88% and 0.65%, respectively (see Appendix E, **Figure E8**). This result is, seemingly, not in line with the findings from Section 6.3, where it was showed that at sufficiently large D_p (i.e., 4-10 mm), the efficiency of the catalyst particles is significantly reduced. This occurs already at 200 °C for the HZSM-5 particle, where the efficiency can drop to 90% for D_p of 10 mm.

Table 6.7. Reaction conditions and reactor geometry used for the PBR and PBMR simulations

Reactor property/condition	Unit	Value PBR	Value PBMR
Inlet temperature (T^{IN})	°C	200	200
Inlet pressure reaction zone ($P^{\text{R,IN}}$)	bar	40	40
GHSV	h^{-1}	32.11	32.11
Feed $\text{H}_2:\text{CO}_2$ ratio	mol/mol	3	3
Cooling water temperature (T_w)	°C	190	178
Reactor length (L_R)	m	18.23	17.72
Reactor inner diameter (D_{ri})	m	3.65	3.54
Reactor outer diameter (D_{ro})	m	3.81	3.70
Memb. area per reac. volume (a_{memb})	$\text{m}^2_{\text{memb}}/\text{m}^3_{\text{reac}}$	-	0.0659
Membrane pressure gradient (ΔP)	bar	-	5
Sweep gas flow ratio (SW)	-	-	1
Sweep gas $\text{H}_2:\text{CO}_2$ ratio	mol/mol	-	3
Bed porosity (ϵ_{bed})	$\text{m}^3_{\text{void}}/\text{m}^3_{\text{reac}}$	0.4	0.4
Catalyst dilution factor (D_{cat})	$\text{m}^3_{\text{SiC}}/\text{m}^3_{\text{cat}}$	0.66	0.66
Zeolite weight fraction (w_{catz})	$\text{kg}_{\text{catz}}/\text{kg}_{\text{cat}}$	0.5	0.5
Catalyst particle diameter (D_p)	mm	3	3

Table 6.8. PBR and PBMR performance determined with the conditions of **Table 6.7** with a 1D pseudo-homogeneous kinetically limited (no MT_{INT}) model and with a 1D pseudo-homogeneous model accounting for pore diffusion phenomena with the Thiele modulus approach (with MT_{INT})

Reactor performance	PBR – no MT_{INT}	PBR with MT_{INT}	PBMR – no MT_{INT}	PBMR with MT_{INT}
CO_2 conversion	37.96%	37.95%	52.28%	52.27%
DME selectivity	83.71%	83.8%	97%	97%
MeOH selectivity	13.42%	13.36%	~ 0%	~ 0%
CO selectivity	2.87%	2.84%	3%	3%

To investigate why the intra-particle mass transfer does not affect the performance of both reactors, the catalyst efficiency for both the CuZA and HZSM-5 particles was calculated over the length of the PBMR (**Figure 6.7a**). From this analysis, it can be observed that the efficiency of both catalysts initially decreases, due to an increase in the reaction temperature in the first section of the reactor (see Chapter 2 for typical temperature profile). Thereafter, the efficiency increases again, displaying an average value of 98% and 21% for the CuZA and HZSM-5, respectively. As a result, the pore diffusion has a little effect on the methanol synthesis, but it should significantly affect the production of DME, which is not the case, as seen in **Table 6.8**.

This suggests that the limitation for the methanol dehydration reaction lies somewhere else. Indeed, **Figure 6.7b** shows that the actual DME concentration in the PBMR corresponds to the thermodynamic equilibrium, which indicates that the

reaction is limited by thermodynamics. As a consequence, a lower or higher reaction rate would not result in any change in the methanol conversion to DME, since the reaction is already sufficiently fast to achieve its thermodynamic equilibrium. Thus, the reduced rate due to the low catalyst efficiency does not affect the reaction performance. **Figure 6.7b** also shows that the methanol concentration along the PBMR is always lower than its thermodynamic value. This, together with the high CuZA efficiency (i.e., 98%) suggests that the methanol synthesis is a kinetically limited system, under these conditions.

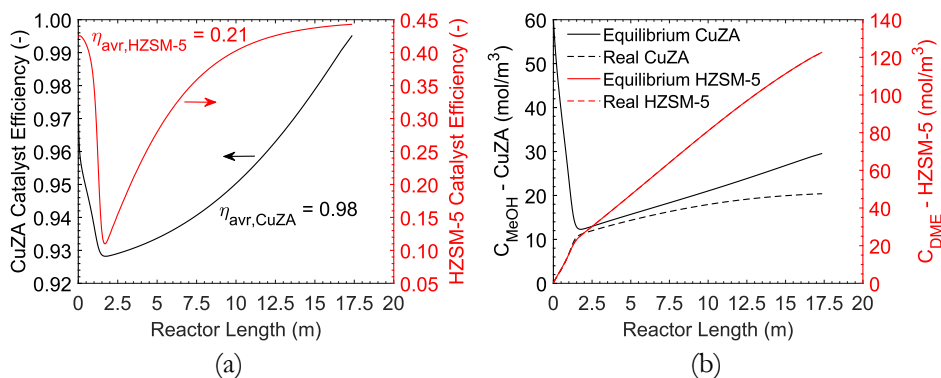


Figure 6.7. Catalyst efficiency (a) and methanol real (i.e., in the reactor) and equilibrium concentration for the CuZA (left axis) and DME real and equilibrium concentration for the HZSM-5 (right axis) as a function of the reactor length. Simulations were carried out on a PBMR, under the conditions reported in **Table 6.7**.

Being the methanol dehydration limited by thermodynamics, a fraction of the zeolite bed could be removed from the reactor, without any effect on the overall reaction performance. Indeed, if ca. 90 wt % of the HZSM-5 is removed from the catalyst bed, the DME concentration along the PBMR shifts downwards with respect to the equilibrium curve (see Appendix E, **Figure E9**), with a corresponding increase in the contribution of the pore-diffusion phenomena to the reaction rate.

Based on these findings, the w_{cat2} was optimized for both the PBR and PBMR and for different catalyst particle size, as reported in **Figure 6.8**. When water is removed from the reaction environment (PBMR), the optimal zeolite fraction was found to be slightly higher (ca. 0.5%), because the membrane alters the equilibrium of the system, reducing the water concentration. As a consequence, the methanol concentration is higher, resulting in the formation of more DME (i.e., dynamic equilibrium). Thus, a larger fraction of zeolite is required to achieve the dynamic equilibrium conditions in the membrane reactor.

Furthermore, when the effects of intra-particle diffusion phenomena are accounted for, for $D_p > 0.5$ mm, the optimal zeolite fraction increases with the particle size. Indeed, with larger catalyst particles, the effect of mass transfer becomes more significant, resulting in a lower methanol dehydration reaction rate. As a consequence, a larger fraction of HZSM-5 is required to achieve the equilibrium

both in the PBR and PBMR. This result is of high relevance, since the effect of the zeolite mass fraction can be significantly underestimated and considered negligible, as often reported in literature [25], [28], when the intra-particle diffusion limitations are not considered, especially for the HZSM-5.

The optimal zeolite weight fraction depends on the catalyst particle size and on the extent of water removal, as well as on the operating temperature and pressure. Thus, the optimization should be carried out for each specific set of conditions.

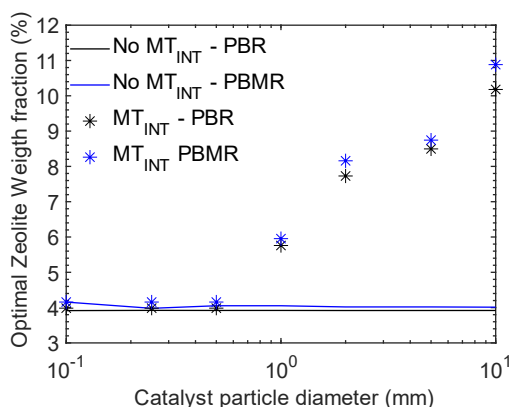


Figure 6.8. Optimal zeolite weight fraction (%) as a function of the catalyst particle diameters for both the PBR and PBMR, determined with a model which does not consider the intra-particle mass transfer (No MT_{INT}) and for a model which accounts for internal mass transfer limitation (MT_{INT}). Simulations were run under isothermal conditions (220 °C) and at $GHSV = 1000 \text{ h}^{-1}$. Other conditions are reported in **Table 6.7**.

6.7 2D PSEUDO-HOMOGENEOUS PACKED BED MEMBRANE REACTOR MODEL: EFFECT OF CONCENTRATION POLARIZATION PHENOMENA

In this section, the 2D PBMR model developed to investigate the relevance of the concentration gradients along the membrane surface (i.e., concentration polarization), is described. Such model is still considered pseudo-homogeneous, since balances in the solid phases were not solved: 1) the intra-particle diffusion limitations were accounted for via the Thiele modulus approach; 2) any mass transfer phenomena occurring in the micro-porous carbon membrane was assumed to be already included in the permeability.

The developed model relies on the following assumptions:

- 1) In the membrane tube, there is no radial concentration, velocity, pressure and temperature profile.
- 2) The radial component of the velocity are negligible.
- 3) There is no radial pressure profile.
- 4) The velocity in the axial direction is constant along the radius of the reactor.

- 5) There are no angular pressure, concentration, velocity or temperature gradients.

The flow rate in the membrane is usually the same or even higher ($SW \geq 1$) than the flow rate in the reaction zone. However, due to the much smaller cross section, the velocity in the membrane tubes is higher than in the reaction zone. Furthermore, the membrane tube is relatively thin (i.e., $L_M/D_M \gg 50$). Thus, such conditions do not favor radial concentration, velocity, pressure and temperature profiles. In reality, the velocity in the radial direction in the reaction zone is not zero, because of the permeation flux. Therefore, the assumption of neglecting the radial component of the velocity could lead to poor results [29]. However, the radial dispersion coefficient used in this model also partially accounts for a flux in the radial direction. In literature, it is really common to neglect the radial pressure profile [10], [29]. Thus, it was also neglected in this work. Furthermore, when the particle diameter is sufficiently small compared to the reactor diameter (i.e., $D_{ri}/D_p \gg 15$), the bed porosity can be considered uniform in the radial direction, resulting in flat profiles of the axial velocity, along the reactor radius [23].

To simplify the implementation of the 2D model, a PBMR with one membrane placed at the center of the reaction zone was considered. Thus, the reactor is symmetrical around the axis, which also yields to the absence of angular gradients, as well as to a zero contribution of the angular component of the velocity.

Finally, since there are already well-established correlations to describe the heat transfer to the reactor wall and the radial heat transfer from/to the membrane is considered negligible, as previously mentioned, the model 2D PBMR model is considered isothermal (i.e., no energy balance is solved).

6.7.1 Governing equations and boundary conditions

The mass balance equations for the reaction and permeation zone, together with their boundary conditions are reported in **Table 6.9**. The mass balance equation for the permeation zone is the same as Eq. 6.27. The mass balance equation in the reaction zone (Eq. 6.31) does not directly account for the permeation flux, since the permeation of species occurs at the boundary between the reaction and permeation zone. Thus, the permeation flux is incorporated in the boundary condition (i.e., at $r = R_{mo}$). As a result, Eq. 6.31 includes a convection term along the reactor axis, a radial dispersion term (described by the radial dispersion coefficient, $D_{rad,i}$, derived via the correlation of Gunn [9]) and a reaction term (R_i), described by Eq. 6.24 (**Table 6.5**), with $C_{i,surf}^R = C_{i,bulk}^R$ and with the Thiele modulus-efficiency from Eq. 6.7 and 6.11.

The second boundary condition for Eq. 6.31 along the radial direction imposes that the flux at $r = R_{ri}$ is zero, since there is no mass flux through the reactor walls. All the other boundary conditions correspond to the ones reported in **Table 6.6**.

Table 6.9. Governing equations and boundary conditions for the mass balances in the reaction and permeation zone of the 2D pseudo-homogeneous isothermal PBMR model.

Equation	Boundary conditions
Mass balance – Reaction zone	
$\frac{\partial(v^R C_i^R)}{\partial z} - \frac{1}{r} \frac{\partial}{\partial r} \left(r D_{\text{rad},i} \frac{\partial C_i^R}{\partial r} \right) = R_i \quad (6.31)$	$z = 0$
	$C_i^R = C_i^{R,IN}$
	$r = R_{ri} \quad r = R_{mo}$
	$\frac{\partial C_i^R}{\partial r} = 0 \quad D_{\text{rad}} \frac{\partial C_i^R}{\partial r} = \phi_i (P_i^R - P_i^P)$
Mass balance – Permeation zone	
Eq. 6.27	$z = 0$
	$C_i^P = C_i^{P,IN}$

6.7.2 Simulation results and discussion

Similarly to the previous sections, first it was assessed whether the concentration polarization phenomenon (i.e., fluid-membrane surface mass transfer) is relevant in a limiting situation. As a result, 2D PBMR simulations were carried out at high temperature (270 °C), to ensure a higher permeation flux (on average), combined with small catalyst particle diameter ($D_p = 25 \text{ mm}$) and low gas velocity (i.e., $v^R = 0.001 \text{ m/s}$), to reduce the mass transfer rate in the radial direction. These conditions result in significant radial concentration gradients, as depicted in **Figure 6.9**. Water (**Figure 6.9b**) shows a particularly steep gradient close to the membrane surface, due to its high permeation flux (i.e., highest permeance, combined with a significant driving force). Similarly, all the species which are not circulated in the sweep gas show a steeper gradient, due to their higher permeation flux.

The water concentration profile hinders the effectiveness of the membrane, by reducing the effective driving force which determines the permeation flux. As a result, the PBMR performance could significantly change when this phenomenon is accounted for, as depicted in **Figure 6.10**. At higher temperatures, the effect of the concentration polarization on the CO_2 conversion becomes quite significant, despite being negligible on the product selectivity. Nevertheless, even if the efficiency of the membrane is reduced, the PBMR still outperforms the PBR.

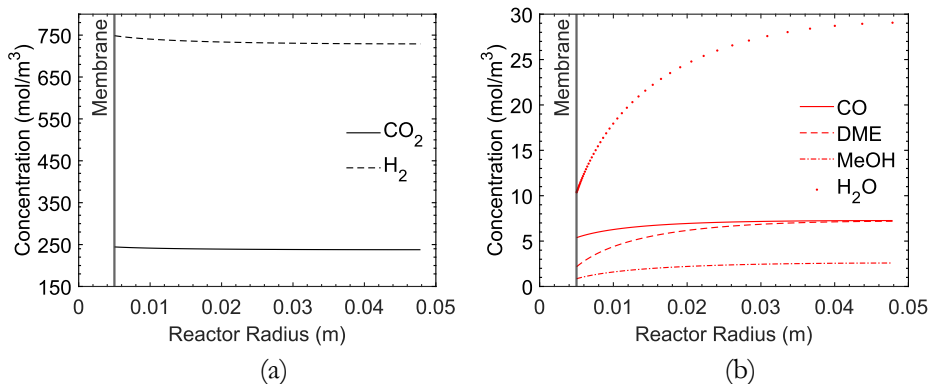


Figure 6.9. Radial concentration profiles of the reactants (a) and products (b) determined via the 2D PBMR model at $z = L/2$. Operating conditions: $T^R = 270$ °C, $p^{R,IN} = 40$ bar, $(C_{H_2}/C_{CO_2})_{IN} = 3$, $GHSV = 50$ h⁻¹, $w_{cat1} = 0.5$ wt %, $\Delta P = 5$ bar, $SW = 1$, $D_p = 0.25$ mm, $L_R = 0.5$ m, $D_{ri} = 0.1$ m, $D_{mo} = 0.01$ m.

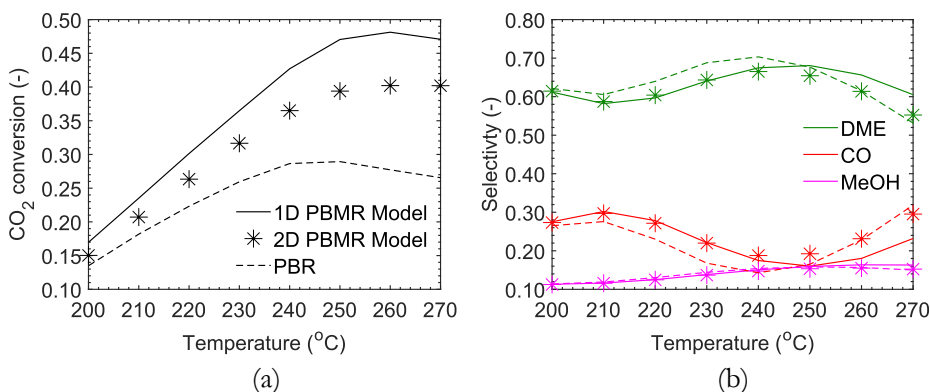


Figure 6.10. CO₂ conversion (a) and product selectivity (b) for a PBR (dashed lines) and a PBMR evaluated via a 1D model (solid line) and a 2D model (stars). Operating conditions: $T^R = 270$ °C, $p^{R,IN} = 40$ bar, $(C_{H_2}/C_{CO_2})_{IN} = 3$, $GHSV = 50$ h⁻¹, $w_{cat1} = 0.5$ wt %, $\Delta P = 5$ bar, $SW = 1$, $D_p = 0.25$ mm, $L_R = 0.5$ m, $D_{ri} = 0.1$ m, $D_{mo} = 0.01$ m.

The 2D PBMR model is computationally expensive, especially when the heat balance needs to be implemented as well. Alternatively, the concentration polarization phenomenon could be accounted for via the definition of a mass transfer coefficient (k_{CP}) determined via correlations, similarly to the approach described in section 6.4 (i.e., heat/mass transfer at the fluid-particle interphase). Boon et al. [10] proposed a correlation to estimate the mass transfer coefficient for the H₂ separation via palladium membranes in an empty column (i.e., gas separation process with no reaction). However, with this correlation, the concentration polarization effect on the reaction performance is significantly underestimated (see Appendix E, **Figure E12**). To the best of our knowledge, in literature there is no correlation describing the CP phenomenon for carbon molecular sieve membranes, especially when they

are implemented in a packed column (i.e., PBMR) and when reaction occurs simultaneously to the separation. Thus, this chapter proposes the development of a Sherwood-type correlation (Eq. 6.32-6.35) to account for the CP via a short-cut method, which does not require the implementation of a 2D model.

$$\text{Sh} = a \text{Re}^b \text{Sc}^c \text{E}^d \quad (6.32)$$

$$\text{Sh} = \frac{k_{\text{CP},i} d_h}{D_m} \quad (6.33)$$

$$\text{Re} = \frac{\rho_i u_{\text{SF}} d_h}{\mu_i \epsilon_{\text{bed}}} \quad (6.34)$$

$$\text{Sc} = \frac{\mu_i}{\rho_i D_{m,i}} \quad (6.35)$$

In Eq. 6.32, a , b , c and d are the coefficients of the correlation that have to be determined, E is a dimensionless number which accounts for entrance effects, and d_h is a characteristic length which we defined as the space between the reactor wall and the membrane selective layer (i.e., $d_h = R_{\text{ri}} - R_{\text{mo}}$). The Reynolds number (Re , Eq. 6.34) is divided by ϵ_{bed} to convert the superficial gas velocity into the interstitial velocity.

The mass transfer coefficient $k_{\text{CP},i}$ was determined from the 2D PBMR simulation results, via Eq. 6.36, where $\langle C_{i,r}^{\text{R}} \rangle$ is the average concentration of component i in the radial direction of the reaction zone and $C_{i,\text{m},\text{surf}}^{\text{R}}$ is its concentration at the membrane surface.

$$k_{\text{CP},i} = \frac{J_{\text{perm},i}}{\langle C_{i,r}^{\text{R}} \rangle - C_{i,\text{m},\text{surf}}^{\text{R}}} \quad (6.36)$$

As a result, using the definition of the $k_{\text{CP},i}$ from Eq. 6.36, in combination with Eq. 6.32, a set of 6800 data of Sherwood numbers was obtained from the results of the 2D PBMR simulations, carried out under a wide range of conditions. These include variations of the GHSV ($10\text{-}2000 \text{ h}^{-1}$), the temperature ($200\text{-}270 \text{ }^\circ\text{C}$), the pressure ($30\text{-}40 \text{ bar}$), the SW ($0.5\text{-}2$), the inlet composition to both zones ($\text{H}_2\text{:CO}_2$ of $1\text{-}4$), the reactor length ($0.1\text{-}10 \text{ m}$), the reactor diameter ($0.02\text{-}1 \text{ m}$), the particle diameter ($0.1\text{-}20 \text{ mm}$), the membrane diameter ($5\text{-}20 \text{ mm}$) and the zeolite weight fraction ($0.25\text{-}0.75$).

The parameters of the Sh correlation (Eq. 6.32) were determined via parametric fitting of the Sh numbers obtained from the rigorous 2D model, similarly to what was done for the Thiele modulus-efficiency correlation in section 6.3. The parameters were fitted in four different cases (**Table 6.10**) with the quality of the fit progressively improving from case 1 to 4 (i.e., $F_{\text{statistic}}$ decreases from 0.1456 to 0.1370, as reported in **Table E3**).

The factor d_h/z used to account for entrance effects in case 1, assumes a high value closer to the entrance. However, the entrance effect should account for two phenomena: 1) how fast the concentration profile develops (i.e., rate of mass transfer in the radial direction), 2) the residence time of the fluid in the reactor. Combining these two aspects, an entrance Peclet number (Pe_{ent}) was defined as in Eq. 6.37, which compares the characteristic time for dispersion in the radial direction (d_h^2/D_{rad}), with the characteristic time for convection in the axial direction (z/v). For large values of Pe_{ent} , the concentration profiles have not been developed yet, while for low value of Pe_{ent} , the fluid has spent enough time in the reactor to have developed the profiles.

$$Pe_{ent} = \frac{vd_h^2}{zD_{rad}} \quad (6.37)$$

Using the Pe_{ent} in Eq. 6.32 significantly improved the quality of the fit (see Appendix E, **Figure E10**). A further improvement was obtained with case 3 (see Appendix E, **Figure E11a**), where the radial dispersion coefficient (D_{rad}) is used instead of the molecular diffusivity ($D_{m,i}$) in the Schmidt number (Sc). Indeed, D_{rad} also accounts for the particle size and the tortuosity of the catalytic bed, which are parameters that are expected to affect the mass transfer in the radial direction. Finally, case 4 proposes two expression for the Sh , defined in two different regimes: 1) for $Pe_{ent} > 1$, the concentration profiles are not developed, thus the correlation needs to account for the entrance effect with the term $(Pe_{ent})^d$; 2) for $Pe_{ent} \leq 1$, the profiles are already developed, thus the dependency on the Pe_{ent} is removed.

Table 6.10. Cases description for the Sherwood number correlation for the mass transfer coefficient $k_{CP,i}$.

Case #	Sh correlation	Sc definition
1	$Sh = a Re^b Sc^c \left(\frac{d_h}{z}\right)^d$	$Sc = \frac{\mu_i}{\rho_i D_{m,i}}$
2	$Sh = a Re^b Sc^c (Pe_{ent})^d$	$Sc = \frac{\mu_i}{\rho_i D_{m,i}}$
3	$Sh = a Re^b Sc^c (Pe_{ent})^d$	$Sc = \frac{\mu_i}{\rho_i D_{rad}}$
4	$Sh = a Re^b Sc^c (Pe_{ent})^d$ for $Pe_{ent} > 1$ $Sh = a Re^b Sc^c$ for $Pe_{ent} \leq 1$	$Sc = \frac{\mu_i}{\rho_i D_{rad}}$

The parameters that were obtained with case 4 are summarized in **Table 6.11** and the quality of the fit is reported in terms of parity plot and $F_{statistic}$ in **Figure E11b** and **Table E3** (Appendix E), respectively. The values of all the parameters are in line with the range commonly proposed in literature for these types of correlations [2], [15]. Furthermore, the exponent of the Schmidt number (c) is close to 0.33, which is a recurrent value in the state of the art mass transfer correlations. Indeed, the term $Sc^{0.33}$ derives from the analytical solution of similar problems. Therefore, a refitting of the parameters is proposed, setting the value of c to 0.33, being this an

assumption with theoretical basis. The re-fitted values of a , b and d do not deviate much from the previous set of parameters and the quality of the fit is not affected. The final correlation proposed for the calculation of the $k_{CP,i}$ is summarized in Eq. 6.38–6.39.

Table 6.11. Fitted parameters for Eq. 6.32– Case 4

Parameter	Value	Refitted value
a	0.4628	0.4338
b	0.3509	0.3583
c	0.3179	0.3330
d	0.2640	0.2634

$$\text{Sh} = 0.43 \left(\frac{\rho_i v_{SF} d_h}{\mu_i \varepsilon_{bed}} \right)^{0.36} \left(\frac{\mu_i}{\rho_i D_{rad}} \right)^{0.33} \left(\frac{v d_h^2}{z D_{rad}} \right)^{0.26} \quad \text{for } \text{Pe}_{ent} > 1 \quad (6.38)$$

$$\text{Sh} = 0.43 \left(\frac{\rho_i v_{SF} d_h}{\mu_i \varepsilon_{bed}} \right)^{0.36} \left(\frac{\mu_i}{\rho_i D_{rad}} \right)^{0.33} \quad \text{for } \text{Pe}_{ent} \leq 1 \quad (6.39)$$

The results reported in **Figure 6.10** were reproduced using the 1D PBMR model developed in section 6.6, implementing a mass balance around the membrane surface, as reported in Eq. 6.40. In such a way, the gradient for the species permeation can be corrected to account for the concentration polarization phenomenon via the $k_{CP,i}$.

$$k_{CP,i} (C_{i,bulk}^R - C_i^R|_{r=R_{mo}}) = \wp_i (P_i^R|_{r=R_{mo}} - P_i^P) \quad (6.40)$$

The prediction of both CO_2 conversion and product selectivity obtained via the 1D PBMR model using the correlation developed in this chapter is quite accurate over the entire region of temperature (**Figure 6.11**). As a result, this method could be used to better estimate the performance of the PBMR accounting for all the relevant mass transfer phenomena without having to implement a complex and computationally expensive 2D model.

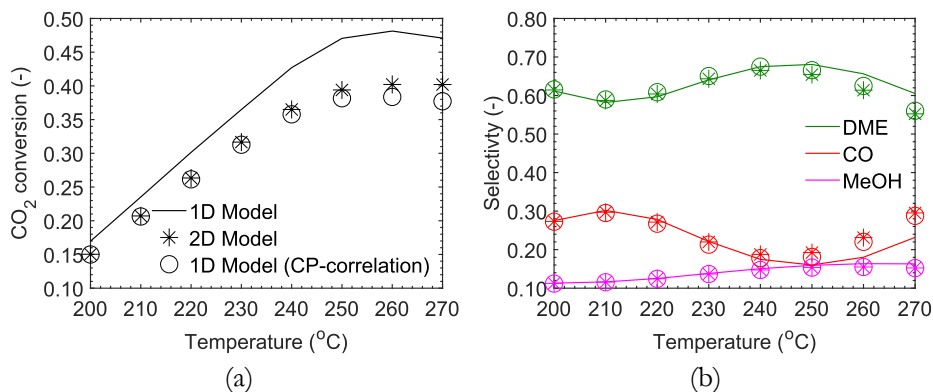


Figure 6.11. CO₂ conversion (a) and product selectivity (b) for a PBMR evaluated via a 1D model which does not account for CP phenomenon (solid line), a 2D model (stars) and a 1D model which accounts for the CP phenomenon using the correlation developed in this section (circles). Operating conditions: $T^R = 270$ °C, $p^{R,IN} = 40$ bar, $(C_{H_2}/C_{CO_2})_{IN} = 3$, $GHSV = 50$ h⁻¹, $w_{cat1} = 0.5$ wt %, $\Delta P = 5$ bar, $SW = 1$, $D_p = 0.25$ mm, $L_R = 0.5$ m, $D_{ri} = 0.1$ m, $D_{mo} = 0.01$ m.

The parameter which affects the radial transport of molecules (and thus the concentration polarization) the most is the velocity, as often reported in literature [9]. As a result, one of the most effective ways to reduce the effect of the CP and to increase the effectiveness of the membrane separation, is to increase the velocity in the reactor. This can be easily done by changing the reactor geometry at constant volume, thus increasing the reactor aspect ratio (i.e., reducing the reaction zone cross section). An example is given in **Figure 6.12**, where the difference in the CO₂ conversion and product selectivity between a model which does not account for the CP phenomenon and a model that accounts for it via the Sh correlation approaches zero as the inlet velocity to the reaction zone increases.

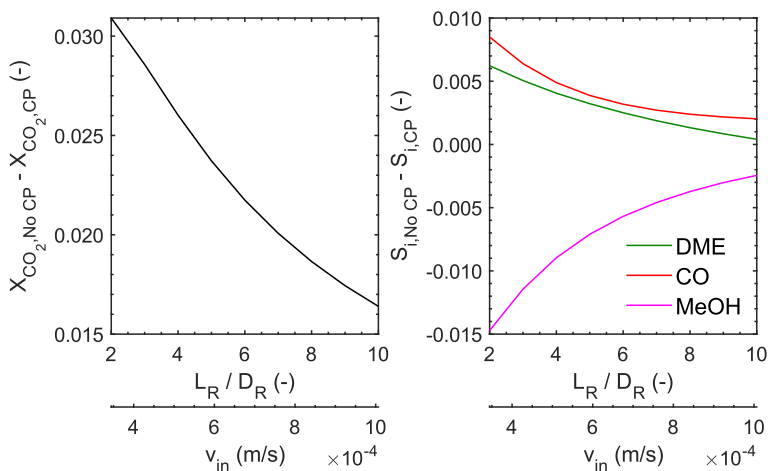


Figure 6.12. Difference of CO₂ conversion and product selectivity between a model which does not account for the CP phenomenon and a model that accounts for it via the Sh correlation. Operating conditions of the PBMR: $T^R = 270 \text{ }^\circ\text{C}$, $p^{R, \text{IN}} = 40 \text{ bar}$, $(C_{\text{H}_2}/C_{\text{CO}_2})_{\text{IN}} = 3$, $\text{GHSV} = 50 \text{ h}^{-1}$, $w_{\text{cat1}} = 0.5 \text{ wt } \%$, $\Delta P = 5 \text{ bar}$, $\text{SW} = 1$, $D_p = 0.25 \text{ mm}$, $D_{\text{mo}} = 0.01 \text{ m}$.

6.8 CONCLUSIONS

This study demonstrates that intra-particle diffusion and concentration polarization are both phenomena that affect the packed bed (membrane) reactor performance for the CO₂ hydrogenation to DME, especially at conditions which are relevant to large scale operation. On the contrary, the intra-particle heat transfer, the particle-fluid mass and heat transfer as well as the axial dispersion were found to have a negligible effect on the reactor behavior.

To consider simultaneously the pore diffusion and the CP effects, a complex 3D PBMR model would be required. However, in this study, useful tools were developed to account for these phenomena using short-cut methods that can be implemented in a 1D pseudo-homogeneous reactor model.

Being the state-of-the-art Thiele modulus approach not applicable to this system, due to the complexity of the reaction network and of the kinetic model, a generalized Thiele modulus (φ) definition was proposed here, where the diffusion term is adjusted with the equilibrium concentration. A correlation for the component-specific efficiency as a function of the Thiele modulus was developed from the simulation results of the rigorous particle model. This correlation predicts an efficiency of $1/\varphi$ for large value of the Thiele modulus, which is a result often found in literature, deriving from analytical solutions of simple systems. The Thiele modulus-efficiency approach proposed here accurately predicts the CO₂ conversion and product selectivity of the rigorous particle-reactor model within a maximum

deviation of 5%. For values of the Thiele modulus larger than 2, this approach overestimates the effects of the pore-diffusion. However, this situation occurs in conditions which are outside the range of interest.

To account for the CP phenomenon in the PBMR model, a Sherwood-type for the calculation of a mass transfer coefficient (k_{CP}) was proposed. In this correlation, a Peclet number, which compares the characteristic time for diffusion in the radial direction with the characteristic time for convection in the axial direction, is used to account for the entrance effects (i.e., not developed concentration profiles). The parameters of the correlation were determined fitting the simulation data obtained via the rigorous 2D PBMR model. The so-developed correlation predicts with high accuracy (i.e., deviations less than 5%) the effect of the CP on the PBMR performance. However, it was found that even in-situations with significant CP, the PBMR still outperforms the PBR. Nevertheless, the CP effects can be mitigated by increasing the velocity in the reactor (e.g., increasing the reactor L/D).

In conclusion, given the findings of this work, a further optimization of the PBMR and PBR was proposed, in view of the relevant mass/heat transfer phenomena. The optimization is mostly based on the fraction of the zeolite in the catalytic bed. In literature, a mass fraction in the range 33-50 wt % is often used and the effect of this parameter on the reaction performance is considered negligible. However, due to the fast methanol dehydration reaction, significantly less zeolite is required to achieve equilibrium conditions. The optimal zeolite loading was found to vary in the range 4-11 wt%, according to the catalyst particle size and the extent of water removal in the membrane reactor. Indeed, when intra-particle diffusion limitations are relevant, the optimal zeolite fraction increases, being the zeolite more affected by pore-diffusion phenomena.

Appendix E

E.1 Kinetic model and validation

Table E1. Kinetic, adsorption and equilibrium constants for the reaction rates Eq. 6.1-6.4 [12][13]. In these expressions, the unit of temperature (T) is Kelvin (K) and the ideal gas constant (R) is 8.314 J/mol/K.

Parameter	Expression
Kinetic constants	
k_1 (mol s ⁻¹ bar ⁻¹ kg _{cat} ⁻¹)	$4.89 \cdot 10^7 \exp\left(-\frac{113\,000}{RT}\right)$
k_2 (mol s ⁻¹ bar ^{-1/2} kg _{cat} ⁻¹)	$1.53 \cdot 10^{10} \exp\left(-\frac{129\,000}{RT}\right)$
k_3 (mol s ⁻¹ bar ⁻¹ kg _{cat} ⁻¹)	$1.71 \cdot 10^1 \exp\left(-\frac{51\,605}{RT}\right)$
k_4 (mol s ⁻¹ bar ⁻² kg _{cat} ⁻¹)	$1.69 \cdot 10^{-2} \exp\left(-\frac{103\,400}{RT}\right)$
Adsorption constants	
b_{CO} (bar ⁻¹)	$2.16 \cdot 10^{-5} \exp\left(\frac{46\,800}{RT}\right)$
b_{CO_2} (bar ⁻¹)	$7.05 \cdot 10^{-7} \exp\left(\frac{61\,700}{RT}\right)$
$\frac{b_{H_2O}}{b_{H_2}^{1/2}}$ (bar ^{-1/2})	$6.37 \cdot 10^{-9} \exp\left(\frac{84\,000}{RT}\right)$
b_{CH_3OH} (bar ⁻¹)	$\exp\left(\frac{-73}{R}\right) \cdot \exp\left(\frac{44.5 \cdot 10^3}{RT}\right)$
$b_{H_2O}^+$ (bar ⁻¹)	$\exp\left(\frac{-182}{R}\right) \cdot \exp\left(\frac{89.6 \cdot 10^3}{RT}\right)$
Equilibrium constants	
K_1 (bar ⁻²)	$\log_{10}(K_1) = \frac{5139}{T} - 12.621$
K_2 (-)	$\log_{10}(K_2) = \frac{-2073}{T} + 2.029$
K_3 (bar ⁻²)	$\log_{10}(K_3) = \frac{3066}{T} - 10.592$
K_4 (-)	$\ln(K_4) = 4019/T + 3.707 \cdot \ln(T) - 2.783 \cdot 10^{-3}T + 3.8 \cdot 10^{-7}T^2 - 6.56 \cdot 10^4/T^3 - 26.64$

The kinetic model has been validated with experimental data obtained with a physical mixture of 50 wt % Cu/ZnO/Al₂O₃ and 50 wt % HZSM-5, as shown in **Figure E1**.

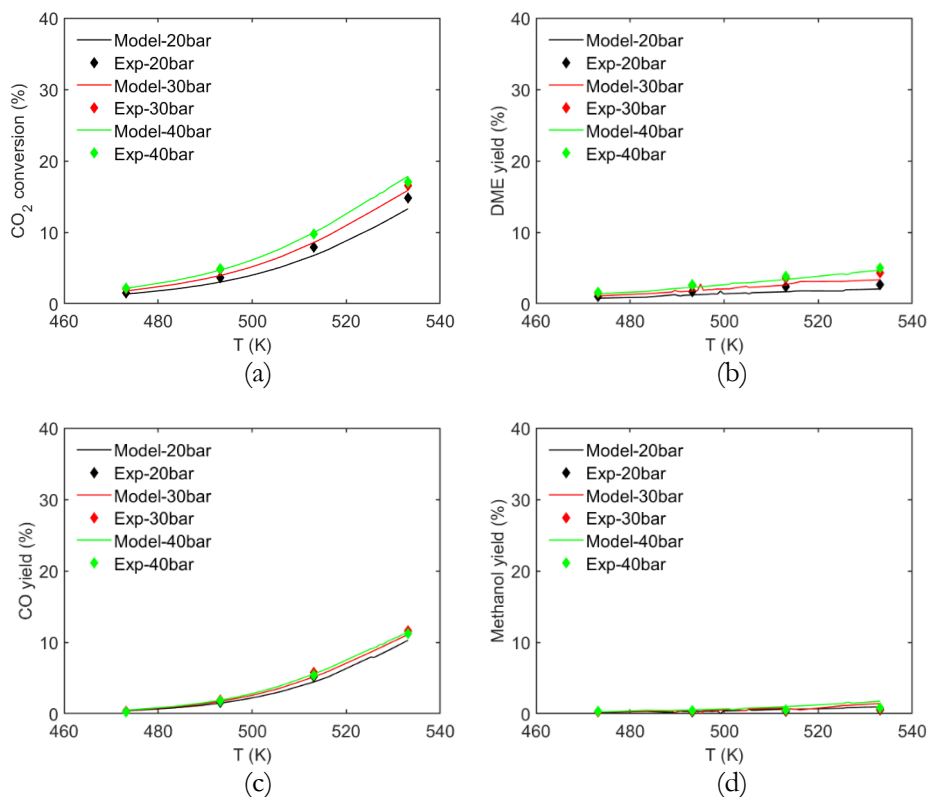


Figure E1. CO_2 conversion (a), DME yield (b), CO yield (c) and methanol yield (d) as a function of pressure at 20 bar (black lines/symbols), 30 bar (red lines/symbols) and 40 bar (green lines/symbols) at $3'400 \text{ NL} \cdot \text{kgcat}^{-1} \cdot \text{h}^{-1}$ and $\text{CO}_2/\text{H}_2/\text{N}_2 = 3/9/1$. Symbols represent the experimental data, continuous lines represent the model prediction (combination of the model by Portha et al. and the model by Ortega et al.)

The physical properties of the catalyst, which were measured experimentally (i.e., using N_2 physisorption and a He-pycnometer) are reported in **Table E2**.

Table E2. Measured physical properties of the CuZA and HZSM-5 catalyst

Property	CuZA	HZSM-5
Catalyst porosity (ϵ_{cat})	0.325	0.4
Average pore diameter (d_{pore})	7.06 nm	0.55 nm
Catalyst density (ρ_{cat})	$1300 \text{ kg}_{\text{cat}}/\text{m}^3_{\text{cat}}$	$720 \text{ kg}_{\text{cat}}/\text{m}^3_{\text{cat}}$

E.2 Membrane properties (CM08 vs fitting curves)

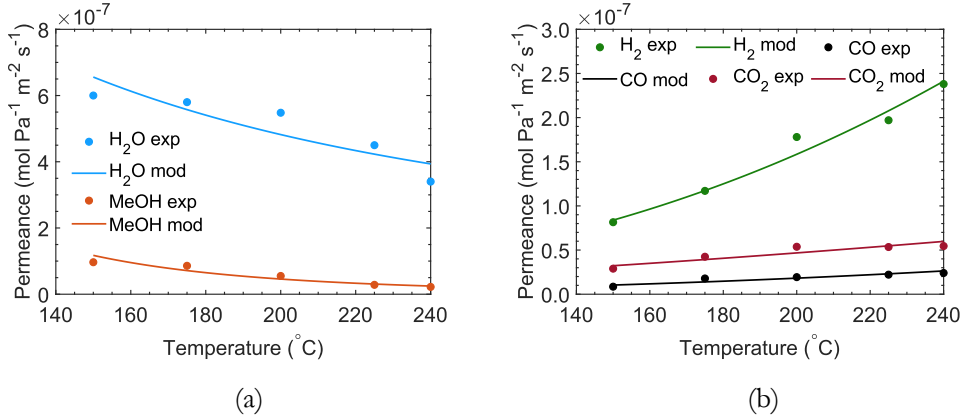


Figure E2. Membrane properties of the carbon membrane CM08 (Chapter 3) in terms of water and methanol permeance (a) and H₂, CO and CO₂ permeance (b): markers and lines represent experimental and simulated data, respectively.

E.3 Physical properties and correlations

The physical properties which are not reported here, were derived according to the methodology reported in Appendix A (section A.1).

The molecular diffusion coefficient for a binary mixture ($D_{m,i,j}$) and a multicomponent mixture ($D_{m,i}$) is given by Eq. E.1 and Eq. E.2, respectively, where $v_{c,i}$ is the diffusion volume of the species i [30].

$$D_{m,i,j} = \frac{\lambda_{\text{mix}} \text{Nu}}{P \left(v_{c,i}^{1/3} + v_{c,j}^{1/3} \right)^2} \quad (\text{E.1})$$

$$D_{m,i} = \frac{1 - y_i}{\sum_{j \neq i} \frac{y_j}{D_{m,i,j}}} \quad (\text{E.2})$$

The Knudsen diffusivity in the catalyst pore ($D_{k,i}$) and the effective diffusion coefficient ($D_{\text{eff},i}$) are described by Eq. E.3 and Eq. E.4, respectively, with ε_{cat} and τ_{cat} being the catalyst porosity and tortuosity (Eq. E.5) [6], [31].

$$D_{k,i} = \frac{d_{\text{pore}}}{3} \sqrt{\frac{8RT}{\pi M_i}} \quad (\text{E.3})$$

$$D_{\text{eff},i} = \frac{\varepsilon_{\text{cat}}}{\tau_{\text{cat}}} \left(\frac{1}{D_{m,i}} + \frac{1}{D_{k,i}} \right)^{-1} \quad (\text{E.4})$$

$$\tau_{\text{cat}} = \frac{c}{1 - (1 - \varepsilon_{\text{cat}})^{2/3}} \quad (\text{E.5})$$

The effective diffusivity is given by the equation of Coté and Konrad [16] (Eq. E.6) where λ_f is the conductivity of the fluid mixture and λ_{cat} is the thermal conductivity of the catalyst particle.

$$\lambda_{eff} = \lambda_{cat}^{1-\varepsilon_{cat}} \cdot \lambda_f^{\varepsilon_{cat}} \quad (E.6)$$

The correlation of Dwivedi for the particle-fluid mass transfer in fixed bed, for the range $0.1 \leq Re \leq 14'000$, is described below [8]:

$$\frac{\varepsilon_{bed} k_{ext,i} Sc^{0.66}}{v_{SF}} = \frac{0.765}{Re^{0.82}} + \frac{0.365}{Re^{0.386}} \quad (E.7)$$

$$Sc = \frac{\mu_i}{\rho_i D_{m,i}} \quad (E.8)$$

$$Re = \frac{\rho_i v_{SF} D_p}{\mu_i} \quad (E.9)$$

The correlation of Gupta et al. for the particle-fluid heat transfer in fixed bed, for the range $0.1 \leq Re \leq 10'000$, is described below [21]:

$$\frac{\varepsilon_{bed} h_{ext} Pr^{0.66}}{C_{p,mix} v_{SF} \rho_f} = \frac{2.876}{Re} + \frac{0.3023}{Re^{0.35}} \quad (E.10)$$

$$Pr = \frac{\mu_i C_{p,mix}}{\lambda_f} \quad (E.11)$$

The axial dispersion coefficient ($D_{ax,i}$) is derived via the correlation of Gunn, as follows [21]:

$$\frac{1}{Pe_{ax}} = \frac{Pe_m}{5} (1-p)^2 + \frac{Pe_m^2}{25} p(1-p)^3 \left(\exp\left(-\frac{5}{p(1-p)Pe_m}\right) - 1 \right) + \frac{1}{\tau_{bed} Pe_m} \quad (E.12)$$

$$p = \frac{0.48}{Sc^{0.15}} + \left(\frac{1}{2} - \frac{0.48}{Sc^{0.15}} \right) \exp\left(-\frac{75Sc}{Pe_m}\right) \quad (E.13)$$

$$Pe_{ax} = \frac{v_{SF} D_p}{D_{ax,i} \varepsilon_{bed}} \quad (E.14)$$

$$Pe_m = \frac{v_{SF} D_p}{D_{m,i} \varepsilon_{bed}} \quad (E.15)$$

The radial dispersion coefficient ($D_{rad,i}$) is also derived from the work of Gunn, as follows:

$$\frac{1}{Pe_{rad}} = \frac{1}{Pe_f} + \frac{\varepsilon_{bed}}{\tau_{bed} Re Sc} \quad (E.16)$$

$$Pe_{rad} = \frac{v_{SF} D_p}{D_{rad,i} \varepsilon_{bed}} \quad (E.17)$$

$$Pe_f = 40 - 29 \exp\left(-\frac{7}{Re}\right) \quad (E.18)$$

The heat is removed from the reactor via external cooling (boiling water): 1) heat is transferred from the bulk fluid to the reactor walls (h_i); 2) the heat is conducted

through the reactor walls (k_w) made of stainless-steel and 3) the heat is transferred to the cooling medium, in the mantle (h_o). The global heat transfer coefficient (U) including these phenomena is defined as follows:

$$\frac{1}{U} = \frac{1}{h_i} + \frac{D_{ri} \ln(D_{ro}/D_{ri})}{2k_w} + \frac{D_{ri}}{D_{ro}} \frac{1}{h_o} \quad (\text{E.19})$$

The coefficients h_i and h_o are derived via the following correlations [32], [33]:

$$Nu = \frac{h_i D_p}{\lambda_f} = 0.17 \left(\frac{Pr}{0.7} \right)^{0.33} Re^{0.79} \quad (\text{E.20})$$

$$h_o = 7.96(T - T_w)^3 \left(\frac{P_o}{P_a} \right)^{0.4} \quad (\text{E.21})$$

Where P_a is the atmospheric pressure and P_o is the saturation pressure of water (in the cooling mantle) at the temperature T_w .

The correlation of Boon et al. for the concentration polarization, developed for H_2 separation via palladium membranes is reported below [10]:

$$Sh = \frac{k_{CP,i} d_h}{D_{m,i}} = 1.07 Gz^{0.42} = 1.07 \left(ReSc \frac{d_h}{z} \right)^{0.42} \quad Gz \geq 62 \quad (\text{E.22})$$

$$Sh = \frac{k_{CP,i} d_h}{D_{m,i}} = Sh_{inf} = 6.18 \quad Gz < 62 \quad (\text{E.23})$$

Where d_h (hydraulic diameter) is the annular space between the wall of the vessel and the membrane, z is the axial distance from the entrance of the vessel.

E.4 Supplementary figures

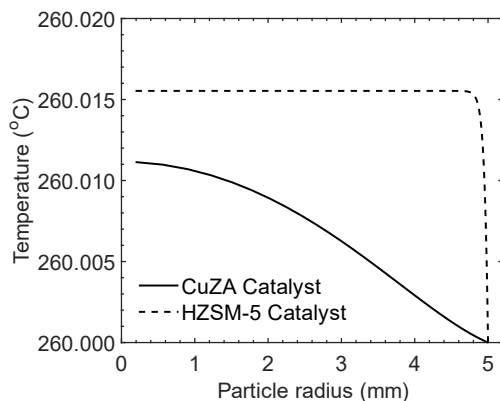


Figure E3. Temperature profile in the CuZA (left axis) and HZSM-5 (right axis) catalyst particle ($T_{surf}=270$ °C, $P=40$ bar, $d_p=10$ mm).

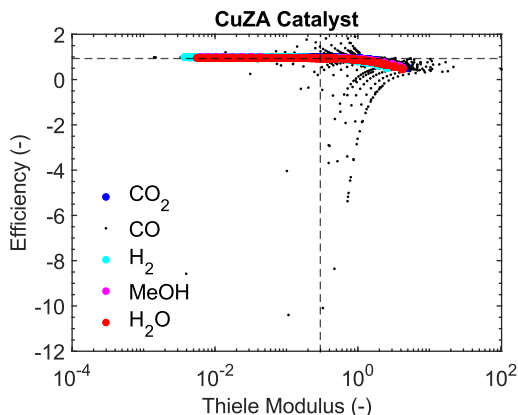


Figure E4. Catalyst efficiency (η_i) as a function of the Thiele modulus (ϕ_i) for the different species in the CuZA catalyst, including CO (**Figure 6.2a** with CO data) for systems with varying particle geometry (slab, cylinder, sphere), temperature (200-270 °C), pressure (30-40 bar), particle size (0.1-20 mm) and surface compositions. Dashed lines indicate the point of significant deviation of η_i from 1.

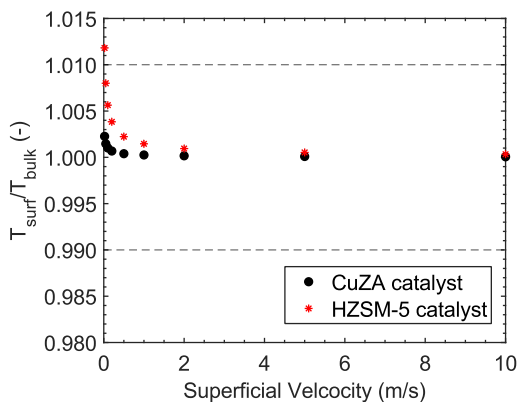


Figure E5. Normalized surface temperature ($T_{\text{surf}}/T_{\text{bulk}}$) of the CuZA (circles) and HZSM-5 (stars) catalysts as a function of the superficial gas velocity determined at a bulk temperature of 270 °C, a pressure of 40 bar, a particle diameter of 10 mm and artificially setting the H_2 thermal conductivity at 0.03 W/m/K. The dashed lines represent a 1% deviation from 1.

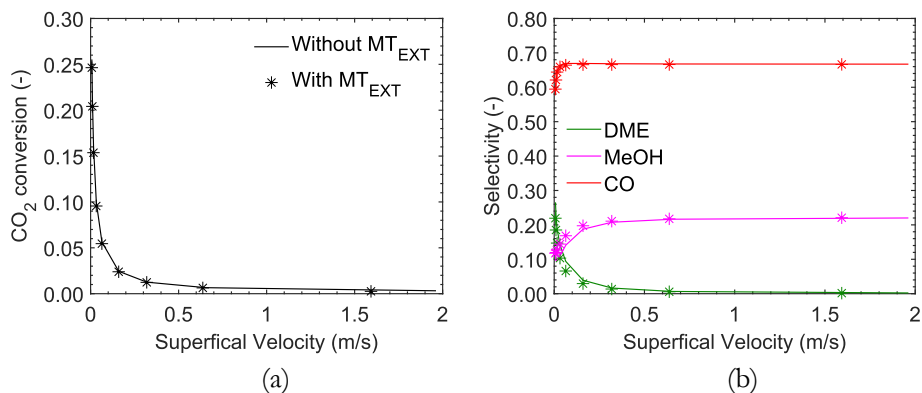


Figure E6. CO₂ conversion (a) and product selectivity (b) as a function of the gas superficial velocity. The solid lines represents a model which does not account for the particle-fluid (external) mass transfer (MT_{EXT}) and the starts represents a model which includes the MT_{EXT}. Conditions used for the simulations: $T = 270^{\circ}\text{C}$, $P_{\text{in}}^{\text{R}} = 40 \text{ BAR}$, $(C_{\text{H}_2}/C_{\text{CO}_2})_{\text{IN,BULK}} = 3$, $\text{GHSV} = 500 \text{ h}^{-1}$, $w_{\text{cat}1} = 0.5$.

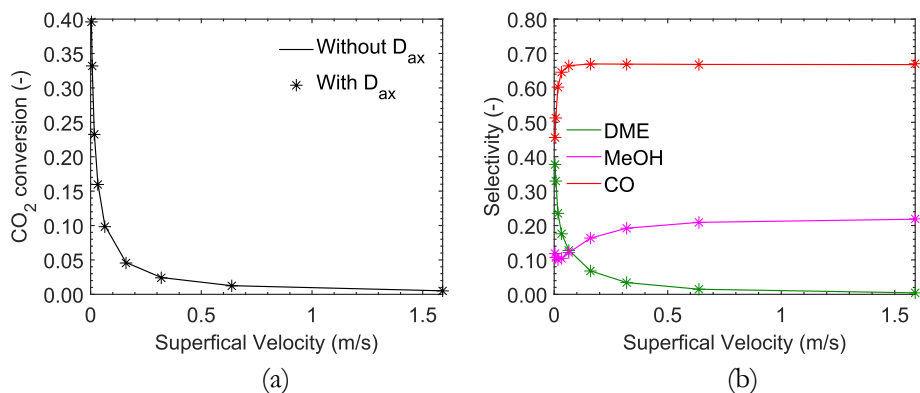


Figure E7. CO₂ conversion (a) and product selectivity (b) as a function of the gas superficial velocity. The solid lines represents the plug flow model and the starts represents the axial dispersion model. Conditions used for the simulations: $T = 270^{\circ}\text{C}$, $P_{\text{in}}^{\text{R}} = 40 \text{ BAR}$, $(C_{\text{H}_2}/C_{\text{CO}_2})_{\text{IN,BULK}} = 3$, $\text{GHSV} = 500 \text{ h}^{-1}$, $w_{\text{cat}1} = 0.5$.

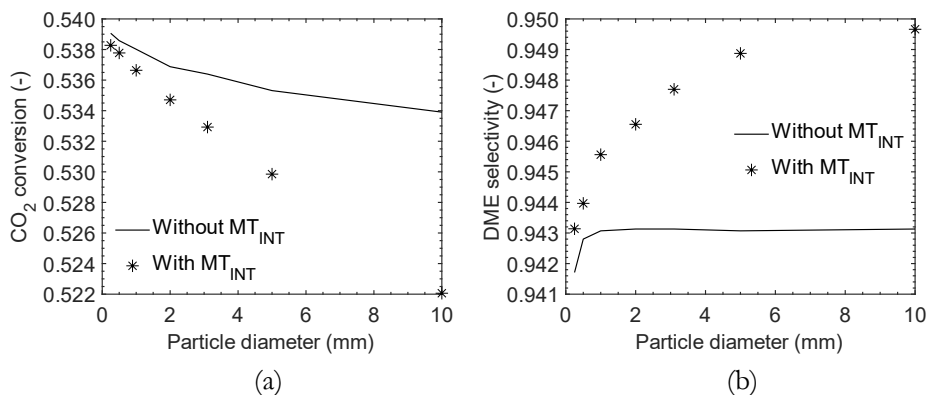


Figure E8. CO₂ conversion (a) and DME selectivity (b) as a function of the particle diameter for the PBMR reactor with the characteristic and conditions reported in **Table 6.7**. The solid line represents a model which does not account for intra-particle diffusion limitation (MT_{INT}), the stars represent a model which account for MT_{INT}.

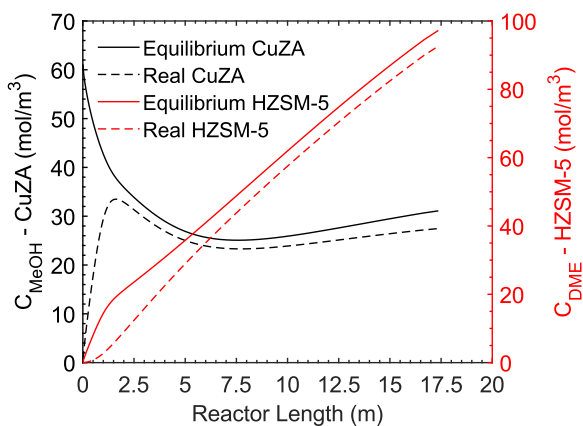


Figure E9. Methanol real (i.e., in the reactor) and equilibrium concentration (left axis) and DME real and equilibrium concentration (right axis) a function of the reactor length. Simulations were carried out on a PBMR, under the conditions reported in **Table 6.7**, using a zeolite weight fraction of 0.1 wt %.

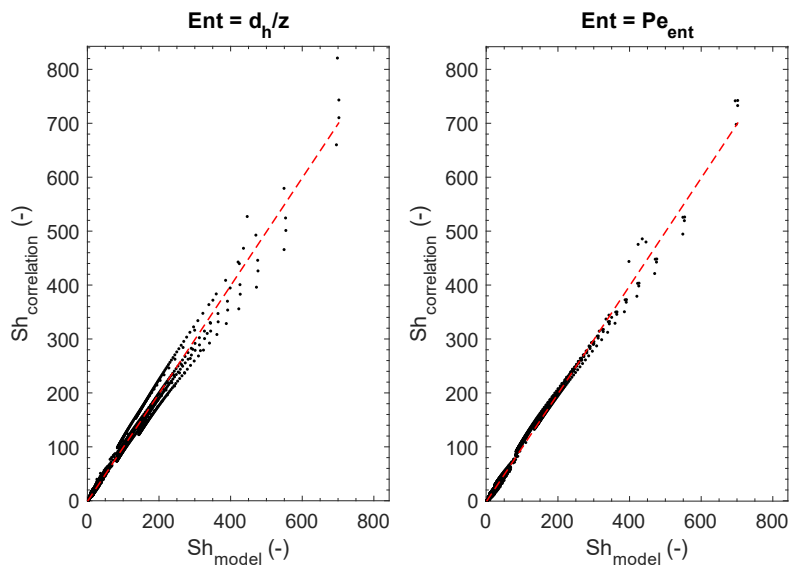


Figure E10. Sherwood number derived via the correlation proposed in Eq. 6.32 ($Sh_{\text{correlation}}$), using d_h/z Case 1 (a) and Pe_{ent} Case 2 (b) for the entrance effect, as a function of the Sherwood number calculated solving the 2D PBMR model (Sh_{model})

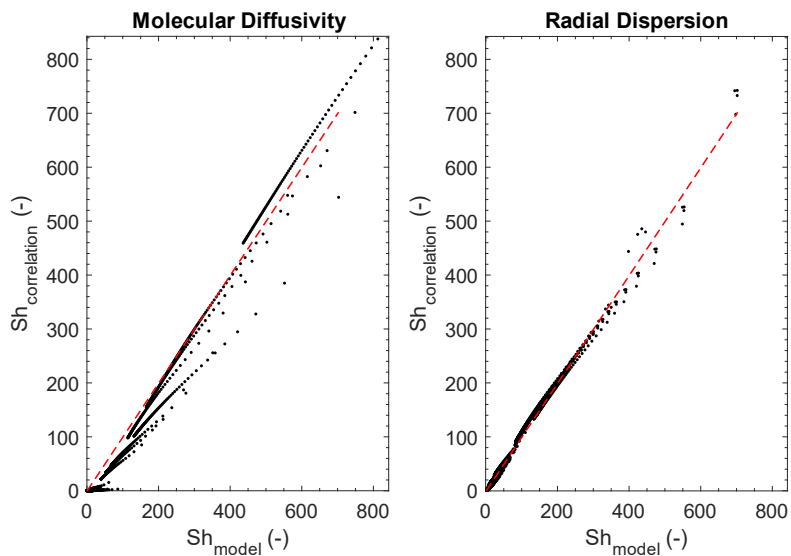


Figure E11. Sherwood number derived via the correlation proposed in Eq. 6.32 ($Sh_{\text{correlation}}$), using $D_{m,i}$ Case 3 (a) and $D_{\text{rad},i}$ Case 4 (b) in the SC number, as a function of the Sherwood number calculated solving the 2D PBMR model (Sh_{model})

Table E3. Values of the $F_{\text{statistic}}$ determined as the ratio of the variance of the lack of fit and the variance of the experimental error compared to the $F_{\text{critical}} = 1$, obtained from the Fisher distribution table with a 95% confidence interval and using N_{data} and $(N_{\text{data}} - N_{\text{param}})$ as degree of freedom [20].

Case #	$F_{\text{statistic}}$
1	0.1456
2	0.1457
3	0.1370
4	0.1369

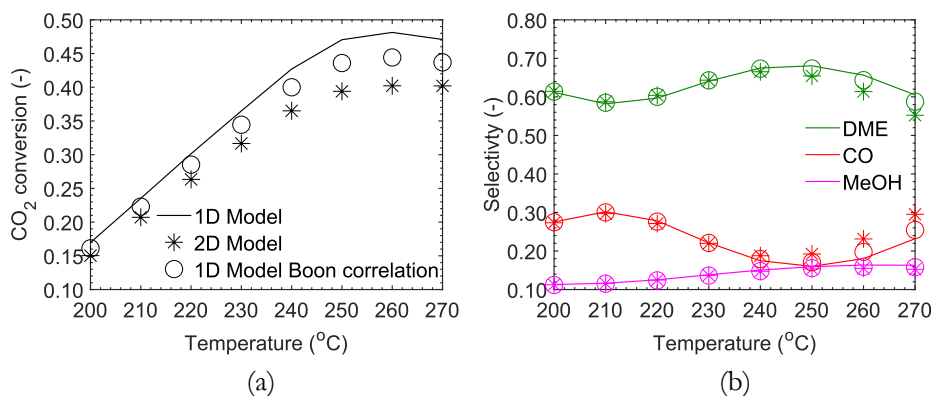


Figure E12. CO_2 conversion (a) and product selectivity (b) for a PBMR evaluated via a 1D model which does not account for CP phenomenon (solid line), a 2D model (stars) and a 1D model which accounts for the CP phenomenon using the correlation of Boon et al. [10] (circles). Operating conditions: $T^{\text{R}} = 270$ °C, $p^{\text{R,IN}} = 40$ bar, $(C_{\text{H}_2}/C_{\text{CO}_2})_{\text{IN}} = 3$, $\text{GHSV} = 50$ h^{-1} , $w_{\text{cat1}} = 0.5$ wt %, $\Delta P = 5$ bar, $\text{SW} = 1$, $D_{\text{p}} = 0.25$ mm, $L_{\text{R}} = 0.5$ m, $D_{\text{r1}} = 0.1$ m, $D_{\text{mo}} = 0.01$ m.

REFERENCES

- [1] O. Levenspiel, *Chemical reaction engineering*, vol. 38, no. 11. 1999.
- [2] H. S. Fogler, *Elements of Chemical Reaction Engineering*, 5th editio. Boston, 1952.
- [3] G. F. Froment, K. B. Bischoff, and J. De Wilde, *Chemical Reactor Analysis and Design*, 3rd editio. New York, 2011.
- [4] B. L. Shin, C. Wonjun, K. P. Dal, and S. Y. En, "Simulation of fixed bed reactor for dimethyl ether synthesis," *Korean J. Chem. Eng.*, vol. 23, no. 4, pp. 522–530, 2006,
- [5] D. Song, W. Cho, G. Lee, D. K. Park, and E. S. Yoon, "Numerical analysis of a pilot-scale fixed-bed reactor for dimethyl ether (DME) synthesis," *Ind. Eng. Chem. Res.*, vol. 47, no. 13, pp. 4553–4559, 2008,
- [6] C. R. Behloul, J. M. Commenge, and C. Castel, "Simulation of Reactors under Different Thermal Regimes and Study of the Internal Diffusional Limitation in a Fixed-Bed Reactor for the Direct Synthesis of Dimethyl Ether from a CO₂-Rich Input Mixture and H₂," *Ind. Eng. Chem. Res.*, vol. 60, no. 4, pp. 1602–1623, 2021,
- [7] Y. Tavan, S. H. Hosseini, M. Ghavipour, M. R. K. Nikou, and A. Shariati, "From laboratory experiments to simulation studies of methanol dehydration to produce dimethyl ether - Part I: Reaction kinetic study," *Chem. Eng. Process. Process Intensif.*, vol. 73, pp. 144–150, 2013,
- [8] P. N. Dwlvedi and S. N. Upadhyay, "Particle-Fluid Mass Transfer in Fixed and Fluidized Beds," *Ind. Eng. Chem. Process Des. Dev.*, vol. 16, no. 2, pp. 157–165, 1977,
- [9] D. J. Gunn, "Axial and radial dispersion in fixed beds," *Chem. Eng. Sci.*, vol. 42, no. 2, pp. 363–373, 1987,
- [10] J. Boon, H. Li, J. W. Dijkstra, and J. A. Z. Pieterse, "2-Dimensional membrane separator modeling: Mass transfer by convection and diffusion," *Energy Procedia*, vol. 4, pp. 699–706, 2011,
- [11] S. Bhattacharya and S. Hwang, "Concentration polarization, separation factor, and Peclet number in membrane processes," *J. Memb. Sci.*, vol. 132, pp. 73–90, 1997.
- [12] S. Ghosh, J. Sebastian, L. Olsson, and D. Creaser, "Experimental and kinetic modeling studies of methanol synthesis from CO₂ hydrogenation using In₂O₃ catalyst," *Chem. Eng. J.*, vol. 416, p. 129120, 2021,
- [13] C. Ortega, M. Rezaei, V. Hessel, and G. Kolb, "Methanol to dimethyl ether conversion over a ZSM-5 catalyst: Intrinsic kinetic study on an external recycle reactor," *Chem. Eng. J.*, vol. 347, no. April, pp. 741–753, 2018,
- [14] N. Diban, A. M. Urtiaga, I. Ortiz, J. Ereña, J. Bilbao, and A. T. Aguayo, "Influence of the membrane properties on the catalytic production of dimethyl ether with in-situ water removal for the successful capture of CO₂," *Chem. Eng. J.*, vol. 234, pp. 140–148, 2013,
- [15] P. Trambouze and J. P. Euzen, *Chemical Reactors*, 1st editio. Paris, 2022.
- [16] B. Ghanbarian and H. Daigle, "Thermal conductivity in porous media: Percolation-

- based effective-medium approximation.," *Water Resour. Res.*, vol. 52 (1), pp. 295–314, 2016.
- [17] K. M. Vanden Bussche and G. F. Froment, "A Steady-State Kinetic Model for Methanol Synthesis and the Water Gas Shift Reaction on a Commercial Cu / ZnO / Al₂O₃ Catalyst," vol. 10, no. 0156, pp. 1–10, 1996.
- [18] H. Graaf, E. J. Stamhuis, and A. A. C. M. Beenackers, "Kinetics of low-pressure methanol synthesis," *Chem. Eng. Sci.*, vol. 43, no. 12, pp. 3185–3195, 1988.
- [19] T. Henkel, "Modellierung von Reaktion und Stofftransport in geformten Katalysatoren am Beispiel der Methanolsynthese," Diss. Technische Universität München, 2011.
- [20] S. Poto, D. Vico van Berkel, F. Gallucci, and M. Fernanda Neira d'Angelo, "Kinetic modeling of the methanol synthesis from CO₂ and H₂ over a CuO/CeO₂/ZrO₂ catalyst: The role of CO₂ and CO hydrogenation," *Chem. Eng. J.*, vol. 435, no. P2, p. 134946, 2022,
- [21] S. N. Gupta, R. B. Chaube, and S. N. Upadhyay, "Fluid-Particle and Heat Transfer Beds," *Chem. Eng.*, vol. 29, pp. 839–843, 1974.
- [22] D. E. Mears, "for Axial," vol. 15, no. 1, 1976.
- [23] J. M. P. Q. Delgado, "A critical review of dispersion in packed beds," *Heat Mass Transf. und Stoffuebertragung*, vol. 42, no. 4, pp. 279–310, 2006,
- [24] J. G. H. Borkink and W. K.R., "Significance of the radial porosity profile for the description of heat transport in wall-cooled packed beds," *Chem. Eng. Sci.*, vol. 49, no. 6, pp. 863–876, 1994,
- [25] F. S. Ramos *et al.*, "Role of dehydration catalyst acid properties on one-step DME synthesis over physical mixtures," *Catal. Today*, vol. 101, no. 1, pp. 39–44, 2005,
- [26] A. Ateka, I. Sierra, J. Ereña, J. Bilbao, and A. T. Aguayo, "Performance of CuO–ZnO–ZrO₂ and CuO–ZnO–MnO as metallic functions and SAPO-18 as acid function of the catalyst for the synthesis of DME co-feeding CO₂," *Fuel Process. Technol.*, vol. 152, pp. 34–45, 2016,
- [27] F. Frusteri, M. Cordaro, C. Cannilla, and G. Bonura, "Multifunctionality of Cu-ZnO-ZrO₂/H-ZSM5 catalysts for the one-step CO₂-to-DME hydrogenation reaction," *Appl. Catal. B Environ.*, vol. 162, pp. 57–65, 2015,
- [28] H. Hamedi and T. Brinkmann, "Valorization of CO₂ to DME using a membrane reactor: A theoretical comparative assessment from the equipment to flowsheet level," *Chem. Eng. J. Adv.*, vol. 10, no. January, p. 100249, 2022,
- [29] M. A. Murmura, C. Rocchetti, and M. C. Annesini, "An enhanced sherwood number to model the hydrogen transport in membrane steam reformers," *Membranes (Basel)*, vol. 11, no. 11, 2021,
- [30] M. De Falco, M. Capocelli, and A. Basile, "Selective membrane application for the industrial one-step DME production process fed by CO₂ rich streams: Modeling and simulation," *Int. J. Hydrogen Energy*, vol. 42, no. 10, pp. 6771–6786, 2017,

- [31] J. P. Du Plessis and J. H. Masliyah, "Flow through isotropic granular porous media," *Transp. Porous Media*, vol. 6, no. 3, pp. 207–221, 1991,
- [32] D. W. Green and M. Z. Southard, "Physical and Chemical Data," in *Perry's Chemical Engineer's Handbook*, 9th editio., McGraw-Hill Education, Ed. 2019, pp. 21–1 to 21–147.
- [33] Smith R., *Chemical process design and integration*, Vol. 68. 2005.

CHAPTER 7

Techno-economic assessment of the one-step CO₂ conversion to dimethyl ether in a membrane-assisted process

Abstract

In this Chapter, the impact of the membrane reactor (MR) technology with in-situ removal of water to boost the performance of the one-step DME synthesis via CO₂ hydrogenation is investigated at process scale. Given the higher efficiency in converting the feedstock, the membrane reactor allows for a remarkable decrease in the main cost drivers of the process, i.e., in the catalyst mass and in the H₂ feed flow, by ca. 39% and 64%, respectively. Furthermore, the MR-assisted process requires 46% less utilities than the conventional process, especially in terms of cooling water and refrigerant, with a corresponding decrease in environmental impact (i.e., 25% less CO₂ emissions). Both the conventional and MR-assisted plants were found effective for the mitigation of the CO₂ emissions, avoiding ca. 1.4-1.6 ton_{CO₂}/ton_{DME}. However, given the higher reactor and process efficiency, the membrane technology contributes to a significant reduction (i.e., 25%) in the operating costs, which is a clear improvement in this OPEX intensive process. Nevertheless, the calculated minimum DME selling price (i.e., 1739 €/ton and 1960 €/ton for the MR-assisted and the conventional process, respectively) is over 3 times greater than the current DME market price. Yet, with the predicted decrease of renewable H₂ price and a zero-to-negative cost for the CO₂ feedstock, the MR-assisted system could become competitive with the benchmark between 2025 to 2050.

This chapter is based on the following paper:

Poto, S., Vink, T., Oliver, P., Gallucci, F., & Neira d'Angelo, M. F. (2023). Techno-economic assessment of the one-step CO₂ conversion to dimethyl ether in a membrane-assisted process. *Journal of CO₂ utilization*, 69, 102419.

7.1 INTRODUCTION

The integration of water selective membranes in a membrane reactor (MR) has proved to be an effective strategy to improve the DME synthesis [1]–[5]. Chapter 2 demonstrates that removal of ca. 96% of the water produced leads to an improvement of the CO₂ conversion and DME yield of 36% and 46%, respectively [6]. A fixed bed membrane reactor configuration with a cocurrent circulation of a sweep gas containing the reactants (i.e., CO₂ and H₂) is proposed in the same Chapter, and the effect of the reaction conditions based on ideal membrane properties is assessed. Such membrane reactor configuration, based on the use of carbon molecular sieve membranes, is demonstrated at laboratory scale in Chapter 5. In literature, only two studies have investigated the integration of the membrane reactor technology for the DME synthesis at plant level. De Falco et al. [7] introduced a specific plant architecture named “Double Recycling Loop DME production” (DRL-DME), which is based on the simultaneous recycle of the CO₂ streams from the permeation zone and the unconverted gas from the reaction zone. In this study, the authors proposed the use of zeolite membranes to promote the water separation, using a CO₂ rich syngas as feedstock. More recently, Hamedi et al. [8] proposed a comparison of the conventional (i.e., with packed beds) direct DME synthesis via CO₂ hydrogenation route with its MR-assisted counterpart, based on an energy assessment of the two technologies. The authors found that the MR technology allows for a reduction of the heating and refrigerant demands of ca. 44.5% and 69.4%, respectively. Nevertheless, neither of these studies has investigated the economics of the two process configurations and, especially the impact of the MR technology on both capital investment and operating costs. Some researchers have already identified the cost of hydrogen as the main bottleneck of any CO₂ hydrogenation process [9]–[12] which is the main factor that currently holds back industries from investing in these technologies.

Therefore, the study in this chapter proposes a comparison on a techno-economic level of two routes for the one-step DME synthesis via CO₂ hydrogenation: 1) the conventional route, based on a packed bed reactor (PBR) technology; and 2) the MR-assisted route, based on the packed bed membrane reactor (PBMR) technology. The two processes are designed at relatively large scale (i.e., 10 kton/y of DME), and optimized with the objective of minimizing the energy requirement and the H₂ consumption, as well as maximizing the efficiency at both reactor and process scale, reducing as much as possible the utilities consumptions. The main goal is to assess whether the membrane reactor technology can significantly improve the performance at process scale, and therefore increase the industrial attractiveness of this CO₂ valorisation route. Furthermore, this chapter also proposes a detailed analysis of the possible conditions which could render this technology more competitive with the DME market price in the future. Different routes for the H₂ production are considered, as well as different scenarios regarding the price of the CO₂ feedstock based on the relationship between the carbon capture cost and the carbon tax. Finally, based on these scenarios and on cost predictions, the objective

of this study is to identify the moment in which this technology will be industrially appealing and the factors which could delay/anticipate its applicability at large scale.

7.2 METHODOLOGY AND ASSUMPTIONS

Mass and energy balance calculations were carried out via process flow modeling using Aspen Plus V11 and MATLAB R2019a software. Process intensification strategies (i.e., the use of membrane reactors), and heat integration were proposed as a way to improve the energy efficiency of the process. Afterward, the impact of the capital investment (CAPEX) and operational cost (OPEX) on the minimum DME selling price (MDSP) necessary to make the system profitable was assessed.

7.2.1 System boundaries

- This analysis focuses on the DME production while the CO₂ capture, purification and transport, as well as the H₂ generation and transport are out of the scope of this work. As a base case, the CO₂ is assumed to be obtained via sorption enhanced water gas shift (SEWGS) process from iron and steel off-gases [13], while H₂ is assumed to be supplied by an integrated pipeline network and produced via a range of the most cost efficient technologies, as determined by the JRC-EU-TIMES [12], [14] a model which considers H₂ production technologies mostly based on steam methane reforming, coal and biomass gasification, coupled with the CCS. Next, a sensitivity analysis on the cost of H₂ and CO₂ is proposed to evaluate different alternatives as well as to consider sustainable production methods, in strive for a lower carbon footprint of the entire supply chain. The H₂ and CO₂ streams are assumed to enter the plant at 3.5 MPa and 25 °C, and ambient conditions, respectively. The purity of both streams entering the plant is assumed 100%, since the purification of such streams generally takes place at the site of generation. This assumption is stronger for the CO₂ stream, where the purification can significantly affect its cost. However, the effect of the purification is incorporated in the sensitivity analysis on the feedstock price.
- The DME production process comprises the following sections: 1) two multistage compression sections for the H₂ and CO₂, respectively, 2) DME synthesis reactor via one-step CO₂ hydrogenation in either PBRs or PBMRs, 3) DME purification via condensation and distillation train, 4) recycle of unconverted gas and recovery of by-product; and 5) the heat exchanger network. All these sections constitute the plant inside battery limits (ISBL). The outside battery limits (OSBL) comprise: 1) the HP-steam generation system, 2) a cooling tower and 3) a refrigeration cycle based on propylene. The electricity is assumed to be derived from the grid.
- Both plants target a DME productivity of 10 kton/ year (kTA). Typical methanol production plants have productivity ranging from 0.03 to 800 kTA [15]. Being methanol the conventional feedstock for the DME production ($2 \text{CH}_3\text{OH} \rightleftharpoons \text{CH}_3\text{OCH}_3 + \text{H}_2\text{O}$), the proposed plant size falls in the range of typical industrial scale plants. Furthermore, a plant lifetime of 20 years is

assumed, with a production time of 8000 hours per year, which corresponds to a capacity factor of 91.3% [12].

- Both technologies are designed to obtain DME *fuel* grade, according to the specification given by the ISO16861 normative developed in 2015 [16].
- The plant is considered to be built in The Netherlands, where the average temperature is 11 °C and can go up to 19.5 °C during summer, with an average humidity of 79% [17]. The current carbon tax in the Netherlands is above average when compared to the rest of Europe [18], making this study more conservative on this aspect. Thus, a sensitivity analysis is proposed also on this parameter to evaluate different scenarios and to reflect various geopolitical situations.

7.2.2 Basis and assumptions for reactor design and sizing

- The packed bed reactor (PBR) and packed bed membrane reactor (PBMR) design is based on a 1D pseudo-homogeneous plug flow reactor model, assuming a unitary catalyst effectiveness (i.e., no internal diffusion limitations), no external mass transfer limitation, and no temperature gradients at the particle scale as well as in the reactor radial direction. These assumptions are supported by the results reported in Chapter 6.
- The reactor model consists of mass and energy balances, coupled with the Ergun equation for the estimation of the pressure drops in the catalytic bed. Details on the model equations are reported in the Appendix F (section F.2).
- The catalytic bed includes a bifunctional catalyst based on a physical mixture of 90 wt % Cu/ZnO/Al₂O₃ for the methanol synthesis and 10 wt % of HZSM-5 for the methanol dehydration, which follows the kinetics proposed by Portha et al. [19] and Ortega et al. [20], respectively. The reaction kinetics were considered to be unaffected by the presence of the membranes. Details on the reaction pathway and kinetics are reported in Chapter 6, together with the experimental validation and optimization of the composition of the catalytic bed (i.e., mass ratio of the Cu/ZnO/Al₂O₃ and HZSM-5). To prevent hot spots, silicon carbide (SiC) is added to the catalyst bed with a volumetric dilution factor of 2/3. An average particle size (d_p) of 3 mm was assumed for both catalyst and diluent. The solid hold-up (ϵ_s) is set to $0.6 \text{ m}_{\text{solid}}^3/\text{m}_{\text{reactor}}^3$.
- A H₂:CO₂ stoichiometric ratio of 3, and a total pressure of 40 bar, based on the work reported in Chapter 2.
- Circulating boiling water in an external reactor shell was selected as heat management solution to guarantee a nearly isothermal operation. Therefore, the temperature of the boiling water (T_w) was optimized accordingly. The flow rate of the boiling water (\dot{m}_w) was determined in such a way that the heat removed from the reaction environment could be used for the production of medium pressure (MP) steam (i.e., latent heat exchange).
- The membrane module of the PBMR consists of tubular ceramic-supported carbon molecular sieve membranes (CMSMs), which show promising performance in terms of vapor/gas separation and stability in hot and humid environment, according to previous chapters. The properties of the membranes

in terms of permeance of H₂O, H₂, CO₂, CO and CH₃OH as a function of temperature were determined experimentally and fitted with an Arrhenius law [21] (details in Chapter 6 and Appendix E). DME permeance was assumed to be 50 times lower than that of H₂O [22]. A relatively low gradient in total pressure ($\Delta P = 5$ bar) between the reaction and permeation zone was selected to ensure the selective removal of water and, at the same time, to retain the reactants in the reaction zone. To the same scope, the reactants (i.e., CO₂, H₂ with H₂:CO₂ of 3) are circulated in the permeation zone as a sweep gas [6]. The SW ratio, defined as the ratio between the flow rate of the sweep gas and the feed flow rate, is another parameter regulating the driving force for the water removal. In Chapter 2, a value for SW of 20 was found optimal to remove effectively both the water and the heat from the reaction environment. However, this would require an excessive H₂ make-up for the sweep gas recirculation, which has been identified as the most critical cost driver of the CO₂ hydrogenation processes [9], [12]. Thus, this work assumes a SW of 1 to reduce H₂ consumption, while the heat management of the PBMR also relies on the circulation of boiling water in an external mantle.

- The reactor operating conditions (i.e., temperature and GHSV) were first optimized for the PBR. Thereafter, the PBMR was assumed to operate in the same conditions and a sensitivity analysis was carried out to determine the optimal normalized membrane area (NA_m), as defined in Eq. 7.1, as well as the composition of the sweep gas in terms of methanol molar fraction.

$$NA_m = \frac{A_m}{\Phi_{in}^R} \quad (7.1)$$

- The PBR and PBMR were sized to meet the target plant productivity, accounting for the DME recovery in the separation section. The length and diameter of the reactors were determined assuming an aspect ratio (L/D) of 5. The maximum reactor length was set to keep the average temperature equal to the optimal value without the need to increase the boiling water flow. As a result, the number of parallel reaction units was calculated. The reactor shell (or cooling mantle) diameter for the circulation of boiling water was designed assuming a maximum pressure drop of 0.5 bar [23].

7.2.3 Basis and assumptions for process modeling

- The flash drums design was based on sensitivity analyses to determine the temperature and pressure necessary to achieve a 95% recovery of DME in the liquid phase. A 95% approach to the thermodynamic equilibrium was assumed.
- The distillation columns design and optimization were carried out using the DTSW and RadFrac models in Aspen Plus. The number of stages (N), reflux ratio (R), feed position and the distillate-to-feed ratio (D/F) were first estimated via the DSTW and later optimized by means of a more rigorous model (RadFrac), which allows to determine the mass and energy balance of the system. A pressure drop per-stage of 7 mbar [24] was assumed, together with a

Murphee efficiency of 85% to account for deviation from the equilibrium. Column internals are trayed and the column diameter, tray spacing and hole area/active area ratio were optimized to avoid drying up and with a 80% approach to flooding.

- The heat exchanger network (HEN) was designed based on the pinch analysis [25]. Counter-current shell and tube heat exchangers were modeled in Aspen Plus, using a shortcut method on design basis. A minimum temperature difference (ΔT_{\min}) of 5 °C was assumed for mild temperature conditions. For temperatures below 0 °C and above 200 °C, the ΔT_{\min} was increased to 10 °C.
- All the turbomachines (compressors, pumps and steam turbines) were modeled in Aspen Plus assuming an isentropic and a mechanical efficiency to determine the thermodynamic conditions of the outlet stream and the energy balance. The isentropic and mechanical efficiency was assumed to be 0.85 and 0.95 for compressors and pumps, respectively. For the MP-steam turbine, an isentropic and mechanical efficiency of 0.8 and 0.99 are assumed, respectively [26].
- HP steam at 40 bar and 250 °C is produced pressurizing and vaporizing the wastewater stream from the separation train. The required heat duty for the boiler is generated by the combustion of natural gas in a furnace. The combustion temperature was set at 1100 °C and the flow of air was determined by assuming a concentration of O₂ in the exhaust of 4 vol. %, to ensure complete combustion. The net thermal efficiency of the industrial boiler was set at 90% [27].
- A cooling tower is used to reduce the costs of the cold utilities via the recirculation of the cooling water in the system. The required air flow as well as the amount of water which evaporates were calculated assuming a relative humidity of the air of 79% and an average air temperature of 20 °C, to design the tower in the worst-case scenario. The cooling water outlet temperature from the tower was set at 25 °C. The make-up of fresh water that needs to be fed to the system corresponds at least to the amount of water that evaporates in the cooling tower.

7.2.4 Basis and assumptions for the economic analysis and economic indicators

The objective of the economic analysis is to determine the minimum DME selling price (MDSP) necessary to make the system profitable, applying the methodology of the discount cash flow analysis (DCFA). The CAPEX was estimated via the factorial method based on Lang factors, according to which the CAPEX is a factor of the purchase equipment cost (PEC), as reported in **Table 7.1** [28]–[30].

Table 7.1. CAPEX estimation methodology via factorial method based on Lang factors [28][29].

Cost component	Lang factor
Purchase Equipment Cost (PEC)	1
Purchase equipment installation	0.39
Instrumentation and controls	0.26
Piping	0.31
Electrical system	0.1
Building (including services)	0.29
Yard improvements	0.12
ISBL	2.47 · PEC
OSBL	0.12 · ISBL
Engineering and supervision	0.32 · (ISBL+OSBL)
Construction expenses	0.34 · (ISBL+OSBL)
Legal expenses	0.04 · (ISBL+OSBL)
Contractor's fee	0.19 · (ISBL+OSBL)
Indirect Costs (IC)	0.89 · (ISBL+OSBL)
Project contingency	0.15 · (ISBL+OSBL+IC)
Process contingency	0.05 · (ISBL+OSBL+IC)
Fixed Capital Investment (FCI)	1.2 · (ISBL+OSBL+IC)
Working Capital (WC)	0.15 · FCI
Start-up costs	0.06 · FCI
CAPEX	1.21 · FCI

For the calculation of the PEC, correlations from W. D. Seider [31] and R. Smith [32] were used, based on 2000 and 2002 as reference year, respectively. The PEC is then actualized to the base year of this study (i.e., 2020) using the Chemical Equipment (CE) index, as reported in Eq. 7.2, where C_p is the purchase cost of equipment.

$$PEC = C_p \frac{CE_{2020}}{CE_{ref}} \quad (7.2)$$

Details on the correlations used for the calculation of the purchase equipment cost of all the equipment are reported in Appendix F (section F.3). The plant operates at temperature between -50 °C and 260 °C and a maximum pressure of 40 bar. As a result, carbon steel is used in most circumstances, while stainless steel was selected for pumps and compressors.

The OPEX is defined as the sum of the variable and fixed operating costs $OPEX_{variable}$ and $OPEX_{fixed}$, respectively. The $OPEX_{variable}$ depends on the cost of the feedstock (i.e., CO₂ and H₂), utilities (i.e., electricity, cooling water, natural gas), the waste water treatment and the annualized cost for the catalyst and membranes, for which a lifetime of 2 and 5 years was assumed, respectively [9],[33]. The values used for these costs are reported in **Table 7.2**. It is important to note that the cost of CO₂ refers to the cost of integrating the SEWGS technology in a steel plant, as

determined by G. Manzolini et al. [13]. The transport of CO₂ is not accounted for in this cost, since this study assumes that the CO₂-to-DME technology will eventually be implemented on-site with respect to the CO₂ emitting source or factory. However, a more detailed analysis on the effect of the CO₂ feedstock price is given in section 7.6.5.

Table 7.2. Prices assumed for the variable operating costs (OPEX_{variable})

Cost voice	Price	Unit	Reference
H ₂ (integrated pipeline network)	2945	€/ton	[12],[34]
CO ₂ (SEWGS)	33	€/ton	[13]
Electricity	0.06	€/kWh	[35]
Cooling water	0.2	€/ton	[31]
Wastewater treatment	0.4	€/ton	[12]
CuO/ZnO/Al ₂ O ₃	95.2	€/kg	[12]
HZSM-5	22	€/kg	[9]
Natural gas	0.036	€/kWh	[35]
Al-supported Carbon Membranes	1950	€/m ²	[33]
Methanol*	390	€/ton	[36]

*The price of methanol was used to determine the selling price of the methanol as a by-product

The OPEX_{fixed} are calculated on an annual basis and the methodology adopted for their estimation is summarized in **Table 7.3**, where all the fixed cost components are reported. The labor requirement is calculated based on the number of operators required on site and on the average yearly salary in the Netherlands (i.e., 55 000 € [37]), as reported in Appendix F (section F.4).

Table 7.3. Methodology for the estimation of the OPEX_{fixed}

Cost component	Value
Supervision	0.25 · Labor
Direct overhead	0.25 · (Labor + Supervision)
General overhead	0.65 · (Labor + Supervision + Direct overhead)
Maintenance labor	0.65 · FCI
Maintenance materials	0.03 · ISBL
Insurance and tax	0.015 · FCI
Financing working capital	Debt interest · WC

To compare the impact of CAPEX and OPEX and to evaluate the total annual cost (TAC), the CAPEX is calculated on an annual basis (ACAPEX), according to the methodology reported in Appendix F (section F.4). The total annual cost (TAC) is determined as follows:

$$\text{TAC} = \text{OPEX} + \text{ACAPEX} \quad (7.3)$$

The minimum DME selling price (MDSP) was determined based on the discounted cash flow (DCF) analysis, reported in Appendix F (section F.4). All the financial parameters and assumptions required for the calculation of the ACAPEX and the

MDSP are reported in **Table 7.4**. The plant is assumed to be financed in a 50/50 debt/equity split. Considering a 4% interest rate on debt according to the recent interest rate charges [38], and a cost of equity of 12%. The capital investment is assumed to be spent in a three-year construction period as follows: 20%, 50% and 30% for each consecutive year. The price of raw materials, utilities, product and by-products are estimated for the year 2020 and are considered constant for the next 20 years, as a base case. The best method of depreciation was evaluated within the analysis, based on the expected cash flow for the generic year n . The plant is expected to be fully depreciated at the end of its life, so no salvage value is expected.

Table 7.4. Financial parameters and assumptions

Parameter	Value
Location	Netherlands
Base year	2020
Project lifetime (y)	20
Construction period (y)	3
Plant availability (h/y)	8000
Tax rate (%)	25
Equity/Debt rate	50/50
Debt interest rate (%)	4
Cost of equity (%)	12
WACC (%)	8
Depreciation period (y)	10
Salvage value (€)	0
Exchange rate (USD/EUR)	1.142

7.2.5 Technical and environmental key performance indicators (KPIs)

The definitions of the CO₂ conversion and DME yield at both reactor (i.e., per-pass) and process scale (i.e., taking into account the recycle streams) are reported in Eq. 7.4-7.6. In the performance evaluated at reactor scale, the subscripts R and P stand for either reaction or permeation zone, respectively. The loss or cofeeding of CO₂ (i.e., through back-permeation of sweep gas in the reaction zone) was considered in the terms $F_{\text{CO}_2,\text{tmb}}$ and $F_{\text{CO}_2,\text{tmb}}^*$ [6]. Another important KPI of the membrane reactor is the efficiency of the water removal (WR, Eq. 7.7), which represents how effectively the membrane removes the water produced by the reaction system. This last indicator can be derived for each species permeating through the membrane.

$$(X_{\text{CO}_2})_{\text{per-pass}} = \frac{F_{\text{CO}_2,0}^{\text{R}} - F_{\text{CO}_2}^{\text{R}} - F_{\text{CO}_2,\text{tmb}}}{F_{\text{CO}_2,0}^{\text{R}} + F_{\text{CO}_2,\text{tmb}}^*} \quad (7.4)$$

$$(Y_{\text{DME}})_{\text{per-pass}} = \frac{2 (F_{\text{DME}}^{\text{R}} + F_{\text{DME}}^{\text{P}})}{F_{\text{CO}_2,0}^{\text{R}} + F_{\text{CO}_2,\text{tmb}}^*} \quad (7.5)$$

$$(X_{\text{CO}_2})_{\text{process}} = \frac{F_{\text{CO}_2}^{\text{in}} - F_{\text{CO}_2}^{\text{out}}}{F_{\text{CO}_2}^{\text{in}}} \quad (7.6)$$

$$WR = \frac{F_{H_2O}^P}{F_{H_2O}^P + F_{H_2O}^R} \quad (7.7)$$

The plant performance was then evaluated in terms of efficiency indexes, as described below.

The cold gas efficiency (CGE, Eq. 7.8), defined as the ratio of the energy content of the valuable products (i.e., DME and methanol) and the energy content of the feed (i.e., H₂), where the energy content refers to the low heating value (LHV).

$$CGE = \frac{\dot{m}_{DME}LHV_{DME} + \dot{m}_{MeOH}LHV_{MeOH}}{\dot{m}_{H_2}LHV_{H_2}} \quad (7.8)$$

A low H₂ consumption reflects a high potential for the commercialization of the process. As a result, an index representing the H₂ consumption per unit of hydrogenation product ($\eta_{H_2 \text{ to DME}}$) is defined according to Eq. 7.9. The $\eta_{H_2 \text{ to DME}}$ can assume a minimum value of 0.26 ton/ton, which corresponds to a complete conversion of H₂ to DME.

$$\eta_{H_2 \text{ to DME}} = \frac{\dot{m}_{H_2}}{\dot{m}_{DME}} \quad (7.9)$$

The definition of the overall plant efficiency (η_{tot}) was re-adapted from previous works [26],[39], as follows:

$$\eta_{tot} = \frac{W_{chem}}{W_{feed} + W_{NG} + \frac{W_{El, in \leftrightarrow out}}{\eta_{El}}} \quad (7.10)$$

The chemical energy (W_{chem}) and the energy of the feed (W_{feed}) correspond to the energy content of the product and of the H₂, respectively, defined in terms of LHV, as in Eq. 7.8. The denominator of η_{tot} represents the energy input to our system, necessary for the production of the chemical energy (W_{chem}) contained in the products. As a result, besides the energy corresponding to the H₂ (W_{feed}), the energy of the natural gas (W_{NG}) required for the production of the HP-steam and the net electricity consumed/produced ($W_{El, in \leftrightarrow out}$) need to be included. Since the production of electricity is not considered in this process, it is assumed that the electricity is produced with a natural gas combined cycle, with a net efficiency (η_{El}) of 58.4 % [26].

Next, the level of heat integration of the process is assessed with the efficiency of the utilities ($Z_{utilities}$), which represents the amount of cooling (i.e., propylene used as refrigerant and cooling water) and heating (i.e., HP-steam) utilities compared to the amount of DME produced (Eq. 7.11).

$$Z_{utilities} = \frac{F_{propyl.} + F_{CW} + F_{steam}}{F_{DME}} \quad (7.11)$$

Where F_{propyl} , F_{CW} and F_{steam} are the molar flow rate of propylene, cooling water and steam and F_{DME} is the molar flow of DME produced by the industrial plant.

The carbon footprint of the produced DME was evaluated in terms of net CO₂ emissions ($\dot{m}_{\text{CO}_2,\text{emissions}}$), and CO₂ avoided or used ($\dot{m}_{\text{CO}_2,\text{avoided}}$), as in Eq. 7.12-7.13. The direct CO₂ emissions ($\dot{m}_{\text{CO}_2,\text{direct}}$) include both the unconverted CO₂ which is not recycled (i.e., purge streams), and the CO₂ produced after the combustion of the natural gas for the HP steam generation. The second term of Eq. 7.12 ($W_{\text{El,in}} \cdot \dot{m}_{\text{CO}_2,\text{CC}}$) represents the indirect CO₂ emissions related to the production of the electricity, assumed on average as 330 gCO₂/kWh as in a natural gas combined cycle [40]. The indirect fraction of $\dot{m}_{\text{CO}_2,\text{emissions}}$ only accounts for the generation of the utilities. The CO₂ emissions related to the feedstock (i.e., H₂ production, CO₂ capture, as well as their storage and transport) are neglected, being a thoroughly life cycle assessment out of the scope of this work.

$$\dot{m}_{\text{CO}_2,\text{emissions}} = \sum \dot{m}_{\text{CO}_2,\text{direct}} + W_{\text{El,in}} \cdot \dot{m}_{\text{CO}_2,\text{CC}} \quad (7.12)$$

$$\dot{m}_{\text{CO}_2,\text{avoided}} = \dot{m}_{\text{CO}_2,\text{in}} - \dot{m}_{\text{CO}_2,\text{emissions}} \quad (7.13)$$

7.3 RESULTS OF PROCESS MODELING

7.3.1 Conventional DME production process

Packed bed reactor design

The effect of the reaction temperature and GHSV on the conversions and yields evaluated under isothermal conditions is depicted in **Figure 7.1**. Given the exothermicity of the desired reactions, temperature has a negative effect on DME yield (Y_{DME}) and CO₂ conversion (X_{CO_2}) in favor of the CO yield (Y_{CO}), as depicted in **Figure 7.1a**. On the other hand, the catalyst requirements to reach the optimal gas hourly space velocity (GHSV) decrease exponentially with temperature (i.e., the catalyst mass decreases by 82% from 200 to 220 °C), while the change in DME yield is almost linear. As a result, a reaction temperature of 220 °C was selected as a trade-off. The optimal GHSV which maximizes Y_{DME} at these conditions is 64.3 h⁻¹ (**Figure 7.1b**), which is comparable to the range of space velocities reported in literature for similar systems [9]. A boiling water temperature (T_w) of 196 °C and a corresponding pressure of 14.3 bar was found optimal, keeping an average temperature of 220 °C. Based on these results, the reactor was sized to meet the target DME productivity. Size characteristics and operating conditions of the reaction unit of the conventional DME production process are summarized in **Table 7.5**. Pressure drops were found negligible (ca. 0.025 bar), given the low gas superficial velocity and the large catalyst particle size.

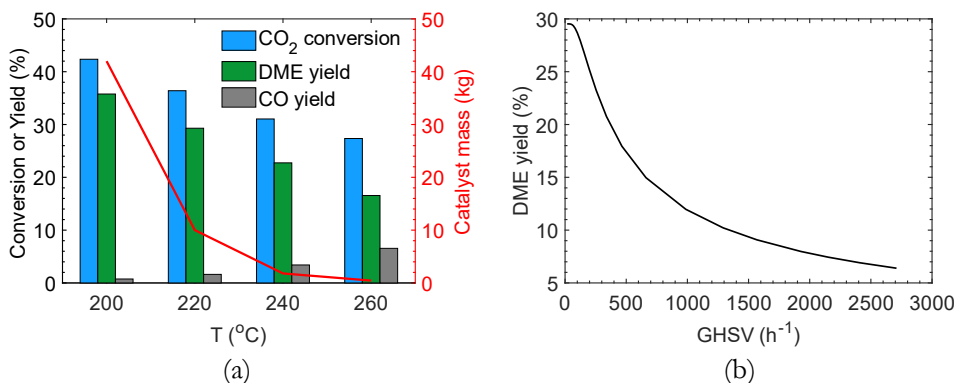


Figure 7.1. CO₂ conversion, DME yield and CO yield (left side bars) and on the catalyst mass (right side line) as a function of temperature (a) and DME yield as a function of the GHSV at 220 °C (b)

Table 7.5. Characteristics of the PBR-based reaction section in terms of size of reactors, number of reactors, catalyst bed properties and operating conditions. The inlet catalyst mass, the inlet volumetric flow and the boiling water mass flow are reported as the sum of the two PBR

Geometrical properties of the PBR section		
Parameter	Unit	Value
Number of reaction units	-	2
Reactor length (L)	m	16.1
Reactor internal diameter (D _{ri})	m	3.22
Reactor external diameter (D _{ro})	m	3.38
Reactor shell internal diameter (D _{si})	m	3.5
Reactor shell external diameter (D _{so})	m	3.55
Catalyst mass per reactor (m _{cat})	ton	63.09
Reaction conditions and properties of the PBR section		
Parameter	Unit	Value
Inlet temperature (T _{in})	°C	200
Inlet pressure (P _{in})	MPa	4
Boiling water temperature (T _w)	°C	196
Boiling water mass flow (ṁ _w)	ton/h	2.14
Bed porosity (ε)	m ³ _{void} /m ³ _{reac.}	0.4
Catalyst particle size (d _p)	mm	3
Catalyst dilution factor	kg _{SiC} /kg _{cat}	1.33
CuZA/HZSM-5 mass ratio	kg/kg	9
Gas hourly space velocity (GHSV)	h ⁻¹	64.3
Inlet volumetric flow (Φ _{in})·10 ⁻³	Nm ³ /h	1.687
H ₂ :CO ₂ feed molar ratio	mol/mol	3

Conventional process description

The process flow diagram of the one-step CO₂ conversion to DME using conventional packed bed reactors is depicted in **Figure 7.2**. CO₂ enters the plant at

ambient conditions (i.e., 1 bar and 25 °C) as stream 28 and it is compressed to 40 bar (i.e., working pressure of the PBR reactor units) via a multistage compressor unit (MCU) comprised of four compressors (C1 to C4) with intermediate cooling. The outlet temperature of each heat exchanger of the MCU is ca. 35 °C. Then, H₂ is fed to the system at 35 bar and 25 °C (stream 36), and it is compressed to 40 bar via a single stage compressor (C6). The pressurized H₂ and CO₂ feed streams (stream 38) mix with the recycle (stream 23), and the resulting stream (stream 25) is first pre-heated to 195 °C in E1 using the heat of the effluent gas from the reaction section, and then to 200 °C (i.e., reactor inlet temperature) in E13 using HP steam. Once conditioned, the gas stream (stream 27) is fed to the reaction section, which comprises two parallel PBRs working at average temperature of 220 °C and pressure of 40 bar. The outlet stream from the reaction zone (stream 0) is then re-compressed to 40 bar to overcome the pressure drops encountered in the reactors (i.e., 0.025 MPa) prior to the recycle. This also allows a high DME recovery ($\geq 95\%$) in the condensation step, which, given the high volatility of DME, takes place in the flash drum V1 at -33.4 °C. To minimize the cooling requirements, this is done in five consecutive heat exchangers (i.e., E1-E5) that allow integration of the heat generated in the reaction in other parts of the process, namely the pre-heating of the inlet stream to the reactor (E1) and heating of the liquid produced at the flash drum V1 (E2). The remaining heat is used to heat up cold utilities (i.e., cooling water for E3 and E4 and propylene for E5). The flash drum V1, separates a vapor phase containing CO, H₂ and part of the CO₂ at the top (stream 8), from a liquid phase stream containing DME, methanol, water and a large portion (i.e., CO₂ mass fraction of 44.1%) of CO₂ at the bottom (stream 7). The gaseous stream (stream 8), together with the CO₂ separated within the distillation train (stream 13), is recycled back to the reactor, with a recycle ratio of 99% (i.e., 1% of the stream is purged as gas waste). The liquid stream from V1 (stream 7), instead, is first heated to 90 °C (E2) and fed to the first distillation tower (T1). The distillation tower T1 operates at 40 bar in a temperature range of 64.7 °C-235.4 °C to separate DME and CO₂ over the top (stream 10) and methanol and water at the bottom (stream 11). The DME/CO₂ stream is cooled down to 45 °C (E6) and fed to the column T2, operating at 40 bar and 4.8 °C-110.6 °C, to separate CO₂ at the top (stream 13) and to produce a *fuel* grade DME (i.e., purity of 99.91 wt %) at the bottom (stream 15). The pure DME stream is then depressurized to 10 bar and cooled down to 35 °C (E11), which are the typical DME liquid storage conditions. Finally, stream 11, bottom product of T1, is depressurized to 30 bar and fed to the last distillation tower (T3), which operates in a temperature range of 185-234 °C, to separate 99.92 wt % pure water at the bottom (stream 21) and industrial grade methanol at the top (stream 18), which is then depressurized to 10 bar and cooled down to 35 °C (E10). Details on the mass balance of the plant (i.e., stream tables) are reported in Appendix F (**Table F1**). The generation and usage of the utilities are also reported in the scheme in **Figure 7.2** with dotted lines.

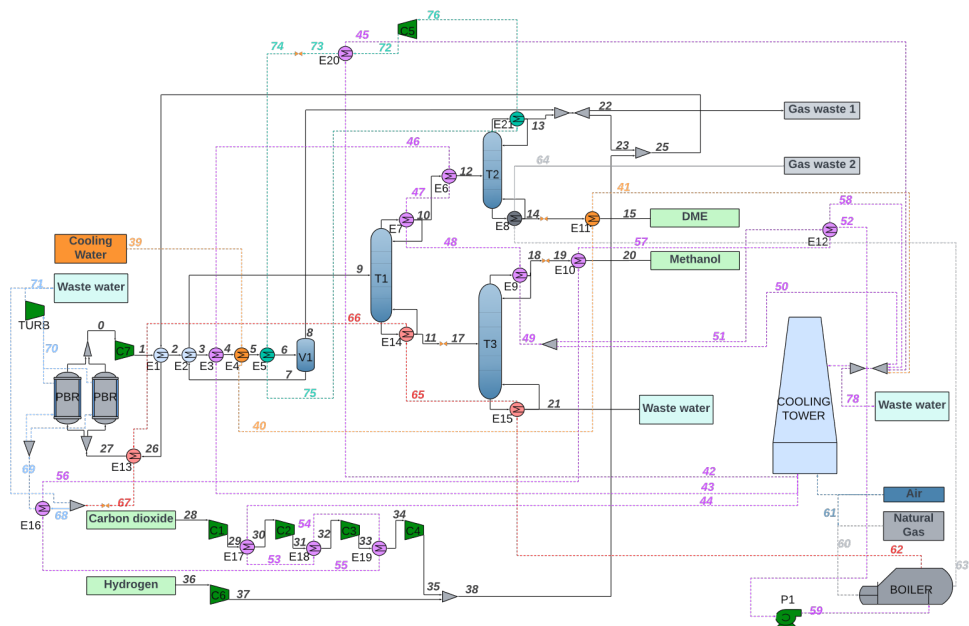


Figure 7.2. Process flow diagram of the one-step CO₂ conversion to DME process via packed bed reactors

7.3.2 MR-assisted DME production process

Packed bed membrane reactor design

The packed bed membrane reactor was designed according to the procedure described in section 7.2.2. The operating pressure and temperature of the reaction zone are the same as those identified for the conventional packed bed reactor, while the conditions regulating the driving force across the membrane (i.e., ΔP and SW) were selected based on the work reported in Chapter 2. To prevent any loss of reactant (especially the costly H₂) across the membrane, a sweep gas with a similar composition and pressure as those in the feed stream is fed to the permeation zone. Nevertheless, this strategy alone is not effective to prevent methanol removal (MR), which can achieve values above 50% (**Figure 7.3a**, right axes), resulting in an increase in Y_{MeOH} and a decrease in Y_{DME} , lowering the efficiency of the membrane reactor. A sensitivity analysis was carried out to determine the normalized membrane area (NA_m) that maximizes Y_{DME} (**Figure 7.3a**). The Y_{DME} displays an optimum corresponding to NA_m of ca. $3.65 \cdot 10^{-2} \text{ m}^2 \cdot \text{h} / \text{Nm}^3$. Greater membrane areas lead to a decrease in Y_{DME} due to the removal of methanol from the reaction zone. Alternatively, the concentration of methanol in the sweep gas can also be optimized to prevent losses. Therefore, the methanol concentration in the sweep gas was optimized to keep the Y_{MeOH} close to zero, which means that all the methanol produced is effectively converted to DME and does not permeate through the membrane. It was found that a molar fraction of methanol of 6.37%, together with

a normalized membrane area of $4.11 \cdot 10^{-2} \text{ m}^2 \cdot \text{h} / \text{Nm}^3$ maximizes Y_{DME} . The gas composition in the permeation zone (**Figure 7.3b**) obtained in these conditions shows that only water is effectively removed from the reaction environment. Indeed, the concentration of the component in the sweep gas (i.e., H₂, CO₂ and methanol) slightly decreases only due to the dilution effect caused by the permeation of water.

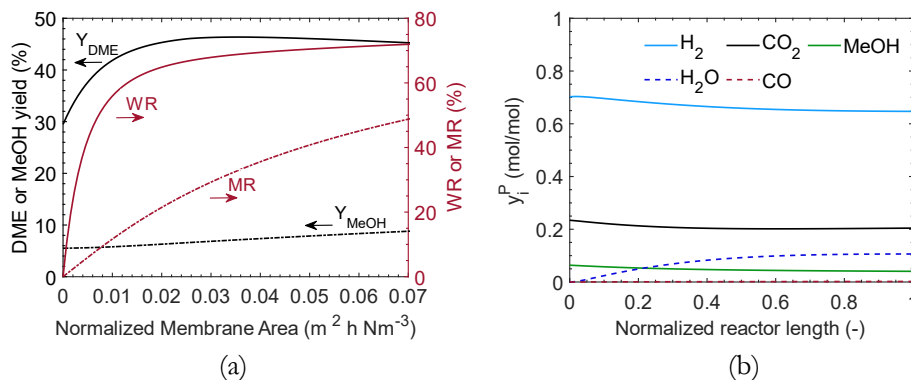


Figure 7.3. PBMR performance in terms of Y_{DME} and Y_{MeOH} (on the left) and water removal (WR) and methanol removal (MR) (on the right) as a function of the normalized membrane area (a); composition of the sweep gas/permeate stream as a function of the normalized reactor length (z/L) when 6.37 mol% of methanol is incorporated in the sweep gas (b).

The optimal temperature of the boiling water (T_w) in this case was 178 °C (i.e., lower than that for the PBR), with a corresponding pressure of 9.6 bar. As a matter of fact, the PBMR achieves higher conversion, leading also to greater heat production. Details on the reaction unit and operating conditions of the MR-assisted DME production process are summarized in **Table 7.6**. Pressure drops are negligible (ca. 0.025 bar), similarly to the PBR.

Table 7.6. Characteristics of the PBMR-based reaction section in terms of size of reactors, number of reactors, catalyst bed and membrane properties and operating conditions.

Geometrical properties of the PBMR section		
Parameter	Unit	Value
Number of reaction units	-	1
Reactor length (L)	m	17.2
Reactor inner diameter (D_{ri})	m	3.45
Reactor outer diameter (D_{ro})	m	3.61
Reactor shell inner diameter (D_{si})	m	3.75
Reactor shell outer diameter (D_{so})	m	3.80
Catalyst mass per reactor (m_{cat})	ton	63.09
Membrane inner diameter (D_{mi})	m	0.007
Membrane outer diameter (D_{mo})	m	0.01
Membrane length (L_m)	m	17.2
Number of membranes (N_m)	-	783

Reaction conditions and properties of the PBMR section		
Parameter	Unit	Value
Inlet temperature reaction zone (T_{in}^R)	°C	200
Inlet temperature permeation zone (T_{in}^P)	°C	200
Inlet pressure reaction zone (P_{in}^R)	MPa	4
Trans-membrane pressure gradient (ΔP)	MPa	0.5
Boiling water temperature (T_w)	°C	178
Boiling water mass flow (\dot{m}_w)	ton/h	1.78
Bed porosity (ϵ)	$m^3_{void}/m^3_{reac.}$	0.4
Catalyst particle size (d_p)	mm	3
Catalyst dilution factor	kg_{SiC}/kg_{cat}	1.33
CuZA/HZSM-5 mass ratio	kg/kg	9
Gas hourly space velocity (GHSV)	h^{-1}	64.3
Inlet volumetric flow (Φ_{in}) $\cdot 10^{-3}$	Nm^3/h	1.029
Sweep gas ratio (SW)	mol/mol	1
H ₂ :CO ₂ feed molar ratio reaction zone	mol/mol	3
H ₂ :CO ₂ feed molar ratio sweep gas	mol/mol	3
Methanol in sweep gas ($y_{MeOH,in}^P$) $\cdot 10^2$	mol/mol	6.37

*R. and P. stands for reaction and permeation zone, respectively.

MR-assisted process description

The process flow diagram of the one-step CO₂ conversion to DME process via packed bed membrane reactors is depicted in **Figure 7.4**. CO₂ enters the plant at ambient conditions as stream 77 and it is compressed to 35 bar (i.e., pressure of the sweep gas of the PBMR units) via the same MCU previously described (i.e., four compressors with intermediate cooling to 35 °C). H₂ is fed to the system at 35 bar and 25 °C as stream 90 and it is split in two streams: 1) stream 91 for the reaction zone feed (51% of stream 90) and 2) stream 92 for the sweep gas make-up (49% of stream 90). With similar proportion, also the CO₂ stream at 3.5 MPa (stream 85) is split in: 1) stream 86, for the reaction zone and 2) stream 87, for the sweep gas. The H₂ and CO₂ streams directed to the reaction zone are both compressed to 40 bar via C6 and C5, respectively, and then mixed with the recycle (stream 20). The resulting stream 43 is first pre-heated to 180 °C via E1, using the heat of the effluent gas from the reaction section, and then to 200 °C (i.e., reactor inlet temperature) via E7 using HP steam. The H₂ and CO₂ streams directed to the sweep gas mixed with two recycle streams: 99% of stream 27 and the methanol separated at the top of T3 (stream 35). The resulting stream 40 is first pre-heated to 193 °C, via E4, using the heat of the permeated stream from the PBMR, and then to 200 °C via E6 using HP steam. Stream 45 and 42 are respectively fed to the reaction and permeation zone of the PBMR, which works at an average temperature of 220 °C and a pressure of 40 bar and 35 bar, respectively. The outlet stream from the reaction zone (stream 0) is re-compressed to 40 bar and cooled down to -26 °C to recover DME in the liquid phase. This is done via three heat exchangers: E1, used to pre-heat the inlet stream to the PBMR reaction zone, and E2-E3 using cold utilities (i.e., cooling water and

propylene). The flash drum (V1) separation is similar to that in the conventional plant, as well as the recycle of the gaseous stream, combined with the CO₂ recovered from the liquid phase.

The permeate stream from the PBMR (stream 21) is cooled down to 36 °C via three heat exchangers, first pre-heating the sweep gas stream (E4), then for heating the liquid phase produced via the second flash drum V2, prior to the distillation (E9) and finally with cooling water (E5). The resulting stream 24 is fed to the flash drum V2, which separates the permanent gas at the top (stream 25) from a liquid stream containing 55.6 wt % of water and 35.8 wt% of methanol at the bottom (stream 26). About 70% of the gaseous stream (stream 25) is recycled to the permeation zone (stream 27), together with the methanol stream recovered from the distillation section (stream 35), as previously mentioned. The remaining 30% (stream 28) is recycled to the reaction zone, after being compressed to 40 bar (C5).

The liquid stream from V1 (stream 6) is first used as internal utility stream in the CO₂ MCU and then fed at 70 °C to the first distillation tower T1. The distillation tower T1 operates at 40 bar and in a temperature range of 80.1 °C-220.4 °C to separate DME and CO₂ over the top (stream 12) and methanol and water at the bottom (stream 13). The DME/CO₂ stream is cooled down to 40 °C and fed to the column T2, operating at 40 bar and between 9.4 °C- 111 °C, to separate CO₂ at the top (stream 15) and to produce a *fuel* grade DME (i.e., purity of 99.91 wt %) at the bottom (stream 16). The pure DME stream is then depressurized 10 bar and cooled down to 35 °C (E16), to achieve the DME liquid storage conditions. The liquid stream from V2 (stream 26), is heated up to 200 °C (E9, E26 and E10) and then mixed with the water/methanol stream from T1, previously depressurized to 30 bar (stream 31). The resulting stream 33 is then heated to 220 °C (E11) and fed to the last distillation tower (T3), which operates at 35 bar and in a temperature range of 185-241 °C, to separate 99.9 wt % pure water at the bottom (stream 36) and 99.9 wt % pure methanol at the top (stream 35), which is recycled to the sweep gas stream, as already mentioned. Details on the mass balance of the plant (i.e., stream tables) are reported in Appendix F (**Table F2**). As for the process flow diagram of the conventional process, the generation and usage of the utilities are also reported in the scheme in **Figure 7.4** with dotted lines. Furthermore, to facilitate their identification, the sweep gas and permeate stream (before the separation) are represented as dashed lines.

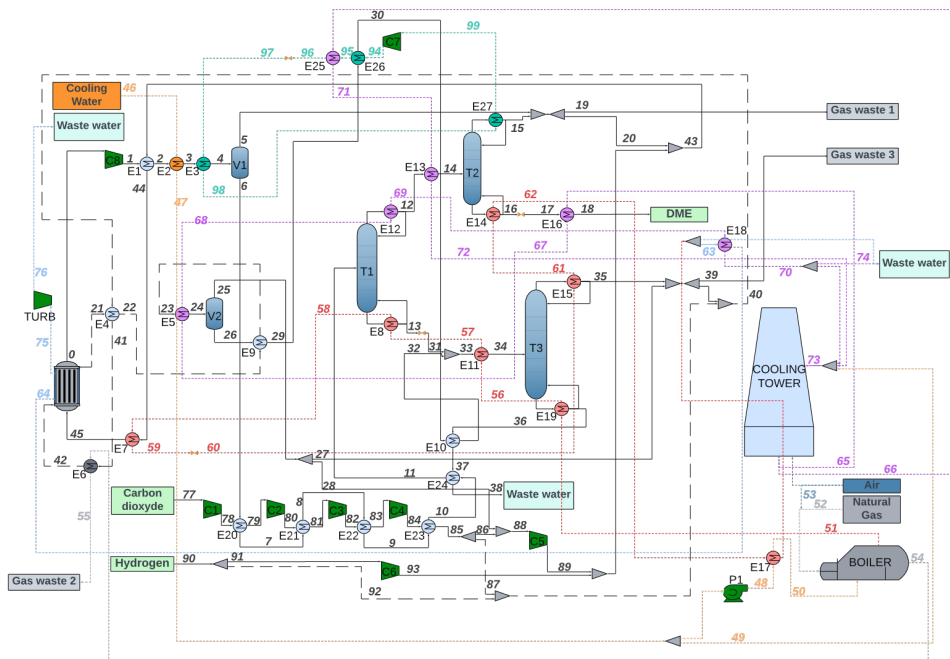


Figure 7.4. Process flow diagram of the one-step CO₂ conversion to DME process via packed bed membrane reactors

7.3.3 Heat integration and generation of the utilities

The hot and cold composite curves of the conventional and MR-assisted process are depicted in **Figure 7.5a** and **b**, respectively. The curves were obtained using the *pinch* method developed by Linnhoff [25] with a ΔT_{\min} of 10 °C. The process minimum energy targets in terms of hot (Q_h) and cold (Q_c) duty were determined for both processes, starting from the stream thermal data (i.e., mass and energy balances). The Q_h for the conventional and MR-assisted process is very similar (i.e., 455 kW and 444 kW, respectively), with the latter being ca. 2.4% lower. As a matter of fact, the DME synthesis is an exothermic process and with the membrane reactor technology, an extra hot stream is produced (i.e., the permeate), from which it is possible to recover the heat for the cold streams. On the other hand, the Q_c of the MR-assisted process is much higher than that of the conventional process (i.e., 421 kW vs 99.3 kW), for the same reason. Indeed, also the permeate stream undergoes some separation (i.e., condensation and distillation of the liquid product), which mainly requires cooling duty. The maximum heat recovery which corresponds to the minimum energy targets is 1588 kW and 1527 kW for the conventional and MR-assisted process, respectively. The heat management of the reaction unit was not included in the construction of the composite curves. However, it should be considered that the conventional process has one more reaction unit than the MR-assisted process, requiring ca. 10% more cooling duty.

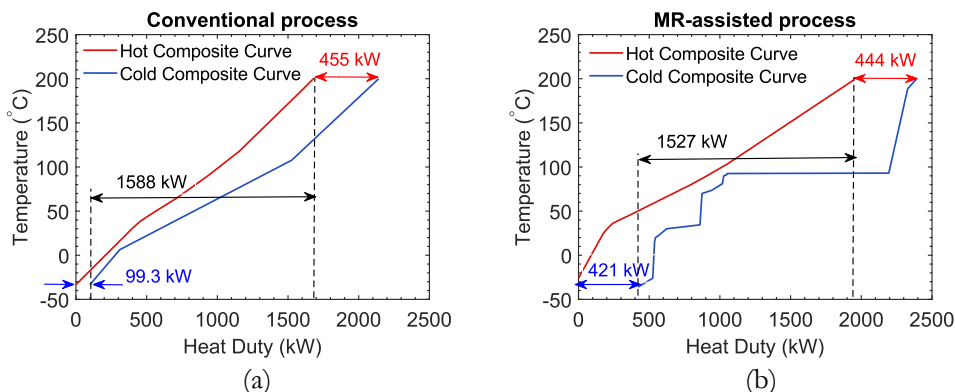


Figure 7.5. Hot (red) and Cold (blue) composite curves obtained for the conventional (a) and for the membrane reactor (MR) assisted (b) one-step DME production process, obtained applying the graphical approach of the Linnhoff method [31] with a ΔT_{\min} of 10 °C.

Following this calculation, the heat integration within the two process was carried out through the maximization of the internal heating and cooling (i.e., using process streams instead of external utilities) and using cooling water, refrigerants and steam when necessary. As a result, the energy saving (i.e., fraction of the maximum heat recovery target) is 62.1% and 75.7% for the conventional and MR-assisted process, respectively. A general overview of the HEN of the two processes is given in **Table 7.7**. The minimum number of heat exchangers (U_{\min}) was determined according to Eq. 7.14, where N_s is the total number of hot and cold streams, L the number of independent loops and S the number of independent subsystems. In our case, $L = 0$ and $S = 1$, which give the same formula proposed by Linnhoff. The amount of heat exchangers used is higher than U_{\min} , due to the internal heat exchange, which allows for a reduction of the utilities and of the OPEX.

$$U_{\min} = N_s + L - S \quad (7.14)$$

Table 7.7. Heat exchangers network specifications of the conventional and MR-assisted processes.

	Conventional process	MR-assisted process
Amount of heat exchangers	21	27
Minimum number of heat exchangers	15	19
Heat exchangers with internal exchange	2	9
Heat exchangers in refrigeration cycle	2	2
Heat exchangers with cooling water	12	7
Heat exchangers with HP steam	5	9

The remaining heat exchangers are based on external utilities. As described above, the flash drum V1 operates at -33.4 °C and -26 °C in the conventional and MR-assisted process, respectively, while the condenser of the tower T2 operates at 5 °C in both cases. Thus, propylene is selected as cooling medium. Propylene can cool

down streams till $-48\text{ }^{\circ}\text{C}$ with a less energy intensive refrigeration cycle, when compared to ethylene. As a matter of fact, propylene requires a lower pressure to achieve its dew point at $35\text{ }^{\circ}\text{C}$. An overview of the refrigeration cycle is given in **Table 7.8**.

Table 7.8. Details of the propylene usage via the refrigeration cycle for the conventional and MR-assisted process.

Conventional process		
	Value	Unit ID
Propylene flow	13045 kg/h	-
$T_{\text{in}}/T_{\text{out}}$ propylene (V1)	$-48/-46\text{ }^{\circ}\text{C}$	E5
$T_{\text{in}}/T_{\text{out}}$ propylene (I2)	$-46/-3\text{ }^{\circ}\text{C}$	E21
Energy for compression	788 kW	C5
MR-assisted process		
	Value	Unit ID
Propylene flow	5470 kg/h	-
$T_{\text{in}}/T_{\text{out}}$ propylene (V1)	$-48/-42\text{ }^{\circ}\text{C}$	E3
$T_{\text{in}}/T_{\text{out}}$ propylene (I2)	$-42/4\text{ }^{\circ}\text{C}$	E27
Energy for compression	327 kW	C7

The remaining cooling duty is supplied via cooling water. Instead of using continuously fresh water, a cooling tower is implemented in both systems to further reduce the OPEX. The cooling tower cools down the water by evaporating a small portion of it, mixing warm water with air. Therefore, the outlet temperature of the water is limited by the air temperature, which in the Netherlands is $11.7\text{ }^{\circ}\text{C}$ as yearly average, or $20\text{ }^{\circ}\text{C}$ in the summer. For a conservative design, the air inlet temperature is set at $20\text{ }^{\circ}\text{C}$, which limits the water outlet temperature to $25\text{ }^{\circ}\text{C}$. For the heat exchangers that require a slightly lower water temperature (i.e., $15\text{ }^{\circ}\text{C}$), extra fresh water is fed to the system at $15\text{ }^{\circ}\text{C}$. This is to avoid the use of more refrigerant, which would otherwise result in a higher OPEX and CO_2 footprint. Instead, the use of more fresh water than the required make-up to the cooling tower results in some purge of warm water before being recycled to the tower. A schematic representation of the cooling water (CW) usage and recycle is given qualitatively in **Figure 7.6**. Fresh CW enters the system at $15\text{ }^{\circ}\text{C}$ with a flow of 9.91 ton/h and 5.40 ton/h for the conventional and MR-assisted process, respectively, to be then mixed with the corresponding 157 ton/h ($43.6\text{ }^{\circ}\text{C}$) and 87.6 ton/h ($52\text{ }^{\circ}\text{C}$) warm water stream from the heat exchangers network (HEN).

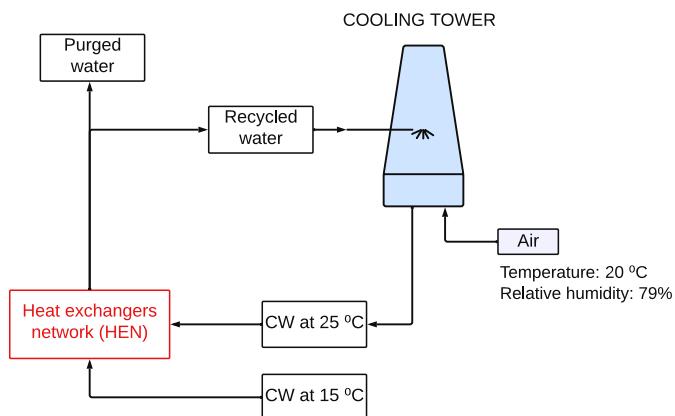


Figure 7.6. Schematic representation of the cooling water usage and recycle via the cooling tower for both processes. CW indicates cooling water.

In both process configurations, a small portion of the warm water which is not recycled to the cooling tower is fed to a pump and a furnace, which burns natural gas and produces HP steam (i.e., steam at 40 bar and 250 °C). The HP steam production and usage is represented in detail in Appendix F (**Figure F1**). As the HP steam is used in the HEN, its quality decreases down to high temperature boiling water, which is used in the reaction unit for the heat management. The medium pressure (MP) steam obtained in this way is fed to a steam turbine to produce electricity. The exhaust gases produced at the furnace are used for the reboiler of the tower T2 (E8) and for the pre-heating of the sweep gas (E6) in the conventional and MR-assisted process configurations, respectively. Further details on the natural gas input and electricity produced from the steam turbine are reported in **Table 7.9**.

Table 7.9. Input and output of the HP steam generation and cycle for the conventional (a) and MR-assisted (b) one-step DME production process.

	Conventional process	MR-assisted process
Natural gas required (m ³ /h)	281	249
Steam turbine output (kW)	261	197

7.4 TECHNICAL ANALYSIS

The two technologies proposed in this study are first compared at the reactor scale (**Table 7.10**). The membrane reactor, removing ca. 72% of the water produced in the reaction zone, allows for an increase of 41% and 63% in the $X_{\text{CO}_2\text{ per pass}}$ and $Y_{\text{DME per pass}}$, respectively. Most importantly, the PBR and PBMR work at the same GHSV, which means that the PBMR requires ca. 40% lower mass of catalyst and flow of reactants to achieve the same DME productivity, given the higher performance of the PBMR. As a result, the membrane reactor technology allows

for a reduction in the number of reaction units required to achieve a specific productivity (i.e., with the PBMR we can remove one parallel reactor). Another important aspect is that the PBMR requires 64% less H_2 per unit mass of DME produced, $\eta_{H_2 \text{ to DME}}$, (i.e., 0.47 and 0.78 for the PBMR and PBR, respectively). This means that the PBMR converts H_2 more efficiently, reducing the impact of one of the main cost driver, as well as bottleneck, of the hydrogenation processes. The PBMR is not only more efficient in terms of conversion/yield, but also in terms of energy efficiency and CO_2 footprint. The amount of boiling water required for the heat management is 17.3% lower than that for the PBR, which means that less energy and natural gas are required for the production of the reactor utility. Finally, the PBMR shows a CGE of 88% versus the 76% of the PBR, which confirms that also the energy conversion of the PBMR is more efficient.

Table 7.10. Key performance indicator (KPI) at the reactor level: comparison of the PBR and PBMR unit for the DME synthesis via CO_2 one-step hydrogenation

KPI	PBR	PBMR
Number of reaction units	2	1
Catalyst mass (m_{cat})	126 ton	77.0 ton
Membrane area (A_m)	0	423 m ²
CO_2 conversion ($X_{CO_2 \text{ per pass}}$)	38.7%	54.6%
DME yield ($Y_{DME \text{ per pass}}$)	32.2%	52.6%
DME selectivity (S_{DME})	83.2%	96.4%
H_2 feed ($\dot{m}_{H_2}^{in}$)	9.16 kton/y	5.59 kton/y
CO_2 feed ($\dot{m}_{CO_2}^{in}$)	66.3 kton/y	40.6 kton/y
DME productivity (\dot{m}_{DME}^{out})	11.8 kton/y	12.0 kton/y
H_2 from recycle	62.4%	47.8%
CO_2 from recycle	62.3%	48.7%
$\eta_{H_2 \text{ to DME}}$	0.78 ton/ton	0.47 ton/ton
Boiling water mass flow (\dot{m}_w)	17.4 kton/y	14.4 kton/y
CGE	76.0 %	87.7 %

Table 7.11 compares the two process configurations (i.e., considering reactor as well as feeding and product separation section) based on their technical performance indicators evaluated from the mass and energy balances. The MR-assisted process allows for a reduction in the H_2 requirement by 15.2%, which is significantly lower than the savings anticipated based on reactor performance alone. This is due to the H_2 make-up required for the sweep gas stream. In terms of product, the two plants were designed to achieve the same productivity (i.e., 10 kton/y of *fuel* grade DME). However, the conventional process also produces 2.6 kton/y of industrial grade methanol as sellable product. On the contrary, the methanol produced in the PBMR is 100% recycled as sweep gas after its purification, to improve the DME selectivity per pass. Thus, the resulting CGE of the two plants remains very similar, with only ca. 1.77% improvement of the MR-assisted over the conventional process (i.e., 89.8% vs 91.3%). Nevertheless, the energy consumption of the MR-assisted process is strikingly (i.e., 49%) lower than the conventional counterpart, mostly due to a 52%

reduction of the energy requirements in the compression of the refrigeration cycle. Similarly, given the difference in size of the recycle streams (**Table 7.10**), the compression of the reactor unit effluents requires only 2.06 kW for the MR-assisted process versus the 5.01 kW of the conventional process. The pump (P1) required for the HP steam production shows a similar consumption for the two processes, while the electricity produced via the steam turbine (TURB) is ca. 24.3% lower for the MR-assisted technology, given the lower boiling water requirement for the reaction unit. The MR-assisted plant has also a lower requirement of HP steam, which corresponds to a natural gas usage ca. 11.3% lower than in the conventional plant. Overall, the MR-assisted process achieves a total energy efficiency of 72.9% versus the 69.9% of the conventional process.

When comparing the two plants in terms of the usage of the utilities per unit of DME produced (**Table 7.12**), the MR-assisted process always require a lower amount of any utility (i.e., propylene, cooling water and steam), with an overall $Z_{\text{utilities}}$ of 45.9% lower, which is mostly attributed to the lower requirement of cold utilities.

Table 7.11. Technical performance comparison of the conventional and MR-assisted one-step DME production process.

	Conventional process	MR-assisted process
Feedstock		
H ₂	425.8 kg/h	360.9 kg/h
CO ₂	3100 kg/h	2629 kg/h
Thermal input (W_{feed})	14.19 MW	12.03 MW
Chemical products		
DME	1368 kg/h	1369 kg/h
Purity	99.99 wt %	99.99 wt %
Methanol	317.5 kg/h	0 kg/h
Purity	99.85 wt %	0 wt %
Thermal output (W_{chem})	12.74 MW	10.99 MW
Cold Gas Efficiency (CGE)	89.76 %	91.35 %
Electricity		
<i>Compressors</i>		
MCU (CO ₂)	0.2563 MW	0.2200 MW
C5	0.7883 MW	0.2270 MW
C6	0.2416 MW	0.1047 MW
C7	$5.010 \cdot 10^{-3}$ MW	0.3724 MW
C8	0 MW	$2.06 \cdot 10^{-3}$ MW
<i>Pumps</i>		
P1	$4.18 \cdot 10^{-3}$ MW	$4.055 \cdot 10^{-3}$ MW
<i>Turbines</i>		
TURB	-0.2608 MW	-0.1974 MW
Total electricity	0.8170 MW	0.4164 MW
Natural gas for HP steam		
Natural gas	193.6 kg/h	171.7 kg/h
Natural gas energy (W_{NG})	2.634 MW	2.336 MW
Total energy efficiency (η)	69.90 %	72.87 %

Table 7.12. Efficiency of the utilities compared to the amount of DME produced for the conventional and MR-assisted process

KPI	Conventional process	MR-assisted process
Z_{propyl}	10.4	4.48
Z_{CW}	311.6	167.4
Z_{steam}	5.32	5.17
$Z_{\text{utilities}}$	327.3	177.1

The analysis of the carbon footprint is also relevant to underline the advantage of using membrane reactor technologies. **Figure 7.7a** shows that the direct CO₂ emissions of the two plants is very similar (i.e., 0.04 ton_{CO₂}/ton_{DME}), in both cases attributed to the residual (ca. 1%) of the unconverted reactant streams which is not recycled. However, the direct emissions only contribute ca. 5-7% to the total CO₂ emissions. The main contributors are the electricity and steam generation (i.e., indirect emissions), which for the MR-assisted plant are 48.1% and 25.3% lower than for the conventional plant, respectively. The lower carbon footprint of the MR-assisted plant is in line with the energy balance and with the utilities requirement (**Table 7.11** and **Table 7.12**).

Overall, the conventional and the MR-assisted processes emit 0.71 and 0.53 ton_{CO₂}/ton_{DME} respectively. However, when the CO₂ emissions are compared to the CO₂ fed to the plant, these numbers become negligible, being these technologies based on CO₂ utilization. As a result, since the conventional plant converts the feedstock with a lower efficiency at the reactor scale, thus requiring more CO₂ per unit of DME produced, the CO₂ avoided is slightly higher for the conventional plant than for the MR-assisted one (1.56 vs 1.39 ton_{CO₂}/ton_{DME}). Therefore, considering the size of the plants, the conventional and MR-assisted process avoid ca. 170 kton/y and 152 kton/y of CO₂, respectively.

Furthermore, when the one-step DME production via CO₂ hydrogenation is compared to the benchmark process (**Figure 7.7b**), where DME synthesis is based on fossil fuels (i.e., syngas produced via steam reforming of natural gas), the CO₂ footprint of the technologies proposed in this study is between 73 and 80% lower. This means that the DME production technology proposed here is much more sustainable. Indeed, the CO₂ emissions for the industrial DME production range between 89-98 gCO₂/M_{DME} [41]–[43]. This number accounts for the NG-to-DME production pathway, independently on the direct or indirect route. When translated in terms of ton_{CO₂}/ton_{DME}, it results in an average value of 2.63. Thus, the technology proposed here is, from one hand, a valuable CO₂ utilization route and, from the other hand, a more eco-friendly pathway for the production of DME.

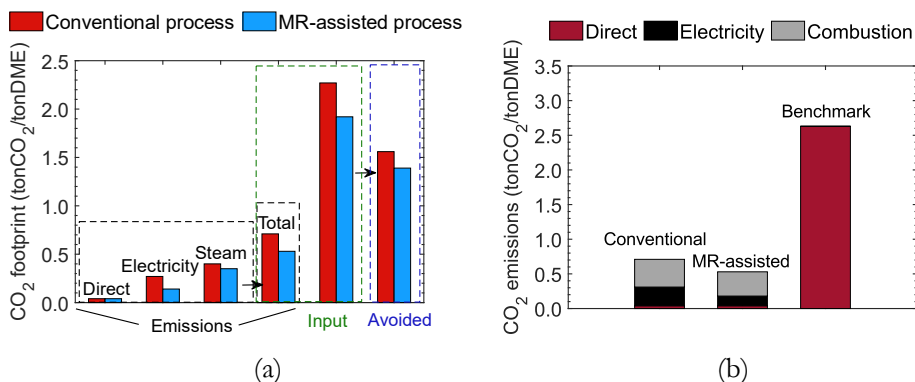


Figure 7.7. CO₂ emissions and usage of the conventional and MR-assisted one-step DME production process (b) CO₂ emissions of the conventional and MR-assisted process compared to the emissions of the benchmark DME production from natural gas.

7.5 ECONOMIC ANALYSIS

The results of the economic analysis are summarised in **Table 7.13**. The purchase equipment cost (PEC) is the same for both process configurations (i.e., 1.809 M€ vs 1.802 M€). As a matter of fact, the MR-assisted process has an extra flash drum (V2) for the permeate stream and a larger number of heat exchangers of the HEN, which result in a PEC contribution increase from 3.82% to 6.53% and from 20.57% to 26.53% for the flash columns and heat exchangers, respectively. On the other hand, the MR-assisted process displays a 45.9% lower cost for the reactor section with respect to the conventional process, due to the removal of one reaction unit. The distributed PEC is graphically represented in **Figure 7.8a**, where we can observe that the main contribution to the PEC is given by the compressors (i.e., 36.8% and 32.1%), followed by the heat exchangers (i.e., 20.6% and 26.5%), distillation towers (i.e., 15.1% and 15.4%) and finally the turbine (18% and 14.7%).

Considering the operating costs, the MR-assisted process has a total variable cost of 15.15 M€/y versus the 19.59 M€/y of the conventional plant, in line with the higher efficiency in converting the feedstock and the lesser utility requirement of the MR-assisted process. As shown in **Figure 7.8b**, the largest contribution to the OPEX is given by the H₂ make-up, which amounts to 57.8% and 62.91% for the conventional and MR-assisted process, respectively. The second contributor to the OPEX is the catalyst cost, with a 29.2% and 22.8% of the total variable cost for the conventional and MR-assisted process. On the other hand, the cost of the utilities (mostly determined by the cost of natural gas and electricity) has a lower impact. Nevertheless, this cost is strongly affected by the geopolitical situation, which introduces some uncertainties on this number (see Section 7.6.6). In the base case, no carbon tax is considered, while a dedicated analysis on this subject is reported in Section 7.6. Therefore, the only cost related to the waste material (i.e., water in our case) is included in the utilities and consists of ca. 4% of the total utilities cost.

When comparing the OPEX with the annualized CAPEX (ACAPEX), it is clear that the impact of the capital investment on the annual costs is negligible. As a result, the TAC follows the same trend as the OPEX, with a value of 24.32 and 20.08 M€/y for the conventional and MR-assisted process, respectively. As a consequence, the minimum DME selling price (MDSP) amounts to 1960 and 1739 €/ton, respectively (i.e., ca. 11.2% reduction in MDSP in the case of the MR-assisted process). These MDSP values align with the range identified by Michailos et al. [9] (i.e., 1828-2322 €/ton). The average MDSP they found is 2193 €/ton for a two-steps DME synthesis process using conventional packed bed reactors and, likewise in this study, using captured CO₂ and H₂ from PEM as feed. By combining the two steps in a single reaction unit and with the use of the membrane reactor technology, this study demonstrates the possibility to decrease the MDSP by 1.26 times, which is a great achievement.

Nevertheless, DME is currently sold for a price of 520 €/ton, which is more than 3 times lower than our MDSP. However, the market price refers to a chemical grade DME, commonly sold as aerosol propellant or as a solvent, thus with a different market value than the fuel grade DME, despite its similar purity specification. The fuel grade DME is not on the market yet, but it is expected to be soon. Thus, it is difficult to predict its value, although it would be reasonably higher than the current DME market price, to be in line with the price of diesel/LPG. Another important aspect to consider is that the DME produced via CO₂ hydrogenation would have a higher value in the perspective of a decarbonization of the fuel and chemical industry, since it derives from an alternative feedstock/waste (i.e., the captured CO₂), rather than from fossil fuels. Despite this, in the current market conditions, the production of DME from CO₂ and renewable H₂ with our technology would not be profitable. Thus, it is crucial to analyze the system in more depth, to understand the bottlenecks and to identify the conditions in which this process would become an attractive solution at industrial level.

Table 7.13. Overview of the economic analysis for the for the conventional and MR-assisted and one-step DME production process

Cost component	Conventional process	MR-assisted process
<i>Initial capital investment</i>		
PEC	1.809 M€	1.802 M€
Compressors	36.77 %	32.14 %
Distillation towers	15.06 %	15.43 %
Flash columns	3.818 %	6.528 %
Heat exchangers	20.57 %	26.63 %
Reactor unit	1.740 %	0.940 %
Turbine	17.99 %	14.69 %
Furnace and boiler	2.834 %	2.877 %
Cooling tower	1.214 %	0.753 %
CAPEX	13.73 M€	13.68 M€
<i>Operating costs</i>		
Total variable cost	19.59 M€/y	15.15 M€/y

Catalyst	29.16 %	22.84 %
Membrane	0 %	1.075 %
Feedstock (H ₂)	57.81 %	62.91 %
Feedstock (CO ₂)	4.717 %	5.134 %
Utilities	8.315 %	8.040 %
Fixed OPEX	3.345 M€/y	3.585 M€/y
OPEX	22.94 M€/y	18.74 M€/y
ACAPEX	1.379 M€/y	1.338 M€/y
TAC	24.32 M€/y	20.08 M€/y
MDSP	1960 €/ton_{DME}	1739 €/ton_{DME}

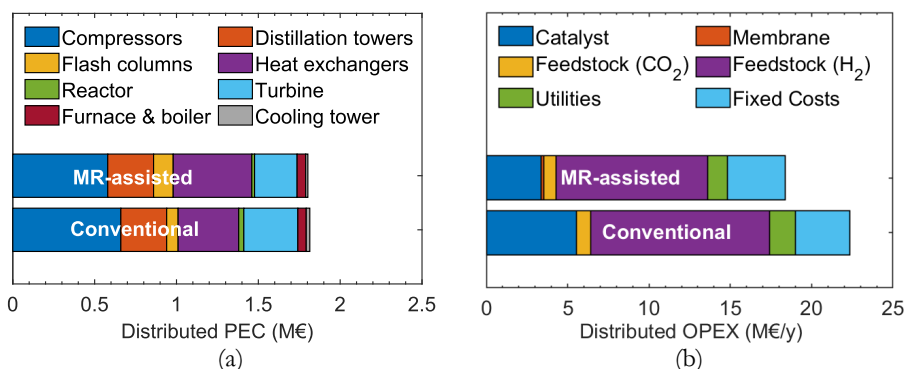


Figure 7.8. Distributed PEC (a) and distributed OPEX (b) for the MR-assisted and conventional one-step DME production process

7.6 FORECASTING AND SENSITIVITY ANALYSIS

The economic analysis (Section 7.5) showed that the one-step DME production via CO₂ hydrogenation route is not yet competitive with the benchmark route (i.e., DME from steam methane reforming or SMR), given the current market conditions. However, the market conditions are expected to change due to the environmental concerns and the needs of decarbonizing the chemical industry. Therefore, this section presents a detailed analysis of the possible conditions which could render the CO₂-to-DME technology industrially appealing in the future.

As learned already from Section 7.5, the one-step DME production via CO₂ hydrogenation is an OPEX intensive process. As a matter of fact, the ACAPEX is ca. the 5.67% and 6.66% of the TAC for the conventional and MR-assisted process, respectively. This means that the MDSP is mainly affected by the OPEX. **Figure 7.9** shows that the H₂ feedstock price is largest contributor to the MDSP, followed by the cost of the catalyst, which strongly depends on its lifetime. Furthermore, the cost of the natural gas as well as of the CO₂ feedstock, both show a minor and similar impact. Finally, both the membrane lifetime and the cost of the electricity do not affect the MDSP significantly. Based on this preliminary analysis, this section proposes some sensitivity analyses on the main cost drivers, as well as further process optimization strategies to reduce the operating costs.

Finally, this section suggests different realistic scenarios which could decrease the MDSP in the next few years at the point in which the DME production cost via CO₂ hydrogenation in membrane reactors balances with the forecasted DME market value.

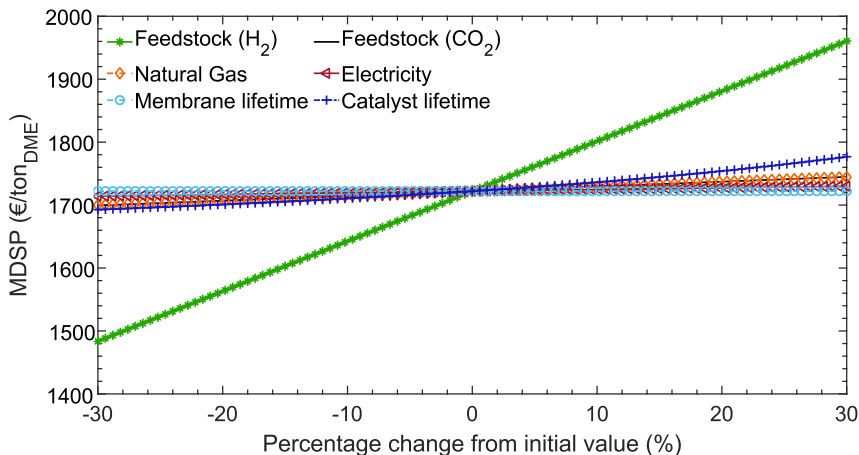


Figure 7.9. Effect of the higher impact cost drivers of the OPEX on the MDSP of the MR-assisted one-step DME production process.

7.6.1 Forecasting of H₂ price according to different production methods

The H₂ price is extremely influenced by the production method. An overview of the available technologies, together with their current cost and its prediction in 2050 is given in **Table 7.14**. The H₂ production methods can be summarized as follows: 1) H₂ from fossil fuels, which include the widely used steam methane reforming (SMR), but also higher hydrocarbon cracking, reforming and gasification; 2) H₂ from electrolysis of water, either from renewable energy and using electricity from the grid (i.e., mostly fossil fuel based). In 2010, about 96% of the H₂ used in industry was produced from fossil fuels (i.e., natural gas, coal and oil) [44]. Currently, this value is still close to 90%, being the SMR technology the cheapest on the market. The remaining 10% is mostly produced via water electrolysis, which still leads to considerable indirect CO₂ emissions, given the electricity requirement. Furthermore, these technologies are 3 to 10 times more expensive than the SMR, especially because these methods are still under development/optimization and they are mainly affected by the price and source of the electricity.

In our base case scenario, H₂ was assumed to be supplied by an integrated pipeline network (i.e., H₂ price of 2.95 €/kg, as reported by Fortes et al. [12]), with H₂ being mostly produced via steam methane reforming and coal and biomass gasification coupled with CCS. Despite the CCS technology, these production routes are energy intensive, thus, not environment friendly. The goal of this research is to promote a sustainable production method of DME, as well as a route for the CO₂ utilization.

As a result, the impact of any indirect CO₂ emission source, such as the emission related to the H₂ production should be also considered and minimized. The only production method which can potentially be 100% renewable is the electrolysis. However, when the electricity from the grid is used, H₂ cannot be considered as renewable. As a matter of fact, nowadays, still 80% of the electricity in the Netherlands is produced using fossil fuels with a CO₂ footprint of 330 gCO₂/kWh [45].

To remove any source of CO₂ emission, H₂ must be produced via electrolysis based on 100% renewable resources, which makes the H₂ production much more expensive (**Table 7.14**). At the moment, the alkaline electrolysis (AE) is the most mature technology and, as a consequence, the cheapest sustainable route. Polymer electrolyte membrane (PEM) electrolysis is approaching the cost of the AE and even the MW-scale systems are currently market ready [46]. On the other hand, the solid oxide electrolyser (SOE) technology is not yet ready for the industrial scales. Detz et al. [46] predicted the H₂ price from different sustainable technologies in the time span from 2015 to 2050, considering that phenomena such as learning-by-doing, learning-by-searching, economies-of-scale, and automation can reduce the renewable H₂ manufacturing costs. According to their prediction, both PEM and SOE are the techniques that in the future (i.e., by 2050) will be able to produce H₂ at comparable prices (i.e., 1.3 €/kg) to the fossil fuel-based technologies.

Table 7.14. Current Price of H₂ and its prediction in 2050 according to different production methods

Production method	Type	Current cost	Cost in 2050	Ref.
Fossil fuels (SMR)	H ₂	1.3 €/kg	-	[47]
Electrolysis [†]	H ₂	2.50-6.7 €/kg	-	[48]
Electrolysis (AE)	REN- H ₂	5.6 €/kg	2.12 €/kg	[46]
Electrolysis (PEM)	REN- H ₂	7.1 €/kg	1.81 €/kg	[46]
Electrolysis (SOEC)	REN- H ₂	6.0 €/kg	1.03 €/kg	[46]
Electrolysis (PEC)	REN- H ₂	10.8 €/kg	1.91 €/kg	[46]

^{*}H₂ from 100% renewable resources is classified as REN-H₂ [46].

[†]In some studies grid-electricity is used, sometimes in combination with renewable energy, so the H₂ production is not 100% renewable.

Therefore, the functions derived by Detz et al. describing the decrease in the H₂ price within the years for both the PEM and SOE technologies were implemented in the economic analysis of the CO₂-to-DME technologies. The effect of changing the H₂ price on the MDSP for both the conventional and MR-assisted process is depicted in **Figure 7.10**, where it is clear that the choice of the electrolysis method between PEM and SOE has a large impact on the MDSP and that, despite the readiness of the technology, the SOE is much more promising in terms of economics. Furthermore, **Figure 7.10** also shows that the MDSP of the MR-assisted technology is always much lower than the one related to the conventional process. As a result, in the next analyses, the MR-assisted technology with the H₂ obtained via SOE will be considered as a new base case scenario.

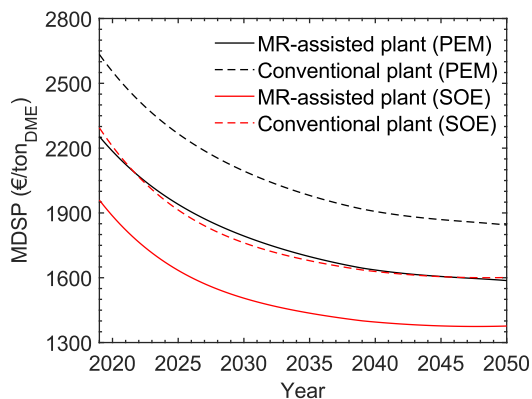


Figure 7.10. MDSP for the conventional (dashed lines) and MR-assisted plant (solid lines) as a function of time (years) considering different H₂ production technologies: PEM (black lines) and SOE (red lines), implementing the H₂ price predicted by Detz et al [46]

7.6.2 Effect of the carbon tax

As learned in Section 7.6.1, with the prediction of the H₂ price by SOE, the MDSP of the MR-assisted technology can be reduced to 1376 €/ton in 2050. This price cannot be directly compared to the DME market price, which corresponds to the benchmark technology. As a matter of fact, the DME production cost from SMR is expected to increase in the next years, due to the extra costs related to the emissions and the corresponding carbon tax. Indeed, the carbon tax in the Netherlands and in Europe (on average) is expected to increase linearly over the years (**Figure 7.11a**) [18]. With this data, the DME market price can be estimated over the years, considering an average emission of 93 gCO₂/M]_{DME} [41]–[43] and assuming that after 2030, the carbon tax will continue to increase linearly (i.e., linear extrapolation). However, this analysis assumes that no carbon tax is included in the current DME market price (year 2020) and that the price of other feedstock, like natural gas, are not influenced by the carbon tax significantly. On the other hand, the effect of the carbon tax on the MDSP related to the one-step DME production via CO₂ hydrogenation is more complex to analyze. It should be considered that this system uses CO₂ as a feedstock. This implies that the carbon tax can have: 1) a negative effect, due to the CO₂ total emissions and 2) a positive effect on the reduction of the CO₂ feedstock price. The latter effect is described in Section 7.6.5. When considering, at the same time, the reduction in the H₂ price from SOE and the negative effect of the carbon tax on the MDSP of the MR-assisted technology, as well as the effect of the carbon tax on the DME market price, a competitiveness curve can be obtained (**Figure 7.11b**) showing that the novel technology based on CO₂ utilization will be competitive with the benchmark method in 2050.

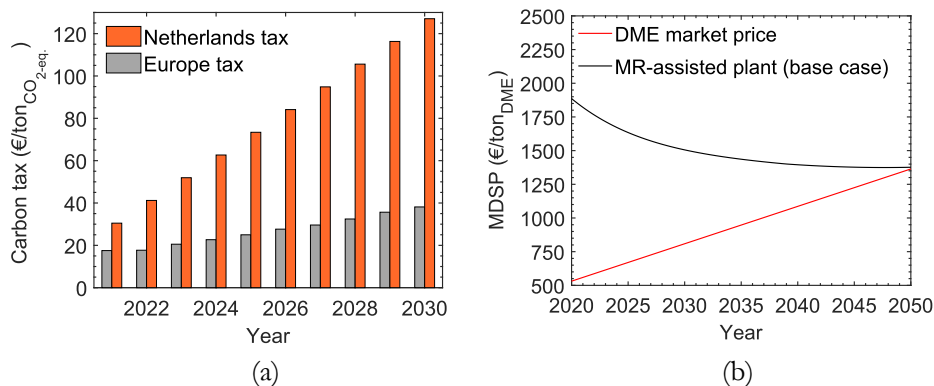


Figure 7.11. The expected carbon tax for the coming years on average in Europe (grey bars) and in the Netherlands (orange bars) (a); MDSP of the MR-assisted plant (solid lines) as a function of time (years) when compared with the DME market price prediction (red line).

7.6.3 Effect of the catalyst lifetime (scenario 1)

The Cu/ZnO/Al₂O₃-HZSM-5 catalyst selected in this study has a lifetime of ca. 2 years, as reported in literature [9], [49]. Its deactivation phenomena usually arise from copper crystallization and aluminum leaching with hot water, possible poisoning from sulfur based compound (i.e., impurities in the feedstock) and coke formation, which is faster and enhanced at higher temperatures (i.e., above 300 °C [50]). However, the catalytic bed of the membrane reactor operates in an almost dry environment, given the removal of water by means of the membranes. Furthermore, a low temperature operation process is promoted here (i.e., an average reactor temperature of 220 °C, with a peak at 260 °C), given the more severe thermodynamic limitations when using pure CO₂ as the sole carbon source and the higher efficiency of the membrane separation in the PBMR. As a result, the catalyst deactivation could be reasonably delayed and its lifetime can be extended from 2 to 5 years, to be compatible with the lifetime of the membranes. Considering a catalyst lifetime of 5 years, the MDSP curve referred to the MR-assisted technology of **Figure 7.11b** will shift downwards of ca. 192 €/ton (scenario 1), becoming even more attractive than the conventional technology and crossing the DME market price already in 2043 (i.e., 7 years earlier).

7.6.4 Optimization of the HP steam cycle and natural gas usage (scenario 2-4)

The third important cost contributor to the MDSP is the cost of natural gas (NG), which also directly influences the CO₂ emissions related to the combustion. The natural gas requirements can be reduced by optimizing the use of the HP steam, which is mainly required at the reboiler of columns T1 and T3. As seen also in **Table 7.13**, the CAPEX has a small impact on the TAC and on the MDSP. Therefore, the number of stages of the distillation tower T1 could be increased to reduce the reflux ratio and, as a result, the reboiler duty. An increase in the number of stages from 18

to 22 corresponds to a decrease in the reflux ratio from 5 to 4 (beyond 22 stages, the reflux ratio changes are not significant). This condition corresponds to a reduction of 15.5% and 12% in the HP steam flow and natural gas requirement, respectively, as well as to a CAPEX increase of 0.06%, which has a negligible effect on the MDSP. On the other hand, no beneficial effects were found in increasing the height of the column T3.

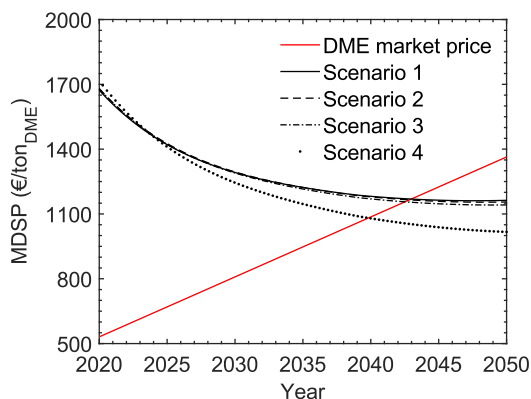
Based on the optimized usage of the HP steam, multiple scenarios can be built on top of scenario 1 (i.e., considering a catalyst lifetime of 5 years):

- Scenario 2: Natural gas is used for the production of the HP steam in the optimized conditions (i.e., 12% NG usage less than the base case);
- Scenario 3: The purge stream of the unconverted gases, which still contains a heating value of ca. 1175 MJ/h due to the presence of H₂ (70 mol.%) and traces of CO, methanol and DME, can be fed to the burner, in combination with a reduced flow of natural gas. This solution further reduces the NG usage of 20%;
- Scenario 4: The natural gas required in scenario 3 is completely replaced with green H₂. As a result, the purge stream is fed to the burner together with H₂. This solution also minimizes the CO₂ emissions.

An overview of the NG requirement and the alternative fuels used for the production of the HP steam in the base case and three scenarios is given in **Table 7.15**, together with the impact on the direct CO₂ emissions. The impact of the three scenarios on the competitiveness curve is depicted in **Figure 7.12**. The MDSP curve related to scenarios 2 and 3 decrease over the years with the same trend of the base case (i.e., curve of **Figure 7.11b**). However, these curves are only slightly shifted downwards due to the lower NG consumption, since in general the impact of the NG cost on the total OPEX is not that significant (see **Figure 7.9**). On the other hand, the curve representing scenario 4 decreases with a quite different slope, due to the implementation of the H₂ decreasing function, together with the reduction of the NG usage and the CO₂ emissions. For the same reason, scenario 4 has initially a higher MDSP than the other scenario, because of the higher cost of H₂ used for the combustion. Nevertheless, with the decrease in the H₂ price over the years and with the increase in the carbon tax, the MDSP decreases faster than the other cases from the year 2025, anticipating the moment from which our technology will be competitive with the benchmark of ca. 3 years (i.e., 2040 instead of 2043).

Table 7.15. Overview of NG requirement and the alternative fuels used for the production of the HP steam in the base case and the three scenarios, together with the corresponding direct CO₂ emissions.

	Base case	Scenario 2	Scenario 3	Scenario 4
Natural gas/DME (ton/ton)	0.13	0.11	0.09	0
Purge streams/DME (ton/ton)	0	0	0.05	0.05
REN-H ₂ /DME (ton/ton)	0	0	0	0.03
CO ₂ emissions/DME (ton/ton)	0.39	0.35	0.31	0.05

**Figure 7.12.** MDSP of the MR-assisted plant (black lines) as a function of time (years) when compared with the DME market price prediction (red line), using REN-H₂ from SOE, a catalyst lifetime of 5 years in the three scenario for the HP steam production.

7.6.5 Effect of the CO₂ feedstock price: carbon capture vs carbon tax (scenario 5-7)

Although the CO₂ feedstock price does not play a significant role on the MDSP, similarly to the natural gas, this variable needs a dedicated section. As a matter of fact, the technology proposed here uses CO₂ as the sole carbon source for the synthesis of DME. Therefore, it is easy to imagine a future scenario in which, heavy CO₂ emitting companies would be keen to buy this CO₂ utilization technology to make profit from a waste rather than paying a tax. In the base case, a CO₂ feedstock price of 33 €/ton was assumed (i.e., CO₂ from SEWGS). Nevertheless, the CO₂ price is expected to change over the years due to the development of the CO₂ capture technologies and to the environmental concerns and the corresponding carbon tax policy. From the moment in which the carbon tax will be higher than the carbon capture price (CCP), companies will start to capture their CO₂ and either sell it or use it directly. This moment can be defined as t_1 , which allows to identify two different time regions: 1) Before t_1 , the price of the CO₂ feedstock for the CO₂-to-DME technology corresponds ca. to the CCP, since CO₂ needs to be purchased from industries/companies which decide to capture CO₂ and sell it with a certain profit. Indeed, industries will not capture their CO₂ for “free”, since paying a carbon

tax would be cheaper; 2) After t_1 , the situation is more complex and three scenarios can be identified:

- Scenario 5: after t_1 the CO₂ feedstock price will be zero;
- Scenario 6: after t_1 the CO₂ feedstock price will correspond to the difference between the carbon tax and the CCP. As a result, the CO₂ feedstock will be seen as a revenue instead of a cost. Indeed, companies would prefer to capture the CO₂, rather than paying a tax, and would pay the difference for the CO₂ utilization process, which could be seen as a waste treatment technology.
- Scenario 7: it is similar to scenario 6, but with a slightly different revenue. The company which decides to capture the CO₂ instead of paying the carbon tax, would prefer to pay for the CO₂ utilization technology less than the difference between the carbon tax and the CCP. This scenario is much more realistic, since it is easy to imagine that if the CO₂ waste treatment and the carbon tax come with the same price, one would still prefer to pay a tax and avoid further capital investments in CO₂ capture technologies. In this scenario it is assumed that the CO₂ emitting companies would pay 14.1% less than the difference between carbon tax and CCP. This % corresponds to the average gross profit margin of primary metal industry [51].

These scenarios can be built on top of scenario 4, described in the previous section, where the usage of the HP steam and of the fuels to produce it are optimized.

Within these scenarios, the case in which, after t_1 , the CO₂ emitting companies would decide only to sell it with a profit margin is not considered, since this will correspond exactly to scenario 4, with the CO₂ feedstock price of the base case. Nevertheless, in the perspective of a CO₂ utilization technology, it is easy to see the CO₂ feedstock as a revenue, since when the CCP is lower than the carbon tax, it is worth for the companies to capture the CO₂. When more and more companies will capture their CO₂, the market will be saturated and if they cannot sell it, they would still need to emit it and pay the carbon tax on top of the CCP. As a result, these companies would be willing to pay a difference between carbon tax and CCP to the CO₂ consumers.

The competitiveness curve related to the new scenario (5, 6 and 7), together with the one of scenario 4 (see section 7.6.4), are depicted in **Figure 7.13**. Scenarios 5, 6 and 7 were all built on top of scenario 4, which was the best scenario found in view of the optimization of the HP steam generation and usage. Starting from 2022 the curves related to the new scenario show a discontinuity, due to a drop in the price of the CO₂ feedstock. As a result, the year 2022 corresponds to t_1 , where the carbon tax has achieved the CCP (i.e., 33 €/ton for the SEWGS). From this point on, it is clear that scenario 6 is more convenient, followed by scenario 7 and scenario 5. In case of scenario 6 and of the more realistic scenario 7, the MR-assisted process could become competitive with the benchmark already in 2032 and 2033, respectively. In case of scenario 5, instead, the CO₂-to-DME process would be competitive in 2038.

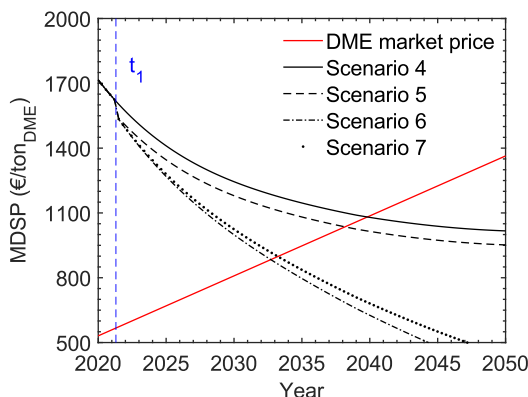


Figure 7.13. MDSP of the MR-assisted plant (black lines) as a function of time (years) when compared with the DME market price prediction (red line), using REN-H₂ from SOE, a catalyst life time of 5 years, H₂ and purge streams for the HP steam production in the three scenario identified for the CO₂ feedstock price. The blue dashed vertical line represents the time t_1 .

7.6.6 Overview and uncertainty analysis

Table 7.16 gives an overview of the scenario built in section 7.6.4 and 7.6.5, in terms of the MDSP, year and carbon tax corresponding to the intersection point between the MDSP curve and the DME benchmark market price (i.e., moment in which the one-step DME synthesis via CO₂ hydrogenation using membrane reactors will become competitive with the benchmark DME synthesis). According to this analysis, the CO₂-to-DME MR-assisted technology could become profitable, and thus industrially applicable, between 2032 and 2040. As a matter of fact, scenario 1 considers a longer catalyst lifetime, which is realistic thanks to the advantages of the membrane reactor technology, as discussed in Section 7.6.3. Furthermore, scenario 2 to 4 depends on an optimization of the fuel used for producing HP steam. Therefore, it is reasonable to consider scenarios on top of scenario 4. Nevertheless, the results reported in **Table 7.16** also show that the moment in which the CO₂-to-DME MR-assisted technology will become competitive with the benchmark not only depends on the different scenarios, but also on the value of the carbon tax. Currently, the carbon tax policy has not been accepted all over the world and its value depends on national regulations. As an example, when focusing on the European countries who have already imposed a carbon tax, its value currently ranges from 116.33 €/ton_{CO₂} for Sweden, to a value of 0.07 €/ton_{CO₂} for Poland [52]. Considering the carbon tax corresponding at year 2020 as a variable and assuming a linear increase with time as in **Figure 7.11a**, the point of intersection of the MDSP of scenario 6 (i.e., the more realistic) shifts. As a result, the year of competitiveness and the corresponding carbon tax value correlates as depicted in **Figure 7.14**, from which it is possible to observe that the carbon tax has to be at least 118 €/ton_{CO₂} to have a MDSP equal to the DME market price by 2050.

Table 7.16. Overview of the different scenario in terms of MDSP, year and carbon tax corresponding to the intersection point between the MDSP curve and the DME benchmark market price.

Intersection point	Base case	1	2	3	4	5	6	7
MDSP (€/ton _{DME})	1376	1179	1179	1159	1083	1038	885	900
Year	2050	2043	2043	2042	2040	2038	2032	2033
Carbon tax (€/ton _{CO₂})	260	260	260	250	230	211	154	161

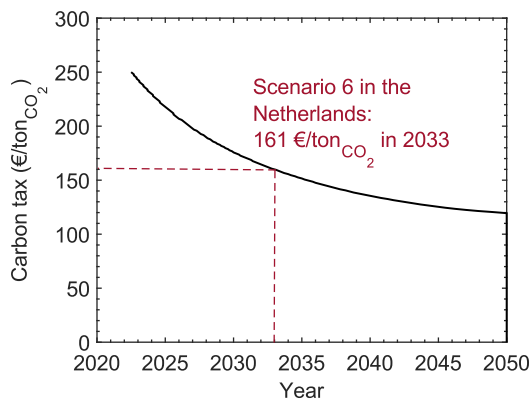


Figure 7.14. Carbon tax corresponding at the year in which our technology will be competitive with the benchmark according to scenario 6, depending on the initial policy on the carbon tax (i.e., at 2020).

The results showed in this section are based on several hypotheses. Although all the variables are based on previous studies and information retrieved from literature, there are some uncertainties which will surely affect the moment in which the technology would become competitive with the DME market value. A list of some of the unknown variables or data which have not been included or have been assumed in this research and that are believed to reduce the accuracy of this prediction is given here:

- The salary change over the years was not taken into account. The salary could increase due to the inflation and increase in the welfare, as example. As a result, it is very difficult to predict its future trend.
- Currently, only the price of the DME chemical grade is known. However, the technology proposed in this study produces a fuel grade DME, which is expected to have a higher market value.
- In case the H₂ production would be integrated in the DME synthesis, the heat generated in the hydrogen production step could be used to replace HP steam completely. As a matter of fact, the SOE process operates at temperature of 500-850 °C and the heat corresponding to the H₂ stream could be used for the reboilers in the distillation towers. Furthermore, the maximum working pressure of the SOE and PEM can vary in a wide range

- (35-200 bar) [53], [54]. This indicates that the cost of compression could be further reduced. However, the electricity cost, as well as the CAPEX, did not show a large impact on the MDSP.
- This analysis does not take into account the possible subsidies related to the use of renewable feedstock/energy. This could reduce our cost significantly and make our system more competitive with the benchmark.
 - The carbon tax in the Netherlands (30 €/ton_{CO₂}) is above the European average (24 €/ton_{CO₂}), which makes it harder for this technology to be competitive in the rest of Europe, on average.
 - The carbon capture price is also expected to be dependent on the technology adopted and on the composition of the waste stream from which the CO₂ needs to be purified. A more expensive technology would delay the moment from which CO₂ could become a cost zero feedstock or even a revenue (t₁). However, as for the H₂, also the CCP is expected to decrease with time, due to the development of the existing or even more efficient technologies. As an example, the use of membrane separation technologies can reduce the cost of solvent based technologies of ca. 28% [55].
 - Changes in the price of natural gas over the years have not been considered in this study. However, the scenarios 4-7 are not affected by this cost, given that the natural gas has been completely replaced with renewable H₂.

7.7 CONCLUSIONS

This work demonstrates that CO₂ can be upgraded from a polluting agent into a valuable feedstock at industrial scale. The use of a membrane reactors in the direct CO₂ hydrogenation to DME shifts the single pass conversion from 39% to 55%, together with a shift in the DME yield from 32% to 53%. The higher efficiency in the conversion of the PBMR allows for a remarkable decrease in both the catalyst mass and in the H₂ feedstock flow to produce 1 ton of DME of ca. 39% and 64%, respectively. Overall, the PBMR displays a cold gas efficiency (CGE) of 88% with respect to the 76% of the PBR. On a process perspective, the MR-assisted plant requires less energy input to produce the same amount of DME.

On the economic aspect, both processes revealed to be OPEX intensive, with the operating costs of the MR-assisted process significantly lower (ca. 23%), due to the lower requirement of H₂, which covers more than 60% of the OPEX.

The minimum DME selling price (MDSP) was found to be 1739 €/ton and 1960 €/ton for the MR-assisted and the conventional process, respectively, in the base case scenario, where no carbon tax is taken into account and the CO₂ feedstock is considered as a cost. This result proves that the combination of the two steps in a single reactor, together with the use of the membrane reactor technology, allows for a reduction in the MDSP of 1.26 times with respect to what has been reported in literature.

Nevertheless, the MDSP of the MR-assisted technology is still 3.3 times higher than the current DME market value. As a result, a feasibility study to predict the moment in which this technology would become competitive with the benchmark was carried out. This analysis showed that when considering the reduction in the H₂ price produced using SOE technology, together with an increase in the catalyst lifetime from 2 to 5 years and an optimization of the HP steam and natural gas usage, the CO₂-to-DME MR-assisted system can be competitive with the benchmark in 2040, if the carbon tax would increase linearly. In addition, if the CO₂ feedstock is considered as a revenue rather than a cost, this process could be profitable ca. 7 years earlier. The result of the competitiveness analysis strongly depends on the carbon tax policy, which varies from country to country. In conclusion, given the uncertainties related to this prediction, it is more correct to identify a region, more than an exact moment, which goes from 2025 to 2050 where the CO₂ direct hydrogenation to DME in membrane reactors will be economically competitive with the benchmark process.

Appendix F

F.1 Stream tables

Table F1. Stream table of the conventional one-step DME production process via CO₂ hydrogenation

	0	1	2	3	4	5	6	7
Temperature (°C)	200.3	201.1	124.1	59	30	20	-33.3	-33.3
Pressure (bar)	39.75	40	40	40	40	40	40	40
Vapor Fraction	1	1	0.88	0.82	0.803	0.791	0.672	0
Mass flow (kg/h)	9498.9	9498.9	9498.9	9498.9	9498.9	9498.9	9498.9	6212.9
Mass fraction								
CO ₂	0.546	0.546	0.546	0.546	0.546	0.546	0.546	0.441
CO	0.007	0.007	0.007	0.007	0.007	0.007	0.007	0.001
DME	0.151	0.151	0.151	0.151	0.151	0.151	0.151	0.22
H ₂	0.075	0.075	0.075	0.075	0.075	0.075	0.075	0
MeOH	0.033	0.033	0.033	0.033	0.033	0.033	0.033	0.051
Water	0.188	0.188	0.188	0.188	0.188	0.188	0.188	0.287
O ₂	0	0	0	0	0	0	0	0
N ₂	0	0	0	0	0	0	0	0
Propylene	0	0	0	0	0	0	0	0
Methane	0	0	0	0	0	0	0	0
Ethane	0	0	0	0	0	0	0	0
Propane	0	0	0	0	0	0	0	0
	8	9	10	11	12	13	14	15
Temperature (°C)	-33.3	90	64.7	235.4	45	4.8	110.6	44.4
Pressure (bar)	40	40	40	40.1	40	40	40.07	10
Vapor Fraction	1	0.366	1	0	0.653	1	0	0.729
Mass flow (kg/h)	3286	6212.9	4113.6	2099.3	4113.6	2745.9	1367.7	1367.7
Mass fraction								
CO ₂	0.743	0.441	0.667	0	0.667	0.998	0.001	0.001
CO	0.018	0.001	0.001	0	0.001	0.001	0	0
DME	0.022	0.22	0.332	0	0.332	0	0.999	0.999
H ₂	0.217	0	0	0	0	0.001	0	0
MeOH	0	0.051	0	0.151	0	0	0	0
Water	0	0.287	0	0.849	0	0	0	0
O ₂	0	0	0	0	0	0	0	0
N ₂	0	0	0	0	0	0	0	0
Propylene	0	0	0	0	0	0	0	0
Methane	0	0	0	0	0	0	0	0
Ethane	0	0	0	0	0	0	0	0
Propane	0	0	0	0	0	0	0	0
	16	17	18	19	20	21	22	23
Temperature (°C)	30	220.8	185	43.5	43.5	234.2	-27.4	-27.4
Pressure (bar)	10	30	30	30	1	30.14	40	40
Vapor Fraction	0	0.077	1	0	0	0	1	1
Mass flow (kg/h)	1367.7	2099.3	317.5	317.5	317.5	1781.9	60.3	5971.6
Mass fraction								
CO ₂	0.001	0	0	0	0	0	0.859	0.859
CO	0	0	0	0	0	0	0.01	0.01
DME	0.999	0	0.001	0.001	0.001	0	0.012	0.012
H ₂	0	0	0	0	0	0	0.118	0.118
MeOH	0	0.151	0.999	0.999	0.999	0	0	0

Water	0	0.849	0.001	0.001	0.001	1	0	0
O ₂	0	0	0	0	0	0	0	0
N ₂	0	0	0	0	0	0	0	0
Propylene	0	0	0	0	0	0	0	0
Methane	0	0	0	0	0	0	0	0
Ethane	0	0	0	0	0	0	0	0
Propane	0	0	0	0	0	0	0	0
	25	26	27	28	29	30	31	32
Temperature (°C)	6.3	195	200	15	91.1	38	117.6	38
Pressure (bar)	40	40	40	1	2.43	2.43	5.9	5.9
Vapor Fraction	1	1	1	1	1	1	1	1
Mass flow (kg/h)	9497.6	9497.6	9497.6	3100.3	3100.3	3100.3	3100.3	3100.3
Mass fraction								
CO ₂	0.867	0.867	0.867	1	1	1	1	1
CO	0.006	0.006	0.006	0	0	0	0	0
DME	0.008	0.008	0.008	0	0	0	0	0
H ₂	0.119	0.119	0.119	0	0	0	0	0
MeOH	0	0	0	0	0	0	0	0
Water	0	0	0	0	0	0	0	0
O ₂	0	0	0	0	0	0	0	0
N ₂	0	0	0	0	0	0	0	0
Propylene	0	0	0	0	0	0	0	0
Methane	0	0	0	0	0	0	0	0
Ethane	0	0	0	0	0	0	0	0
Propane	0	0	0	0	0	0	0	0
	33	34	35	36	37	38	39	40
Temperature (°C)	118.1	38	130.4	15	29.2	61.4	15	24.4
Pressure (bar)	14.4	14.4	40	35	40	40	1.01	1.01
Vapor Fraction	1	1	1	1	1	1	0	0
Mass flow (kg/h)	3100.3	3100.3	3100.3	425.8	425.8	3526.1	9908.4	9908.4
Mass fraction								
CO ₂	1	1	1	0	0	0.879	0	0
CO	0	0	0	0	0	0	0	0
DME	0	0	0	0	0	0	0	0
H ₂	0	0	0	1	1	0.121	0	0
MeOH	0	0	0	0	0	0	0	0
Water	0	0	0	0	0	0	1	1
O ₂	0	0	0	0	0	0	0	0
N ₂	0	0	0	0	0	0	0	0
Propylene	0	0	0	0	0	0	0	0
Methane	0	0	0	0	0	0	0	0
Ethane	0	0	0	0	0	0	0	0
Propane	0	0	0	0	0	0	0	0
	41	42	43	44	45	46	47	48
Temperature (°C)	35	25	25	25	37.8	39.1	45.8	69.9
Pressure (bar)	1.01	1.01	1.01	1	1.01	1.01	1.01	1.01
Vapor Fraction	0	0	0	0	0	0	0	0
Mass flow (kg/h)	9908.4	11710	16214	23420	11709 9	16214	16214	16214
Mass fraction								
CO ₂	0	0	0	0	0	0	0	0
CO	0	0	0	0	0	0	0	0
DME	0	0	0	0	0	0	0	0
H ₂	0	0	0	0	0	0	0	0
MeOH	0	0	0	0	0	0	0	0

Water	1	1	1	1	1	1	1	1
O ₂	0	0	0	0	0	0	0	0
N ₂	0	0	0	0	0	0	0	0
Propylene	0	0	0	0	0	0	0	0
Methane	0	0	0	0	0	0	0	0
Ethane	0	0	0	0	0	0	0	0
Propane	0	0	0	0	0	0	0	0
	49	50	51	52	53	54	55	56
Temperature (°C)	100	100	100	100	26.5	28.8	31.1	33.5
Pressure (bar)	1.01	1.01	1.01	1.01	1	1	1	1
Vapor Fraction	0.002	0.002	0.002	0	0	0	0	0
Mass flow (kg/h)	16214	13367	2846.4	2846.4	23420	23420	23420	23420
Mass fraction								
CO ₂	0	0	0	0	0	0	0	0
CO	0	0	0	0	0	0	0	0
DME	0	0	0	0	0	0	0	0
H ₂	0	0	0	0	0	0	0	0
MeOH	0	0	0	0	0	0	0	0
Water	1	1	1	1	1	1	1	1
O ₂	0	0	0	0	0	0	0	0
N ₂	0	0	0	0	0	0	0	0
Propylene	0	0	0	0	0	0	0	0
Methane	0	0	0	0	0	0	0	0
Ethane	0	0	0	0	0	0	0	0
Propane	0	0	0	0	0	0	0	0
	57	58	59	60	61	62	63	64
Temperature (°C)	38	38.1	100.4	25	25	250.4	303.8	124.8
Pressure (bar)	1	1	40	1.01	1.01	40	1.01	1.01
Vapor Fraction	0	0	0	1	1	1	1	1
Mass flow (kg/h)	23420	23420	2846.4	193.6	4650	2846.4	4843.6	4843.6
Mass fraction								
CO ₂	0	0	0	0.008	0	0	0.109	0.109
CO	0	0	0	0	0	0	0	0
DME	0	0	0	0	0	0	0	0
H ₂	0	0	0	0	0	0	0	0
MeOH	0	0	0	0	0	0	0	0
Water	1	1	1	0	0	1	0.087	0.087
O ₂	0	0	0	0	0.222	0	0.057	0.057
N ₂	0	0	0	0.008	0.778	0	0.747	0.747
Propylene	0	0	0	0	0	0	0	0
Methane	0	0	0	0.904	0	0	0	0
Ethane	0	0	0	0.075	0	0	0	0
Propane	0	0	0	0.005	0	0	0	0
	65	66	67	68	69	70	71	72
Temperature (°C)	250.4	245	238.6	196	196	196	81.3	125.5
Pressure (bar)	40	40	40	14.3	14.3	14.3	0.5	15
Vapor Fraction	0.53	0	0	0.13	0	1	0.898	1
Mass flow (kg/h)	2846.4	2846.4	2846.4	2142.4	2142.4	2142.4	2142.4	13045
Mass fraction								
CO ₂	0	0	0	0	0	0	0	0
CO	0	0	0	0	0	0	0	0
DME	0	0	0	0	0	0	0	0
H ₂	0	0	0	0	0	0	0	0
MeOH	0	0	0	0	0	0	0	0
Water	1	1	1	1	1	1	1	0

O ₂	0	0	0	0	0	0	0	0
N ₂	0	0	0	0	0	0	0	0
Propylene	0	0	0	0	0	0	0	1
Methane	0	0	0	0	0	0	0	0
Ethane	0	0	0	0	0	0	0	0
Propane	0	0	0	0	0	0	0	0
	73	74	75	76	77	78		
Temperature (°C)	35	-48	-48	-3.2	43	43		
Pressure (bar)	15	1	1	1	1	1		
Vapor Fraction	0	0.552	0.991	1	0	0		
Mass flow (kg/h)	13045	13045	13045	13045	15282 7	10968		
Mass fraction								
CO ₂	0	0	0	0	0	0		
CO	0	0	0	0	0	0		
DME	0	0	0	0	0	0		
H ₂	0	0	0	0	0	0		
MeOH	0	0	0	0	0	0		
Water	0	0	0	0	1	1		
O ₂	0	0	0	0	0	0		
N ₂	0	0	0	0	0	0		
Propylene	1	1	1	1	0	0		
Methane	0	0	0	0	0	0		
Ethane	0	0	0	0	0	0		
Propane	0	0	0	0	0	0		

Table F2. Stream table of the MR-assisted one-step DME production process via CO₂ hydrogenation

	0	1	2	3	4	5	6	7
Temperature (°C)	198.8	199.5	77.5	20	-26	-26	-26	-10.7
Pressure (bar)	39.75	40	40	40	40	40	40	40
Vapor Fraction	1	1	0.887	0.778	0.647	1	0	0.001
Mass flow (kg/h)	4560.8	4560.8	4560.8	4560.8	4560.8	1286.6	3274.2	3274.2
Mass fraction								
CO ₂	0.479	0.479	0.479	0.479	0.479	0.694	0.395	0.395
CO	0.009	0.009	0.009	0.009	0.009	0.029	0.001	0.001
DME	0.312	0.312	0.312	0.312	0.312	0.055	0.413	0.413
H ₂	0.063	0.063	0.063	0.063	0.063	0.222	0	0
MeOH	0.035	0.035	0.035	0.035	0.035	0	0.049	0.049
Water	0.102	0.102	0.102	0.102	0.102	0	0.142	0.142
O ₂	0	0	0	0	0	0	0	0
N ₂	0	0	0	0	0	0	0	0
Propylene	0	0	0	0	0	0	0	0
Methane	0	0	0	0	0	0	0	0
Ethane	0	0	0	0	0	0	0	0
Propane	0	0	0	0	0	0	0	0
	8	9	10	11	12	13	14	15
Temperature (°C)	5.6	19.5	20	70	80.1	220.4	40	9.4
Pressure (bar)	40	40	40	40	40	40.12	40	40
Vapor Fraction	0.002	0.003	0.003	0.225	1	0	0.195	1
Mass flow (kg/h)	3274.2	3274.2	3274.2	3274.2	2642.6	631.6	2642.6	1305.5
Mass fraction								
CO ₂	0.395	0.395	0.395	0.395	0.489	0	0.489	0.99

7. Techno-economic assessment of the CO₂-to-DME process

CO	0.001	0.001	0.001	0.001	0.001	0	0.001	0.002
DME	0.413	0.413	0.413	0.413	0.51	0.009	0.51	0.008
H ₂	0	0	0	0	0	0	0	0.001
MeOH	0.049	0.049	0.049	0.049	0	0.253	0	0
Water	0.142	0.142	0.142	0.142	0	0.738	0	0
O ₂	0	0	0	0	0	0	0	0
N ₂	0	0	0	0	0	0	0	0
Propylene	0	0	0	0	0	0	0	0
Methane	0	0	0	0	0	0	0	0
Ethane	0	0	0	0	0	0	0	0
Propane	0	0	0	0	0	0	0	0
	16	17	18	19	20	21	22	23
Temperature (°C)	111	44.4	30	-19.6	-19.6	198.8	130.5	120.3
Pressure (bar)	40.08	10	10	40	40	35	35	35
Vapor Fraction	0	0.734	0	1	1	1	0.956	0.931
Mass flow (kg/h)	1337.1	1337.1	1337.1	25.9	2566.2	8044.6	8044.6	8044.6
Mass fraction								
CO ₂	0	0	0	0.843	0.843	0.659	0.659	0.659
CO	0	0	0	0.015	0.015	0.012	0.012	0.012
DME	1	1	1	0.032	0.032	0.002	0.002	0.002
H ₂	0	0	0	0.11	0.11	0.093	0.093	0.093
MeOH	0	0	0	0	0	0.094	0.094	0.094
Water	0	0	0	0	0	0.14	0.14	0.14
O ₂	0	0	0	0	0	0	0	0
N ₂	0	0	0	0	0	0	0	0
Propylene	0	0	0	0	0	0	0	0
Methane	0	0	0	0	0	0	0	0
Ethane	0	0	0	0	0	0	0	0
Propane	0	0	0	0	0	0	0	0
	24	25	26	27	28	29	30	31
Temperature (°C)	36	36	36	36	36	125	128.5	217.1
Pressure (bar)	35	35	35	35	35	35	35	35
Vapor Fraction	0.848	1	0	1	1	0.01	0.011	0.02
Mass flow (kg/h)	8044.6	6045.5	1999.1	4225.5	1820	1999.1	1999.1	631.6
Mass fraction								
CO ₂	0.659	0.849	0.084	0.849	0.849	0.084	0.084	0
CO	0.012	0.016	0	0.016	0.016	0	0	0
DME	0.002	0.003	0.001	0.003	0.003	0.001	0.001	0.009
H ₂	0.093	0.123	0	0.123	0.123	0	0	0
MeOH	0.094	0.007	0.358	0.007	0.007	0.358	0.358	0.253
Water	0.14	0.002	0.556	0.002	0.002	0.556	0.556	0.738
O ₂	0	0	0	0	0	0	0	0
N ₂	0	0	0	0	0	0	0	0
Propylene	0	0	0	0	0	0	0	0
Methane	0	0	0	0	0	0	0	0
Ethane	0	0	0	0	0	0	0	0
Propane	0	0	0	0	0	0	0	0
	32	33	34	35	36	37	38	39
Temperature (°C)	200	203.1	220	185.8	241.4	135.7	38.7	81.4
Pressure (bar)	35	35	35	35	35.14	35.14	35.14	35
Vapor Fraction	0.137	0.112	0.468	1	0	0	0	0.974
Mass flow (kg/h)	1999.1	2630.7	2630.7	1038.1	1592.6	1592.6	1592.6	52.6
Mass fraction								
CO ₂	0.084	0.064	0.064	0.162	0	0	0	0.714
CO	0	0	0	0.001	0	0	0	0.013

DME	0.001	0.003	0.003	0.008	0	0	0	0.004
H ₂	0	0	0	0	0	0	0	0.099
MeOH	0.358	0.332	0.332	0.828	0.01	0.01	0.01	0.169
Water	0.556	0.6	0.6	0.001	0.99	0.99	0.99	0.002
O ₂	0	0	0	0	0	0	0	0
N ₂	0	0	0	0	0	0	0	0
Propylene	0	0	0	0	0	0	0	0
Methane	0	0	0	0	0	0	0	0
Ethane	0	0	0	0	0	0	0	0
Propane	0	0	0	0	0	0	0	0
	40	41	42	43	44	45	46	47
Temperature (°C)	73.4	193	200	22.5	180	200	15	64.4
Pressure (bar)	35	35	35	40	40	40	1	1
Vapor Fraction	0.979	1	1	1	1	1	0	0
Mass flow (kg/h)	6701.6	6701.6	6701.6	5885.1	5885.1	5885.1	5404.6	5404.6
Mass fraction								
CO ₂	0.751	0.751	0.751	0.854	0.854	0.854	0	0
CO	0.01	0.01	0.01	0.012	0.012	0.012	0	0
DME	0.003	0.003	0.003	0.015	0.015	0.015	0	0
H ₂	0.103	0.103	0.103	0.118	0.118	0.118	0	0
MeOH	0.131	0.131	0.131	0.002	0.002	0.002	0	0
Water	0.001	0.001	0.001	0.001	0.001	0.001	1	1
O ₂	0	0	0	0	0	0	0	0
N ₂	0	0	0	0	0	0	0	0
Propylene	0	0	0	0	0	0	0	0
Methane	0	0	0	0	0	0	0	0
Ethane	0	0	0	0	0	0	0	0
Propane	0	0	0	0	0	0	0	0
	48	49	50	51	52	53	54	55
Temperature (°C)	65.5	64.4	168	250.4	25	25	273.2	251.7
Pressure (bar)	40	1	40	40	1.01	1.01	1.01	1.01
Vapor Fraction	0	0	0	1	1	1	1	1
Mass flow (kg/h)	2567.2	2837.4	2567.2	2549.2	171.7	4121.4	4810.6	4810.6
Mass fraction								
CO ₂	0	0	0	0	0.008	0	0.111	0.111
CO	0	0	0	0	0	0	0	0
DME	0	0	0	0	0	0	0	0
H ₂	0	0	0	0	0	0	0	0
MeOH	0	0	0	0	0	0	0	0
Water	1	1	1	1	0	0	0.093	0.093
O ₂	0	0	0	0	0	0.222	0.057	0.057
N ₂	0	0	0	0	0.008	0.778	0.739	0.739
Propylene	0	0	0	0	0	0	0	0
Methane	0	0	0	0	0.904	0	0	0
Ethane	0	0	0	0	0.075	0	0	0
Propane	0	0	0	0	0.005	0	0	0
	56	57	58	59	60	61	62	63
Temperature (°C)	250.4	250.4	230	210.9	178	178	178	178
Pressure (bar)	40	40	40	40	9.55	9.55	9.55	9.55
Vapor Fraction	0.507	0.186	0	0	0.094	0.609	0.471	0.229
Mass flow (kg/h)	2549.2	2549.2	2549.2	2549.2	2549.2	2549.2	2549.2	1780
Mass fraction								
CO ₂	0	0	0	0	0	0	0	0
CO	0	0	0	0	0	0	0	0
DME	0	0	0	0	0	0	0	0

7. Techno-economic assessment of the CO₂-to-DME process

H ₂	0	0	0	0	0	0	0	0
MeOH	0	0	0	0	0	0	0	0
Water	1	1	1	1	1	1	1	1
O ₂	0	0	0	0	0	0	0	0
N ₂	0	0	0	0	0	0	0	0
Propylene	0	0	0	0	0	0	0	0
Methane	0	0	0	0	0	0	0	0
Ethane	0	0	0	0	0	0	0	0
Propane	0	0	0	0	0	0	0	0
	64	65	66	67	68	69	70	71
Temperature (°C)	178	25	25	31	80.1	87.8	99.6	34.9
Pressure (bar)	9.55	1	1	1	1	1	1	1
Vapor Fraction	0	0	0	0	0	0	0.007	0
Mass flow (kg/h)	1780	17295	64855	17295	17295	17295	17295	64855
Mass fraction								
CO ₂	0	0	0	0	0	0	0	0
CO	0	0	0	0	0	0	0	0
DME	0	0	0	0	0	0	0	0
H ₂	0	0	0	0	0	0	0	0
MeOH	0	0	0	0	0	0	0	0
Water	1	1	1	1	1	1	1	1
O ₂	0	0	0	0	0	0	0	0
N ₂	0	0	0	0	0	0	0	0
Propylene	0	0	0	0	0	0	0	0
Methane	0	0	0	0	0	0	0	0
Ethane	0	0	0	0	0	0	0	0
Propane	0	0	0	0	0	0	0	0
	72	73	74	75	76	77	78	79
Temperature (°C)	37.3	52	52	178	81.3	15	91.1	25
Pressure (bar)	1	1	1	9.55	0.5	1	2.43	2.43
Vapor Fraction	0	0	0	1	0.905	1	1	1
Mass flow (kg/h)	64855	83167	1820.2	1780	1780	2628.6	2628.6	2628.6
Mass fraction								
CO ₂	0	0	0	0	0	1	1	1
CO	0	0	0	0	0	0	0	0
DME	0	0	0	0	0	0	0	0
H ₂	0	0	0	0	0	0	0	0
MeOH	0	0	0	0	0	0	0	0
Water	1	1	1	1	1	0	0	0
O ₂	0	0	0	0	0	0	0	0
N ₂	0	0	0	0	0	0	0	0
Propylene	0	0	0	0	0	0	0	0
Methane	0	0	0	0	0	0	0	0
Ethane	0	0	0	0	0	0	0	0
Propane	0	0	0	0	0	0	0	0
	80	81	82	83	84	85	86	87
Temperature (°C)	102.6	25	103.1	25	102.7	100	100	100
Pressure (bar)	5.9	5.9	14.4	14.4	35	35	35	35
Vapor Fraction	1	1	1	1	1	1	1	1
Mass flow (kg/h)	2628.6	2628.6	2628.6	2628.6	2628.6	2628.6	1314.3	1314.3
Mass fraction								
CO ₂	1	1	1	1	1	1	1	1
CO	0	0	0	0	0	0	0	0
DME	0	0	0	0	0	0	0	0
H ₂	0	0	0	0	0	0	0	0

MeOH	0	0	0	0	0	0	0	0
Water	0	0	0	0	0	0	0	0
O ₂	0	0	0	0	0	0	0	0
N ₂	0	0	0	0	0	0	0	0
Propylene	0	0	0	0	0	0	0	0
Methane	0	0	0	0	0	0	0	0
Ethane	0	0	0	0	0	0	0	0
Propane	0	0	0	0	0	0	0	0
	88	89	90	91	92	93	94	95
Temperature (°C)	49.1	63	15	15	15	29.2	133.8	130.6
Pressure (bar)	35	40	35	35	35	40	15	15
Vapor Fraction	1	1	1	1	1	1	1	1
Mass flow (kg/h)	3134.3	3134.3	360.9	184.5	176.4	184.5	5470.5	5470.5
Mass fraction								
CO ₂	0.912	0.912	0	0	0	0	0	0
CO	0.009	0.009	0	0	0	0	0	0
DME	0.002	0.002	0	0	0	0	0	0
H ₂	0.071	0.071	1	1	1	1	0	0
MeOH	0.004	0.004	0	0	0	0	0	0
Water	0.001	0.001	0	0	0	0	0	0
O ₂	0	0	0	0	0	0	0	0
N ₂	0	0	0	0	0	0	0	0
Propylene	0	0	0	0	0	0	1	1
Methane	0	0	0	0	0	0	0	0
Ethane	0	0	0	0	0	0	0	0
Propane	0	0	0	0	0	0	0	0
	96	97	98	99				
Temperature (°C)	35	-48	-42.4	4.3				
Pressure (bar)	15	1	1	1				
Vapor Fraction	0	0.552	1	1				
Mass flow (kg/h)	5470.5	5470.5	5470.5	5470.5				
Mass fraction								
CO ₂	0	0	0	0				
CO	0	0	0	0				
DME	0	0	0	0				
H ₂	0	0	0	0				
MeOH	0	0	0	0				
Water	0	0	0	0				
O ₂	0	0	0	0				
N ₂	0	0	0	0				
Propylene	1	1	1	1				
Methane	0	0	0	0				
Ethane	0	0	0	0				
Propane	0	0	0	0				

F.2 Reactor model

The reactor model relies on the same hypothesis reported in Chapter 2.

The methanol synthesis is assumed to follow the kinetic of Portha et al. [56], while the methanol dehydration to DME over a HZSM-5 catalyst, follows the kinetic of Ortega et al. [57]. The kinetic model is described in Chapter 6, together with its

experimental validation. The CM08 (Chapter 3) membrane properties were implemented in the PBMR, as described in Chapter 6.

The model equations are also reported here for both the PBR and PBMR, for completion.

PBR model

Mole balances were solved for each component according to the following equation:

$$\frac{dF_i}{dz} = \frac{\pi}{4} (D_{ri}^2) D_{cat} (1 - \varepsilon) \left[\sum_{j=1}^{N_{r,cat1}} (r_{j,cat1} \nu_{ji,cat1}) x_{vol,cat1} \rho_{cat1} + \sum_{j=1}^{N_{r,cat2}} (r_{j,cat2} \nu_{ji,cat2}) x_{vol,cat2} \rho_{cat2} \right] \quad (F.1)$$

Where F_i is the mole flow rate of component i , D_{ri} is the reactor inner diameter, D_{cat} is the catalyst dilution factor based on volume, ε is the bed porosity (assumed $0.4 \text{ m}_{void}^3/\text{m}_{reactor}^3$), r_j is the reaction rate of reaction j , ν_{ji} is the stoichiometric number of component i in reaction j , ρ_{cat} is the catalyst density and x_{vol} is the volumetric fraction of each catalyst. The subscript cat1 and cat2 stand for the Cu/ZnO/Al₂O₃ (CuZA) and HZSM-5 catalyst, respectively.

The energy balance is described as follows:

$$\sum_{i=1}^{N_s} (F_i c_{p_i}) \frac{dT}{dz} = \frac{\pi}{4} (D_{ri}^2) D_{cat} \cdot (1 - \varepsilon) \left[\sum_{j=1}^{N_{r,cat1}} (-\Delta H_{j,cat1}) (r_{j,cat1} \nu_{ji,cat1}) x_{vol,cat1} \rho_{cat1} + \sum_{j=1}^{N_{r,cat2}} (-\Delta H_{j,cat2}) (r_{j,cat2} \nu_{ji,cat2}) x_{vol,cat2} \rho_{cat2} \right] - U(T - T_w) \pi D_{ri} \quad (F.2)$$

Where ΔH_j is the heat of reaction determined at the temperature T , T_w is the temperature of the boiling water flowing in the external jacket and U is the global heat transfer coefficient, calculated as reported in Appendix E.

The pressure drops are determined via the Ergun equation, as follows:

$$\frac{dP}{dz} = \frac{150 \mu_{mix} (1 - \varepsilon)^2 v}{\varepsilon^3 d_p^2} + \frac{1.75 (1 - \varepsilon) \rho_{mix} v^2}{\varepsilon^3 d_p} \quad (F.3)$$

A macroscopic heat balance for the boiling water is solved to determine the mass flow of water required (\dot{m}_w) in order to exchange only latent heat (i.e., the heat of vaporization) and to produce steam (Eq. F.4-F.5).

$$\frac{dQ}{dz} = \pi D_{ro} U (T - T_w) \quad (F.4)$$

$$\dot{m}_w = \frac{Q(@z = L)}{\Delta H_{\text{vap, mass}}} \quad (F.5)$$

Where Q is the heat exchanged, D_{ro} the reactor outer diameter and $\Delta H_{\text{vap, mass}}$ the heat of vaporization of water at the temperature T_w , defined per unit of mass.

The catalyst mass in the reactor was optimized using the gas hourly space velocity (GHSV) defined as follows:

$$\text{GHSV} = \frac{F_{in}}{V_{cb}} \quad (F.6)$$

With F_{in} the total molar flow rate in the packed bed side and V_{cb} the volume of the reactor available for the catalytic bed (i.e., inner reactor volume).

As common practice in the design of heat exchangers, the diameter of the reactor jacket is sized according to a maximum pressure drop of the boiling water flowing. The pressure drop in the shell side is determined according to the following equations [58]:

$$\Delta P_{\text{shell}} = f \frac{1}{2} \rho_w \left(\frac{u_w}{\rho_w A_{\text{shell}}} \right)^2 \quad (F.7)$$

$$f = \exp(0.576 - 0.19 \ln(\text{Re}_w)) \quad (F.8)$$

$$\text{Re}_w = \frac{\rho_w u_w D_{si}}{\mu_w} \quad (F.9)$$

Where with the subscript w we indicate the physical properties of the boiling water. As a result, the shell or jacket diameter was determined via a trial and error procedure, assuming a maximum pressure drop of 0.5 bar, which is typical for heat exchangers.

PBMR model

Mole balances were solved for each component in the reaction (R) and permeation (P) zone according to Eq. F.10 and F.11, respectively.

$$\frac{dF_i^R}{dz} = \frac{\pi}{4} (D_{ri}^2 - N_m D_{mo}^2) D_{cat} \cdot (1 - \varepsilon) \cdot \left[\sum_{j=1}^{N_{r,cat1}} (r_{j,cat1} v_{j,cat1}) x_{vol,cat1} \rho_{cat1} + \sum_{j=1}^{N_{r,cat2}} (r_{j,cat2} v_{j,cat2}) x_{vol,cat2} \rho_{cat2} \right] - J_i N_m \pi D_{mo} \quad (F.10)$$

$$\frac{dF_i^P}{dz} = J_i N_m \pi D_{mo} \quad (F.11)$$

With N_m the number of membranes and D_{mo} the membrane outer diameter. The permeation flux of each species (J_i) is defined as in Chapter 2 and 6, using the permeation properties of the membrane CM08, fitted with the Arrhenius equation, as in Chapter 6.

Given that the flow of the sweep gas is the same as the feed flow to the reaction zone and that the heat transfer between the membrane module and the reaction side is fast, an overall energy balance between the membrane and the reactor can be solved (Eq. F.12), assuming that the two zones are at the same temperature (i.e., $T^R = T^P$).

$$\sum_{i=1}^{N_s} (F_i^R c_{p_i}^R + F_i^P c_{p_i}^P) \frac{dT^R}{dz} = \frac{\pi}{4} (D_{ri}^2) D_{cat} \cdot (1 - \varepsilon) \cdot \left[\sum_{j=1}^{N_{r,cat1}} (-\Delta H_{j,cat1}) (r_{j,cat1} v_{j,cat1}) x_{vol,cat1} \rho_{cat1} + \sum_{j=1}^{N_{r,cat2}} (-\Delta H_{j,cat2}) (r_{j,cat2} v_{j,cat2}) x_{vol,cat2} \rho_{cat2} \right] - U(T^R - T_w) \pi D_{ri} \quad (F.12)$$

The global heat transfer coefficient is determined as in the PBR model, considering the cross section of the reactor being modified by the introduction of the membranes.

The pressure drops are determined only for the reaction side (Ergun equation) and are considered negligible for the permeation side. The design of the external jacket is carried out in the same way of the PBR.

F.3 Methods for the evaluation of the purchase equipment cost

In this section the correlations and factors used for the calculation of the PEC are summarized.

Reactor units

The reactor vessel and cooling jacket is assumed to be a shell-and-tube heat exchanger. The reactor PEC is calculated as follows [31]:

$$C_P = F_P F_M F_L C_B \quad (\text{F.13})$$

$$F_M = 1 + \left(\frac{A}{100}\right) \quad (\text{F.14})$$

$$F_P = 0.9803 + 0.018 \left(\frac{P}{100}\right) + 0.0017 \left(\frac{P}{100}\right)^2 \quad (\text{F.15})$$

$$C_B = \exp(11.0545 - 0.9228 \ln(A) + 0.09861 (\ln(A))^2) \quad (\text{F.16})$$

Where A is the mass transfer area in ft² and P is the total pressure in psig. The CE of the reference year for the reactor cost is 394.

Flash drums

The PEC of the flash drums is calculated according to Eq. F.17-F.19, with the reference CE of 394 [31]. The cost term C_{PL} in Eq. F.17 refers to the added cost for platform and ladders and depends on the size of the vessel (Eq. F.19).

$$C_P = F_M C_V + C_{PL} \quad (\text{F.17})$$

$$C_V = \exp(7.0132 + 0.18255 \ln(w) + 0.02297 (\ln(w))^2) \quad (\text{F.18})$$

$$C_{PL} = 361.8D_i^{0.7396}L^{0.70684} \quad (\text{F.19})$$

In Eq. F.18-F.19, w is the weight of the shell and the two heads in lb, D_i and L are the diameter and length of the vessel in ft. Carbon steel is used as material, which results in a F_M of 1. Details for the flash drums of the conventional and MR-assisted process are given in **Table F3**.

Table F3. Specifications of the flash drums necessary for the calculation of the PEC

	Conventional process	MR-assisted process
Flash drum V1		
Length (ft)	12	12
Diameter (ft)	3.5	3
Weight (lb)	18265	15601
Flash drum V2		
Length (ft)	-	12
Diameter (ft)	-	3
Weight (lb)	-	12557

Distillation towers

The PEC of the distillation towers is calculated according to Eq. F.20-F.25, with the reference CE of 394 [31]. The C_P needs to account also for the costs of the trays (C_T) given by Eq. F.23-F.25.

$$C_P = F_M C_V + C_{PL} + C_T \quad (F.20)$$

$$C_V = \exp(7.2756 + 0.18255 \ln(w) + 0.02297 (\ln(w))^2) \quad (F.21)$$

$$C_{PL} = 300.9 D_i^{0.63316} L^{0.80161} \quad (F.22)$$

$$C_T = N_T F_{NT} F_{TT} F_{TM} C_{BT} \quad (F.23)$$

$$F_{NT} = \frac{2.25}{1.0414^{N_T}} \text{ if } F_{NT} < 20 \text{ and } F_{NT} = 1 \text{ if } F_{NT} \geq 20 \quad (F.24)$$

$$C_{BT} = 468 \exp(0.1739 D_i) \quad (F.25)$$

Where N_T is the number of stages, w is the weight of the shell and the two heads in lb, D_i and L are the diameter and length of the vessel in ft. Carbon steel is used as material, which results in a F_M of 1. Details of the distillation towers of the conventional and MR-assisted process are given in **Table F4**.

Table F4. Specifications of the distillation towers necessary for the calculation of the PEC

	Conventional process	MR-assisted process
Distillation tower T1		
Length (ft)	50	58
Diameter (ft)	1.8	1.5
Weight (lb)	17300	15000
Number of trays (-)	15	18
Distillation tower T2		
Length (ft)	38	42
Diameter (ft)	1.4	105
Weight (lb)	5100	6500
Number of trays (-)	11	12
Distillation tower T3		
Length (ft)	70	60
Diameter (ft)	1.2	1.5
Weight (lb)	21100	25800
Number of trays (-)	22	18

Heat exchangers

The cost of the heat exchangers is determined according to the method reported by the book of R. Smith [32] (Eq. F.26), for which the reference CE index is 435.8.

$$C_P = C_B \left(\frac{Q}{Q_B} \right)^M F_M F_P F_T \quad (F.26)$$

Where C_B is the base cost for the heat exchangers (32800 \$), M is the scaling factor, Q is the capacity of the heat exchanger, which corresponds to its heat transfer area

and Q_B is the base case capacity (80 m²). The C_B is then multiplied by three correction factors: F_M for the material, F_P for the design pressure and F_T for the design temperature. The capacity factors and the correction factors adopted for all the heat exchangers for the conventional and MR-assisted process are reported in **Table F5** and **Table F6**, respectively.

Table F5. Capacity factors and correction factors for the calculation of the PEC of the heat exchangers of the conventional one-step DME production process.

Conventional process							
Heat exchanger	C_B (\$)	Q (m ²)	Q_B (m ²)	M	F_M	F_P	F_T
E1	32800	99.8	80	0.68	1	1.5	1.6
E2	32800	16.8	80	0.68	1	1.5	1
E3	32800	28.9	80	0.68	1	1.5	1
E4	32800	23.6	80	0.68	1	1.5	1
E5	32800	24.0	80	0.68	1	1.5	1
E6	32800	3.5	80	0.68	1	1.5	1
E7	32800	13.5	80	0.68	1	1.5	1
E8	32800	10.7	80	0.68	1	1.5	1
E9	32800	7.3	80	0.68	1	1.5	1.6
E10	32800	2.8	80	0.68	1	1.5	1
E11	32800	19.3	80	0.68	1	1.5	1
E12	32800	0.1	80	0.68	1	1.5	1
E13	32800	4.0	80	0.68	1	1	1.6
E14	32800	6.2	80	0.68	1	1.5	1.6
E15	32800	3.9	80	0.68	1	1.5	1.6
E16	32800	0.5	80	0.68	1	1.5	1.6
E17	32800	1.5	80	0.68	1	1.5	1
E18	32800	1.9	80	0.68	1	1.5	1.6
E19	32800	2.1	80	0.68	1	1.5	1
E20	32800	0.5	80	0.68	1	1.5	1
E21	32800	251	80	0.68	1	1	1

Table F6. Capacity factors and correction factors for the calculation of the PEC of the heat exchangers of the MR-assisted one-step DME production process.

MR-assisted process							
Heat exchanger	C_B (\$)	Q (m ²)	Q_B (m ²)	M	F_M	F_P	F_T
E1	32800	54.4	80	0.68	1	1.5	1.6
E2	32800	43.2	80	0.68	1	1.5	1
E3	32800	9.1	80	0.68	1	1.5	1
E4	32800	45.7	80	0.68	1	1.5	1.6
E5	32800	70.0	80	0.68	1	1.5	1
E6	32800	0.1	80	0.68	1	1.5	1.6
E7	32800	2.5	80	0.68	1	1.5	1.6
E8	32800	8.6	80	0.68	1	1.5	1.6
E9	32800	16.2	80	0.68	1	1.5	1
E10	32800	12.0	80	0.68	1	1.5	1
E11	32800	1.6	80	0.68	1	1.5	1.6

E12	32800	11.9	80	0.68	1	1.5	1
E13	32800	1.8	80	0.68	1	1.5	1
E14	32800	134	80	0.68	1	1	1.6
E15	32800	16.3	80	0.68	1	1.5	1.6
E16	32800	9.6	80	0.68	1	1	1
E17	32800	4.6	80	0.68	1	1.5	1.6
E18	32800	9.6	80	0.68	1	1.5	1.6
E19	32800	0.7	80	0.68	1	1.5	1.6
E20	32800	1.0	80	0.68	1	1.5	1
E21	32800	1.4	80	0.68	1	1	1
E22	32800	0.1	80	0.68	1	1	1
E23	32800	6.0	80	0.68	1	1.5	1
E24	32800	2.1	80	0.68	1	1.5	1
E25	32800	93.5	80	0.68	1	1	1
E26	32800	2.0	80	0.68	1	1	1
E27	32800	0.7	80	0.68	1	1	1

Compressors and Turbines

The cost of compressors and turbines is also estimated using the method proposed by the book of R. Smith, using Eq. F.26. The parameters used together with the capacities of all the compressors and the steam turbines used in the conventional and MR-assisted process are summarized in **Table F7** and **Table F8**, respectively. The reference CE index is 435.8 and 525.4 for the compressors and turbines, respectively [26], [59].

Table F7. Capacity factors and correction factors for the calculation of the PEC of compressors and turbines of the conventional one-step DME production process.

Unit	Conventional process						
	C _B (\$)	Q (m ²)	Q _B (m ²)	M	F _M	F _P	F _T
C1	98400	58.1	250	0.46	1	1	1
C2	98400	62.4	250	0.46	1	1	1
C3	98400	62.8	250	0.46	1	1	1
C4	98400	73.0	250	0.46	1	1.5	1
C5	98400	788.3	250	0.46	1	1.5	1
C6	98400	24.2	250	0.46	1	1.5	1
C7	98400	5.0	250	0.46	1	1	1
TURB	38.5·10 ⁶	264	200·10 ³	0.7	1	1.5	1

Table F8. Capacity factors and correction factors for the calculation of the PEC of compressors and turbines of the MR-assisted one-step DME production process.

Conventional process							
Unit	C _B (\$)	Q (m ²)	Q _B (m ²)	M	F _M	F _P	F _T
C1	98400	49.2	250	0.46	1	1	1
C2	98400	50.8	250	0.46	1	1	1
C3	98400	51.1	250	0.46	1	1	1
C4	98400	50.9	250	0.46	1	1.5	1
C5	98400	22.7	250	0.46	1	1.5	1
C6	98400	10.5	250	0.46	1	1.5	1
C7	98400	372.4	250	0.46	1	1.5	1
C8	98400	2.1	250	0.46	1	1	1
TURB	38.5·10 ⁶	197	200·10 ³	0.7	1	1.5	1

HP steam generation and cooling tower

The costs of the cooling tower and of the equipment required for the generation of the HP steam (i.e., pump and boiler) are evaluated again using Eq. F.26, using a reference CE index of 435.8. The capacity factor for the cooling tower, boiler and pump is the flow of water (m³/h), the steam produced (kg/h) and the power (kW), respectively. An overview for both the conventional and MR-assisted process is given in **Table F9**.

Table F9. Capacity factors and correction factors for the calculation of the PEC of compressors and turbines of the MR-assisted one-step DME production process.

Unit	C _B (\$)	Q (m ²)	Q _B (m ²)	M	F _M	F _P	F _T
Conventional process							
Cooling tower	4.43·10 ³	153 m ³ /h	10 m ³ /h	0.63	1	1	1
Boiler	3.28·10 ⁵	2846 kg/h	20·10 ³ kg/h	0.81	1	1.5	1.6
Pump	1.97·10 ³	4.18 kW	1 kW	0.35	1	1.5	1
MR-assisted process							
Cooling tower	4.43·10 ³	83.4 m ³ /h	10 m ³ /h	0.63	1	1	1
Boiler	3.28·10 ⁵	2549kg/h	20·10 ³ kg/h	0.81	1	1.5	1.6
Pump	1.97·10 ³	4.05 kW	1 kW	0.35	1	1.5	1

F.4 Supplementary equations for the economic analysis

The labor requirement depends on the number of operators required on site (N_{OL}), which is calculated according to Eq. F.27. Here, P is the number of solid handling steps (zero in this case) and N is the number of non-particulate processing steps (i.e., compression, heating, cooling, mixing and reaction). For each N_{OL}, 4 operators are considered, since the plant operates 24 h/day and for 8000 h/year, with shifts of 8 h per operator.

$$N_{OL} = (6.29 + 31.7 P^2 + 0.23 N)^{0.5} \quad (\text{F.27})$$

The ACAPEX is determined by multiplying the CAPEX by the annualization factor, as shown in the following equation:

$$\text{ACAPEX} = \text{CAPEX} \cdot \frac{r(1+r)^{L_t}}{(1+r)^{L_t} - 1} \quad (\text{F.28})$$

Where r corresponds to the average cost of capital (WACC) and L_t to the assumed lifetime of the plant. The WACC is given in Eq. F.29, where D_R is the debt ratio, i_d the debt interest rate and i_e is the cost of equity.

$$\text{WACC} = D_R \cdot i_d + (1 - D_R) \cdot i_e \quad (\text{F.29})$$

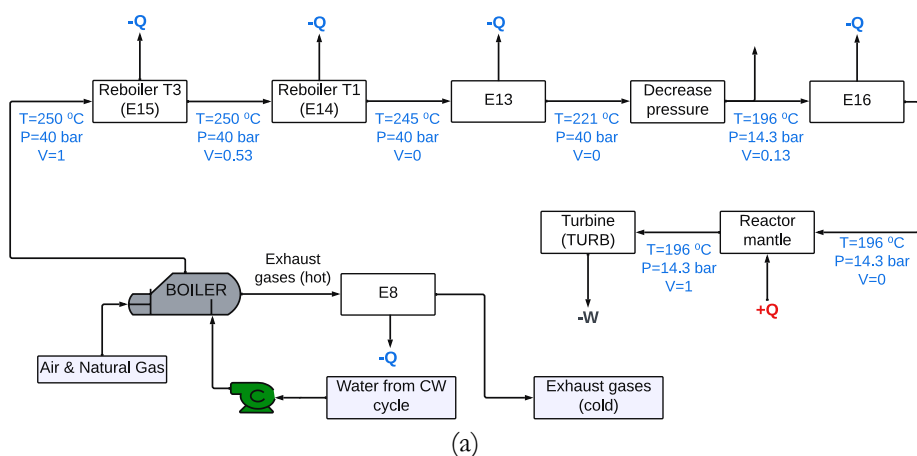
The minimum DME selling price (MDSP) was determined based on the discounted cash flow (DCF) analysis, setting the net present value (NPV) equal to zero and the interest rate equal to the discount rate (IRR), as in Eq. F.30.

$$\sum_{n=1}^{L_t} \frac{CF_n}{(1 + \text{IRR})^n} = 0 \quad (\text{F.30})$$

CF_n corresponds to the cash flow at the year n and is defined in Eq. F.31, where P_n is the gross profit, t is the tax rate and D_n is the depreciation.

$$CF_n = P_n(1 - t) + D_n t \quad (\text{F.31})$$

F.5 Supplementary figures



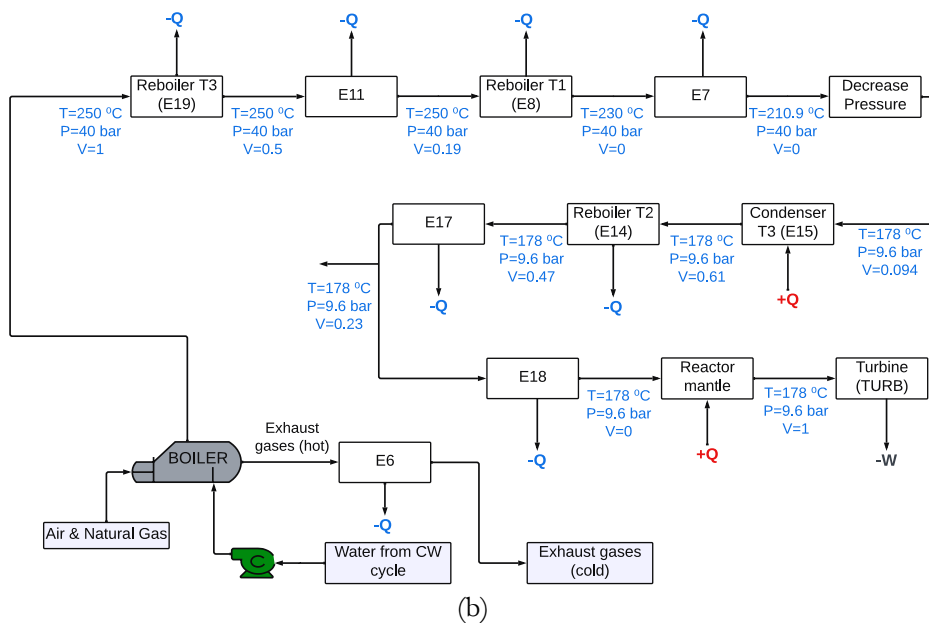


Figure F1. Overview and details of the HP steam generation and cycle for the conventional (a) and MR-assisted (b) one-step DME production process.

REFERENCES

- [1] M. De Falco, M. Capocelli, A. Basile, and C. B. Roma, "ScienceDirect Selective membrane application for the industrial one-step DME production process fed by CO₂ rich streams : Modeling and simulation," *Int. J. Hydrogen Energy*, vol. 42, no. 10, pp. 6771–6786, 2017,
- [2] P. Rodriguez-Vega *et al.*, "Experimental implementation of a catalytic membrane reactor for the direct synthesis of DME from H₂+CO/CO₂," *Chem. Eng. Sci.*, vol. 234, 2021,
- [3] A. Ateka, P. Rodriguez-Vega, T. Cordero-Lanzac, J. Bilbao, and A. T. Aguayo, "Model validation of a packed bed LTA membrane reactor for the direct synthesis of DME from CO/CO₂," *Chem. Eng. J.*, vol. 408, no. October 2020, 2021,
- [4] M. Farsi, A. Hallaji Sani, and P. Riasatian, "Modeling and operability of DME production from syngas in a dual membrane reactor," *Chem. Eng. Res. Des.*, vol. 112, pp. 190–198, 2016,
- [5] N. Diban, A. M. Urtiaga, I. Ortiz, J. Erenãa, J. Bilbao, and A. T. Aguayo, "Improved performance of a PBM reactor for simultaneous CO₂ capture and DME synthesis," *Ind. Eng. Chem. Res.*, vol. 53, no. 50, pp. 19479–19487, 2014,
- [6] S. Poto, F. Gallucci, and M. F. Neira, "Direct conversion of CO₂ to dimethyl ether in a fixed bed membrane reactor : Influence of membrane properties and process conditions," *Fuel*, vol. 302, no. February, p. 121080, 2021,
- [7] M. De Falco, M. Capocelli, and A. Giannattasio, "Membrane Reactor for one-step DME synthesis process: Industrial plant simulation and optimization," *J. CO₂ Util.*, vol. 22, no. July, pp. 33–43, 2017,
- [8] H. Hamedi and T. Brinkmann, "Valorization of CO₂ to DME using a membrane reactor: A theoretical comparative assessment from the equipment to flowsheet level," *Chem. Eng. J. Adv.*, vol. 10, no. January, p. 100249, 2022,
- [9] S. Michailos, S. Mccord, V. Sick, G. Stokes, and P. Styring, "Dimethyl ether synthesis via captured CO₂ hydrogenation within the power to liquids concept : A techno-economic assessment," *Energy Convers. Manag.*, vol. 184, no. October 2018, pp. 262–276, 2019,
- [10] K. Atsonios, K. D. Panopoulos, and E. Kakaras, "Investigation of technical and economic aspects for methanol production through CO₂ hydrogenation," *Int. J. Hydrogen Energy*, vol. 41, no. 4, pp. 2202–2214, 2016,
- [11] J. Zhang, Z. Li, Z. Zhang, R. Liu, B. Chu, and B. Yan, "Techno-Economic Analysis of Integrating a CO₂Hydrogenation-to-Methanol Unit with a Coal-to-Methanol Process for CO₂Reduction," *ACS Sustain. Chem. Eng.*, vol. 8, no. 49, pp. 18062–18070, 2020,
- [12] M. Pérez-Fortes, J. C. Schöneberger, A. Boulamanti, and E. Tzimas, "Methanol synthesis using captured CO₂ as raw material: Techno-economic and environmental assessment," *Appl. Energy*, vol. 161, pp. 718–732, 2016,

- [13] G. Manzolini, A. Giuffrida, P. D. Cobden, H. A. J. van Dijk, F. Ruggeri, and F. Consonni, "Techno-economic assessment of SEWGS technology when applied to integrated steel-plant for CO₂ emission mitigation," *Int. J. Greenh. Gas Control*, vol. 94, no. February 2019, p. 102935, 2020,
- [14] S. Simoes *et al.*, "The JRC-EU-TIMES model. Assessing the long-term role of the SET Plan Energy technologies, Scientific and Policy Report by the Joint Research Center of the European Commission.," 2014.
- [15] F. Dalena, A. Senatore, A. Marino, A. Gordano, M. Basile, and A. Basile, *Methanol Production and Applications: An Overview*. Elsevier B.V., 2018.
- [16] International Organization for Standardization (ISO), "Petroleum products - Fuels (class F) - Specifications of dimethyl ether (DME) - ISO 16861." 2015. [Online]. Available: <https://www.iso.org/standard/57835.html>
- [17] "KNMI. Normale waarden temperatuur - langjarig gemiddelde 1991-2020," 2021.
- [18] Chris Winkelman and Niels Muller, "Pricing NL taxation Energy transition, carbon Webcast series 'State of Tax.'"
- [19] J. F. Portha *et al.*, "Kinetics of Methanol Synthesis from Carbon Dioxide Hydrogenation over Copper-Zinc Oxide Catalysts," *Ind. Eng. Chem. Res.*, vol. 56, no. 45, pp. 13133–13145, 2017,
- [20] C. Ortega, M. Rezaei, V. Hessel, and G. Kolb, "Methanol to dimethyl ether conversion over a ZSM-5 catalyst: Intrinsic kinetic study on an external recycle reactor," *Chem. Eng. J.*, vol. 347, no. August 2017, pp. 741–753, 2018,
- [21] J. A. Medrano, M. A. Llosa-Tanco, D. A. Pacheco-Tanaka, and F. Gallucci, *Transport mechanism and modeling of microporous carbon membranes*. Elsevier Inc., 2019.
- [22] N. Diban, A. M. Urtiaga, I. Ortiz, J. Ereña, J. Bilbao, and A. T. Aguayo, "Influence of the membrane properties on the catalytic production of dimethyl ether with in-situ water removal for the successful capture of CO₂," *Chem. Eng. J.*, vol. 234, pp. 140–148, 2013,
- [23] R. Mukherjee, "Effectively design shell-and-tube heat exchangers," *Chem. Eng. Prog.*, no. February, 1998.
- [24] T. Barletta, J. Nigg, S. Ruoss, J. Mayfield, and W. Landry, "Reprinted from: Diagnose flooding Using field pressure data , a refiner made a low-capital modification on a," no. JULY, 2001.
- [25] L. March, "Introduction to Pinch Technology," 1998.
- [26] V. Spallina *et al.*, "Techno-economic assessment of different routes for olefins production through the oxidative coupling of methane (OCM): Advances in benchmark technologies," *Energy Convers. Manag.*, vol. 154, no. September, pp. 244–261, 2017,
- [27] C. E. Baukal, *Industrial Combustion Testing*. 2010.
- [28] R. S. G. Towler, "Chapter 7 - Capital cost estimating," in *Chemical Engineering Design*,

- 2nd ed., Butterworth-Heinemann, Ed. Boston, 2013, pp. 307–354.
- [29] J.R. Couper, *Process Engineering Economics*. University of Arkansas, Fayetteville, Arkansas (USA), 2003.
- [30] T. R. Brown, *Capital cost estimating*, vol. 79, no. 10. 2000.
- [31] R. G. and K. M. N. Warren D. Seider, Daniel R. Lewin, J. D. Seader, Soemantry Widagdo, *Product and Process Design Principles - Synthesis, Analysis and Evaluation*, 4th editio. 2016.
- [32] R. Smith, *Chemical process design and integration*, Vol. 68. 2005.
- [33] M. Nordio, S. A. Wassie, M. Van Sint Annaland, D. A. Pacheco Tanaka, J. L. Viviente Sole, and F. Gallucci, “Techno-economic evaluation on a hybrid technology for low hydrogen concentration separation and purification from natural gas grid,” *Int. J. Hydrogen Energy*, vol. 46, no. 45, pp. 23417–23435, 2021,
- [34] H. Groenemans, G. Saur, C. Mittelsteadt, J. Lattimer, and H. Xu, “Techno-economic analysis of offshore wind PEM water electrolysis for H₂ production,” *Curr. Opin. Chem. Eng.*, vol. 37, p. 100828, 2022,
- [35] “Statista. Industrial prices for electricity in the Netherlands 1995-2020,” 2021.
- [36] “Methanex Monthly Average Regional Posed CO₂ Contract Price History,” 2021. [Online]. Available: <https://www.methanex.com/our-business/pricing>
- [37] “PayScale: Chemical Operator Salary in the Netherlands.” https://www.payscale.com/research/NL/Job=Chemical_Operator/Salary
- [38] F. Mac., “30-Year Fixed-Rate Mortgages Since 1971.”
- [39] C. Brencio, M. Maruzzi, G. Manzolini, and F. Gallucci, “Butadiene production in membrane reactors: A techno-economic analysis,” *Int. J. Hydrogen Energy*, vol. 47, no. 50, pp. 21375–21390, 2022,
- [40] “European Environment Agency. Greenhouse gas emission intensity of electricity generation.”
- [41] R. K. D. and H. H. Edwards R. larivé J., Rickeard D., Weindorf W., GODwin S., Hass H., Krasenbrink A., Lonza L., Nelson L. Reid A., “Well-to-tank report version 4.a: Jec well-to-wheels analysis (LD-NA-26237-EN-N),” 2014.
- [42] D. Berkely, “California Dimethyl Ether Multimedia Evaluation Tier I,” 2015.
- [43] U. Lee *et al.*, “Well-to-Wheels Emissions of Greenhouse Gases and Air Pollutants of Dimethyl Ether from Natural Gas and Renewable Feedstocks in Comparison with Petroleum Gasoline and Diesel in the United States and Europe,” *SAE Int. J. Fuels Lubr.*, vol. 9, no. 3, pp. 546–557, 2016,
- [44] A. Trattner, M. Klell, and F. Radner, “Sustainable hydrogen society – Vision, findings and development of a hydrogen economy using the example of Austria,” *Int. J. Hydrogen Energy*, vol. 47, no. 4, pp. 2059–2079, 2022,
- [45] IEA, “Energy policy review - The Netherlands 2020. Technical report.”

- [46] R. J. Detz, J. N. H. Reek, and B. C. C. Van Der Zwaan, "The future of solar fuels: When could they become competitive?," *Energy Environ. Sci.*, vol. 11, no. 7, pp. 1653–1669, 2018,
- [47] "IEA CHG Technical report. Economic Evaluation of SMR based standalone (Merchant) hydrogen plant with CCS."
- [48] K. Schoots, F. Ferioli, G. J. Kramer, and B. C. C. van der Zwaan, "Learning curves for hydrogen production technology: An assessment of observed cost reductions," *Int. J. Hydrogen Energy*, vol. 33, no. 11, pp. 2630–2645, 2008,
- [49] M. De Falco, M. Capocelli, and A. Basile, "Selective membrane application for the industrial one-step DME production process fed by CO₂ rich streams: Modeling and simulation," *Int. J. Hydrogen Energy*, vol. 42, no. 10, pp. 6771–6786, 2017,
- [50] P. Pérez-Urriarte, A. Ateka, M. Gamero, A. T. Aguayo, and J. Bilbao, "Effect of the Operating Conditions in the Transformation of DME to olefins over a HZSM-5 Zeolite Catalyst," *Ind. Eng. Chem. Res.*, vol. 55, no. 23, pp. 6569–6578, 2016,
- [51] IFRS financial reporting and analysis software., "Gross margin-breakdown by industry," 2020.
- [52] Elke Asen, "Carbon Tax in Europe," 2021.
- [53] S. Shiva Kumar and V. Himabindu, "Hydrogen production by PEM water electrolysis – A review," *Mater. Sci. Energy Technol.*, vol. 2, no. 3, pp. 442–454, 2019,
- [54] L. Bernadet, G. Gousseau, A. Chatroux, J. Laurencin, F. Mauvy, and M. Reytier, "Influence of pressure on solid oxide electrolysis cells investigated by experimental and modeling approach," *Int. J. Hydrogen Energy*, vol. 40, no. 38, pp. 12918–12928, 2015,
- [55] P. T. Chang, Q. H. Ng, A. L. Ahmad, and S. C. Low, "A critical review on the techno-economic analysis of membrane gas absorption for CO₂ capture," *Chem. Eng. Commun.*, vol. 209, no. 11, pp. 1553–1569, 2022,
- [56] S. Ghosh, J. Sebastian, L. Olsson, and D. Creaser, "Experimental and kinetic modeling studies of methanol synthesis from CO₂ hydrogenation using In₂O₃ catalyst," *Chem. Eng. J.*, vol. 416, p. 129120, 2021,
- [57] C. Ortega, M. Rezaei, V. Hessel, and G. Kolb, "Methanol to dimethyl ether conversion over a ZSM-5 catalyst: Intrinsic kinetic study on an external recycle reactor," *Chem. Eng. J.*, vol. 347, no. April, pp. 741–753, 2018,
- [58] R. Mukherjee, "Effectively design shell-and-tube heat exchangers," *Chem. Eng. Prog.*, 1998.
- [59] Smith R., *Chemical process design and integration*, Vol. 68. 2005.

CHAPTER 8

Conclusions and Outlook

8.1 CONCLUSIONS

In this work, the use of the membrane reactor technology for the in-situ removal of water in the one-step CO₂ conversion to DME was assessed at different scales and under different perspectives.

In **Chapter 2**, a 1D phenomenological reactor model was developed in order to evaluate the potential of the in-situ removal of water as means to overcome the thermodynamic limitations of the CO₂-to-DME reaction. First, a membrane reactor configuration in which a sweep gas containing the reactants (CO₂+H₂) is circulated in cocurrent mode has been proposed as effective way to simultaneously promote the removal of water and heat from the reaction environment. The model was then used to study the effect of the membrane properties, in terms of water permeance and perm-selectivity, on the reaction performance, in order to gain insights into suitable membrane materials. The optimal properties showed good agreement with the state of the art. Nevertheless, carbon molecular sieve membranes were proposed as a promising material, given their superior thermo-chemical stability in hot humid environment.

Thereafter, the effect of process conditions, such as the sweep gas ratio (SW) and the pressure gradient across the membrane (ΔP) was assessed. The SW ratio showed higher influence on the water removal than the ΔP , lowering the demands on the membrane mechanical stability. Furthermore, the circulation of a sweep gas in cocurrent mode proved an effective strategy to selectively remove the water from the reaction zone as well as to optimize the temperature profile. In this configuration, when 96% of the water is removed, CO₂ conversion and DME yield display an improvement of 36% and 43% each, with respect to a conventional packed bed reactor working in the same conditions.

In **Chapter 3** and **4**, alumina-supported carbon molecular sieve membranes (CMSM) were studied to prove their potential to selectively separate water from (H₂-rich) gaseous mixtures at relatively high temperature (i.e., 150-250 °C), conditions which are relevant for the CO₂ hydrogenation to methanol/DME reactions.

Given the possibility to easily tune the properties of these membranes for a specific separation by acting on different synthesis parameters, in this thesis, CMSM properties were modified in order to achieve the target set in **Chapter 2**.

In particular, in **Chapter 3**, boehmite nanosheets were incorporated in the dipping solution used for the preparation of the membranes, as a way to increase their hydrophilicity. Indeed, the addition of boehmite induces an optimum in the membrane affinity to water, while, at larger boehmite content, the probability for

boehmite to condense to the less hydrophilic γ -Al₂O₃ within the carbonization step increases. Boehmite was found to not significantly affect the pore size distribution of the membranes. However, the cross section of the CMSM shows an increase in the thickness of the composite carbon layer for larger boehmite content. The water permeability shows an optimum with the initial boehmite content of 0.8 wt %, which is in line with the optimum found in the hydrophilicity, despite being slightly shifted to a lower value. This shift was found to be induced by the increase in tortuosity introduced by the boehmite/alumina nanosheet at higher concentrations. For the same reason, also the water/gas perm-selectivity shows an optimum which is shifted to higher boehmite content (i.e., 1.2 wt %). Indeed, given their generally larger kinetic size with respect to water, gases (i.e., H₂, CO₂, CO, CH₄, N₂) are more affected by changes in the tortuosity of the porous structure. Furthermore, in line with the expectations, the H₂O/i selectivity generally increases for larger gas molecules, which is a clear indication of molecular sieving being the dominant mechanism of gas permeation. The water permeance and H₂O/i selectivity was found to decrease with temperature and increase with the ΔP (across the membrane), indicating that capillary condensation and adsorption diffusion can both play a significant role in the water permeation. The mechanism of water permeation was further investigated via the implementation of the *6 flow models*, which indicates that the water vapor flow through the membrane pores transform from capillary condensation to multi- and monolayer surface flow combined with molecular Knudsen gas flow, as temperature increases.

The CMSM studied in **Chapter 3** were all carbonized at the same temperature (i.e., 500 °C). However, the carbonization temperature (T_{carb}) is an important synthesis parameter to tune, since during the carbonization/pyrolysis step, the dense polymeric membrane precursor gradually transforms into a porous carbon molecular sieve membrane with completely different physicochemical properties. Thus, in **Chapter 4**, boehmite-phenolic CMSM were prepared based on the previously optimized composition (i.e., 0.8 wt % boehmite content), carbonizing the membranes in the temperature range 450-750 °C. First, via FTIR analysis, it was found that the membrane loses its OH and aliphatic CH groups for $T_{\text{carb}} \geq 600$ °C. The aromaticity, instead, disappear at higher temperatures (700-750 °C), with the resin gradually transforming into a char-like structure. The membrane hydrophilicity, studied via in-situ FTIR analysis, was found to be optimal at T_{carb} of 500 °C, to then gradually decrease with the carbonization temperature, as the hydrophilic functional groups are being removed. CMSM were found to be inert to H₂, CO and N₂, while CO₂ adsorption was found to be significant and to increase with T_{carb} , due to an increase in the surface area and to the transformation of the amine group into pyridine/pyridone structure, which displays stronger affinity to CO₂. The permeance of all gases and vapors tested showed the same behavior with T_{carb} , displaying an optimum at 600-700 °C, where the membranes are characterized by a bi-modal pore size distribution, with the largest fraction of molecular sieve (MS) pores. This led to the conclusion that the trend induced by the carbonization

temperature in the gas/vapor permeation is solely influenced by the pore size distribution.

On the other hand, the trend induced by the operating temperature is strongly influenced by the transport mechanism. Water, methanol and CO₂ permeates mostly via adsorption diffusion, while the inert gases (H₂, CO and N₂) permeates via molecular sieving. This conclusion is in line with the results found in **Chapter 3**. Nevertheless, for higher carbonization temperature, the membranes display smaller pores (i.e., in the MS region), which favors the surface diffusion over the capillary condensation for both water and methanol. Furthermore, the increasing affinity to CO₂ for higher T_{carb} also shifts the dominant mechanism from molecular sieving to adsorption diffusion.

When comparing the properties of the membranes studied in **Chapter 3-4** with the optimal properties derived in **Chapter 2**, it is clear that the target in the permeance of H₂O was achieved, while for most of the H₂O/*i* selectivity (S_{H₂O/*i*}) it was not the case. The S_{H₂O/H₂} is always the smallest perm-selectivity, due to the very similar size of the two molecules. Furthermore, S_{H₂O/CO} is always greater than S_{H₂O/CO₂}, since CO₂ shows significant affinity to the membrane surface, such that, for some membranes, adsorption diffusion dominates over molecular sieving. On the other hand, S_{H₂O/CO} and S_{H₂O/MeOH} show the expected behavior, achieving the target in most of the cases.

In **Chapter 5**, a membrane reactor, based on the incorporation of carbon molecular sieve membrane in a conventional CuO-ZnO-Al₂O₃/HZSM-5 bifunctional catalyst bed, was tested at laboratory scale for the one-step CO₂ conversion to dimethyl ether (DME). Despite the CMSM used in this work displays much higher permeance and lower H₂O/*i* selectivity than expected, given the results of previous chapter, the packed bed membrane reactor (PBMR) was found to outperform the packed bed reactor (PBR) in most of the tested conditions.

In particular, larger improvement was measured at lower space velocities, due to the system approaching thermodynamic equilibrium (i.e., larger water content). Nevertheless, the PBMR was found to improve more the formation of CO (i.e., r-WGS) over DME, especially for temperatures higher than 200 °C. Indeed, among all products, also methanol is being considerably removed from the reaction zone, reducing its possibility to be further converted into DME. Expectedly, the SW ratio was found to have a positive effect on all the reaction performance, with the removal of water achieving ca. 80% at SW=5. Given the higher permeability of this CMSM, the ΔP showed to have a negative effect on both CO₂ conversion and product yield, given the high extent of H₂ and CO₂ removal (i.e., 98-99% at ΔP of 3 bar). Finally, the reactor model previously developed in **Chapter 2** and then improved in **Chapter 6** was found to describe the performance of both the PBR and PBMR quite accurately in the range of tested conditions.

The relevant heat and mass transfer phenomena occurring at the different scales in the packed bed (membrane) reactor were investigated in **Chapter 6**. Intra-particle

diffusion limitation and concentration polarization were found to have a significant influence on the reactor performance when simulated at conditions/sizes which are relevant to large scale operation. Given the complexity of the model obtained with the incorporation of both these phenomena, short-cut methods were developed to account for such effects, to be implemented in a simplified 1D pseudo-homogeneous reactor model. In particular, a correlation for the component-specific efficiency as a function of the Thiele modulus was developed from simulation data obtained via the rigorous particle model. This correlation showed the typical behavior found in literature for simple reaction networks. To account for the concentration polarization phenomena, a Sherwood-type correlation for the calculation of the mass transfer coefficient was proposed. The parameters of the correlation were determined fitting the simulation data obtained via the 2D rigorous reactor model. When implementing this short-cut methods, the simplified model showed to predict the results of the more rigorous model with maximum deviations below 5%. The findings of this work allowed for a further optimization of both the PBR and PBMR, leading to a significant reduction in the catalyst mass as a consequence of the decrease in the optimal zeolite weight fraction required for the methanol dehydration to DME.

In **Chapter 7**, the impact of using either the PBR or the PBMR technology for the one-step conversion of CO₂ to DME was evaluated at process scale. The two processes were compared on both a technical and economic perspective. Besides the already established higher performance of the PBMR with respect to the PBR, the membrane reactor (MR) assisted plant was found to require less energy input to produce the same amount of DME, given the higher efficiency of the conversion step (i.e., reactor). Indeed, the PBMR show a cold gas efficiency of 88% versus the 76% of the PBR. On the economic aspect, both processes revealed to be OPEX intensive, with the operating cost of the MR-assisted plant being significantly lower (i.e., 23%), due to the lower requirement of catalyst and of H₂, which covers ca. 60% of the OPEX. However, despite the MR technology allows for a decrease in the minimum DME selling price (MDSP) of ca. 11%, the MDSP is still more than 3 times higher than the current DME market price. A feasibility study was carried out to predict the moment in which this technology (i.e., CO₂-to-DME) could become competitive with the benchmark (i.e., syngas conversion to DME) was carried out. It was found that, with further process optimization and with the predicted decrease of renewable H₂ price and a zero-to-negative cost for the CO₂ feedstock, the MR-assisted system could become competitive with the benchmark between 2025 to 2050.

8.2 OUTLOOK AND RECOMMENDATION FOR FUTURE RESEARCH

The use of membranes to promote the in-situ removal of water from the reaction environment proved an effective strategy to improve both the reaction and process performance of the one-step CO₂ conversion to DME.

In this work, carbon molecular sieve membranes were proposed and studied, in view of their high stability under the process conditions of interest. Since the target initially set for the properties of the membranes was only partially achieved, further optimization and investigation would be required on these materials, especially into the direction of higher H₂O/i selectivity. As an example, the membrane selectivity could be improved increasing the thickness of the selective layer, sacrificing the water permeability, which in most of the cases was found to exceed the target value. A thicker carbon layer could be obtained with the deposition of a second layer on top of the first one, repeating the dip coating, drying and carbonization step or by increasing the viscosity of the dipping solution acting on the composition (i.e., solvent/polymer ratio). Furthermore, the H₂O/CO₂ selectivity could be improved reducing the membrane affinity to CO₂, by limiting the content of N-containing groups, replacing the ethylenediamine with another component.

The membrane reactor experiments showed a considerable removal of methanol which would reduce its possibility to be further converted into DME. Thus, the H₂O/methanol selectivity was found to be another critical parameter. Given the larger kinetic diameter of methanol with respect to water (i.e., 0.38 vs 0.265 nm), this selectivity could be improved by preparing membranes with smaller pores. This could be done by using different polymeric precursors or using different types of post-treatment aimed at narrowing the pore size distribution of the membrane [1], [2]. Finally, further investigation is required in terms of the reproducibility of the CMSM. Indeed, as shown in Chapter 5, when changing one synthesis parameters (i.e., diluting the dipping solution with more solvent), the membrane properties could be enormously affected. Thus, it is very important to control all the steps involved in the membrane preparation and to optimize all the parameters for a specific application.

In order to further increase the credibility of the model developed in this work, the effect of the catalyst particle size as well as of the concentration polarization phenomena should be validated. Thus, more experiments would need to be conducted using catalyst pellets and reactors with larger diameters, able to develop relevant radial concentration gradients both at the particle and reactor scale.

Finally, to remove most of the uncertainties and to more accurately predict the conditions to make the one-step CO₂ conversion to DME an industrially attractive process, the techno-economic analysis should be repeated on a more integrated system. This means that a specific CO₂ emitting source should be selected, in order to implement the most efficient CO₂ capture technology. At the same time, the most cost effective H₂ production method should be also incorporated in the system (i.e.,

on-site H₂ production). This scenario would allow further optimization of the energy requirements, leaving as sole uncertainty the cost of electricity/natural gas.

Once covered all the previous points, the membrane reactor technology should be demonstrated at larger scale, to assess the effect of impurities in the feedstock as well as to study the membrane stability over an industrially relevant period of time. Results from this type of demonstration phase could be used to further validate the reactor and process models developed in this work, to finally have a technology ready to be implemented at industrial scale.

REFERENCES

- [1] M. Kiyono, P. J. Williams, and W. J. Koros, "Effect of polymer precursors on carbon molecular sieve structure and separation performance properties," *Carbon N. Y.*, vol. 48, no. 15, pp. 4432–4441, 2010,
- [2] H. C. Lee *et al.*, "Use of steam activation as a post-treatment technique in the preparation of carbon molecular sieve membranes," *Ind. Eng. Chem. Res.*, vol. 52, no. 3, pp. 1122–1132, 2013,

LIST OF PUBLICATIONS

JOURNAL ARTICLES

- **S. Poto**, F. Gallucci, and M.F. Neira d'Angelo, "Direct conversion of CO₂ to dimethyl ether in a fixed bed membrane reactor : Influence of membrane properties and process conditions", *Fuel*, vol. 302, no. February, p. 121080, 2021.
- **S. Poto**, J. G. H. Endepoel, M.A. Llosa-Tanco, D.A. Pacheco-Tanaka, F. Gallucci, and M.F. Neira d'Angelo, "Vapor/gas separation through carbon molecular sieve membranes: Experimental and theoretical investigation", *Int. J. Hydrogen Energy*, vol. 47, no. 21, pp. 11385–11401, 2022.
- **S. Poto**, A. Aguirre, F. Huigh, M.A. Llosa-Tanco, D.A. Pacheco-Tanaka, F. Gallucci, and M. F. Neira d'Angelo, "Carbon molecular sieve membranes for water separation in CO₂ hydrogenation reactions: effect of the carbonization temperature", *Journal of Membrane Science*, vol. 677, no. July, p. 121613, 2023.
- **S. Poto**, M.A. Llosa-Tanco, D.A. Pacheco-Tanaka, F. Gallucci, and M. F. Neira d'Angelo, "Experimental investigation of a packed bed membrane reactor for the direct conversion of CO₂ to dimethyl ether", *Submitted to Journal of CO₂ utilization*
- **S. Poto**, H.L. van den Bogaard, F. Gallucci, and M. F. Neira d'Angelo, "Evaluation of the relevant mass and heat transfer phenomena in a packed bed membrane reactor for the direct conversion of CO₂ to dimethyl ether", *Submitted to Fuel*.
- **S. Poto**, T. Vink, P. Oliver, F. Gallucci, and M. F. Neira d'Angelo, "Techno-economic assessment of the one-step CO₂ conversion to dimethyl ether in a membrane-assisted process", *Journal of CO₂ utilization*, vol. 69, p. 102419, 2023.

JOURNAL ARTICLES OUT OF THE SCOPE OF THIS THESIS

- **S. Poto**, D. Vico van Berkel, F. Gallucci, and M. F. Neira d'Angelo, "Kinetic modeling of the methanol synthesis from CO₂ and H₂ over a

CuO/CeO₂/ZrO₂ catalyst: The role of CO₂ and CO hydrogenation”, *Chem. Eng. J.*, vol. 435, no. P2, p. 134946, 2022.

- D. Caccavo, S. Cascone, **S. Poto**, G. Lamberti, and A. A. Barba, “Mechanics and transport phenomena in agarose-based hydrogels studied by compression-relaxation tests,” *Carbohydr. Polym.*, vol. 167, 2017.
- E. E. L. Maassen, R. Anastasio, **S. Poto**, R. Cardinaels, R.P. Sijbesma, L.C. van Breemen and J.P. Heuts, “Strain-induced post-curing of acrylate networks”, *J. Polym. Sci.*, vol. 59, no. 12, pp. 1200–1208, 2021.

ORAL PRESENTATIONS

- **S. Poto**, M.A. Llosa-Tanco, D. A. Pacheco-Tanaka, F. Gallucci, and M. F. Neira d’Angelo, “CO₂ direct hydrogenation to DME via membrane reactors”, International workshop on CO₂ capture and utilization, February, 16-17, 2021, *Online*.
- **S. Poto**, M.A. Llosa-Tanco, D. A. Pacheco-Tanaka, F. Gallucci, and M. F. Neira d’Angelo, “Effect of boehmite nanoparticles on alumina supported carbon molecular sieve membranes for vapor/gas permeation”, World Online Conference on Sustainable Technologies (WOCST), March, 17-19, 2021, *Online*.
- **S. Poto**, F. Gallucci, and M.F. Neira d’Angelo, “Direct conversion of CO₂ to dimethyl ether in a fixed bed membrane reactor”, 11th International Symposium on Catalysis in Membrane Reactors (CAMURE-11), March 21-24, 2021, *Online*.
- **S. Poto**, D. Vico van Berkel, F. Gallucci, and M. F. Neira d’Angelo, “Kinetic modeling of the methanol synthesis from CO₂ and H₂ over a CuO/CeO₂/ZrO₂ catalyst: The role of CO₂ and CO hydrogenation”, The 23rd Netherlands’ Catalysis and Chemistry Conference (NCCC), May 9-11, 2022, Noordwijkerhout (The Netherlands).
- **S. Poto**, F. Gallucci, and M.F. Neira d’Angelo, “Direct conversion of CO₂ to dimethyl ether in a fixed bed membrane reactor”, The 27th North American Catalysis Society Meeting (NAM-27), May 22-27, 2022, New York (USA).

- **S. Poto**, M.A. Llosa-Tanco, D. A. Pacheco-Tanaka, F. Gallucci, and M. F. Neira d'Angelo, "Vapor/gas separation through carbon molecular sieve membranes: experimental and theoretical investigation", The 15th International Conference on Catalysis in Membrane Reactors (ICCMR-15), July 31- Aug. 4, 2022, Waseda University, Tokyo (Japan).
- **S. Poto**, F. Gallucci, and M.F. Neira d'Angelo, "Direct conversion of CO₂ to dimethyl ether in a fixed bed membrane reactor", The 15th International Conference on Catalysis in Membrane Reactors (ICCMR-15), July 31- Aug. 4, 2022, Waseda University, Tokyo (Japan).

POSTER PRESENTATIONS

- **S. Poto**, T. Vink, F. Gallucci, and M. F. Neira d'Angelo, "Techno-economic assessment of the dimethyl ether synthesis via CO₂ hydrogenation: conventional vs membrane-assisted process", The 17th Netherlands' Process Technology Symposium (NPS-17), April 4-5, 2022, TU Delft, Delft (The Netherlands).
- **S. Poto**, D. Vico van Berkel, F. Gallucci, and M. F. Neira d'Angelo, "Kinetic modeling of the methanol synthesis from CO₂ and H₂ over a CuO/CeO₂/ZrO₂ catalyst: The role of CO₂ and CO hydrogenation", The 27th North American Catalysis Society Meeting (NAM-27), May 22-27, 2022, New York (USA).

ACKNOWLEDGEMENTS

Approaching the end of this journey, it seems necessary to thank all those who have accompanied, guided, and supported me during this important chapter of my life.

First and foremost, I would like to thank my supervisors, Fausto and Fernanda, for giving me the opportunity to carry out my PhD research at the Sustainable Process Engineering (SPE) group. Thank you for being not only a scientific guide, but also an example to follow in my personal growth.

Dear Fausto, thank you for believing in my abilities from the very beginning and for always finding the time to discuss my project, even for a brief chat, despite your busy schedule. Our discussions have always been stimulating for me, they have always helped me clarify my ideas and find the right path to solve various problems. Thank you for offering me the opportunity to carry out my research as part of a European project. The various collaborations with the project partners taught me a lot and contributed to my professional growth. In addition to the solid scientific guidance, I also appreciate how you are always present for all of us PhD students and your commitment to maintaining harmony in the group. Thanks also for the countless (real) coffees that made me feel at home.

Dear Fernanda, a special thank you goes to you for all the time you dedicated to me over the years. Our meetings went often beyond the scheduled time because we always had so much to talk about. You always helped me to critically analyze my results, and to think about how to make my ideas achievable, putting me in touch with other researchers, even (very) outside the university. Thank you for your countless pieces of advice that allowed me to improve and grow in so many ways. You always listened to me with great interest when I needed to sort through my results and find a logical connection between the various points, even when I came to our meetings with an indefinite number of slides. I also very much appreciated all the discussions during our Friday group meetings, where we all had the opportunity to exchange advice and ideas on how to continue with our projects. There is still so much to thank you for, but I would especially like to thank you for this last period, where even with your commitments to your new job, we still managed to chat over a coffee. I felt comfortable enough to confide my prospects for the future in you and you gave me precious advice.

Dear Luca, Joris, and Roberto, I want to thank you too in particular for helping and supporting me in one of the most challenging tasks of the project, namely the realization of the prototype. Thank you for all the meetings and for your patience. You taught me so much, even from a technical point of view. It was one of the most formative experiences of this journey, although at times it stole some of the time I preferred to devote to my research. Thank you for making fun with me of all the

absurd requests we were given about it, I very much appreciated your support, even from a moral point of view.

Thanks also to Margot and Alfredo for the fruitful collaboration. Both of you have been an important guide on this journey. Thank you for the time you dedicated to discuss my results and to revise my work. Thank you also for always being open to listen to my ideas.

To the members of the committee, Prof. Dr. Ir J. van der Schaaf, Prof. Dr. Ž. Tomović, Prof. Dr. A. Urakawa, Prof. Dr. M. De Falco, and Margot, thank you for the time you spent reading and evaluating my work and for the valuable comments that helped me to improve it.

An enormous thank you goes to the technical staff: Joris, Erik, Marlies, Peter, and Carlo, for helping me in my experimental work, always offering your support and patience to solve all the problems that arose, from setup modifications, frequent GC maintenance, and I could continue with a very long list.

A special thank you to all the students (master and bachelor). Without your collaboration, this thesis would have been much shorter. Your work was essential to complete all the projects and ideas I had in mind. Your input helped me make this thesis better. I hope I have been a good guide for you. Thanks to your work and dedication, I managed to maintain high motivation, even in difficult moments.

To all my colleagues and friends at SPE, thank you for making these four years unforgettable. I am very happy to have met people like you who made all the days spent at work light and enjoyable. Every time I felt the need to take a break, I knew I could always meet one of you at the coffee machine, available for a chat. Thank you for the support you gave me and above all, thank you for the beautiful moments we spent outside of the university, sharing drinks, karaoke nights, and occasionally even at the gym (yes, Brandon, Iolanda, Giulia, I'm referring to you in particular). Due to the various lockdowns, we didn't have many opportunities to travel together, but I will always remember our trip to Japan.

A very special thank you goes to you, Camilla, for all the emotional and technical support, thanks to which we were able to overcome difficult low motivation moments. Thank you for all the time you dedicated to listening to me, giving me advice, helping me develop my ideas and resolving my doubts. Our endless conversations have always been a great inspiration for me. I have always considered your judgment very important both in work and in life. I have always admired your determination and precision in your work. I can never thank you enough for the support you have given me during this journey. I am grateful that this experience has also given us such a beautiful friendship.

Dear Jessica, a special thank you to you too, because since we moved to Eindhoven, you have been like a second sister. We learned together to "survive" away from home and you can imagine how happy I was to know that you would also be embarking on your PhD program here in Eindhoven. You have always been there when I needed to relax, always lifting my mood, and you have always listened to me when I wanted to tell you about my work and experiences.

Being so far away from home has not been (and is not) easy at all, but I have been extremely lucky to have friends like you, Luigi, Joel, Jessica, Camilla (double thank you, as part of the group), Prakhyat and Jessica. Thank you for all the beautiful moments we have spent together. Especially during Covid, when due to lockdowns, curfews, etc. we always found a way to see each other, spend time together with good food, board games and improvised cocktails.

Un grazie va anche a tutti i miei amici/amiche che nonostante la distanza mi hanno sempre sostenuto e soprattutto a voi, Alessia e Federico (Peccoli!), per tutti i momenti di spensieratezza trascorsi insieme, e alle tante altre avventure che ci aspettano.

Un grazie davvero speciale vorrei dedicarlo a tutta la mia famiglia per il costante sostegno e la forza che avete mostrato nel vedermi lontana da casa, ma felice di poter realizzare i miei sogni. Mamma, Papá e Alessia, mi siete sempre stati vicino, mostrandovi orgogliosi di ogni traguardo raggiunto, sia personalmente che professionalmente, da sempre. Non potrei mai ringraziarvi abbastanza di tutti gli insegnamenti che mi avete dato, senza di voi non sarebbe stato possibile per me arrivare fino a questo punto. Vi voglio un bene immenso.

Finally, Fabio, the biggest thank you goes to you, for many reasons. I will never forget that hug you gave me when I told you I would stay in Eindhoven for my PhD, because, after all, we had already chosen each other, we stayed and we'll always be there for each other. I couldn't wish for anything more beautiful than what we have built together. Thank you for your unconditional support, and, above all, for your immense patience in listening to me every time I came home, sometimes with enthusiasm to tell you about my day or bring you good news, sometimes with disappointment when things didn't go as I wanted. Thank you for the lightness you give me every day, for being even happier than me for my successes and for contributing to make this journey one of the most significant experiences of my life.

Eindhoven, June 2023

Serena

CURRICULUM VITAE



Serena Poto was born on March 22, 1994 in Battipaglia, Italy. She completed her secondary (high school) education in 2013 at Liceo Scientifico E. Medi in Battipaglia. She received her Bachelor's degree in Chemical Engineering in September 2016, from the University of Salerno, Italy, for her thesis entitled: "Poro-visco-elastic behavior of agarose-based hydrogels: experimentation and modeling". Serena then enrolled in the Chemical Engineering Master's program at the same university, where she focused on innovative processes and nanotechnologies. Thanks to the Erasmus scholarship, she carried out her internship and graduation project at Eindhoven University of Technology, in the Polymer Technology group, researching photo curable polymers under the supervision of Dr. Ir. L.C.A. van Breemen, R.M. Cardinaels and Dr. R. Anastasio. She received her Master's degree in Chemical Engineering cum laude in March 2019, for her thesis entitled: "Strain induced post-curing of acrylate thermosets: effect of process conditions".

Serena began her PhD program on June 3, 2019, as part of the European project C2Fuel, in the Sustainable Process Engineering group at Eindhoven University of Technology under the supervision of Prof. Dr. Eng. F. Gallucci and Dr. M. F. Neira d'Angelo. Her research focused on the development of a membrane reactor technology to upgrade and convert carbon dioxide to dimethyl ether, a green fuel. This dissertation is a culmination of the results obtained within her PhD project.

